2004

Rare and exotic mineralogy of the western subcomplex of the Deadhorse Creek "diatreme", Northwestern Ontario

Potter, Eric Gordon

THE RARE AND EXOTIC MINERALOGY OF THE WESTERN SUBCOMPLEX OF THE DEADHORSE CREEK 'DIATREME', NORTHWESTERN ONTARIO

by

Eric Gordon Potter

A thesis submitted in partial fulfillment of
the requirements for the degree of:

Master of Science in Geology

2004
Lakehead University
955 Oliver Road
Thunder Bay, Ontario
P7B 5E1

Your file Votre référence
ISBN: 0-612-96995-9
Our file Notre référence
ISBN: 0-612-96995-9

Abstract

THE RARE AND EXOTIC MINERALOGY OF THE WESTERN SUBCOMPLEX OF THE DEADHORSE CREEK DIATREME, NORTHWESTERN ONTARIO.

by Eric Gordon Potter

Supervisor: Dr. R.H. Mitchell
Department of Geology

The Deadhorse Creek 'Diatreme' is a Proterozoic vent breccia that probably formed in response to early mid-continent rifting. Following emplacement of the breccia, the western subcomplex experienced three alteration events, producing the complex mineralogy observed in the main mineralized zone. Each event has produced a unique mineral paragenesis and the timing of each has been deduced from both textural and compositional evidence. While independent, these events made use of the same pre-existing fracture system along which the western subcomplex is situated. In order, these events were: intrusion of granitic fluids, alkaline metasomatism, and thermal metamorphism due to the emplacement of the Coldwell alkaline complex. Following the alteration events, and presumably a result of denudation, oxidization and leaching of the main mineralized zone has produced a supergene paragenesis of: calcite, tyuyamunite, hollandite and barite. The main mineralized zone was enriched in first- and second-row transition metals, rare-earth elements, beryllium, Th and U. The mineralization is represented by the presence of: aegirine-jervisite, aegirine-natalyite, barite, barylite, hollandite, coffinite, hematite, ilmenorutile, magnetite, monazite-(Ce), phenakite, pyrite, rutile, thorite, thorogummite, thortveitite, tyuyamunite, uraninite, V-crichtonite, xenotime-(Y), zircon, zircon-thorite-coffinite solid solutions and a few unnamed mineral species. The resulting mineralogy is both unique and complex, with several rare minerals and new compositional extremes reported (i.e., Nb-V-rutile, aegirine-jervisite, aegirine-natalyite, zircon-thorite-coffinite solid solutions, Dy-xenotime-(Y), thortveitite, baotite, barylite and V-crichtonite). In addition, unique parageneses are reported, giving further insight into the geochemistry of Be, Ba, Sc, V, Nb, Ti and Cr and conditions of formation of phenakite, barylite, thortveitite, crichtonite, ilmenorutile, barian feldspars and zircon-thorite-coffinite solid solutions.

TABLE OF CONTENTS

LIST OF FIGURES

ACKNOWLEDGMENTS

The author wishes to thank Dr. Roger Mitchell for his support, guidance and whose wealth of knowledge (and patience!) made this project possible. The assistance of Allan MacKenzie, from Lakehead University's Instrument Laboratory, with electron microscopy and X-ray diffraction work and Anne Hammond's preparation of all of the difficult samples was greatly appreciated. In addition, Mark Smyk of the Ministry of Northern Development and Mines generously provided access to samples and resources within the Ministry. Last but not least, this list would be amiss if I did not mention the tremendous support and encouragement of my parents and family.

STATEMENT OF PURPOSE

The Western subcomplex of the Deadhorse Creek 'Diatreme' is host to a highly unusual occurrence enriched in first- and second-row transition metals, rare-earth elements, beryllium, Th and U. This peculiar enrichment has given rise to several rare and exotic mineral species and has identified the occurrence as a potential source of Be, U, Th, Zr, and Y. Despite the economic interest, little is known about the genesis of the occurrence and/or mode of mineralization. Therefore, the main objective of this study is to provide a detailed mineralogical examination of the occurrence and present a geological record of the complex from the data. In addition to the genetic information, the rare mineral species are described in detail, providing new information on parageneses, geochemistry and conditions of formation. After a brief introduction in Chapter One, the unusual minerals are described in detail in Chapter Two. Chapter Three focuses in mineral parageneses within each geological unit and Chapter Four includes a discussion of the results and presents conclusions.

CHAPTER ONE: INTRODUCTION

1.1 Literature Review

The Deadhorse Creek diatreme complex is located approximately 25 kms northwest of the town of Marathon, 4 kms north of the intersection of the Deadhorse Creek access road and Highway 17, at approximately 48°50'30" latititude and 86°40'25"W longitude (Figure 1.1) (Platt and Mitchell, 1996; Sage, 1982). The Deadhorse Creek diatreme complex was initially discovered by members of the Lakehead University Geology Field School and was later claimed by prospectors working for Gulf Minerals in 1977, when they identified a series of highly radioactive zones (Sage, 1982). These discoveries led to extensive uranium exploration activity and initial geological examination of the property by Gulf Minerals Canada in 1977 and 1978 (Smyk *et al.* 1993). During this period, the property was briefly described by Mitchell and Platt (1977). During this exploration stage, Gulf Minerals sank eight diamond drill holes on the property, with a total length of 944 m (Kennedy and Sherlock, 1989). Sage (1982) visited and mapped the diatreme complex, and subdivided the diatreme complex into a number of subcomplexes based on their local distribution. In 1987, interest was renewed in the property when personnel from Highwood Resources collected samples that contained high contents of Y, Zr, Sc, Be and V (Smyk *et al.* 1993). This led to Unocal Canada Ltd optioning the property. Unocal re-examined the Gulf Minerals drill core and carried out an extensive exploration program involving: stripping, mapping, geochemistry, radiometric and magnetic surveys, and sampling (Kennedy and Sherlock, 1989; Knox, 1987). However, due to the limited tonnage and overall low Y contents (despite some significant Be, Zr, Y and Sc contents), the option agreement was discontinued and no further exploration work has been undertaken to date. The mineralogy of the main mineralized zone is extremely complex, and exhibits an unusual mineralogy with mineralization involving first-order transition elements (Sc, Ti, V, Cr, Mn and Fe), second-row transition elements (Zr and Nb), rare-earth elements (REE) and the actinides: Th and U (Platt and Mitchell, 1996). In the main mineralized zone of the West subcomplex, minerals bearing these elements include: phenacite, zircon, uraninite, thorite, monazite-(Ce),

xenotime-(Y), barylite, thortveitite, hollandite, tyuyamunite, crichtonite, transition metal rutiles and titanites, barite, thorogummite, aegirine-natalyite, aegirine-jervisite and a number of unknown and as of yet, undescribed mineral species (Platt and Mitchell, 1996; Mitchell and Platt, 1977; this work).

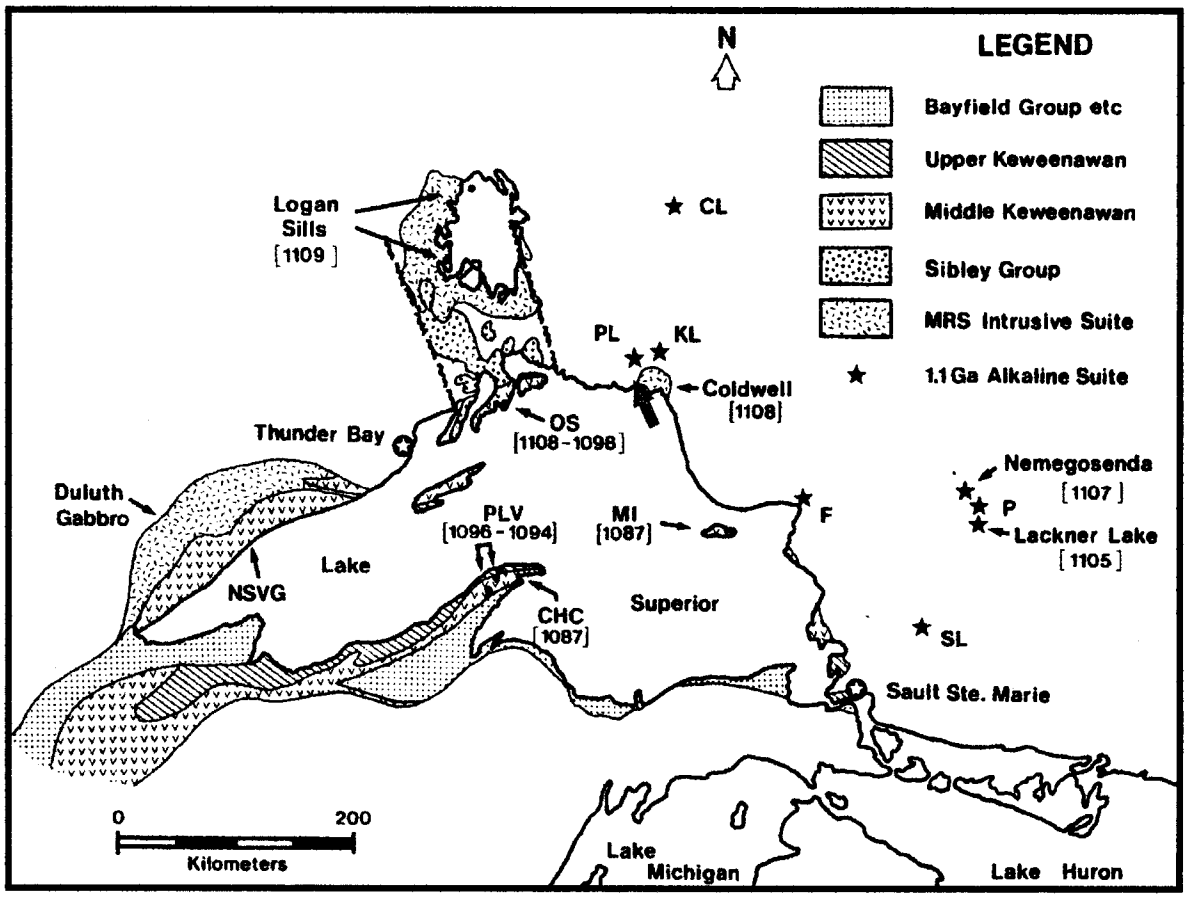

Figure 1.1: Geological setting of the Deadhorse Creek diatreme, from Heaman and Machado (1992). The location of the Deadhorse Creek diatreme is indicated by the red arrow. Abbreviations used: NSVG=North Shore Volcanic Group; PLV=Portage Lake Volcanics; CHC=Copper Harbor Conglomerate; OS=Osler Series; MI=Michipicoten Island; PL= Prairie Lake; KL=Killala Lake; CL= Chipman Lake; F=Firesand; P=Portage; and SL=Seabrook Lake. Age determinations are given in the square brackets [ ].

1.2 Local Geology

The Deadhorse Creek diatreme is one of five so called "diatreme complexes" that have been identified within the Marathon area (Gold Range diatreme; Slate Islands diatremes; Neys diatreme; and McKellar Creek diatreme) (Figure 1.2) It must be stressed that the term diatreme is applied with reference solely to the igneous nature of the breccia. These 'diatremes' might actually be better referred to as vent breccias, as they are not well characterized with respect to their emplacement style. The diatreme complex is emplaced predominantly in metasedimentary rocks of the Neoarchean (approximately 2.75Ga) Schrieber – White River greenstone belt of the Wawa subprovince (Platt and Mitchell, 1996). Locally, the diatreme complex transects northwest-trending supracrustal rocks consisting of intermediate-to-mafic metavolcanics, turbiditic metasedimentary rocks and derived schists (Smyk *et al.* 1993). The metavolcanic rocks consist of banded amphibolite, pillowed metavolcanics, and massive amphibolite. The width of the metavolcanic unit does not match on either side of Deadhorse Creek, suggesting the presence of a fault along the creek bed (Sage, 1982). According to Sage (1982), lesser biotite trondhjemite, diabase, carbonate-rich lamprophyre, and aplite dikes are also present. The diatreme is located roughly 1 km east of the western contact of the Mesoproterozoic Coldwell alkaline complex, well within the thermal metamorphic aureole, and 20 km south of the Prairie Lake carbonatite complex (Platt and Mitchell, 1996). Detailed U-Pb zircon and baddeleyite age determinations by Heaman and Machado (1992) indicate that the Coldwell complex was emplaced into the Archean crust at 1108 ± 1 Ma. The geological setting of the 'diatreme' is shown in Figure 1.1. The Coldwell alkaline complex, Prairie Lake carbonatite, Killala Lake carbonatite, Chipman Lake fenites and carbonatite dikes, and the Slate Islands, Neys and McKellar Creek diatremes are likely related to magmatism associated with the Keweenawan mid-continental rifting and are situated along on a north-trending extension of the Thiel fault, which is the northern part of the Trans-Superior Tectonic Zone (Sage, 1982; 1991; Smyk *et al.*, 1993). An unpublished U-Pb zircon age determination undertaken by M. C. Smyk, T. E. Krogh and L.Wilkenson at the University of Toronto yielded an age of 1128.7 ± 6 Ma at 1.82% discordance for the Deadhorse Creek complex.

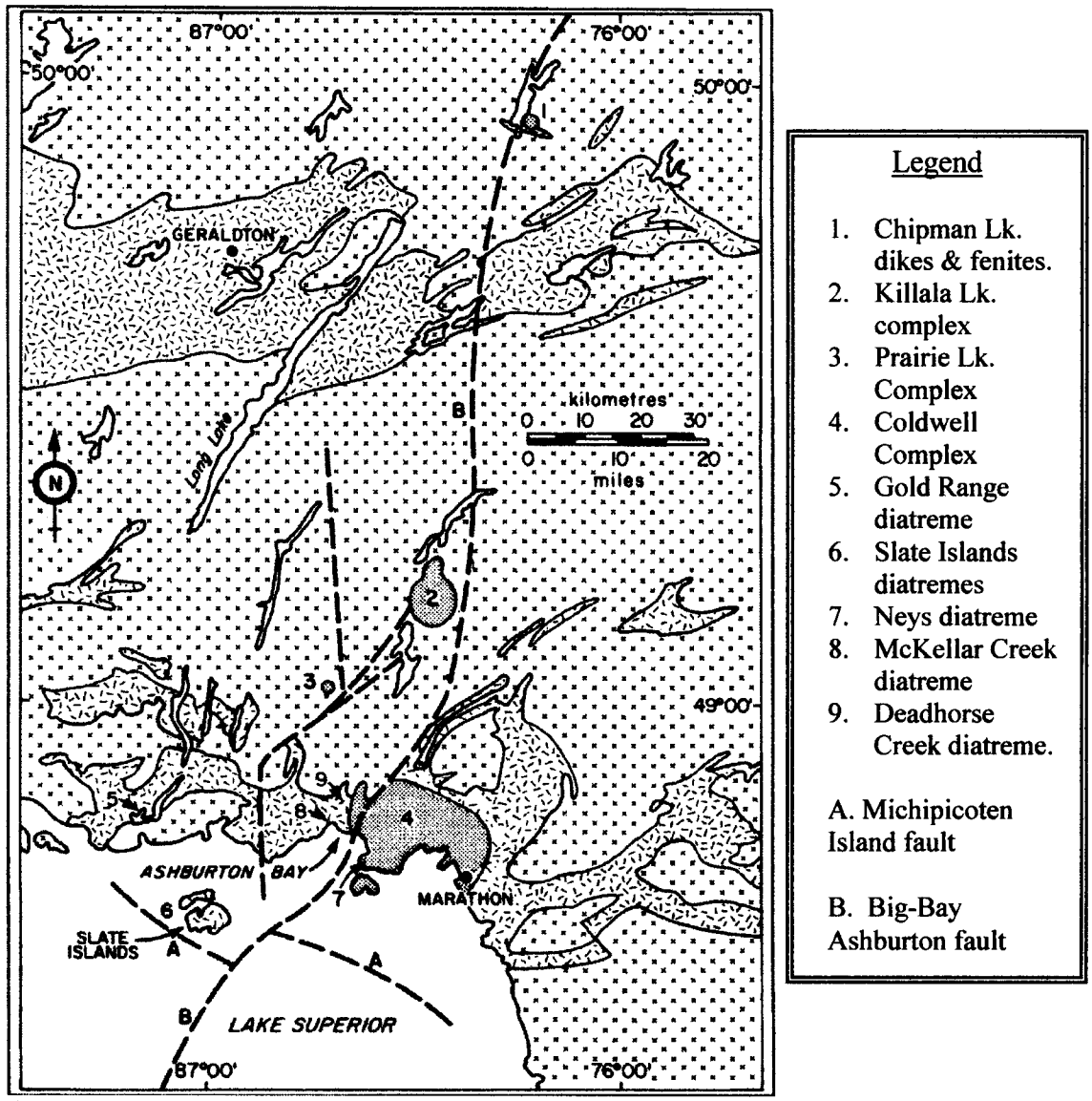

Figure 1.2: Location of Lake Superior 'diatreme' complexes. Also shown are the locations of alkaline complexes and major faults within the region. From Sage (1982).

The complex consists of a north-northeast elongated zone of brecciated rock with maximum dimensions of 1600 m by 400 m (Sage, 1982; Platt and Mitchell, 1996). To facilitate discussion, Sage (1982) subdivided the complex into five subcomplexes, termed the East, North, Central, South and West, respectively. Each subcomplex occurs as lobate masses, which have both sharp and gradational contacts with the surrounding host rocks (Smyk *et al.* 1993). These features are illustrated in Figure 1.3. The breccia consists of

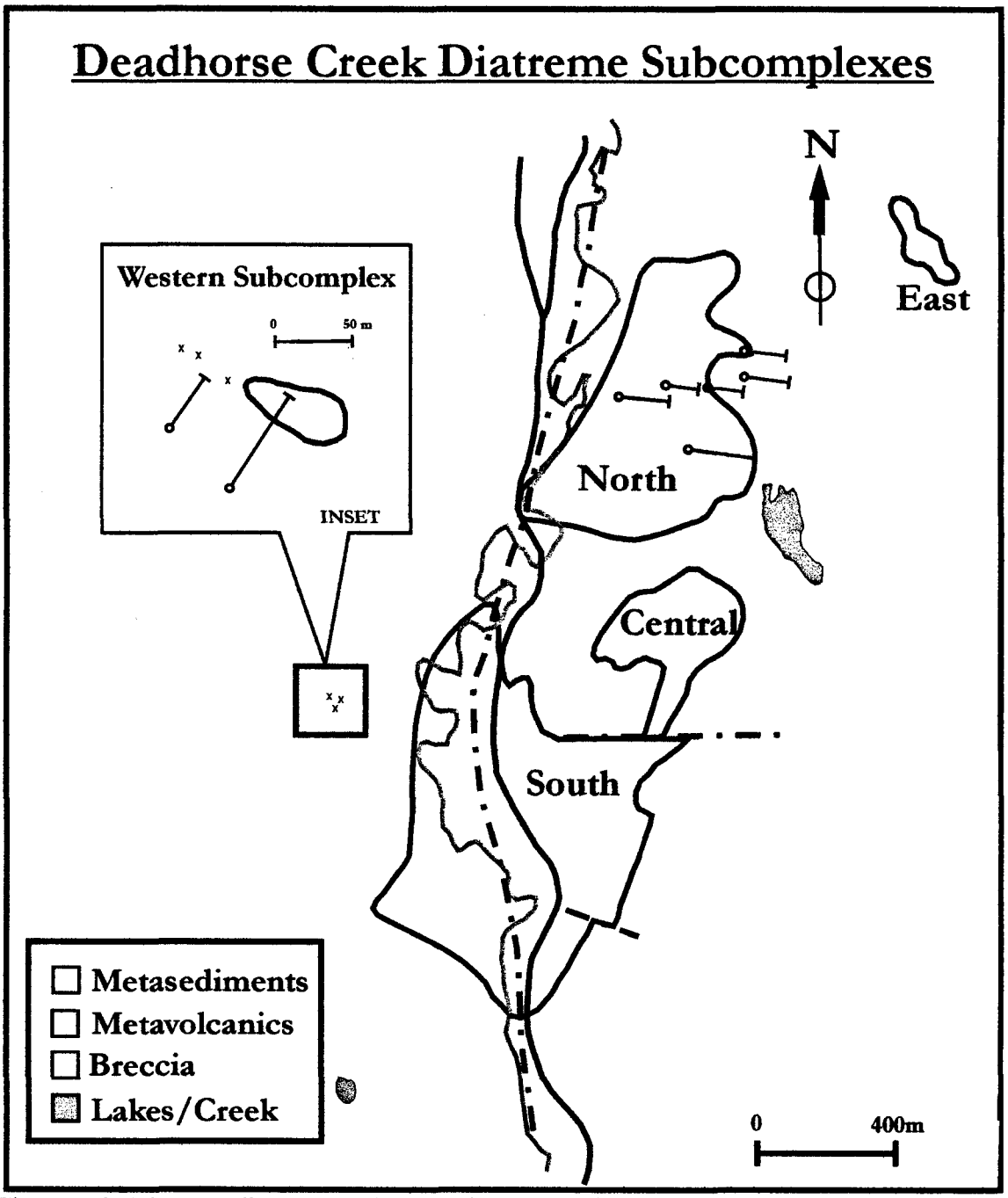

Figure 1.3: The Deadhorse Creek Complex. Locations of diamond-drill holes are also illustrated. After Sage (1982).

variably sized angular-to-subrounded clasts of locally derived rocks, predominantly greenstone, set in a matrix of comminuted rock debris in which secondary potassium feldspar and pyroxene have developed. In addition, the clasts have undergone varying degrees of hematite, silica and/or scapolite alteration. In the West subcomplex, the clasts

have been intensely-hematitized and silicified, as indicated by the bright red coloration and conchoidal fracturing within the clasts. In addition, these hematitized breccias give a strong response to a gamma-ray spectrometer for potassium (Sage, 1982). The scapolite replacement breccia is largely confined to the northeastern portion of the South Deadhorse Creek subcomplex. Within the South subcomplex, the scapolite grains are visually identifiable on weathered clasts as white prismatic fibers. Although all compositions of clasts have experienced some degree of scapolite replacement, the more siliceous clasts appear to have been preferentially-affected by the replacement (Sage, 1982). Another feature unique to the South subcomplex is the occurrence of mica and quartz within the breccia matrix (Sage, 1982; Platt and Mitchell, 1996; Smyk *et al.* 1993).

The Western subcomplex is hosted mainly in metasedimentary rocks and is approximately 140 m by 30 m in area (Smyk *et al.* 1993). Smyk *et al.* (1993) have divided the western subcomplex into three geological units: the heterolithic diatreme breccia, a carbonatite dike and the crosscutting main mineralized zone (Figure 1.4). The main mineralized zone, which transects the diatreme breccia, is orientated in a west-northwest trend. This steeply-dipping zone is tabular in form and occurs over 82 m in length, with an average width of 1.5 m (Kennedy and Sherlock, 1989; Smyk *et al.* 1993). According to Knox (1987), the main mineralized zone was intersected at depth via the diamond drilling, but mineralization was poor. Knox (1987) further states that the structure is apparently closed at both ends, yet as Smyk *et al.* (1993) state: "the structure, in which the main mineralized zone is situated, crosscuts the diatreme breccia, is exposed for 140 m, and may continue under overburden." As noted by Knox (1987), the main mineralized zone consists of strongly-hematitized and silicified rocks, which have been brecciated and veined by quartz. When hosted in heterolithic diatreme breccia, the zone consists of vein breccias and irregular, anastomosing quartz veins in a hematitized host. Although distributed variably, the highest-grade rocks and most strongly-radioactive samples are identifiable in the field as hard, chocolate-brown, massive, aphanitic-to-glassy rocks that have a conchoidal fracture with vitreous luster (Smyk *et al.* 1993; Sage, 1982). Trenching over the entire length of the main mineralized zone produced samples averaging 0.058% Y_2O_3, 1.85% ZrO_2, 0.202% BeO, and 0.031% U_3O_8 (Kennedy and Sherlock, 1989). Two drill holes from the West subcomplex (Gulf Minerals) were examined in this study. Although noted in the Gulf Minerals Limited drill logs, the main mineralized zone does not appear to continue at depth. The holes do

appear to have intersected diatreme breccia, but the characteristic chocolate-brown, aphanitic texture of the mineralized zone was not observed. Further petrographic examination confirmed these observations.

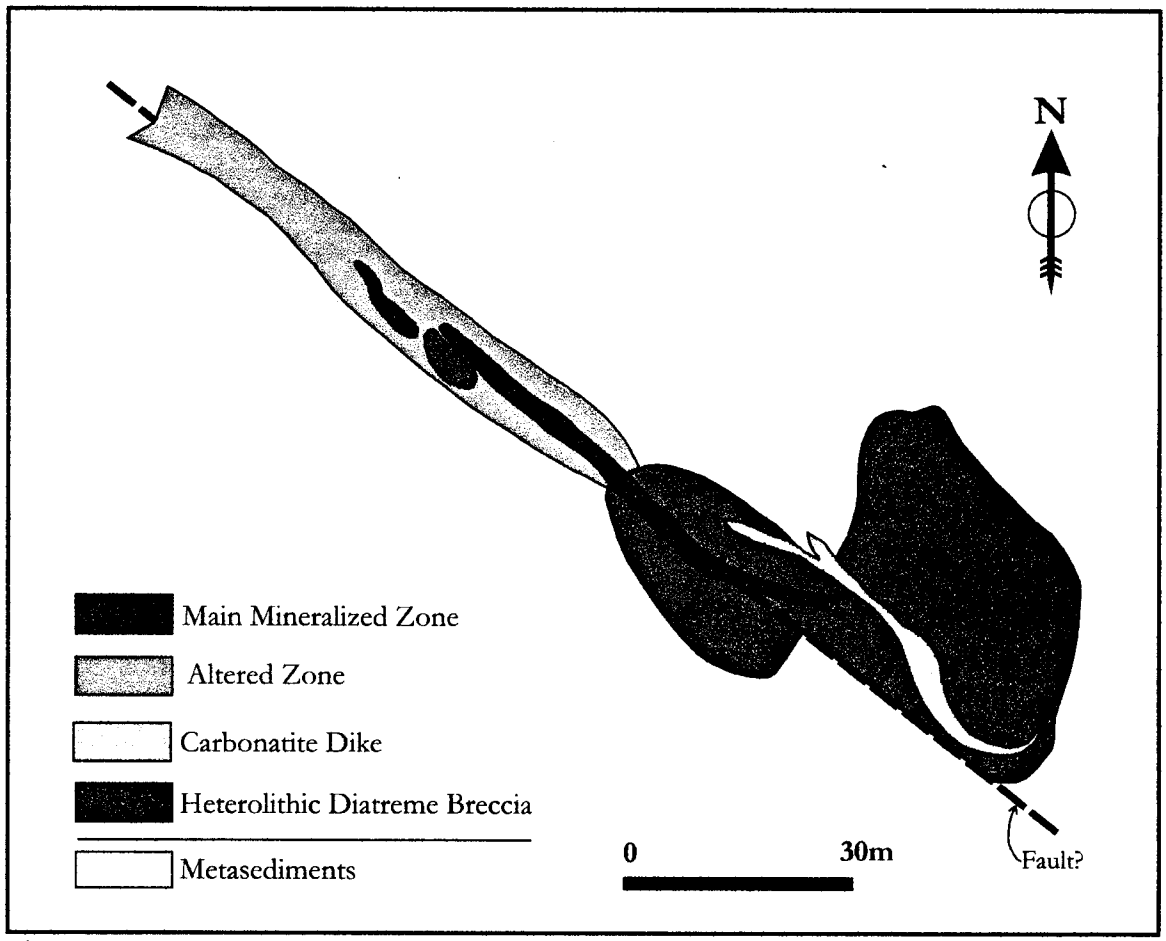

Figure 1.4: Expanded view of the western subcomplex (after Smyk *et al.* 1993).

The carbonatite dike, which cuts the diatreme breccia but not the main mineralized zone, also hosts some minor mineralization, with average contents of 0.23% Y_2O_3 and 0.40% ZrO_2 over a length of 52 m at a width of 1.65 m (Kennedy and Sherlock, 1989). These data reflect the presence of relatively-abundant xenotime-(Y) and zircon. In addition to xenotime-(Y) and zircon, the dike is host to significant amounts of barite, monazite-(Ce) and thorite. The dike dips steeply and appears to pinch out over strike, where its contacts are roughly parallel to the curved diatreme contact (Knox, 1987). Hematitization occurs near each pinch in the dike and the wall rocks have been carbonatized for approximately 70

cm (Smyk *et al.* 1993). Smyk *et al.* (1993) suggest this carbonatite dike may be related to the carbonate-rich lamprophyre dikes described by Sage (1982), which are best exposed in the South Subcomplex. The 'unmineralized' diatreme breccia is also host to some mineralization, with a radiometric response 2 to 3 times the background average and locally reaching as much as 40 times the background readings where clasts have been strongly hematitized. Both the diatreme breccia and carbonatite dike also have high concentrations of LREE ($\sum$LREE 1291 ppm to 2724 ppm), high La/Lu ratios (11.5-12.3) and a slight negative Eu anomaly. These data are is direct contrast to the main mineralized zone, which displays HREE enrichment, lower La/Lu ratios (0.6) and a slightly positive Eu anomaly (Smyk *et al.*, 1993). The chondrite-normalized REE distribution patterns of the three lithological units of the western Deadhorse Creek subcomplex are shown in Figure 1.5, with data taken from Smyk *et al.*, (1993. Such geochemical differences imply that the diatreme breccia and carbonatite dikes are not genetically related to the main mineralized zone, rather they may have simply made use of the same pre-existing fracture zone to reach the surface.

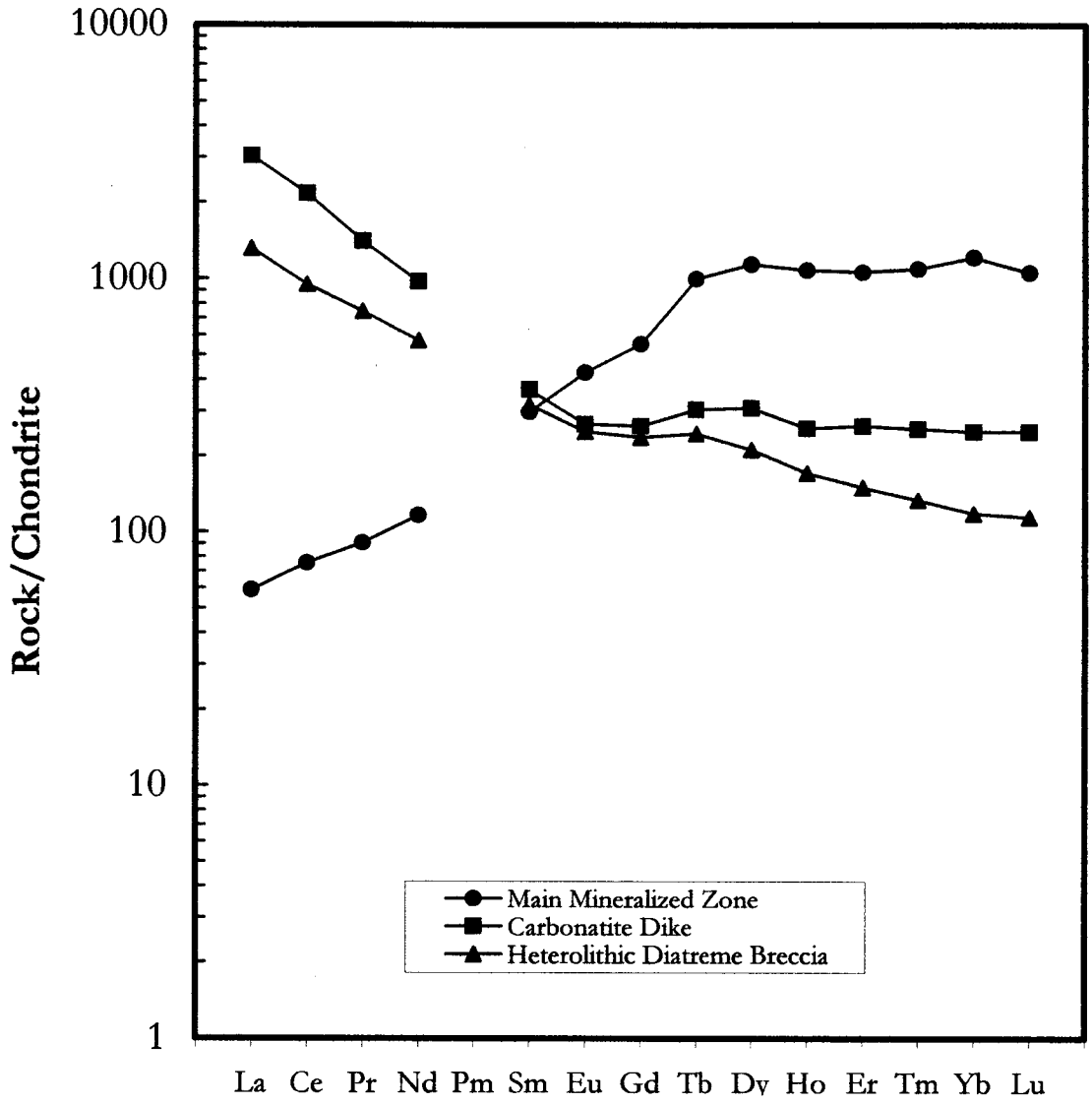

Figure 1.5: Chondrite-normalized rare-earth element distribution pattern of the lithological units of the Deadhorse Creek complex. Data from Smyk *et al.* (1993) and normalized to averages given by McDonough and Sun (1995) (For complete data, see Appendices A and B).

1.3 Analytical Methods

Polished thin sections were obtained from previous work undertaken by Mitchell and Platt (1977) and Platt and Mitchell (1996). In addition, several new samples were collected from the complex, especially from the main mineralized zone. Once cut, the polished thin sections were carbon-coated to prevent electrical charging during analysis. All mineral compositions were determined by Energy-Dispersion X-ray Spectrums (EDS) using a JEOL 5900 LV scanning electron microscope (SEM) equipped with a LINK ISIS 300 analytical system incorporating a Super ATW Element Detector (133 eV FwHm MnK). Raw EDS were acquired for a minimum of 50 seconds (live time) with an accelerating voltage of 20 kV, and beam current of 0.475 nA on a Ni standard. The spectra were processed with the LINK ISIS-SEMQUANT software package, with full ZAF algorithm corrections. The following well-characterized synthetic and mineral samples were used: pyroxene glass standard DJ35 (Si, Na, Mg, Al in pyroxenes), ilmenite (Fe, Ti), zircon (Zr, Si, Hf), barite (Ba, S), apatite (Ca,P), wollastonite (Ca), orthoclase (K), $SrTiO_3$ (Sr), LaF_3, CeF_3, YF_3, and pure metals of Pb, Nb, Cr, Mn, Sc, U, Th, Zn and V. Recalculation of SEM-EDS obtained FeO_T to ferric and ferrous iron has been performed where possible, following the approach outlined by Droop (1987). It should be stressed that for any mineral possessing complex cation substitutions, only the minimal level of Fe^{3+} contents may be estimated and an apparent lack of Fe^{3+} is a consequence of low total cations in the microprobe analysis as compared to the theoretical number of cations.

Due to the small size of many of the mineral grains analysed, activation of the surrounding phases was a possibility. Care was taken to eliminate possible contamination, with many spurious analyses being rejected, as acquisition of quantitative data was not possible. In such cases, attempts were made to generate the best possible EDS for identification. Although limitations in the methodology precluded the analysis of beryllium-bearing minerals, phenakite was abundant enough to permit identification by powder X-ray diffraction. This was performed at Lakehead University's Instrument Laboratory using a Phillips P3710 X-ray diffractometer (CuKα radiation) equipped with APD software. The instrument was operated in a step-scan mode (5-110° 2θ, 0.02 Δ2θ, 4 s per step) at 40 kV and 30 mA. Mineral identification and structural refinements from the diffraction pattern were undertaken using Bruker EVA and TOPAS software packages (Bruker, 2002; 2003).

CHAPTER TWO: MINERAL COMPOSITIONS

2.1 Allanite-(Ce)

Allanite-(Ce), an epidote-group mineral, is present in trace amounts within the main mineralized zone of the Deadhorse Creek "diatreme". Historically, the epidote group has been considered to have the general formula $A_2M_3(SiO_4)_3(OH)$. However, Ecrit (2002) notes: (a) there are two large cation sites (A1 and A2), one of which strongly prefers Ca, the other REE; (b) there are two distinct groupings of silicate anions within the structure, Si_2O_7 dimers and SiO_4 islands; and (c) the octahedrally-coordinated M-sites are highly-ordered and are the distinguishing factor for the epidote subgroup minerals. Given such considerations, the crystal-chemical formula for allanite-(Ce) should be written as: $Ca(Ce,La,Ca)(Fe^{2+},Fe^{3+})(Al,Fe^{3+})AlSi_2O_7(SiO_4)O(OH)$. The epidote group is subdivided into two subgroups, based on the dominance of the A2-site. The allanite subgroup consists of seven members in which the A2-site is dominated by Y or REE. Within the epidote subgroup, Ca dominates the A-sites and one or more of the following elements fill the M-sites: Al, Fe, Pb, Sr, Mn and V.

At Deadhorse Creek, allanite-(Ce) occurs as anhedral-to-subhedral lath-like grains set in quartz and associated with biotite. Individual grain sizes are no larger than 10 μm in length (Figure 2.1). Due to the small size of the grains, accurate compositions were difficult to obtain without matrix contamination. In addition, the crystal structure of epidote-group minerals are highly susceptible to damage from alpha particles, and the presence of even low levels of actinide elements can cause considerable structural damage (Ercit, 2002). In addition to the minor amounts of Th present within allanite-(Ce), trenching of the main mineralized zone yielded an average of 0.031% U_3O_8 and minor amounts of Th; sufficient amounts of actinide elements to cause structural damage in the allanite-(Ce). As the analytical totals were well below the cut-off of 96 wt.% (including calculated H_2O) suggested by Ercit (2002), no formula calculations are presented. Rather, a mean composition derived from 10 analyses is shown in Table 2.1.

Table 2.1: Mean composition of allanite-(Ce) from Deadhorse Creek

	Mean
MgO	1.0
Al_2O_3	12.5
SiO_2	33.4
CaO	8.7
TiO_2	0.8
FeO	16.5
La_2O_3	3.5
Ce_2O_3	11.9
ThO_2	0.2
Totals	88.5

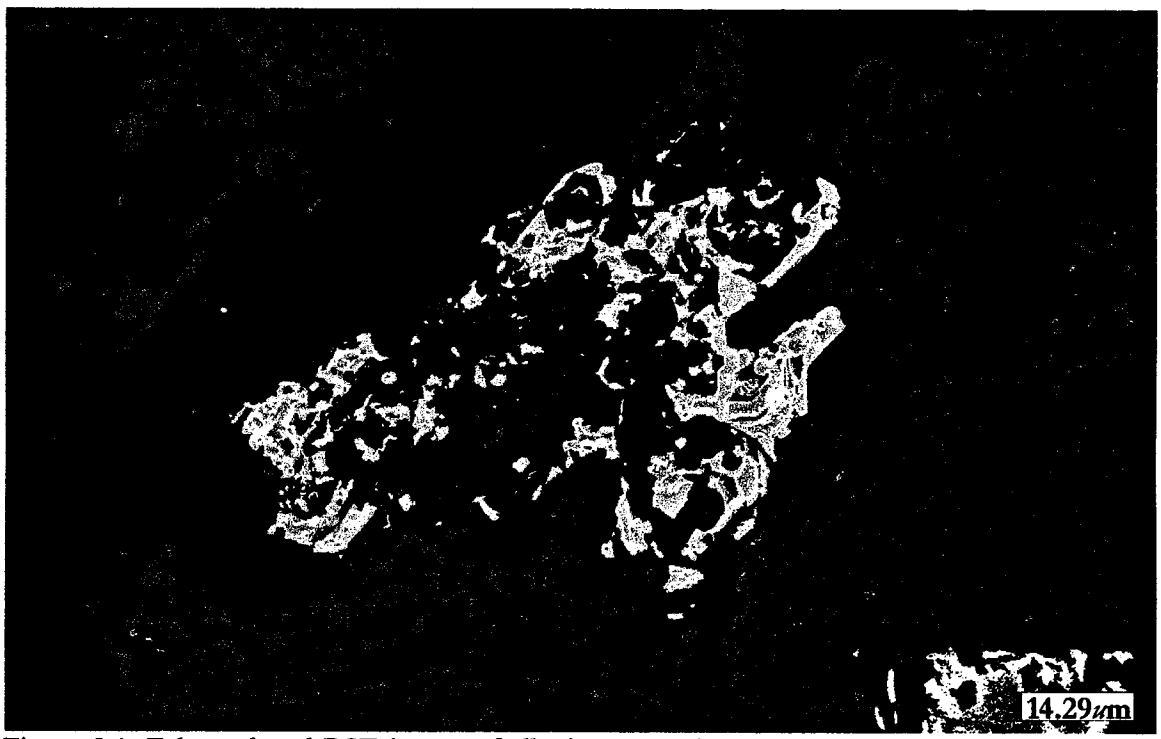

Figure 2.1: False-colored BSE-image of allanite-Ce set in quartz (black) and associated with biotite (blue) and titanite (light blue).

2.2 Apatite

Apatite [$Ca_5(PO_4)_3(F,OH,Cl)$] occurs throughout the main mineralized zone and diatreme breccia as a common accessory mineral. Typically, the mineral occurs as subhedral-to-euhedral grains set in calcite. Commonly associated phases include a hydrated calcium zirconosilicate, rutile, and crichtonite. In addition, the few noted occurrences of thortveitite were in proximity to fluorapatite grains. Although fluorapatite from the main mineralized zone tends to have more euhedral habits, the composition never varies between the two geological units. Table 2.2 presents representative compositions from each unit and an EDS of fluorapatite from the main mineralized zone is shown in Figure 2.2. As noted in Table 2.2, the fluorapatite from Deadhorse Creek contains minor SrO, Ce_2O_3 and Fe_2O_3, ranging from 0.6 to 3.06 wt.%; 0 to 1.5 wt.%; and 0 to 0.97 wt.% respectively. Sr typically occurs in apatite-group minerals from peralkaline, carbonatitic and alkali-ultramafic rocks (Chakhmouradian *et al.* 2002). Figures 2.3 a & b illustrate the compositional variation in apatite-group minerals from alkaline rocks, with (b) illustrating the composition of the Deadhorse Creek fluorapatite. In the apatite structure with space-group symmetry $P6_3/m$, Sr tends to be ordered at the seven-coordinated site denoted as Ca(2) (Hughes *et al.* 1991). Therefore, in the majority of cases it is incorporated into the apatite structure by either: $^{[7]}Ca^{2+} \leftrightarrow {}^{[7]}Sr^{2+}$ (solid solution towards strontium-apatite), or $3^{[7]}Ca^{2+} + 2^{[9]}Ca^{2+} \leftrightarrow 3^{[7]}Sr^{2+} + {}^{[9]}Na^{+} + {}^{[9]}LREE^{3+}$ (solid solution towards belovite) (Pushcharovskii *et al.* 1987; Rakovan and Hughes, 2000). However, Chakhmouradian *et al.* (2002) point out that these schemes are simplified as they only reflect the tendency of individual elements to partition into a specific site and do not account for cation-disorder observed in the actual minerals. Furthermore, the authors note that it remains uncertain whether the degree of order decreases or increases with increasing proportions of Sr relative to Ca. In addition, if other elements such as Na and light rare-earths (LREE) substitute for Ca, the pattern of order becomes more complex, involving up to six crystallographically independent positions (Khomyakov *et al.* 1996). Recent work by Chakhmouradian *et al.* (2002) has confirmed the existence of a complete, continuous solid-solution between naturally occurring apatite and Sr-apatite; implying that the fluorapatite from Deadhorse Creek formed under relatively constant, but Na-, Sr- and LREE-poor environments. In comparison, Sr-apatite from Murun and Lovozero formed by

reaction of primary fluorapatite with deuteric fluids, becoming progressively enriched in Sr at essentially constant levels of Na, LREE and Si. At Murun, this evolutionary trend culminated at approximately 54 mol.% $Sr_5(PO_4)_3(F,OH)$ (see Figure 2.3a) (Chakhmouradian *et al.* 2002). Figures 2.4 and 2.5 illustrate the textural types of fluorapatite present at Deadhorse Creek.

Table 2.2: Representative compositions of fluorapatite from the Deadhorse Creek Diatreme.

	1	2	3	4	5	6	7
Na_2O	0.6	0.8	0.5	0.4	0.2	0.2	0.3
P_2O_5	42	41.8	42.5	41	41.7	41.2	41.8
CaO	52.1	52.7	52.9	53.2	53.7	52.7	52.9
FeO	0.2	0.1	0.2	1	0.6	-	0.8
SrO	1.6	1.2	1.1	2	1.7	3.1	2.2
Ce_2O_3	1.1	0.8	0.5	-	-	-	0.1
F	2.4	2.6	2.2	2.6	1.9	2.6	1.7
Cl	0.1	0.1	0	0.1	0.1	0.2	0.2
Less O=F,Cl	0.6	0.6	0.5	0.6	0.4	0.6	0.4
Total	99.5	99.5	99.4	99.7	99.5	99.4	99.6
Na^+	0.1	0.1	0.1	0.1	-	-	-
P^{5+}	3.0	3.0	3.0	2.9	3.0	3.0	3.0
Ca^{2+}	4.8	4.8	4.8	4.8	4.9	4.8	4.8
Fe^{2+}	-	-	-	0.1	-	-	0.1
Sr^{2+}	0.1	0.1	0.1	0.1	0.1	0.2	0.1
Ce^{3+}	-	-	-	-	-	-	-
Totals	8.0	8.0	8.0	8.0	8.0	8.0	8.0
F^-	0.7	0.7	0.6	0.7	0.5	0.7	0.5
Cl^-	-	-	-	-	-	-	-

Note: 1-3 fluorapatite from diatreme breccia; 4-7 fluorapatite from the main mineralized zone.

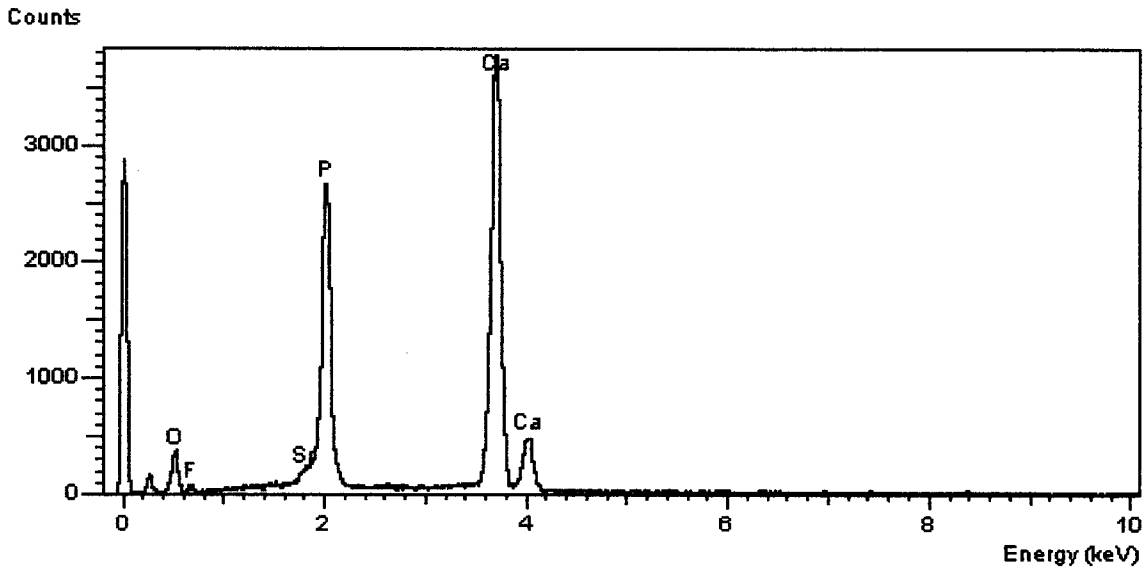

Figure 2.2: EDS of fluorapatite from the main mineralized zone.

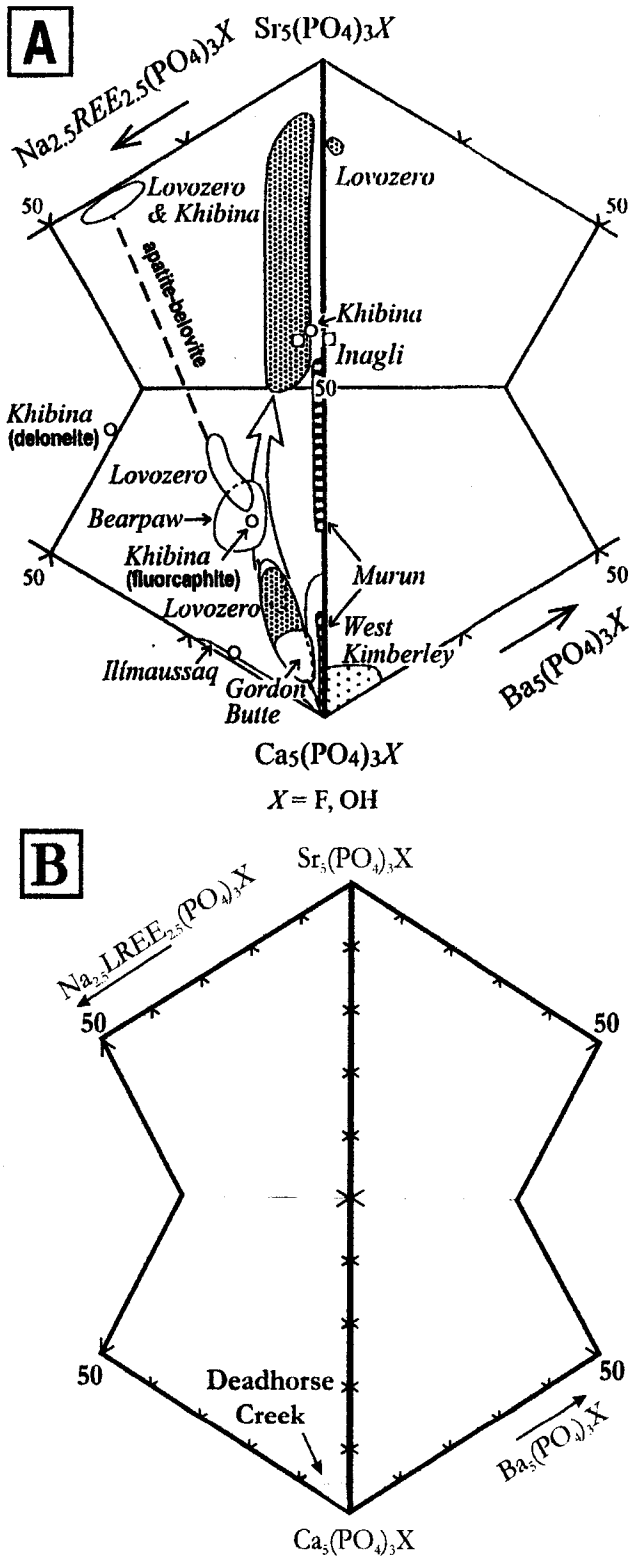

Figure 2.3: (A) compositional variation in apatite-group members from alkaline rocks. Samples from Lovozero are heavily dotted (Chakhmouradian et al. 2002). (B) Compositional variation of the Deadhorse Creek fluorapatites.

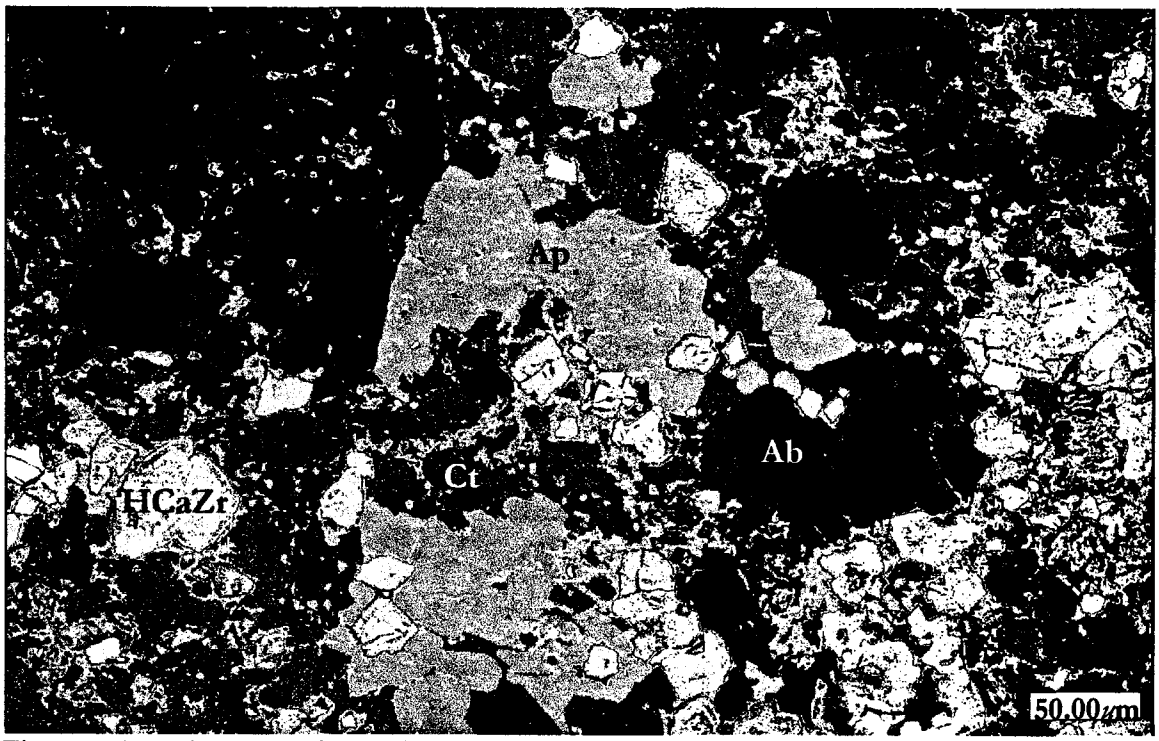

Figure 2.4: False-colored BSE-image of fluorapatite (Ap) from the main mineralized zone. Also shown are the HCaZr (HCaZr), zircon (white), albite (Ab) and hematite (red) set in a calcite matrix.

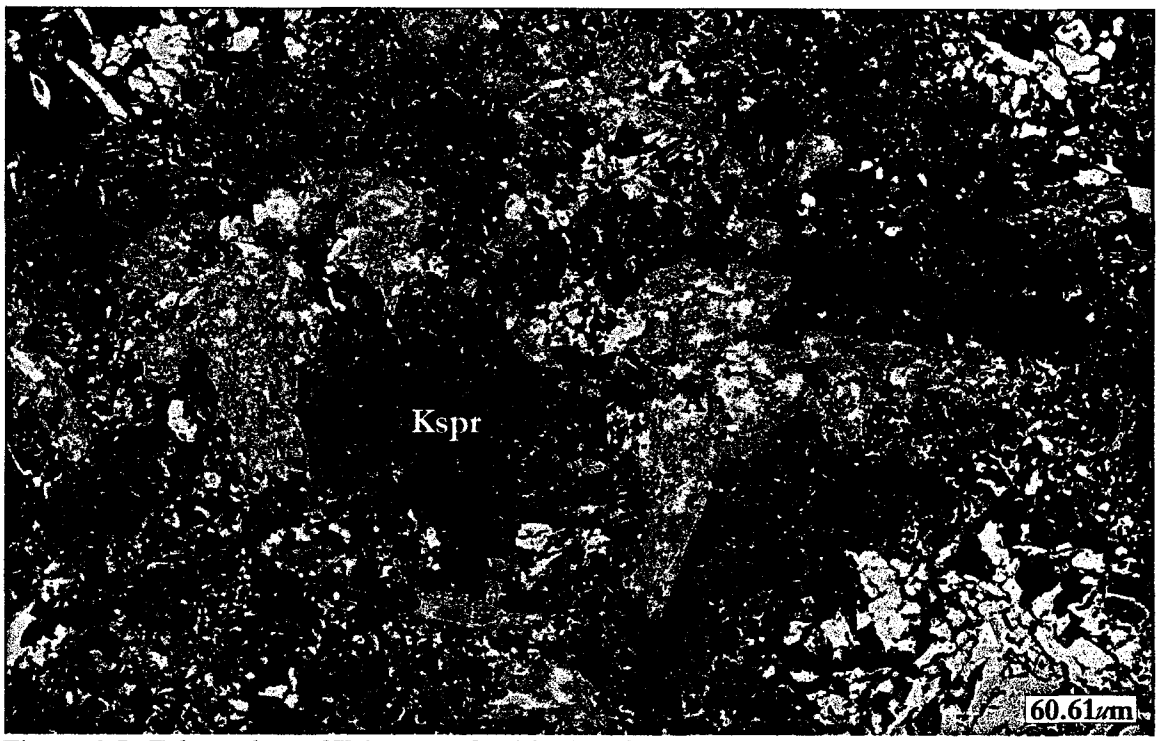

Figure 2.5: False-color BSE-image of subhedral fluorapatite (Ap) set in potassium feldspar (Kspr) matrix along with subhedral laths of aegirine-augite (Ae).

2.3 (Ba,K)-feldspar

Barian feldspars occur in trace amounts (<1 vol.%) within the "diatreme" breccia of the complex. The barian feldspars, which include: orthoclase [$KAlSi_3O_8$], hyalophane [$(K,Ba)Al(Si,Al)_2O_8$] and celsian [$BaAl_2Si_2O_8$], were found in close association with biotite and exhibit a range of compositions from 1 to 86 mole.% celsian (Cn). Within this wide range, two compositional gaps are present; from 40 to 48 and 68 to 80 mole % celsian. These gaps are expressed as three distinct phases in backscattered-electron images (BSE). In larger grains, complex zoning representing the three distinct compositions is present, with the highest concentration of barium commonly occurring in the core (Figures 2.6, 2.7 and 2.8). These textures are similar to those observed by McSwiggen *et al.* (1994), who interpreted the zoning to represent replacement textures, with crystallization occurring before re-equilibration into a single homogeneous composition. As shown in the BSE-images, the (Ba,K)-feldspars occur as aggregations of small, anhedral grains set in a cementing matrix consisting mostly of diopside. The (Ba,K)-feldspars occur in close association with biotite, some of which contain small amounts of BaO (1-3 wt. %) (Table 2.3). The Ba-bearing biotite occurs as small, anhedral-to-subhedral grains (<10 μm), whereas larger, subhedral biotite grains are free of barium.

Expressed in terms of the ternary system celsian-orthoclase-albite (Cn-Or-Ab) (Figure 2.9), albite concentrations are generally low, with most data below the maximum 12 mole.% albite found. Also evident in the Cn-Or-Ab plot are the two compositional gaps. Representative compositions and mole percent end-members are given in Table 2.4. In addition, an EDS in Figure 2.10 illustrates the absence of other elements, notably iron.

Occurrences of celsian and hyalophane are typically associated with sedimentary and metasedimentary rocks (Bjørlykke and Griffin, 1973; Reinecke, 1982), Mn-rich iron formation (McSwiggen *et al.* 1994), stratabound barite-sulfide deposits (Coats *et al.* 1980, 1984; Chabu and Boulègue, 1992; Devaraju *et al.* 1999; Fortey and Beddoe-Stephens, 1982; Fortey *et al.* 1993; Kribeck *et al.* 1996; Pouit and Bois, 1986), alkaline, particularly potassic, rocks (Zhang *et al.* 1993; Ferguson and Cundari, 1982; Flohr and Ross, 1990; Hamilton and Rock, 1990; Langworthy and Black, 1978; Larsen, 1981; LeCheminant *et al.* 1987; Nakamura and Yoder, 1973; van Kooten, 1980; Whitney *et al.* 1988), and Archean mica-schists (Pan and

Fleet, 1991). Most of the aforementioned occurrences, with the exception of alkaline-hosted occurrences, are associated with exhalative hydrothermal processes or low-to-medium-grade metamorphism (Moro *et al.* 2001). Investigations of the alkaline-hosted occurrences suggest a magmatic origin of hyalophane, mainly as a late-stage phase during crystallization of evolved K-rich magmas (Zhang et al. 1993).

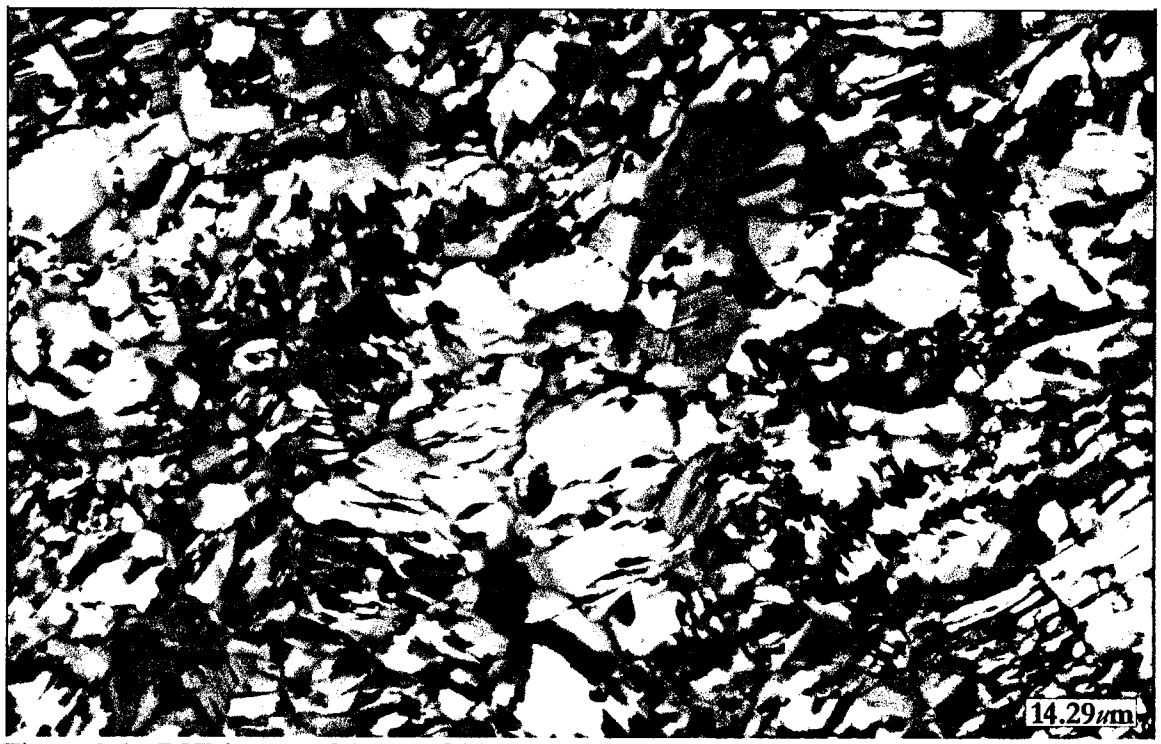

Figure 2.6: BSE-image of (Ba,K) feldspars from Deadhorse Creek. Higher concentrations of barium are indicated by lighter colors (white).

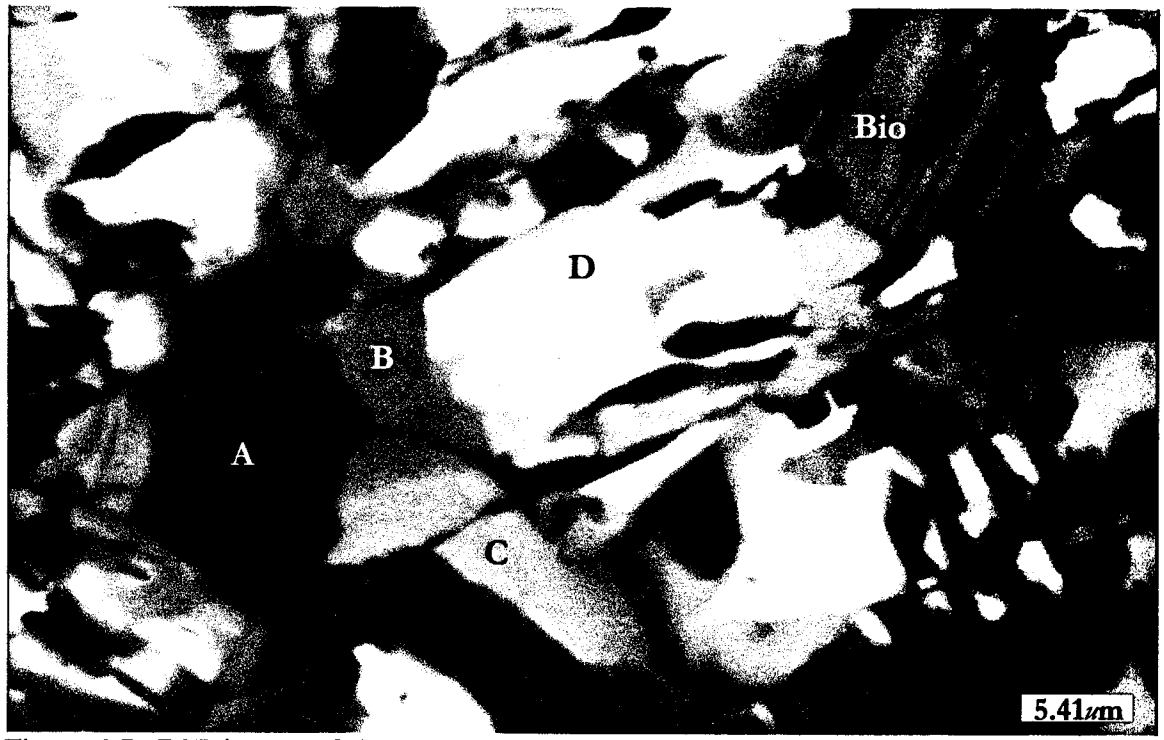

Figure 2.7: BSE-image of (Ba,K) feldspar and Ba-bearing biotite (Bio) from Deadhorse Creek. Weight % BaO at points: (A) 0.5-2.5; (B) 9.66; (C) 13.77; (D) 28.34; (Bio) 2.89.

Figure 2.8: BSE-image of (Ba,K) feldspars (light gray to white), with BaO content increasing to the left. Set in a matrix of mostly diopside, with some biotite (light gray) and subeuhedral fragment of potassium feldspar (dark gray/black).

Table 2.3: Composition of barium-bearing biotite associated with the (Ba,K) feldspars

Na_2O	0.1	0.1	-	0.3	0.3	0.1
MgO	12.4	12.0	11.8	12.5	12.2	13.1
Al_2O_3	14.9	15.1	15.2	14.9	16.0	15.3
SiO_2	34.6	35.6	34.6	34.4	37.1	35.1
K_2O	6.9	6.4	7.1	6.8	6.9	6.5
CaO	0.1	0.4	-	0.1	0.2	0.1
TiO_2	2.4	2.0	3.0	2.1	1.4	1.8
MnO	0.4	0.6	0.4	0.4	0.4	0.3
FeO	18.9	17.1	19.1	19.5	19.0	19.1
BaO	3.3	3.7	3.1	2.9	1.3	1.7
F	0.5	0.9	0.3	0.5	-	1.0
Less O=F	0.1	0.2	0.1	0.1	-	0.2
Totals	94.4	93.7	94.5	94.3	94.8	93.9

Table 2.4: Representative orthoclase, hyalophane and celsian compositions from the Deadhorse Creek complex.

Na_2O	0.1	0.2	0.8	0.9	0.9	1.1	0.3	0.7
Al_2O_3	19.8	19.4	21.3	21.4	21.8	23.9	25.5	26.7
SiO_2	62.7	61.4	58.0	57.9	53.9	49.3	43.7	35.0
K_2O	16.7	15.9	12.7	12.6	10.9	8.2	6.0	1.7
BaO	0.6	2.3	7.1	7.5	11.9	17.1	24.7	36.0
Totals	99.9	99.2	99.9	100.3	99.4	99.6	100.2	100.1
Na^+	-	-	0.1	0.1	0.1	0.1	-	0.1
Al^{3+}	1.1	1.1	1.2	1.2	1.3	1.5	1.6	1.9
Si^{4+}	2.9	2.9	2.8	2.8	2.7	2.6	2.4	2.1
K^+	1.0	1.0	0.8	0.8	0.7	0.5	0.4	0.1
Ba^{2+}	-	-	0.1	0.1	0.2	0.3	0.5	0.8
Totals	5.0	5.0	5.0	5.0	5.0	5.0	4.9	5.0
Mol. %								
Cn	1.2	4.4	13.5	14.5	23.8	34.7	53.9	86.1
Or	98.8	95.6	78.9	79.3	71.4	54.2	42.8	13.3
Ab	0.0	0.0	7.5	6.1	4.8	11.1	3.4	0.6

Note: Cations calculated based on 8 oxygens.

Monoclinic celsian is stable from room temperature to 1590°C, at which it slowly converts to "hexacelsian" (Moro *et al.* 2001). Although "hexacelsian" may persist metastably on cooling, the lack of natural occurrences suggests that it is not stable under crustal conditions (Lin and Foster, 1968). Hyalophane is an intermediate phase that occurs along the binary solid-solution series between $KAlSi_3O_8$ and $BaAl_2Si_2O_8$. According to Deer *et al.* (2001), hyalophane generally contains between 2 and 80 mole % celsian, although hyalophanes with more than ~60 mole % celsian are especially rare. In this study, concentrations as great as 68 mole % Cn are recorded in the intermediate phase. As noted by Guo and Green (1989), the best scheme for Ba substitution in hyalophane is: Ba + Al = (K,Na) + Si. This is clearly illustrated in a plot of $BaO + Al_2O_3$ versus $SiO_2 + K_2O + Na_2O$ (Figure 2.11).

Gay and Roy (1968) postulated that the rarity of Ba-rich feldspar in nature is not due to difficulties in accommodating Ba^{2+} into the feldspar structure, but rather due to lack of suitable conditions in nature for its genesis. Therefore, these authors suggest that $BaAl_2Si_2O_8$ should be regarded as part of the quaternary feldspar system. Furthermore, they suggest that near the solidus of the series, celsian is confined to 90 to 100 mole % Cn, whereas in the low-temperature structural state there is a compositional gap between hyalophane and celsian (e.g. 65 to 80 mole % Cn). This work is summarized by the schematic representation of the subsolidus relations in Figure 2.12. The data presented here indicates an almost complete series from orthoclase to hyalophane, with a compositional gap occurring from 68 to 80 mole % Cn, in agreement with a significant compositional gap. However, data presented by Devaraju *et al.* (1999), Pan and Fleet (1991) and Chabu and Boulègue (1992) report compositions that fall directly within this range (68 to 100 mole % Cn). Figure 2.9(B) illustrates the various compositions in an Ab-Or-Cn plot. As noted by McSwiggen *et al.* (1994), disagreements in the position of the miscibility gaps may have arisen due to several reasons: the rocks equilibrated at different temperatures; the hyalophane grains contain variable amounts of other components (sodium); and that the hyalophane grains investigated had truly not equilibrated.

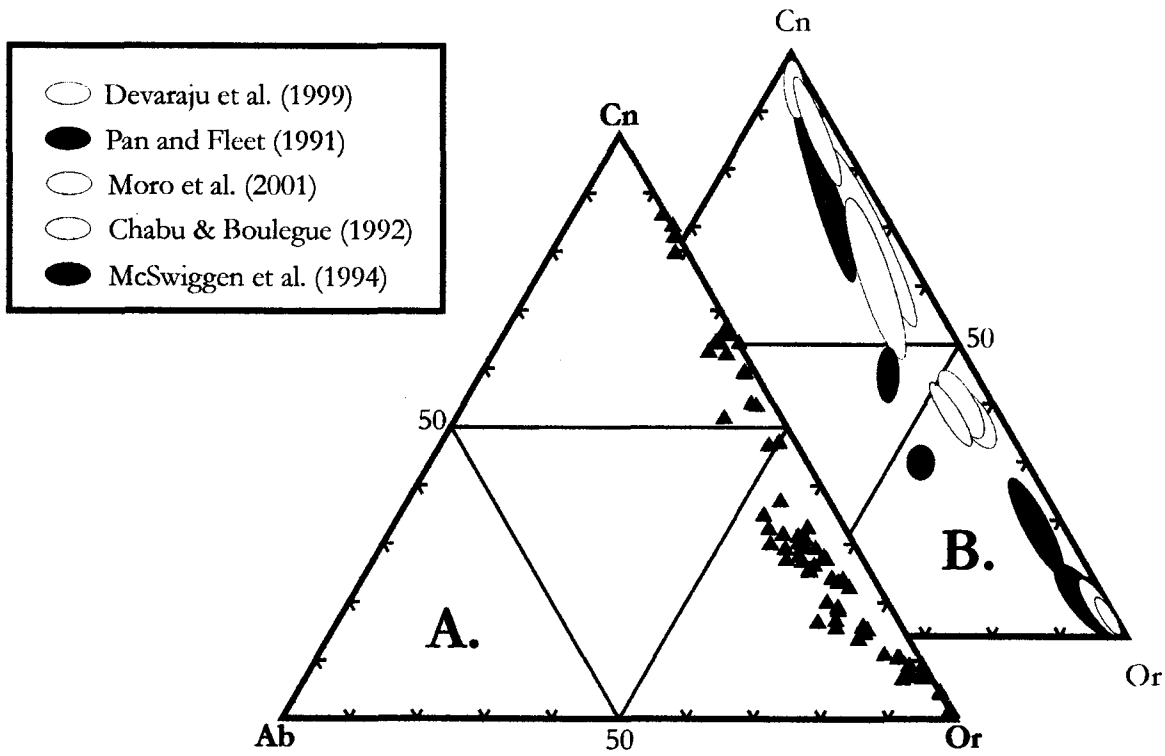

Figure 2.9: A. Composition of Deadhorse Creek (Ba,K)-feldspars in terms of albite (Ab), celsian (Cn) and orthoclase (Or). Number of analyses: 73. B. Plot of (Ba,K)-feldspars from sources listed.

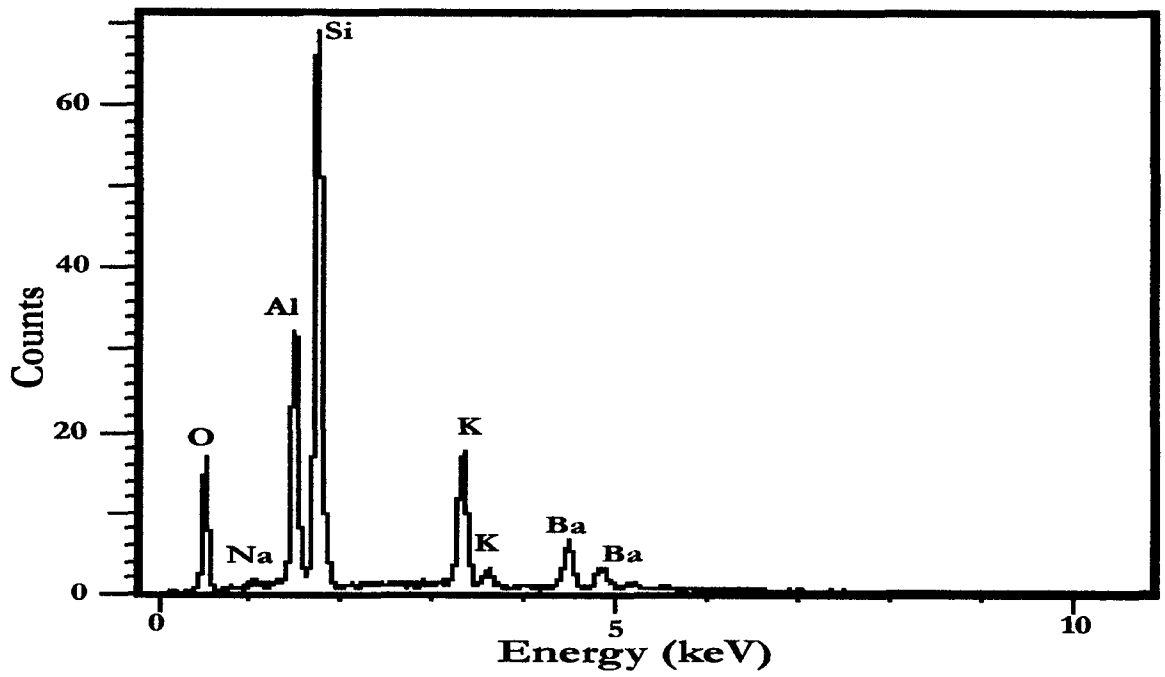

Figure 2.10: EDS of hyalophane from Deadhorse Creek.

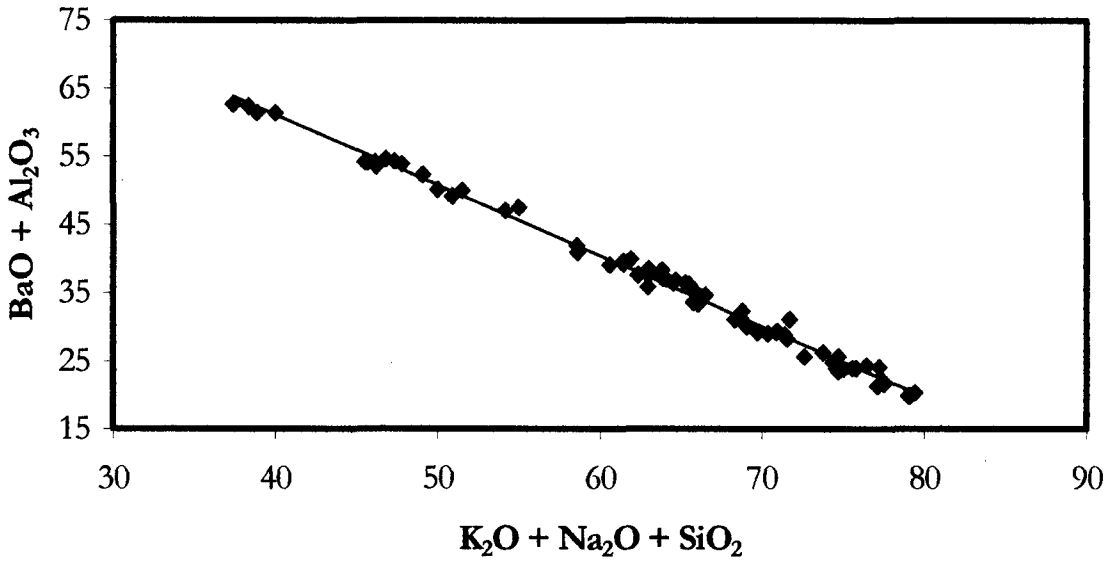

Figure 2.11: Plot of BaO + Al_2O_3 versus SiO_2 + K_2O + Na_2O illustrating the main substituting scheme present in the (Ba,K)-feldspars; n=73.

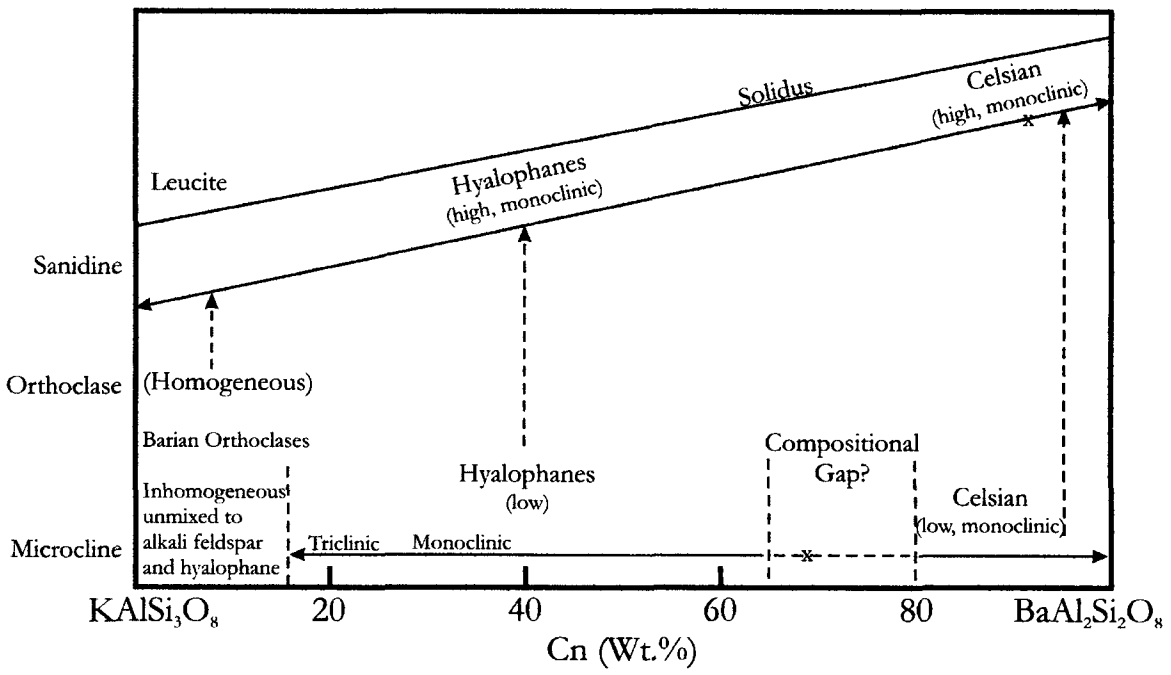

Figure 2.12: Schematic representation of subsolidus relations in the orthoclase-celsian system (after Gay and Roy, 1968).

(Ba,K)-feldspars are believed to form via one of three processes: replacement of authigenic barite; crystallization from an earlier Ba-Al-Si gel; or as a late-stage phase during crystallization of evolved K-rich magmas. In the first process, barite is replaced by the barian feldspars during a later diagenetic or metamorphic event. During the metamorphic or diagenetic event, the barite dissolves and re-precipitates because of a more reducing environment, as hyalophane (McSwiggen *et al.* 1994). As Moro *et al.* (2001) note, barite dissolution under metamorphism or early diagensis could occur in an environment where the Eh value may have reached <-300 mV, with neutral to slightly alkaline pH values. Not surprisingly, at some localities this process results in pseudomorphic grains (Bjørlykke and Griffin, 1973) or relict grains enclosed in (Ba,K)-feldspars (Moro *et al.* 2001; Chabu and Boulègue, 1992). Furthermore, in studies done by Moro *et al.* (1994), the isotopic characteristics of the barite, associated sulfides and carbonates support a replacement process.

At other localities, (Ba,K)-feldspar are believed to form as an authigenic phase from an Ba-Al-Si-gel (Coates *et al.* 1980). This multi-stage process begins with the formation of harmotome [$BaAl_2Si_2O_8*6H_2O$] or an unnamed hydrous Ba-silicate [$BaAl_2Si_2O_8*4H_2O$] (Jakobsen, 1990). Harmotome experiences a series of essentially dehydration reactions to form, cymrite [$BaAl_2Si_2O_8*nH_2O$] and finally celsian [$BaAl_2Si_2O_8$] (Jakobsen, 1990; Matsubara, 1985; Fortey and Beddoe-Stephens, 1982). According to Coates *et al.* (1980), support for this process is gathered from the textural relationships among massive, fine-grained beds of celsian, barite, phosphate and sulfides in the Dalradian schist, Scotland.

In the third process, magmatic hyalophane forms as a late-stage, interstitial phase in differentiates of alkaline mafic rocks. This process usually creates mantles of normally-zoned hyalophane, although Zhang *et al.* (1993) have noted reverse-zoned grains of magmatic origin. The authors propose that the zoning patterns are controlled by the distribution coefficients for Ba between hyalophane and the melt ($K_{Ba}^{af/liq}$) and by the Ba contents of the melts. $K_{Ba}^{af/liq}$ is a function of: pressure, temperature, melt composition and possibly volatile contents, while the Ba content of the melts depend on, among other factors, evolution pathways of parental magmas and paragenesis.

Unfortunately, none of the above textures or relict grains occur within the barian feldspars at Deadhorse Creek. However, the presence of Ba-bearing biotite and the complex zoning of the grains implies that the barian feldspars formed by replacement of an earlier

phase during thermal metamorphism associated with the intrusion of the Coldwell Alkaline complex. In studies of barian feldspar and muscovite from the nearby Hemlo area, Pan and Fleet (1991) ascribed the formation of barian feldspars to the influx of hydrothermal fluids introduced along regional planar structures immediately following the peak of a second regional metamorphic event. From fluid inclusion studies of matrix quartz grains, the authors suggest homogenization temperatures of 530 ± 15 °C and indications of a dilute fluid (<2.5 wt.% NaCl equivalent; *cf.* Potter and Brown, 1977; Potter *et al.* 1978), which is in agreement with previous estimates for the White River-Schreiber greenstone belt (Pan and Fleet, 1990). Unfortunately, the timing of these events, gathered from field and textural relations, quantitative P-T-X-t data from mineral equilibria, oxygen isotope geothermometry, fluid inclusion studies, U-Pb and $^{40}Ar/^{39}Ar$ geochronology, indicate an age of 2672-2670 Ma (Pan and Fleet, 1995). An unpublished U-Pb age of 1128.7 ± 6 Ma (M. Smyk, pers. comm.) for the Deadhorse Creek Complex indicates that, although the complex shares some of the unusual mineralogy with the Hemlo deposit, it represents a much younger event. Therefore, while Ba-rich fluids were initially mobilized in the Archean during regional metamorphism, a second event is required in order to explain the occurrence of the barium-species at Deadhorse Creek. One possible scenario involves thermal metamorphism from the emplacement of the adjacent Coldwell Complex, which may have caused the remobilization of Ba-rich fluids into the Deadhorse Creek Complex. Due to the proximity of the Coldwell complex and permeable nature of the breccia, it would be an excellent destination for fluids traveling along strike to the regional foliation.

2.4 Baotite

Baotite, a rare Ba-Ti-Nb chlorosilicate, occurs within the diatreme breccia as anhedral grains poikilitically enclosed in: titanite and titanite plus rutile; and as an exsolved phase along with Mn-ilmenite and ilmenorutile within a rutile host. These phases are set in the potassium feldspar and aegirine-diopside matrix, which dominates the diatreme breccia (Figures 2.13 and 2.14). Although ilmenorutile is present elsewhere in the diatreme breccia, none of the rutile associated with baotite contains niobium, and is essentially stoichiometric TiO_2. Similarly, titanite associated with baotite does not contain any other substituting elements. Compositionally, the Deadhorse Creek baotite is close to the ideal chemical formula $[Ba_4(Ti,Nb)_8Si_4O_{28}Cl]$, with minor amounts of calcium, iron and vanadium present. The baotite structure consists of $[Si_4O_{12}]$ rings and columns of Ti-Nb octahedra aligned parallel to the c-axis (Simonov, 1960; Nekrasov *et al.* 1970). Chlorine atoms occupy the large cavity between each pair of metasilicate rings, while barium atoms fill channels in the framework between the metasilicate rings and Ti-Nb octahedron columns (Cooper, 1996). Representative compositions are illustrated in Table 2.5 and an energy dispersion X-ray spectrum (EDS) is shown in Figure 2.15. As with previous analyses of baotite (Peng, 1959; Nekarsov *et al.* 1971; Shurgia *et al.* 1980; Johan *et al.* 1991; Cooper, 1996), the majority of data exhibit cation deficiencies at the Si- and Ba-sites, suggesting natural vacancies within the structure. In contrast to the majority of previous data, the Deadhorse Creek baotite contains greater than 1.0 atom Cl^- per formula unit (*apfu*), with an average value of 1.25 *apfu* (26 analyses). Analyses reported by Johan *et al.* (1991) also indicated chlorine contents of 1.2 atoms per formula unit. In addition, the role of chlorine remains somewhat of an enigma since it is not required to balance (electrostatically) the structure. Semenov *et al.* (1961) suggested that chlorine was involved in the replacement $Nb^{5+} + Cl^- \leftrightarrow Ti^{4+}$, but as noted by Nemeč (1987), the presence of Cl in essentially Nb-free baotite would seem to contradict this hypothesis.

Baotite is the dominant barium-bearing mineral present in the "diatreme" breccia and is one of the few chlorine-bearing mineral within the complex. In common with the main

mineralized zone, barium is also present in the diatreme breccia as small, rounded, anhedral grains of barite set within the groundmass.

Baotite was first described in quartz veins associated with alkaline granites and syenites from Inner Mongolia (China) by Peng (1959) and Semenov *et al.* (1961). Since then, it has been described as an accessory mineral in carbonatites, fenites and carbothermal veins associated with lamprophyre dike swarms (Cooper, 1996). At the type locality, Bayan Obo, baotite occurs in late-stage quartz veins and other veins related to hydrothermal activity. Associated minerals include: quartz, aegirine, riebeckite and albite (Peishan *et al.* 1995).

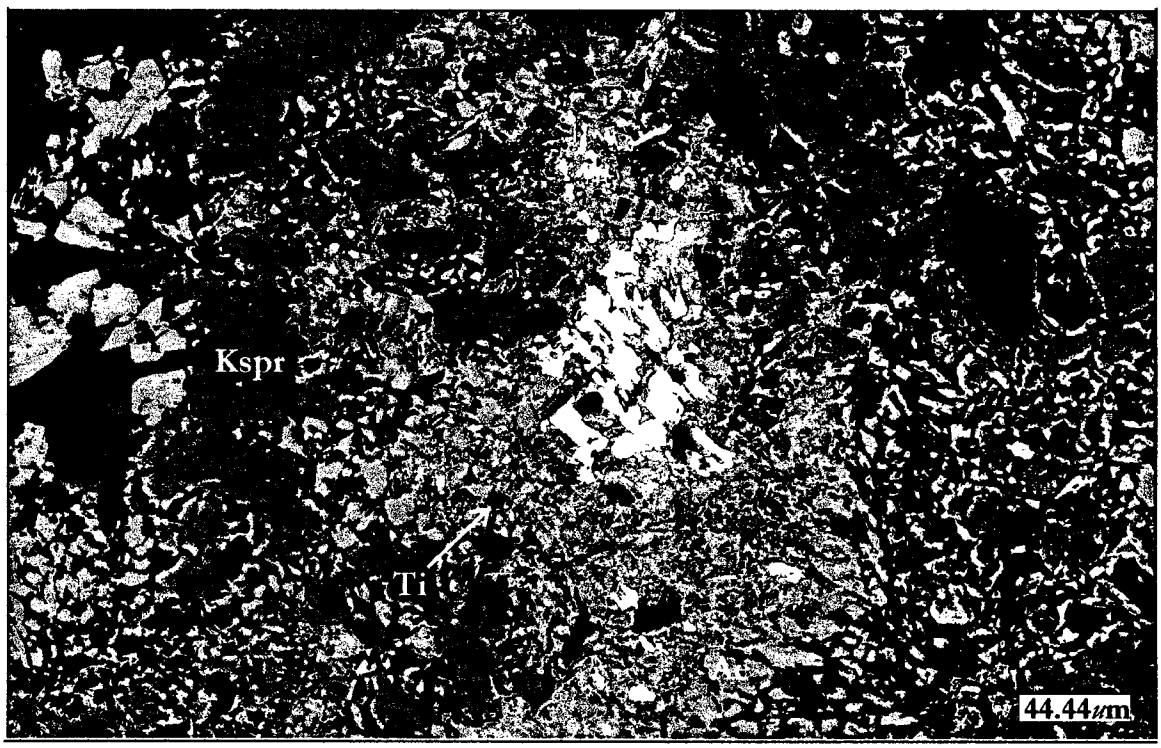

Figure 2.13: BSE-image of baotite (white) mantled by titanite (Ti-red) set in potassium feldspar (Kspr-blue) and aegirine-augite (Ae-green).

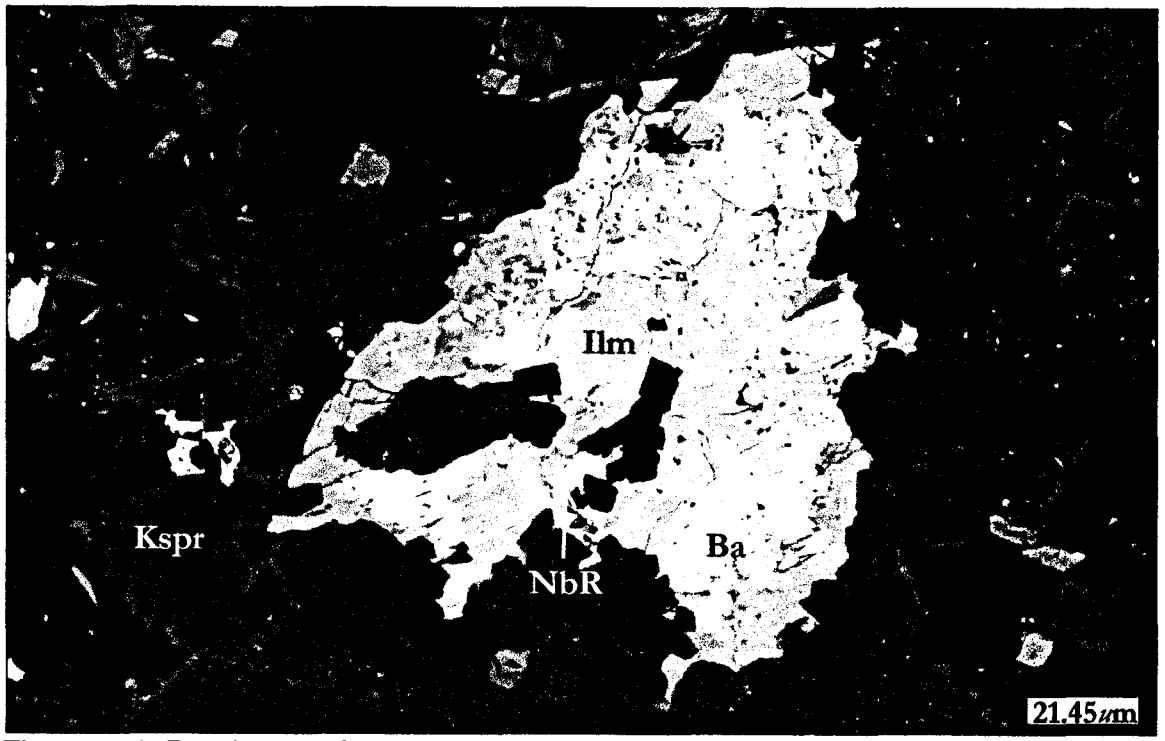

Figure 2.14: BSE-image of baotite (white) and ilmenorutile (NbR) exsolved from an Mn-bearing ilmenite host (Ilm), all set in a potassium feldspar plus aegirine-augite groundmass.

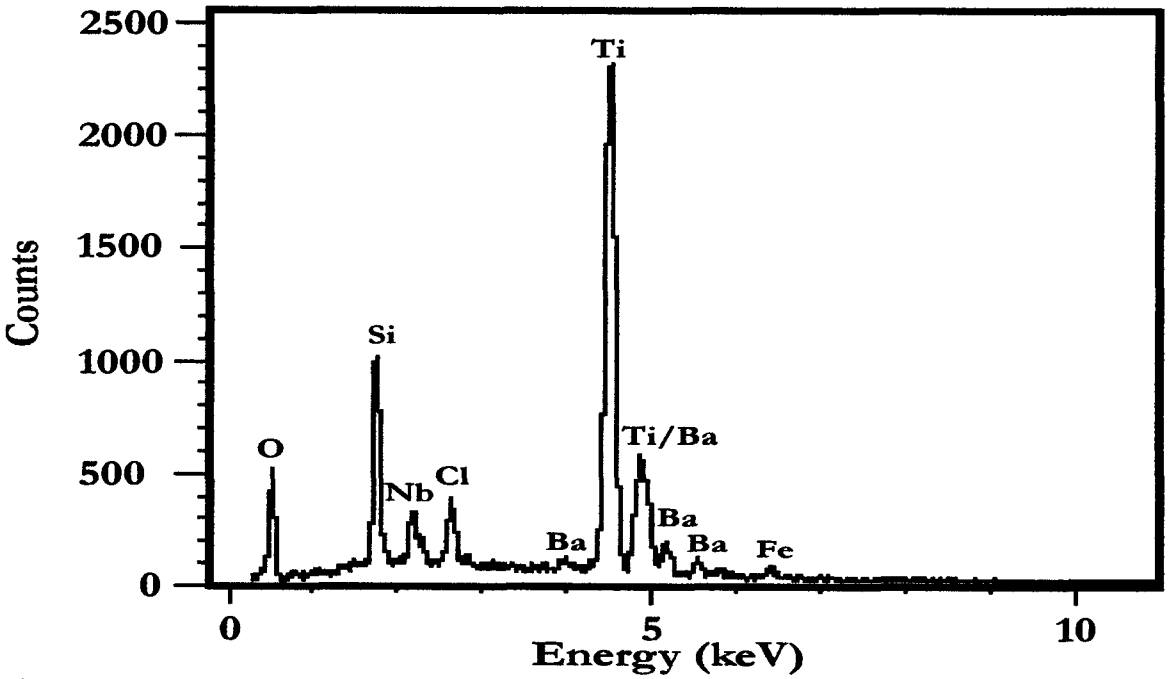

Figure 2.15: EDS of baotite from the diatreme breccia. Due to overlapping TiKβ1 and BaKα1 peaks, the amount of BaO appears lower than actual.

Table 2.5: Representative compositions of baotite from Deadhorse Creek.

	1	2	3	4	5	6	7	8
SiO_2	15.5	16.0	16.0	15.2	15.8	15.6	15.7	15.4
CaO	2.4	0.6	2.7	0.2	0.1	0.2	0.3	0.4
TiO_2	37.5	36.9	37.6	39.1	38.5	38.2	37.9	38.0
V_2O_5	0.9	0.6	0.3	0.3	0.5	0.6	0.6	0.4
FeO	0.9	1.3	0.9	0.5	0.6	0.7	0.8	1.2
Nb_2O_5	5.6	5.6	6.0	2.4	2.6	3.2	3.2	5.0
BaO	35.8	36.8	34.0	40.5	40.7	39.7	40.1	37.9
Cl	2.8	3.0	2.5	3.0	3.0	3.1	2.9	2.8
Less O=Cl	0.6	0.7	0.6	0.7	0.7	0.7	0.7	0.6
Totals	100.8	100.1	99.4	100.5	101.1	100.6	100.8	100.5
Si^{4+}	3.8	4.0	4.0	3.9	4.0	4.0	4.0	3.9
Ti^{4+}	7.0	7.0	7.0	7.6	7.4	7.3	7.3	7.3
V^{5+}	0.2	0.1	0.1	-	0.1	0.1	0.1	0.1
Fe^{2+}	0.2	0.3	0.2	0.1	0.1	0.1	0.2	0.3
Nb^{5+}	0.6	0.6	0.7	0.3	0.3	0.4	0.4	0.6
Σ	8.0	8.0	8.0	8.0	7.9	7.9	8.0	8.3
Ba^{2+}	3.5	3.6	3.3	4.1	4.1	4.0	4.0	3.8
Ca^{2+}	0.6	0.2	0.7	0.1	-	-	0.1	0.1
Σ	4.1	3.8	4.0	4.2	4.1	4.0	4.1	3.9
Total	15.9	15.8	16.0	16.1	16.0	15.9	16.1	16.1
Cl^-	1.2	1.3	1.1	1.3	1.3	1.3	1.3	1.2

Note: Cation proportions calculated based on 28 oxygens.

2.5 Barite

Barite [$BaSO_4$] is found throughout the Deadhorse Creek complex. In the main mineralized zone, the dominant habit is that of small veinlets, which cross cut all features, save for smaller calcite veins. Some of these smaller calcite veins also contain uranium-vanadium mineralization. The barite veinlets are less than 15 μm in width and although they have a corroded appearance, can be traced across the entirety of most thin sections. A typical cross-section of the veinlets involves (from center to edge): barite; hematite; pyrite and occasionally biotite. To a lesser extent, barite is also present as anhedral, rounded blebs set in groundmass calcite or quartz. Within the diatreme breccia, barite occurs as small, rounded, anhedral grains similar to the small, anhedral blebs found within the mineralized zone. In all instances these anhedral grains are confined to the groundmass, which consists of a mosaic of potassium feldspar and aegirine-diopside. Although the rounded barite grains were small (≤15 μm), the composition never varies from the ideal formula $BaSO_4$. However, the barite found in veinlets within the main mineralized zone contains small amounts of SrO and PbO, ranging from 0.32 to 1.45 wt.% and trace to 1.24 wt. % respectively. Representative compositions of the veinlet-barite are given in Table 2.6 and images in Figures 2.16 and 2.17.

Table 2.6: Representative compositions of the veinlet-barite from the mineralized zone.

	1	2	3	4	5	6	7	8
SO_3	34.5	34.2	34.9	34.3	33.3	34.8	34.7	34.6
SrO	1.7	1.5	0.5	1.9	1.3	0.8	0.3	1.0
BaO	64.3	64.5	65.6	62.8	64.7	65.0	65.8	64.0
PbO	1.2	0.7	0.6	0.9	0.4	0.4	-	0.9
Totals	101.7	100.9	101.6	99.9	99.7	101.0	100.8	100.5

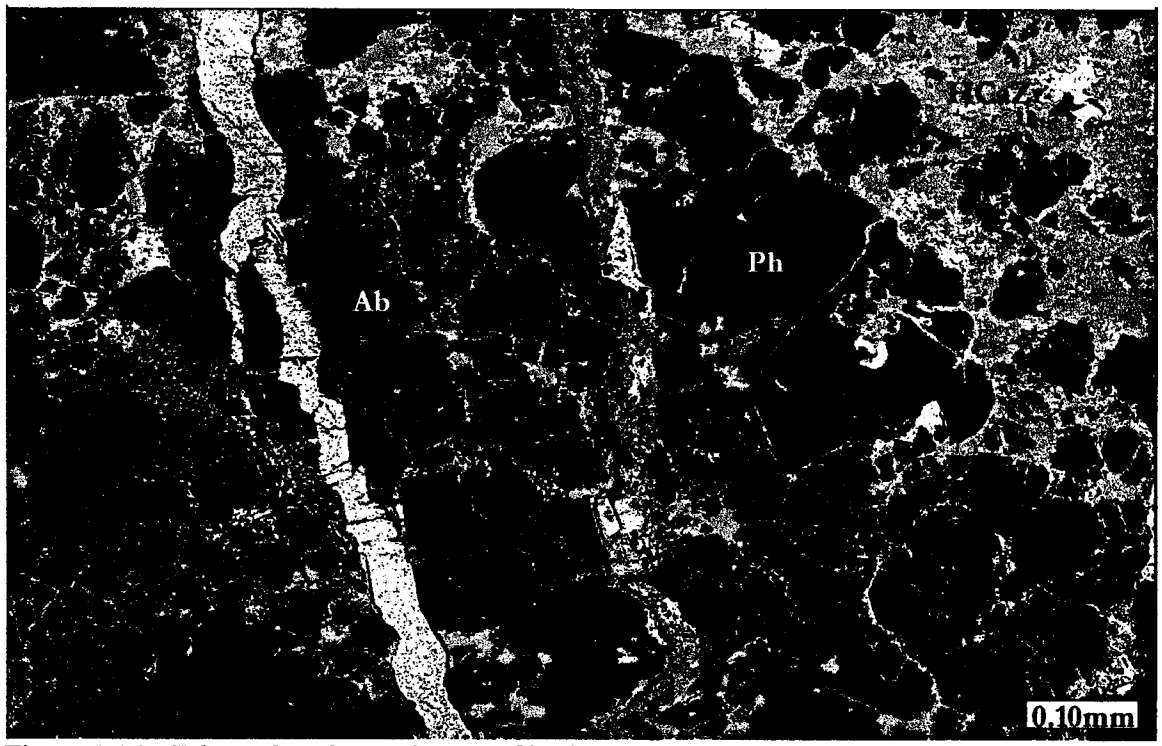

Figure 2.16: False-colored BSE-image of barite (red) cross-cutting phenakite (Ph) and albite matrix (Ab). Also shown are: calcite vein (Ct) and hydrated calcium zirconosilicate (green).

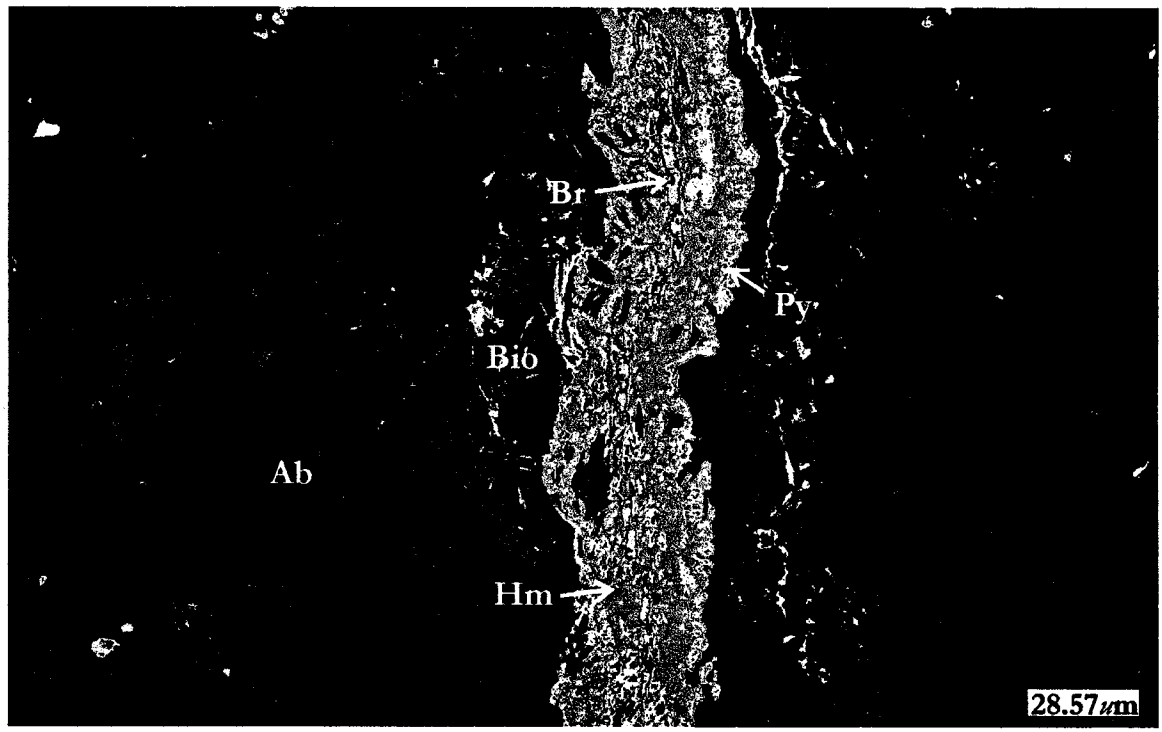

Figure 2.17: False-colored BSE-image of barite veinlet (red/pink) sheathed by hematite (Hm), pyrite (Py) and biotite (Bio), all set in an albite matrix (Ab).

2.6 Barylite

Barylite [$BaBe_2Si_2O_7$] is found exclusively within the main mineralized zone. It occurs as euhedral grains, which range in habit from plates to laths, set solely within quartz (Figures 2.18 and 2.19). Beryllium was not identified spectroscopically, as light elements cannot be detected by this methodology. Previous work by Platt and Mitchell (1996) has identified barylite within the main mineralized zone and the inferred beryllium concentrations agree with published data. Representative compositions including calculated beryllium concentrations of the Deadhorse Creek barylite are shown in Table 2.7.

Although barylite occurs in trace amounts, it is one of the two beryllium-bearing minerals identified within the complex. Both of these occur in close association with quartz veins and vein breccias. However, unlike the predominantly anhedral phenakite (which occurs in greater concentrations), barylite exhibits an euhedral habit. Environments from which barylite is reported to occur include: skarns, veins and vugs in iron and manganese ores, nepheline syenite pegmatites, fenites and veins in alkalic and fenitized rocks (Grew, 2002). The latter occurrences are from the Ilímaussaq alkaline complex were barylite occurs in analcime – sørensenite veins within the complex and strongly fenitized sandstones 15 kilometers north-east of the complex. In both instances, barylite is believed to represent a late hydrothermal phase, with barylite from within the complex forming a pseudomorph after chkalovite [$Na_2BeSi_2O_6$] (Petersen *et al.* 1991). Compositional data of the Deadhorse Creek barylites are in good agreement with those presented by Petersen *et al.* (1991). In common with Ilímaussaq barylite, minor amounts of K_2O are present in the Deadhorse Creek barylite (0 – 0.86 wt.%).

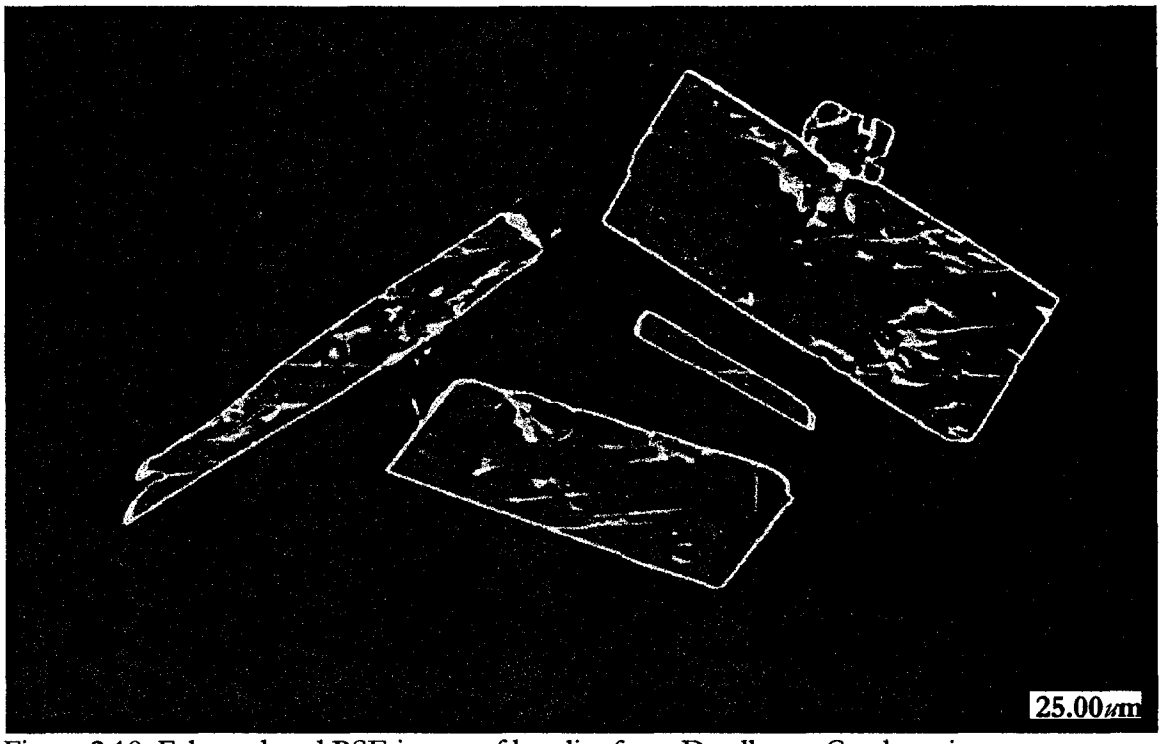

Figure 2.18: False-colored BSE image of barylite from Deadhorse Creek set in quartz.

Table 2.7: Representative compositions of Deadhorse Creek barylite

	1	2	3	4	5	6	7	8
SiO_2	37.6	37.3	38.1	38.4	37.6	38.5	37.9	38.9
K_2O	0.6	0.3	0.6	0.9	0.4	0.5	0.4	0.2
BaO	45.7	45.9	46.3	44.9	46.0	45.3	45.6	44.5
BeO*	16.1	16.5	15.0	15.8	16.0	15.7	16.1	16.4
Totals	100.0	100.0	100.0	100.0	100.0	100.0	100.0	100.0
Si^{4+}	2.0	2.0	2.0	2.0	2.0	2.0	2.0	2.0
K^{1+}	-	-	-	0.1	-	-	-	-
Ba^{2+}	0.9	1.0	1.0	0.9	1.0	0.9	0.9	0.9
Be^{2+}	2.1	2.1	1.9	2.0	2.0	2.0	2.0	2.1
Totals	5.0	5.1	4.9	5.0	5.0	4.9	4.9	5.0

Note: Cation proportions calculated based on 7 oxygens. * BeO weight percent calculated by difference.

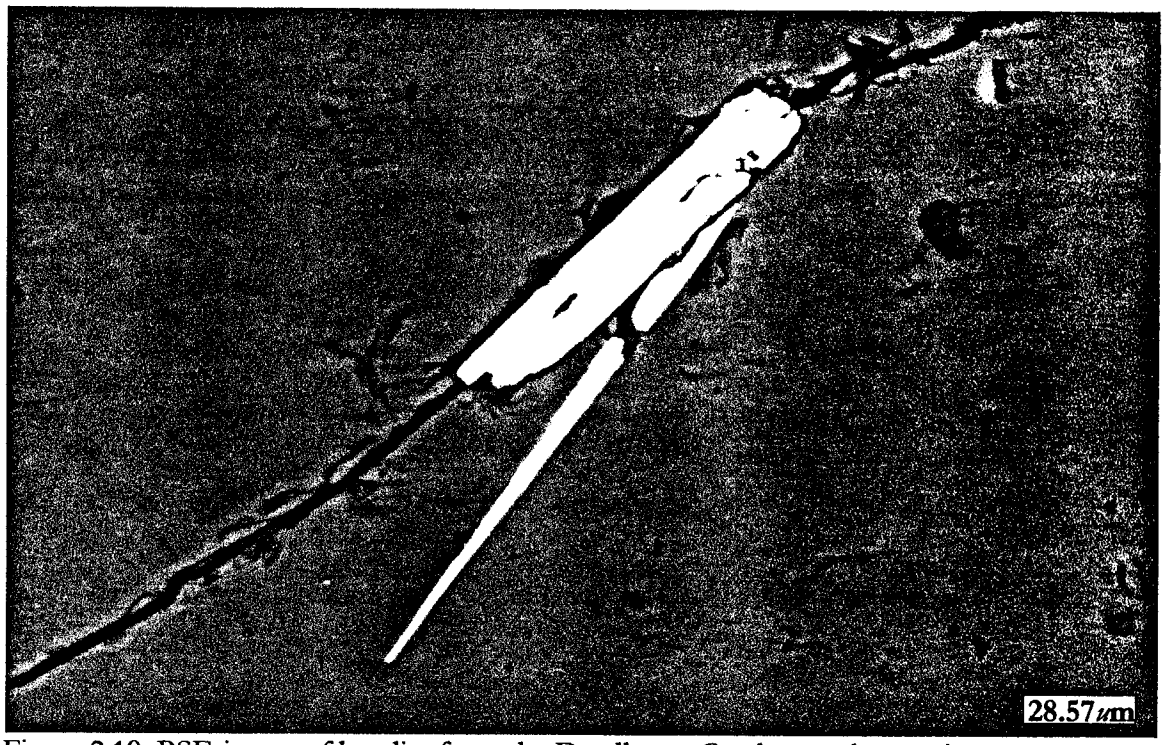

Figure 2.19: BSE-image of barylite from the Deadhorse Creek complex, set in quartz.

2.7 Unidentified Ca-Mn-Silicate

Within the main mineralized zone, an unidentified hydrated Ca-Mn-silicate occurs in association with a hydrated calcium zirconosilicate (HCaZr). Only a few occurrences of this phase were observed, although in all instances, it appears to have formed as a reaction product with the HCaZr and formed along the grain boundaries (Figures 2.20 and 2.21). These grains were set in a fractured albite groundmass. Despite the small size of the grains and inter-grown relationship, analyses of the phase produced consistent results. Comparison of these data with known hydrated Ca-Mn-silicates did not produce any matches. Searched databases included online sources: Athena Mineralogy and Web Mineral, and the Inorganic Crystal Structure Database (ICSD). Due to the presence of phenakite within the main mineralized zone, beryllium-bearing manganese silicates were also searched, and again no matches were found. Therefore, it has been assumed that the phase represents an as-of-yet unidentified species. Compositional data for the phase are shown in Table 2.8 and an energy-dispersion X-ray spectrum (EDS) in Figure 2.22. The other Mn-bearing phases within the main mineralized are Ba-Mn-hollandite and Mn-bearing ilmenite; both of which were not associated with the unidentified phase. The Ba-Mn-hollandite occurs primarily as late-stage veinlets, whereas the Mn-ilmenite was found associated with intergrown titanite and rutile.

Table 2.8: Compositional data for unknown Ca-Mn-silicate from Deadhorse Creek.

	1	2	3	4	5	6	7	8
MgO	1.5	1.5	1.0	1.4	1.6	2.0	2.1	1.6
Al_2O_3	4.1	3.7	4.9	4.4	5.2	4.6	4.5	4.6
SiO_2	33.3	33.4	34.0	33.5	33.9	33.4	33.9	33.4
CaO	19.4	19.9	19.3	20.1	20.3	20.3	19.4	20.6
TiO_2	1.7	1.6	1.1	1.3	1.1	1.5	1.4	1.6
V_2O_3	0.7	0.5	0.7	0.6	0.8	0.5	0.5	0.6
MnO	17.9	17.9	21.2	18.9	19.0	16.7	17.3	18.4
FeO	7.7	8.0	4.7	7.3	6.6	8.6	8.0	7.4
ZrO_2	1.2	0.6	0.2	0.3	0.1	0.3	0.3	0.3
PbO	0.4	-	0.2	-	-	-	-	-
Totals	87.9	87.1	87.3	87.8	88.6	87.9	87.4	88.5

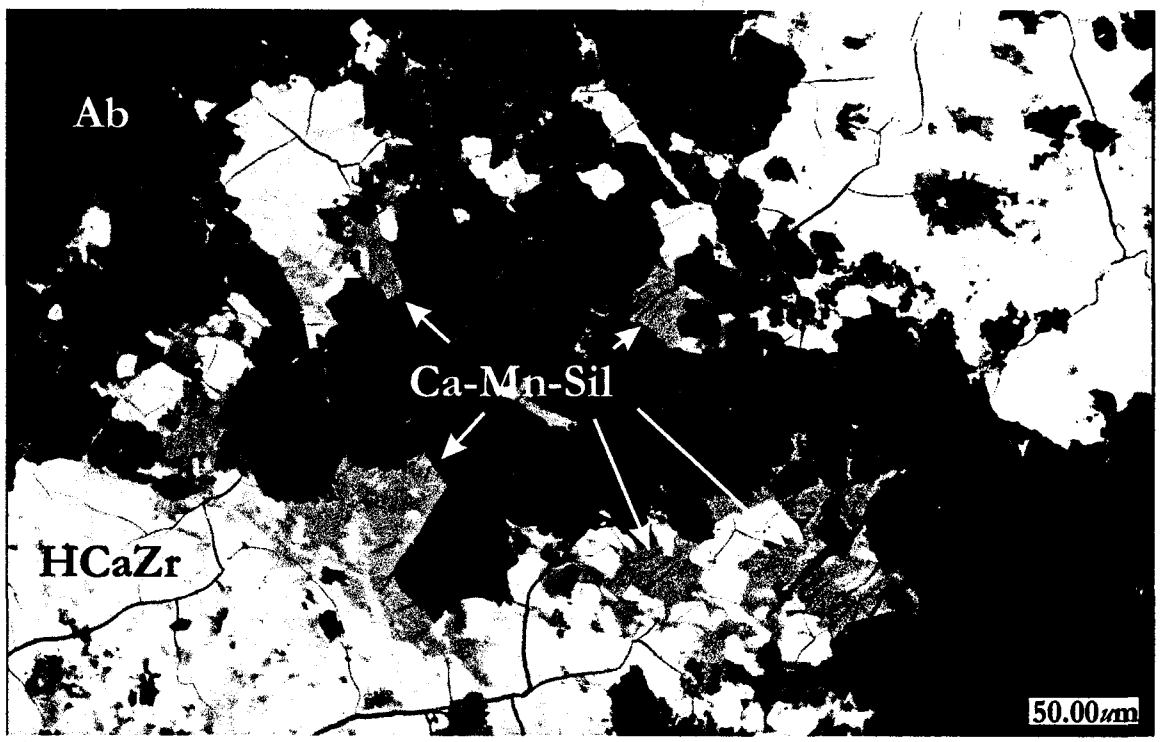

Figure 2.20: BSE-image of unidentified Ca-Mn-silicate (medium gray) associated with the hydrated calcium zirconosilicate (HCaZr) set in an albite groundmass, which is veined by calcite. The white patches represent thorite grains.

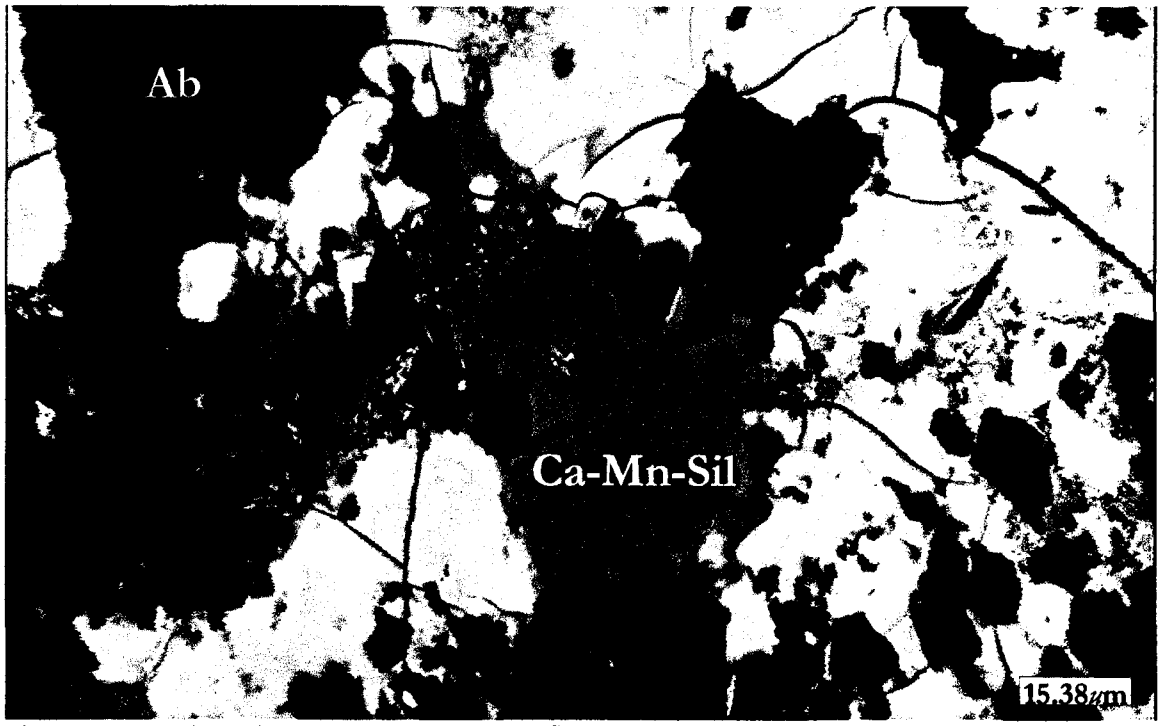

Figure 2.21: BSE-image of the unidentified Ca-Mn-silicate (center) surrounded by the hydrated calcium zirconosilicate (HCaZr) and albite (Ab). Also shown are grains of hematite (white).

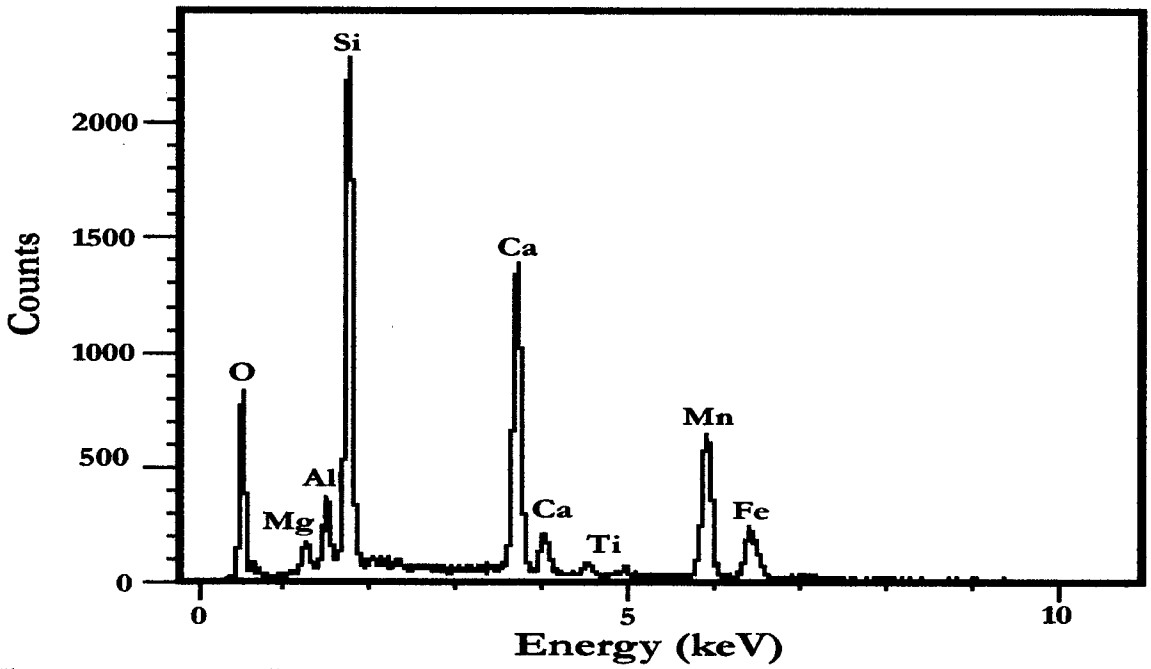

Figure 2.22: Energy-dispersion X-ray spectrum (EDS) of the unidentified Ca-Mn-silicate from the Deadhorse Creek complex.

2.8 Crichtonite

Historically, members of the crichtonite mineral group have been classified based on the large A-site cation, where the structural formula is: $AM_{21}O_{38}$. Typically, the large cation may be: Sr (crichtonite); Ca (loveringite); Na (landauite); U + REE (davidite); Pb (senaite); Ba (lindsleyite); K (mathiasite); or Sr + Pb (dessauite) (Grey and Lloyd, 1976; Gatehouse *et al.*, 1978, 1979; Grey and Gatehouse, 1978; Kelly *et al.*, 1979; Rouse and Peacor, 1968; Sarp *et al.*, 1981; Haggerty *et al.*, 1984; Orlandi *et al.*, 1997). In all members of the series, the smaller M-sites are dominated by Ti, with smaller amounts of Fe, Mg, Cr, Nb, Zr, Mn, Zn and V accounting for approximately 40% of the occupancy (Haggerty *et al.*, 1991). As determined by Grey *et al.*, (1976), the crystal structure of crichtonite consists of a framework of close-packed oxygens in a rhombohedral cell. This corresponds to space group R3 in which there are eighteen octahedral cation sites (M3, M4, M5; principally occupied by Ti, Fe and V in this case), two tetrahedral sites (M2) and one additional octahedral site (M1). The remaining anion site is occupied by the large radius cation (i.e., Ba, Sr, etc.), which is coordinated by twelve atoms of oxygen (Haggerty, 1991). Orlandi *et al.*, (1997) suggest that the series is best described by the crystal-chemical formula: $ABC_{18}T_2O_{38}$, as the previously adopted formula incorporates very different cation sites into one generalized M-site. The compositional differences of the various end-members become more evident using this approach; especially when considering members of the group in which the same element dominates the A-site cation. According to the crystal-chemical formula, the generalized M-site is divisible into: two tetrahedral T-sites (M2), and the octahedral B- and C-sites. The significant difference in site dimensions between the B- and C-sites distinguishes the two: B-cations are located in the larger, high-symmetry M1 site, whereas the C-cations are situated in the smaller M3, M4 and M5 sites (Orlandi *et al.*, 1997). Although the formula, $AM_{21}O_{38}$, has been preferred in previous studies, recent discoveries illustrating the various solid solutions between end-members of the series warrants the application of the crystal-chemistry formula.

As with most members of the group, the C-sites of the Deadhorse Creek crichtonite are dominated by TiO_2 (65.4 to 71.7% of the C-site occupancy). The remaining C-site cations consist of (in terms of occupancy %): V_2O_3 (16.6 – 22.5%), FeO (5.1 – 8.6%), Cr_2O_3 (0.95 – 7.3%) and MnO (0.37 – 3.0%). Silicon, scandium, calcium and niobium fill the B-site.

Potassium, rare earths and uranium are absent. Table 2.9 and an EDS (Figure 2.23) illustrate representative compositions.

Table 2.9: Representative composition of crichtonite from Deadhorse Creek.

Na_2O	0.5	0.3	0.5	0.3	0.3	0.4	0.4	0.4
SiO_2	0.4	0.2	0.6	0.3	0.2	0.5	0.2	0.3
CaO	0.8	0.7	0.8	0.9	0.7	0.7	0.9	1.0
Sc_2O_3	1.7	1.6	1.6	0.6	0.5	0.2	0.4	0.3
TiO_2	52.9	53.6	52.0	55.1	57.2	56.6	57.1	57.2
V_2O_3	15.4	15.5	15.5	14.5	14.4	12.9	13.8	13.0
Cr_2O_3	5.2	4.8	5.8	5.0	4.2	4.9	4.7	5.3
MnO	0.4	0.3	0.4	1.7	1.9	1.8	2.0	2.0
FeO	4.0	6.2	4.0	5.8	7.3	7.0	6.3	6.4
Fe_2O_3	8.6	5.7	8.3	7.5	6.2	6.5	7.4	7.0
SrO	1.7	2.1	1.8	4.4	4.5	3.8	4.6	4.1
Y_2O_3	1.2	1.8	1.3	0.3	0.5	0.4	0.4	0.7
Nb_2O_5	4.5	4.0	4.4	3.2	2.0	3.6	1.8	2.2
PbO	3.4	3.0	3.1	0.6	0.8	0.6	0.4	0.8
Totals	100.7	99.8	100.1	100.2	100.7	99.9	100.4	100.7
				Cation Proportions				
Na^{+}	0.3	0.2	0.3	0.2	0.1	0.2	0.2	0.2
Si^{4+}	0.1	0.1	0.2	0.1	-	0.1	0.1	0.1
Ca^{2+}	0.2	0.2	0.2	0.3	0.2	0.2	0.3	0.3
Sc^{3+}	0.4	0.4	0.4	0.2	0.1	0.1	0.1	0.1
Ti^{4+}	11.9	12.1	11.8	12.0	12.3	12.4	12.2	12.3
V^{3+}	3.7	3.7	3.7	3.4	3.3	3.0	3.1	3.0
Cr^{3+}	1.2	1.2	1.4	1.1	1.0	1.1	1.1	1.2
Mn^{2+}	0.1	0.1	0.1	0.4	0.5	0.4	0.5	0.5
Fe^{2+}	1.0	0.9	1.0	1.1	1.7	1.7	1.5	1.5
Fe^{3+}	1.9	1.9	1.9	1.9	1.3	1.4	1.6	1.5
Sr^{2+}	0.3	0.4	0.3	0.7	0.7	0.6	0.8	0.7
Y^{3+}	0.2	0.3	0.2	0.1	0.1	0.1	0.1	0.1
Nb^{5+}	0.2	0.3	0.2	0.6	0.6	0.5	0.6	0.5
Pb^{2+}	0.3	0.2	0.3	-	0.1	-	-	0.1
Totals	21.8	22.0	22.0	22.1	22.0	21.8	22.2	22.1

Structural formulae calculated based on 38 oxygen.

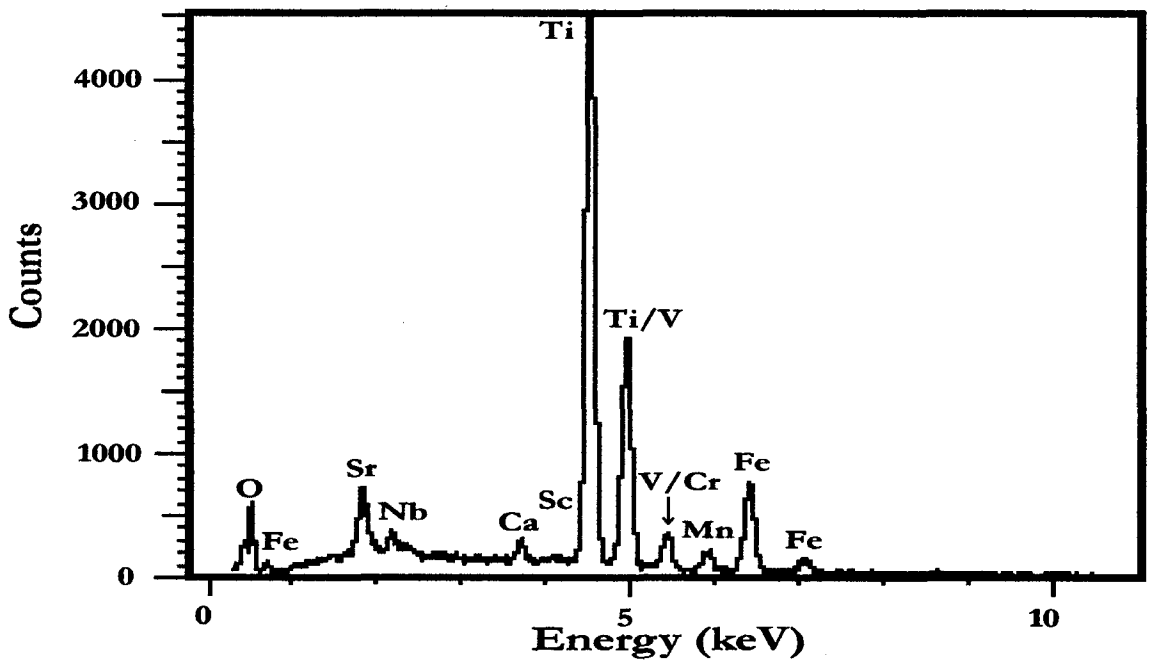

Figure 2.23: EDS of crichtonite from Deadhorse Creek.

The A-site of the Deadhorse Creek crichtonite is dominated by SrO, with smaller amounts of Na_2O, PbO and Y_2O_3. Therefore, on the basis of the established A-site nomenclature, the Deadhorse Creek crichtonites are best termed vanadium-rich analogues of crichtonite. In addition to the enrichment in vanadium, the crichtonite at Deadhorse Creek is distinguished by the enrichment in niobium. The only other members of the crichtonite series, which contain niobium, are lindsleyite and mathiasite ("LIMA"). However, LIMA are reported to be specific to upper mantle xenoliths. As previously noted by Platt and Mitchell (1996), not only does Nb_2O_5 occur in the Deadhorse Creek crichtonite, it reaches some of the highest recorded concentrations (1.96 to 6.56 wt.%).

According to Haggerty (1991), at all localities bearing 'LIMA', Mg-Al chromite is an associated mineral (in addition to armalcolite, Nb-Cr rutile and Cr-ilmenite at Bultfontein and Jagersfontein, South Africa). Haggerty (1991) states, "chromium is an essential component of 'LIMA' and reaction of spinel with metasomatising fluids enriched in Ba, K, Ti, Zr, Nb and REE, results in either lindsleyite or mathiasite; excess Ti, Fe and Mg are subsequently precipitated in armalcolite, ilmenite and rutile". Lindsleyite has also been reported from zircon-bearing MARID xenoliths (mica-amphibole-rutile-ilmenite-diopside; Dawson and

Smith, 1977), but due to the presence of either olivine or orthopyroxene these rocks differ from the classic MARID and as such, bear a closer affinity to harzburgites (Haggerty and Gurney, 1984; Haggerty, 1991). Although chromium is present in the Deadhorse Creek crichtonite, associated Mg-Al chromite, armalcolite or Cr-ilmenite has not been observed.

In Figures 2.24a-c, the weight percentages of V_2O_3, FeO_{Total}, and Nb_2O_5 are plotted against TiO_2. While Nb_2O_5 exhibits an inverse correlation to TiO_2, FeO_{Total} illustrates a positive correlation. Figures 2.24d and e illustrate the variation in FeO_{Total} versus Sc_2O_3 and (Y_2O_3 + PbO) versus SrO, respectively. As shown in (e), the A-site cations Y_2O_3 and PbO plot an inverse correlationship with the dominant SrO.

In the main mineralized zone, crichtonite grains are present in two habits, which are similar to those of the Nb-V-enriched rutile: small (<10 μm) anhedral blebs or larger (≤150 μm in length) subhedral-to-euhedral fractured grains, which may display a corroded 'atoll' texture. Both phases are preferentially set in a calcite matrix, along with a hydrated calcium zirconosilicate, albite and apatite. In both cases, the hydrated calcium zirconosilicate is present as anhedral, cryptocrystalline aggregates, whereas the apatite and albite grains occur as euhedral-to-subhedral grains. In such cases, calcite commonly fractures the albite grains while apatite remains unbrecciated. In one sample, a crichtonite grain was crosscut by a calcite veinlet bearing tyuyamunite.

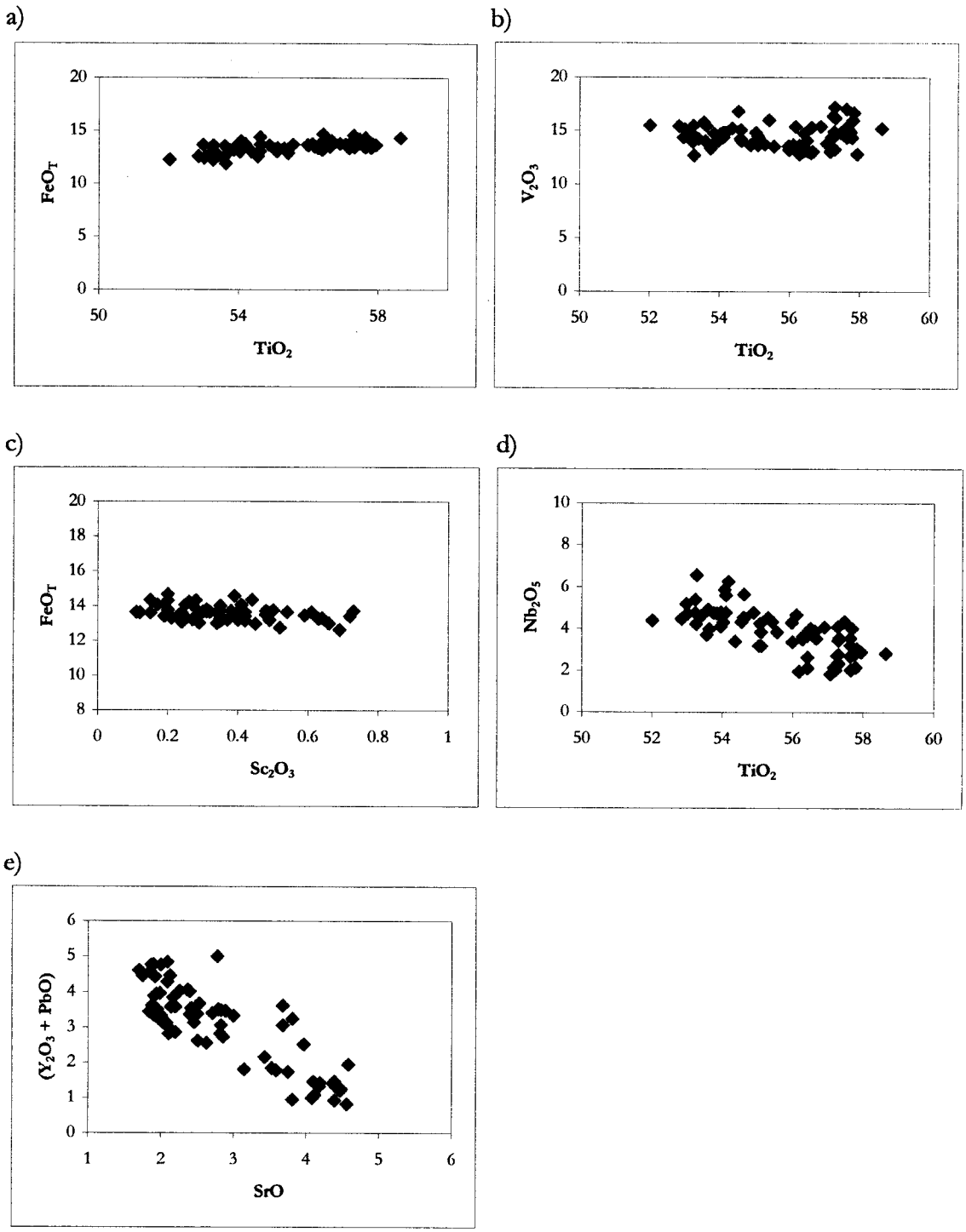

Figure 2.24a-c: Plots of V_2O_3, FeO_{Total} and Nb_2O_5 against TiO_2; d: Plot of FeO_{Total} versus Sc_2O_3; e: plot of $(Y_2O_3 + PbO)$ against SrO.

In Figure 2.25, the $FeO+Fe_2O_3+MgO$ contents are plotted against TiO_2. Using the terminology of Haggerty (1991), the Deadhorse Creek crichtonites plot in the upper mantle quadrant of the diagram, very near the field defined by LIMA. As noted by Platt and Mitchell (1996), these are the only non-LIMA crichtonites to plot in this quadrant. As a result, the authors have suggested that this quadrant be more appropriately termed the alkali metasomatic quadrant, since the geologic setting of the Deadhorse Creek is not an upper mantle ultramafic environment.

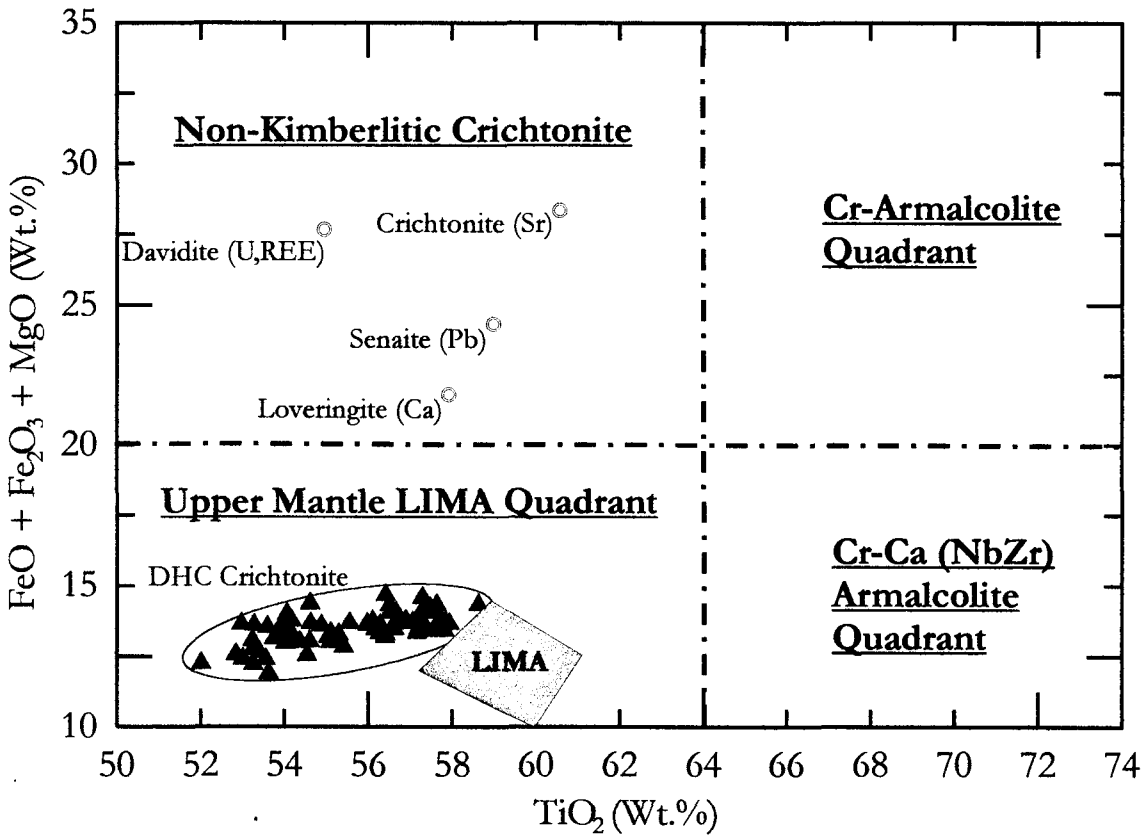

Figure 2.25: Plot of $FeO+Fe_2O_3+MgO$ vs. TiO_2 for the Deadhorse crichtonites (solid triangles). Open circles represent compositional points for crichtonite, senaite, loveringite and davidite. Shaded area and quadrant divisions after Haggerty (1991).

Interestingly, when V_2O_3 is included in a plot of $FeO+Fe_2O_3+MgO$ vs. TiO_2 for the Deadhorse crichtonites, the grains plot closer to the ideal composition of crichtonite (well within the non-kimberlitic quadrant of the diagram). However, due to some replacement of titanium by niobium, iron and chromium, the samples plot lower in terms of TiO_2, as compared to the ideal member. This is shown below, in Figure 2.26. Figures 2.27, 2.28 and 3.29 illustrate the habits of the Deadhorse Creek crichtonites.

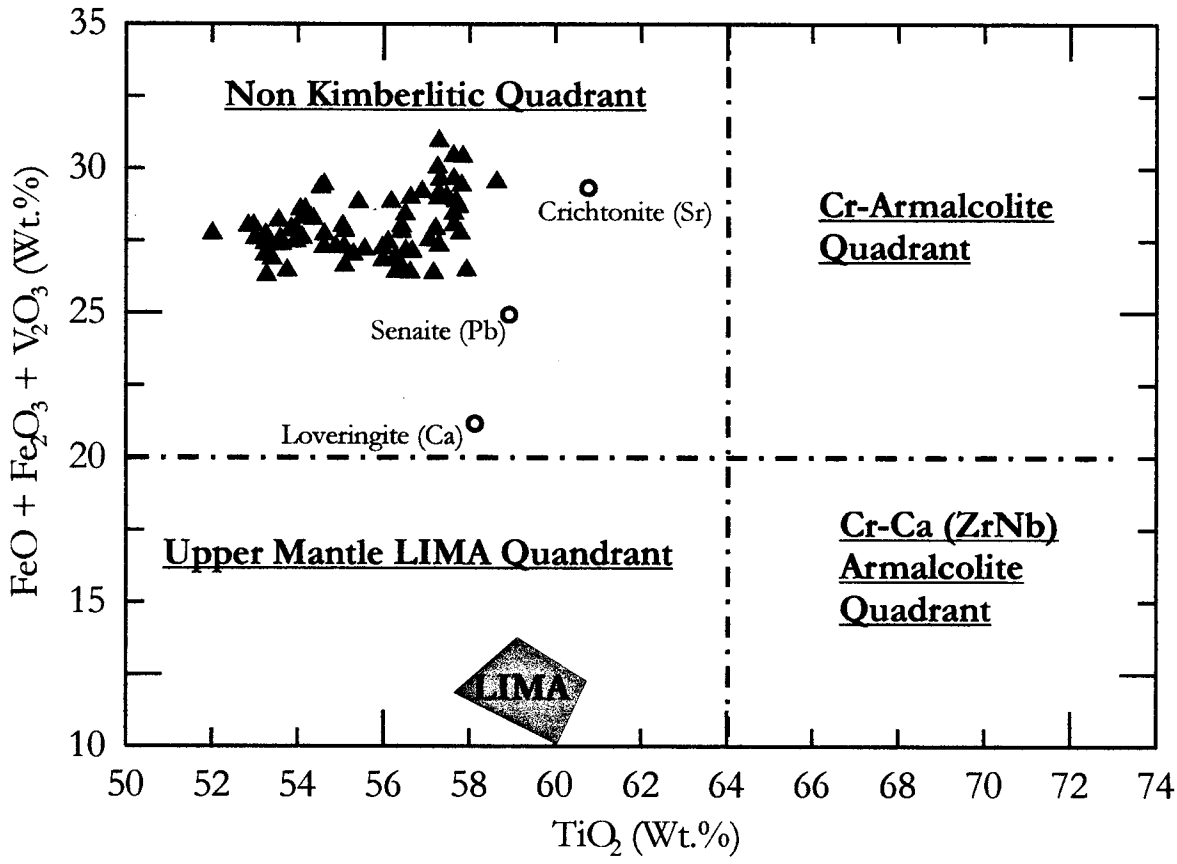

Figure 2.26: Plot of $FeO+Fe_2O_3+MgO$ (+ V_2O_3) vs. TiO_2 for the Deadhorse Creek crichtonites. Solid triangles represent the samples, whereas open circles represent the ideal end-members. After Haggerty (1991).

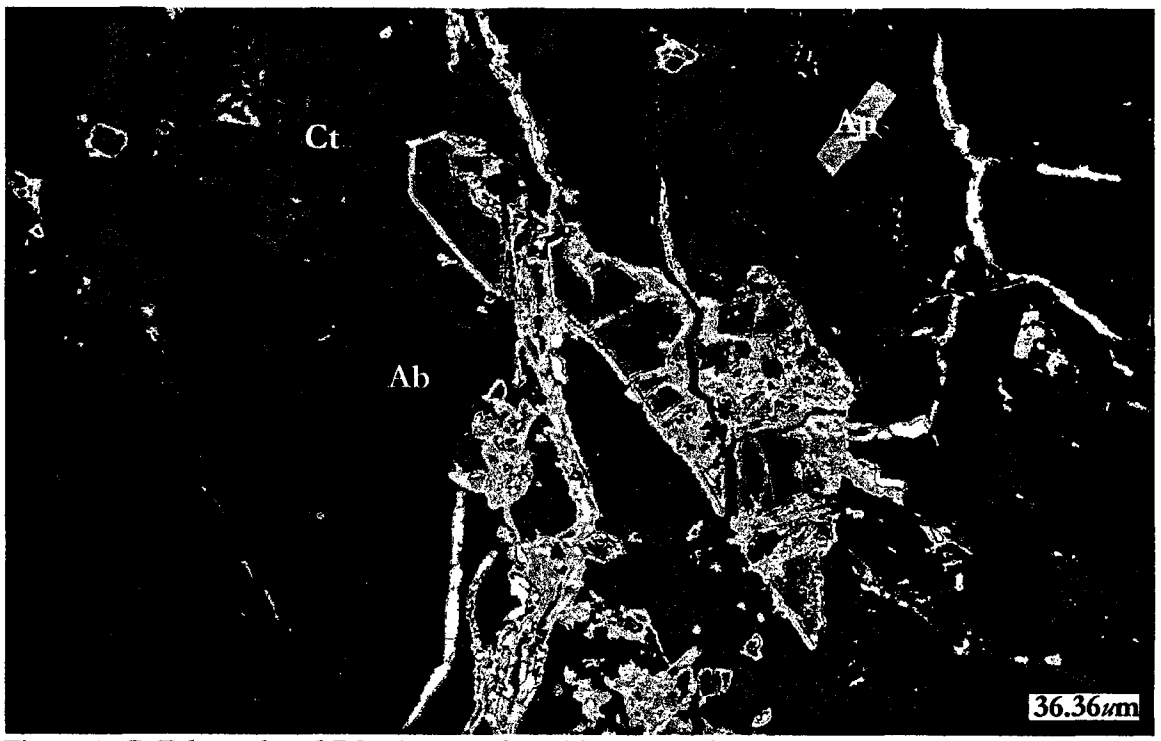

Figure 2.27: False-colored BSE-image of a subhedral crichtonite grain (Cr) set in calcite (Ct) and albite (Ab). The crosscutting veinlet hosts tyuyamunite.

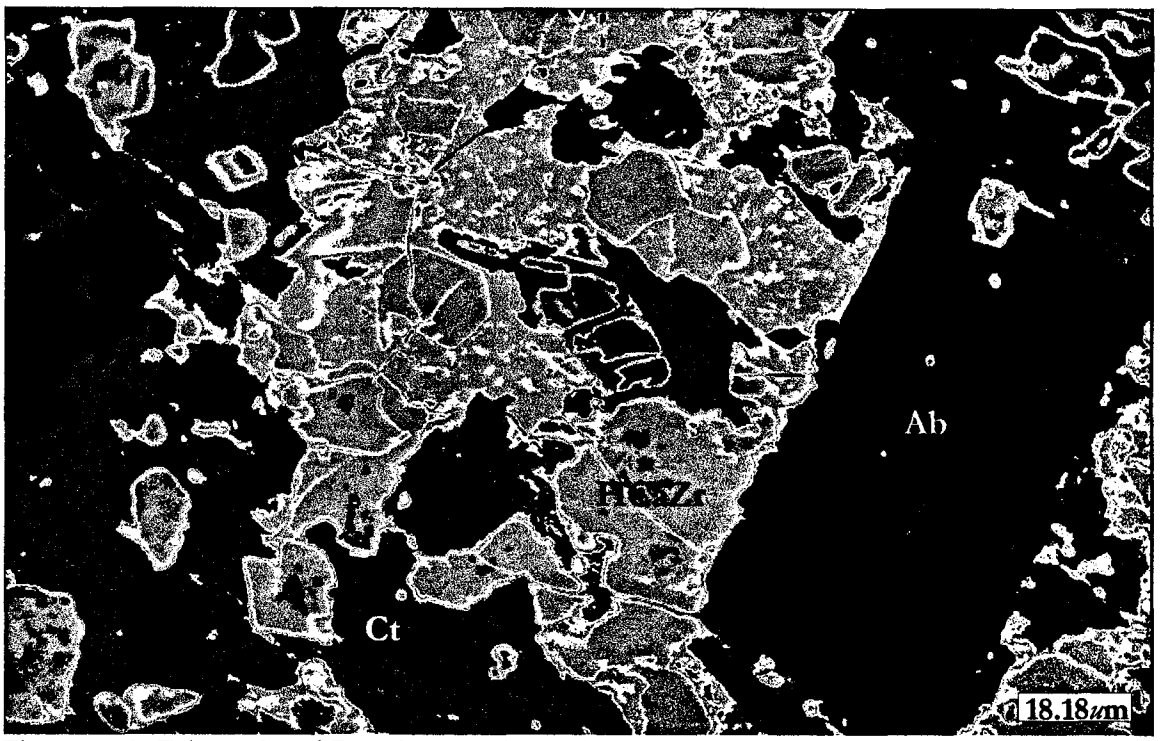

Figure 2.28: False-colored BSE-image of an anhedral crichtonite grain (Cr) set in quartz, which also hosts euhedral albite grains (Ab), titanite (green) and a hydrated calcium zirconosilicate (HCaZr).

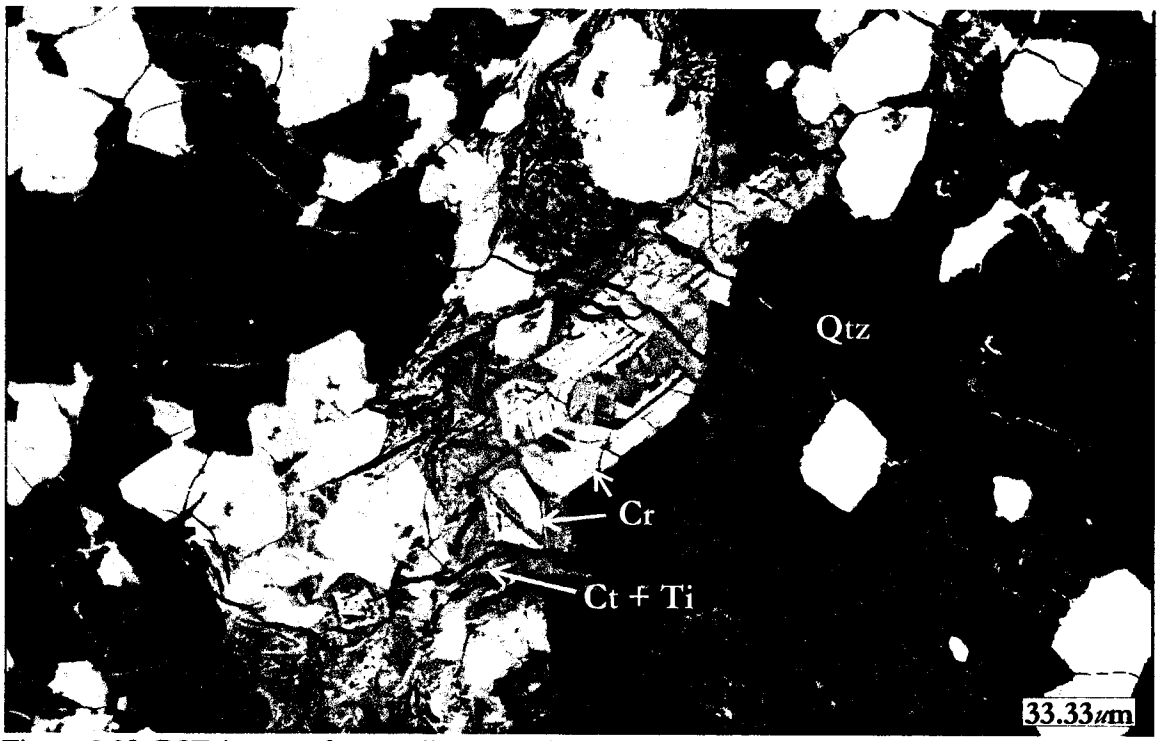

Figure 2.29: BSE-image of an 'atoll' textured crichtonite (Cr) set in a mix of calcite and titanite (Ct + Ti), all set in a fractured quartz groundmass which contains grains of a hydrated calcium zirconosilicate (HCaZr).

2.9 Hollandite

Hollandite [$Ba(Mn^{4+},Mn^{2+})_8O_{16}$] is a member of the cryptomelane group of minerals, which have received considerable attention as possible repositories for industrial fission products (Ringwood *et al.* 1979) and hosts of large-ion lithophile elements in crustal and mantle rocks (e.g. Zhang *et al.* 1993; Foley *et al.* 1994). The group is subdivided into two chemically distinct subgroups; manganates and titanates. The manganates have the general formula $AMn_8(O,OH)_{16}$ and include several species that differ by the occupancy of the A-site (Ba, K, Na, Pb, and Sr). With the exception of priderite [$(K_{1.2}Ba_{0.4})(Ti_{6.7}Fe_{1.1}Mg_{0.2})_{\Sigma 8.0}O_{16}$], the titanates have the same general formula as the manganates, with either V^{3+} or Cr^{3+} replacing Ti in the octahedral coordinated B-site, and the A-site dominated by Ba (Mitchell *et al.* 2000).

Hollandite is present only in the main mineralized zone of the Deadhorse Creek complex. Within this narrow zone, hollandite occurs either in late-stage veinlets or small, interstitial anhedral grains. The anhedral grains are set in a calcite plus apatite groundmass, interstitial to large, rounded phenakite grains. Unfortunately, due to the small size of the hollandite grains and veinlets, no accurate compositions could be obtained. Qualitatively, the grains were identified as being close to the ideal formula for hollandite, with small concentrations of PbO (<3 wt.%), FeO (<2 wt.%) and some SiO_2 and CaO matrix contamination (Figures 2.30, 2.31 and 2.32). These late-stage calcite veinlets are also host to barite and tyuyamunite mineralization. In common with the tyuyamunite mineralization, which is believed to have formed by interaction of circulating meteoric fluids enriched in uranyl and vanadate ions, hollandite mineralization has been primarily ascribed to supergene enrichment or precipitation through weathering processes (Vasconcelos, 1999; Nicholson, 1992). In his detailed study of manganese oxides Nicoholson (1992) listed only one rare occurrence of non-supergene hollandite; a hydrothermal hot-spring in northern Chile (Ossa, 1970). Such similarities suggest that both phases formed due to weathering processes in a supergene-type environment. In addition, secondary calcite formation has been ascribed to alteration in a zone of supergene alteration (Zak *et al.* 1997).

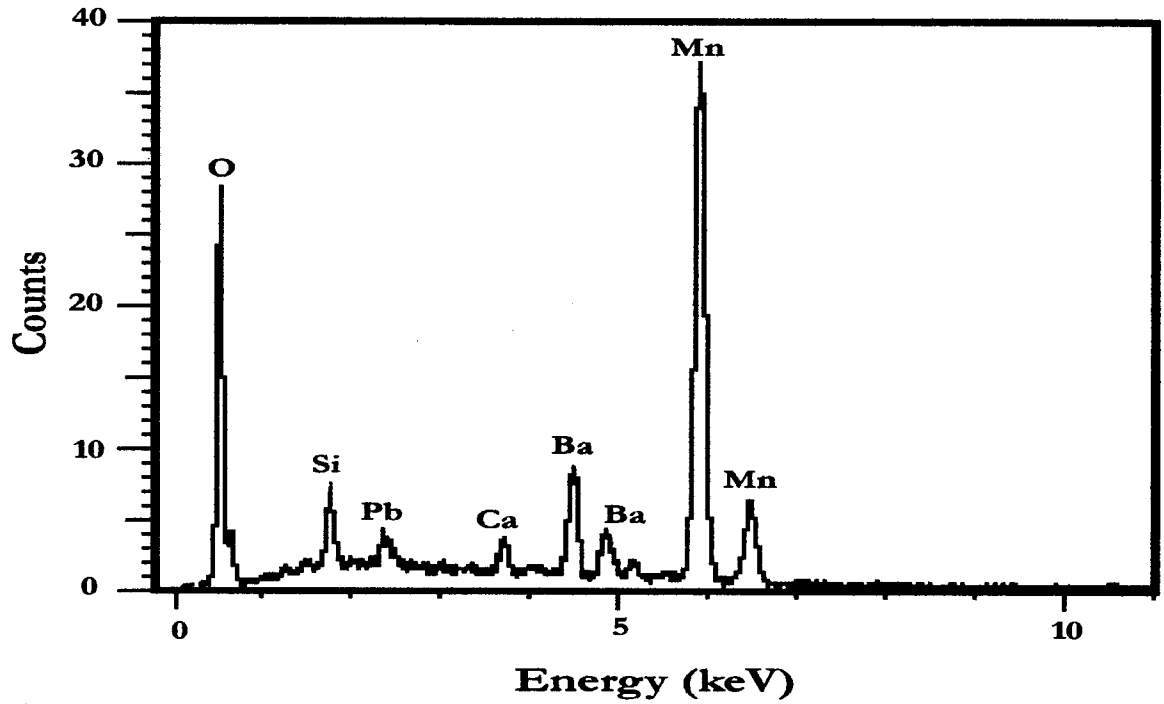

Figure 2.30: Energy dispersion X-ray spectrum (EDS) of hollandite veinlet, illustrating the background contamination (Ca and Si).

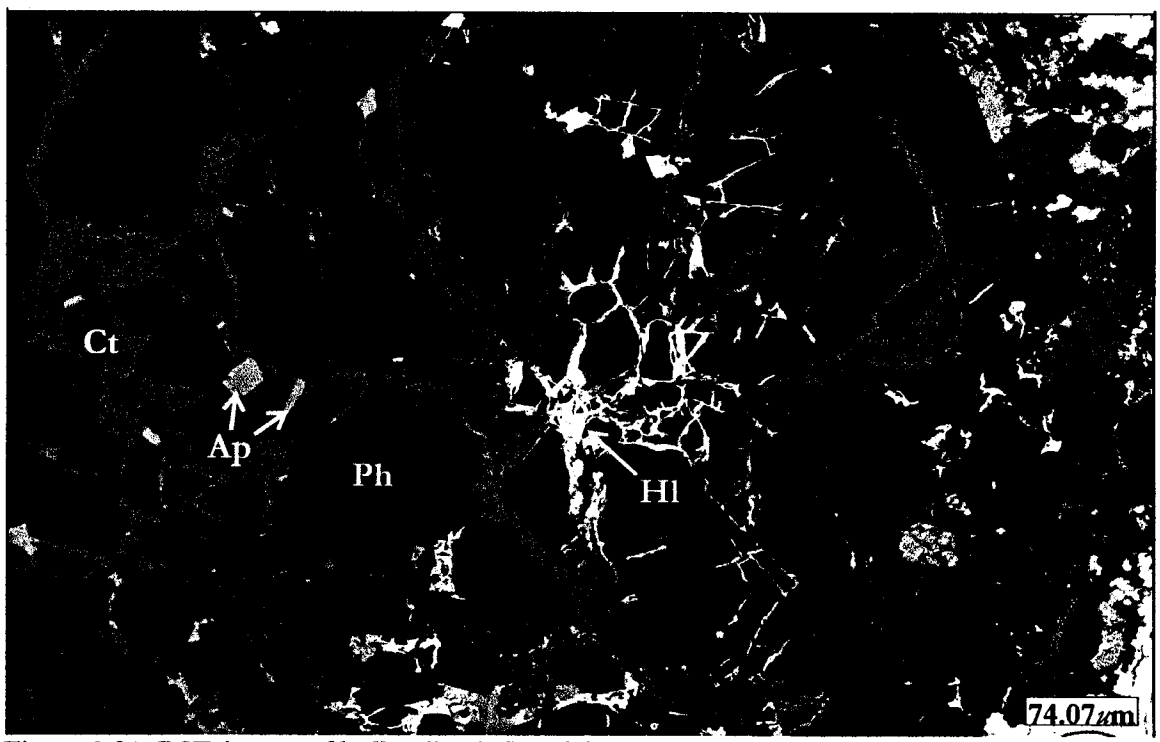

Figure 2.31: BSE-image of hollandite (Hl), calcite (Ct) and apatite grains (Ap) interstitial to large phenakite grains (Ph).

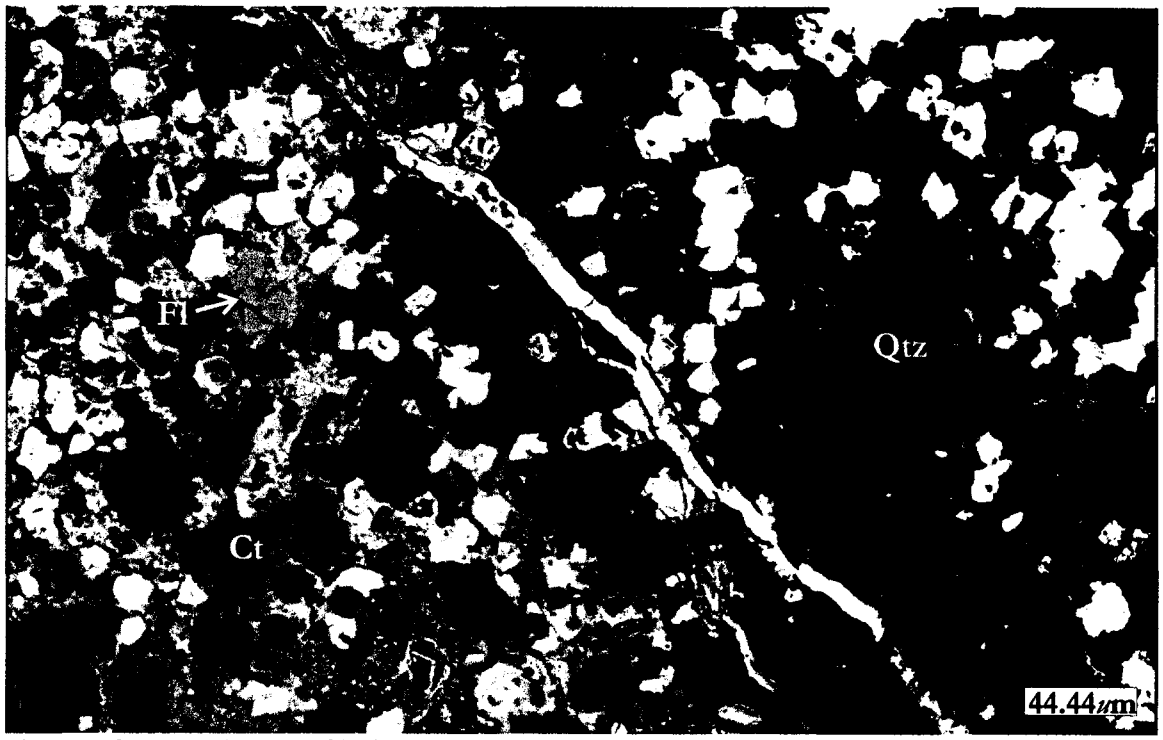

Figure 2.32: BSE-image of hollandite vein (white) cross-cutting quartz (Qtz) and calcite matrix (Ct). Also shown: the hydrated calcium zirconosilicate (light gray) with zircon remnants within and fluorite (Fl).

2.10 Monazite-(Ce)

Monazite-(Ce) [$(Ce,La,Th)PO_4$] is present in the main mineralized zone, the diatreme breccia and the cross-cutting carbonatite dike. Monazite occurs in greatest amounts within the carbonatite dike and unmineralized diatreme breccia. In all three occurrences, monazite forms predominantly small (10 to 30 μm), anhedral, blebs set within the groundmass. In the diatreme breccia, monazite occurs in a groundmass of potassium feldspar, while within the main mineralized zone, it is found in calcite. In a few instances, monazite from the main mineralized zone and carbonatite dike occurs in a larger (up to 0.14 mm long), acicular habit, with several grains clustered together. In the main mineralized zone, these are commonly associated with chlorite and hosted within a calcite groundmass. Within the carbonatite dike, the acicular grains occur in the same calcite plus dolomite–ankerite groundmass as the smaller, anhedral grains.

A second habit of monazite within the diatreme breccia consists of larger (up to 30 μm long), anhedral grains associated with chlorite and the HCaZr, all set in a potassium feldspar matrix. In Figure 2.33, an EDS illustrates the composition of monazite from the diatreme breccia. Interestingly, Nd is present in minor amounts within the monazite from the diatreme breccia, and the carbonatite dike. Figures 2.34, 2.35 and 2.36 illustrate the various textural types present.

Monazite-(Ce) is a relatively rare mineral which occurs as an accessory phase in peraluminous granites, syenitic and granitic pegmatites, quartz veins, carbonatites, charnokites, migmatites and pargneisses (Förster, 1998*a*; Rapp and Watson, 1986). The incorporation of actinides within the monazite structure is relatively common, with thorium being preferentially incorporated over uranium. Reported thorium concentrations range from not detectable to 21.9 wt. % (van Emden *et al.* 1997). Possible substitution schemes for the incorporation of actinides include two mechanisms: (1) $(TH,U)^{4+} + Ca^{2+} \leftrightarrow 2REE^{3+}$; and (2) $(Th,U)^{4+} + Si^{4+} \leftrightarrow REE^{3+} + P^{5+}$, which may occur in conjunction with each other or independently (van Emden *et al.* 1997). Although uranium commonly substitutes into the monazite structure, it generally only occurs in minor amounts (e.g. $Th/U \geq 10$) (Förster, 1998*a*). Förster (1998*a*) notes U-rich magmas do not necessarily crystallize U-rich monazites. Rather, U^{4+} shows a strong tendency to form uraninite or uranothorite rather

than substituting preferentially into monazite or xenotime. This observation is in agreement with relationships from the Deadhorse Creek complex, where abundant uranium mineralization is manifested in uraninite and tyuyamunite, yet monazite-(Ce) does not contain appreciable amounts of uranium.

As noted above, monazite-(Ce) from the diatreme breccia and carbonatite dike contains Nd_2O_3. Typical concentrations of Nd_2O_3 in monazite-Ce from granitic rocks range from 8-12 wt.%, with exceptional cases reaching up to 21.7 wt.%. Enrichment in Nd is usually also accompanied by increased amounts of Sm_2O_3 (up to 5.3 wt.%). Within composite granitic plutons, Nd_2O_3 incorporation is highest in aplites (Förster, 1998*a*).

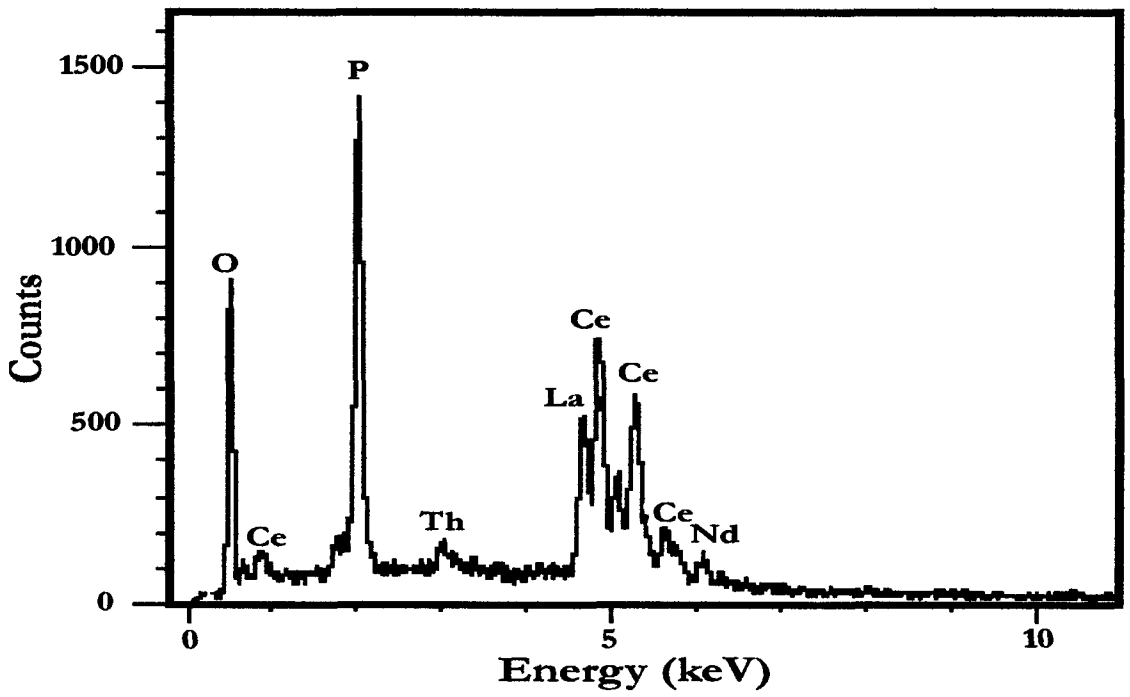

Figure 2.33: EDS of monazite from the diatreme breccia illustrating the presence of La, Th and Nd.

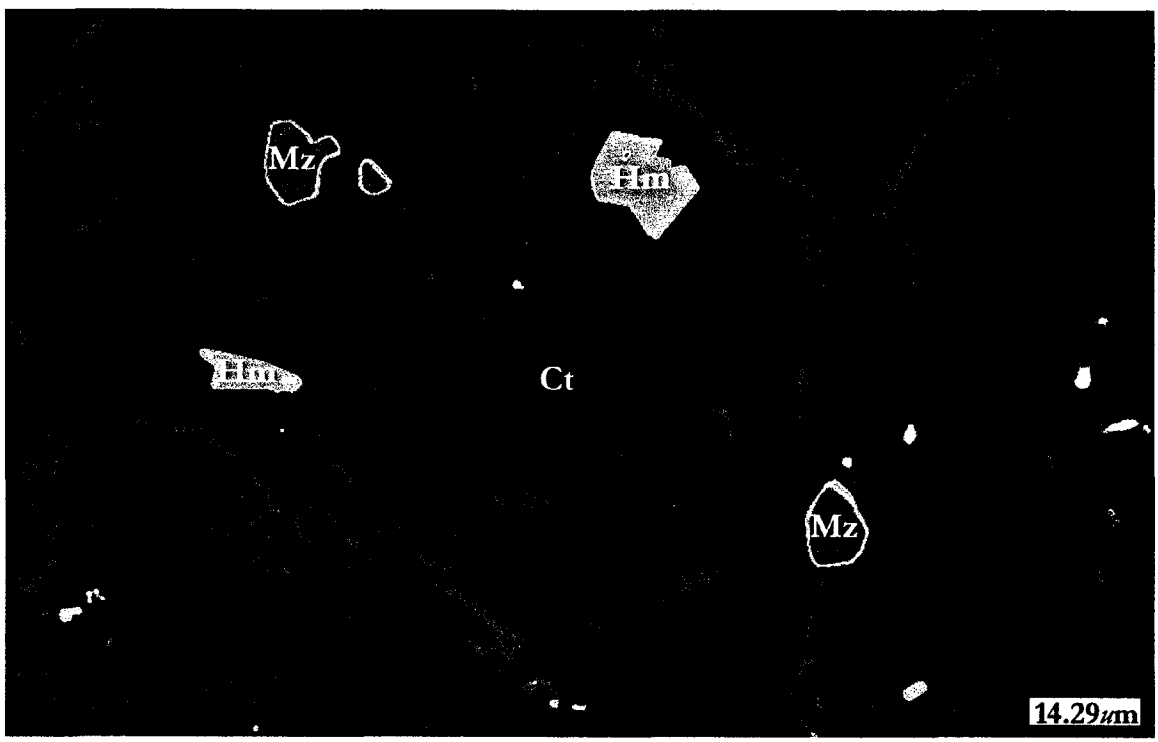

Figure 2.34: False-colored BSE-image of anhedral monazite-(Ce) (Mz) and hematite (Hm) from the main mineralized zone set in calcite.

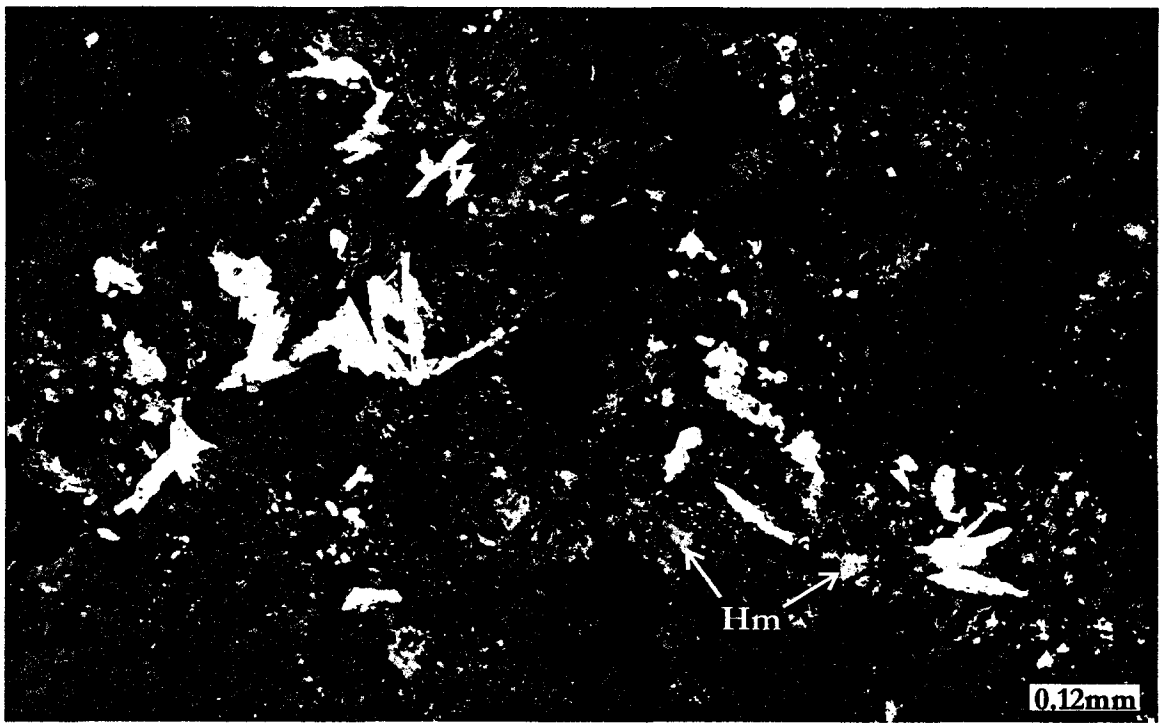

Figure 2.35: BSE-image of large monazite grains (white) and hematite (Hm) from the diatreme breccia, set in a mosaic of aegirine-augite plus potassium feldspar.

Figure 2.36: BSE-image of acicular monazite-(Ce) (white) from the MMZ associated with anhedral hematite and set in a calcite groundmass. The largest monazite grain is approximately 0.1 mm in length.

2.11 Phenakite

Phenakite [Be_2SiO_4] occurs only within the main mineralized zone of the complex. The mineral occurs as large, rounded, anhedral aggregates and subhedral, radiating grains (Figures 2.37, 2.38 and 2.39). These grains commonly reach several millimeters in length and can be recognized as pink grains by the naked eye in hand sample. Both habits are associated with quartz, although they also occasionally occur within a calcite and calcite plus albite groundmass. Phenakite was most abundant in samples characterized by quartz veins and vein breccias [quartz-(II)]. In thin section, in cross-polarized light, the phenakite grains display high-order birefringence colors, which stand out prominently against quartz and the fine-grained matrix. In backscattered electron images (BSE), the phenakite grains appear as black voids containing approximately 50% SiO_2, as beryllium cannot be detected by this methodology. Therefore, quantitative data were not acquired for the phenakite, although qualitatively it can be noted that the phenakite is free of impurities. In order to identify the phase, a powder X-ray diffraction pattern (XRD) was obtained. This was done by initially crushing and sieving the sample, creating a 75-to-100 μm powder. Next, bromoform ($CHBr_3$; specific gravity = 2.87) was used to remove the more dense material (phenakite has a relative specific gravity of 2.9-2.98). This dense material was further subdivided according to magnetic susceptibility. After several runs through an electromagnetic separator, all that remained where tiny grains of pink phenakite. These grains were then reground to a fine powder for powder XRD in an agate mortar. The resulting XRD pattern is shown in Figure 2.40, with a difference plot (difference between calculated pattern and actual) shown below in gray. A preferred orientation in the sample caused an exaggeration in the intensity of some peaks. Attempts to compensate for this preferred orientation were unsuccessful; nonetheless, the pattern conclusively proves the presence of phenakite in the main mineralized zone.

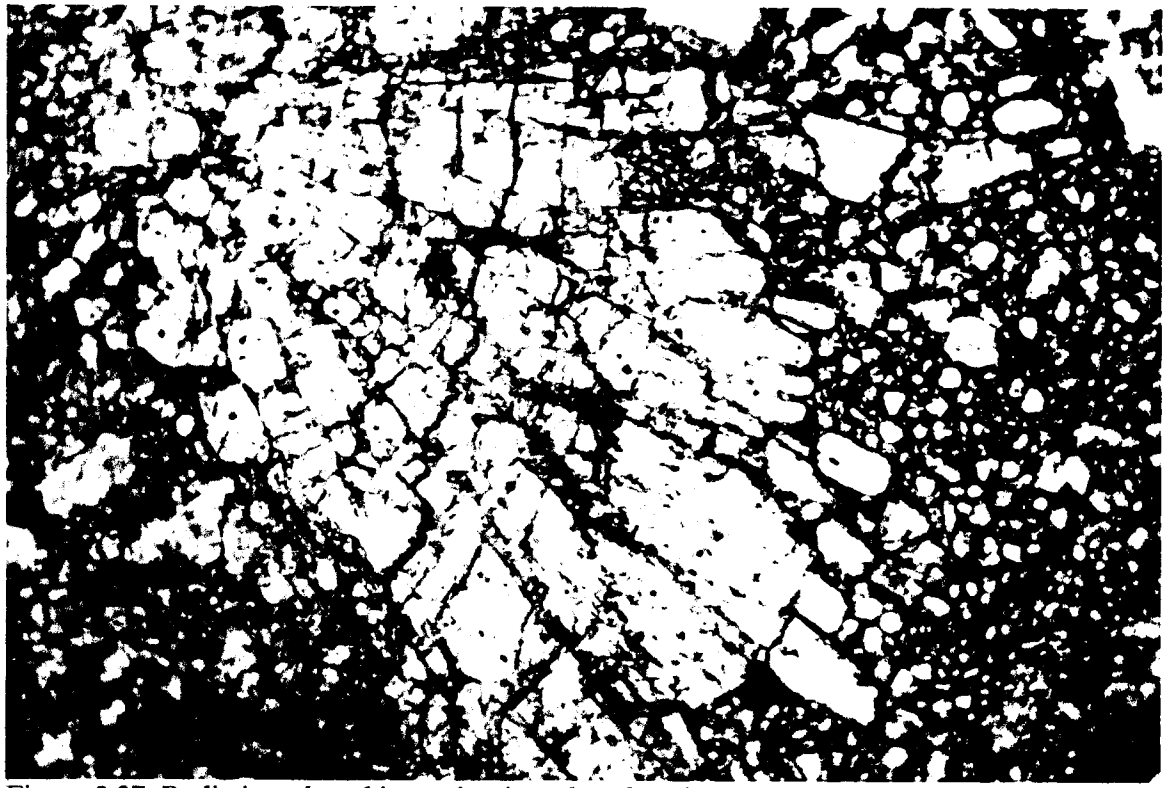

Figure 2.37: Radiating phenakite grain viewed under plane-polarized light. The field of view (F.O.V.) is 4.5 mm

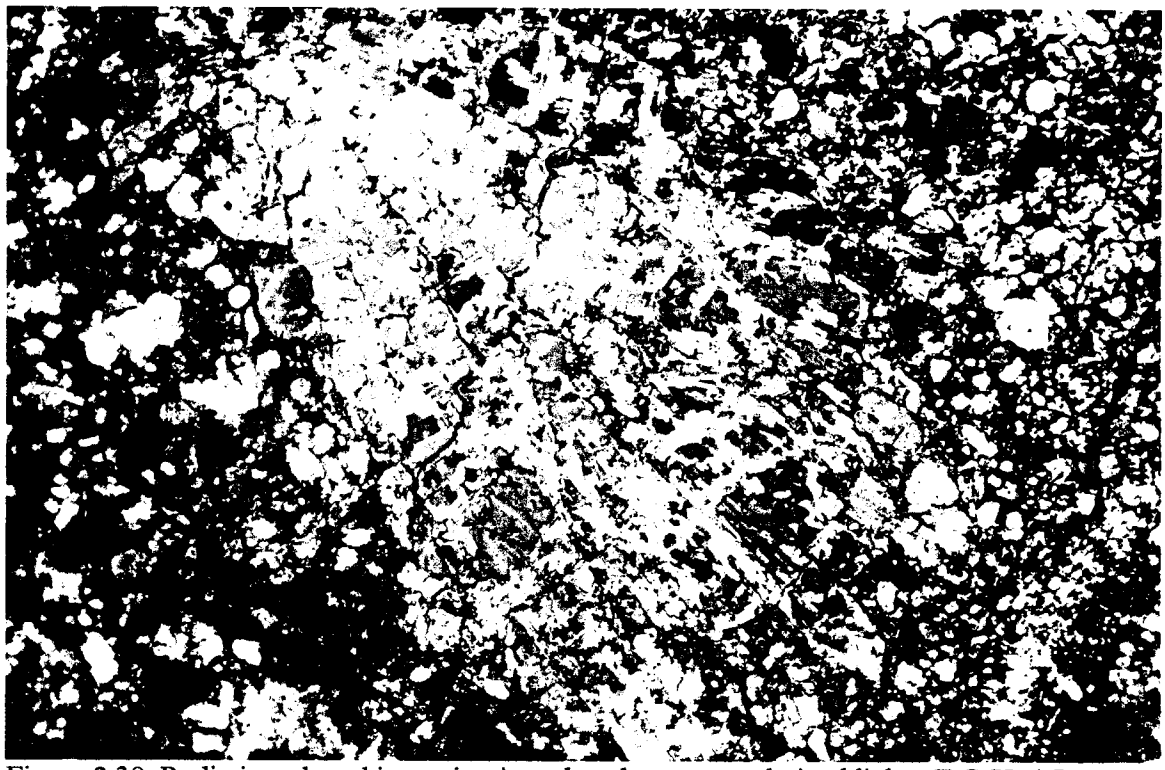

Figure 2.38: Radiating phenakite grain viewed under cross-polarized light. F.O.V. 4.5 mm

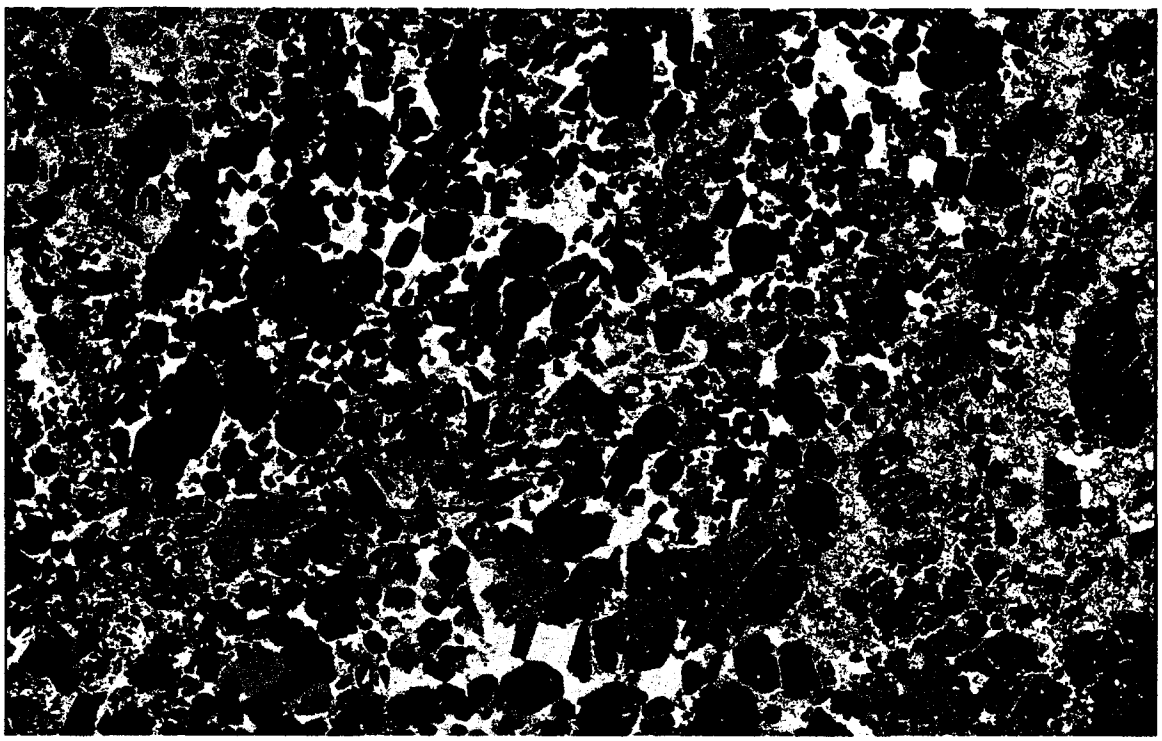

Figure 2.39: False-colored BSE image of phenakite (black) set in quartz (dark blue), calcite (light blue) with accessory apatite (yellow-green), thorite (white) and the HCaZr (pink).

The majority of phenakite occurrences throughout the world have been described from granite pegmatites (Grew, 2002). In these, phenakite occurs in three different mineral associations. The most common type is in miarolitic cavities, as a relatively late-phase. The other types include: formation by alteration of beryl, and in association with greenish-beryl to emerald and chrysoberyl in phlogopite-rich endocontacts of desilicated pegmatites (Černý, 2002). Other environments from which phenakite has been described include: nepheline-syenite pegmatite, trachyte, alpine fissures, greisens, hydrothermal fluorite mineralization, metasomatic rocks and in hematite skarns (Grew, 2002).

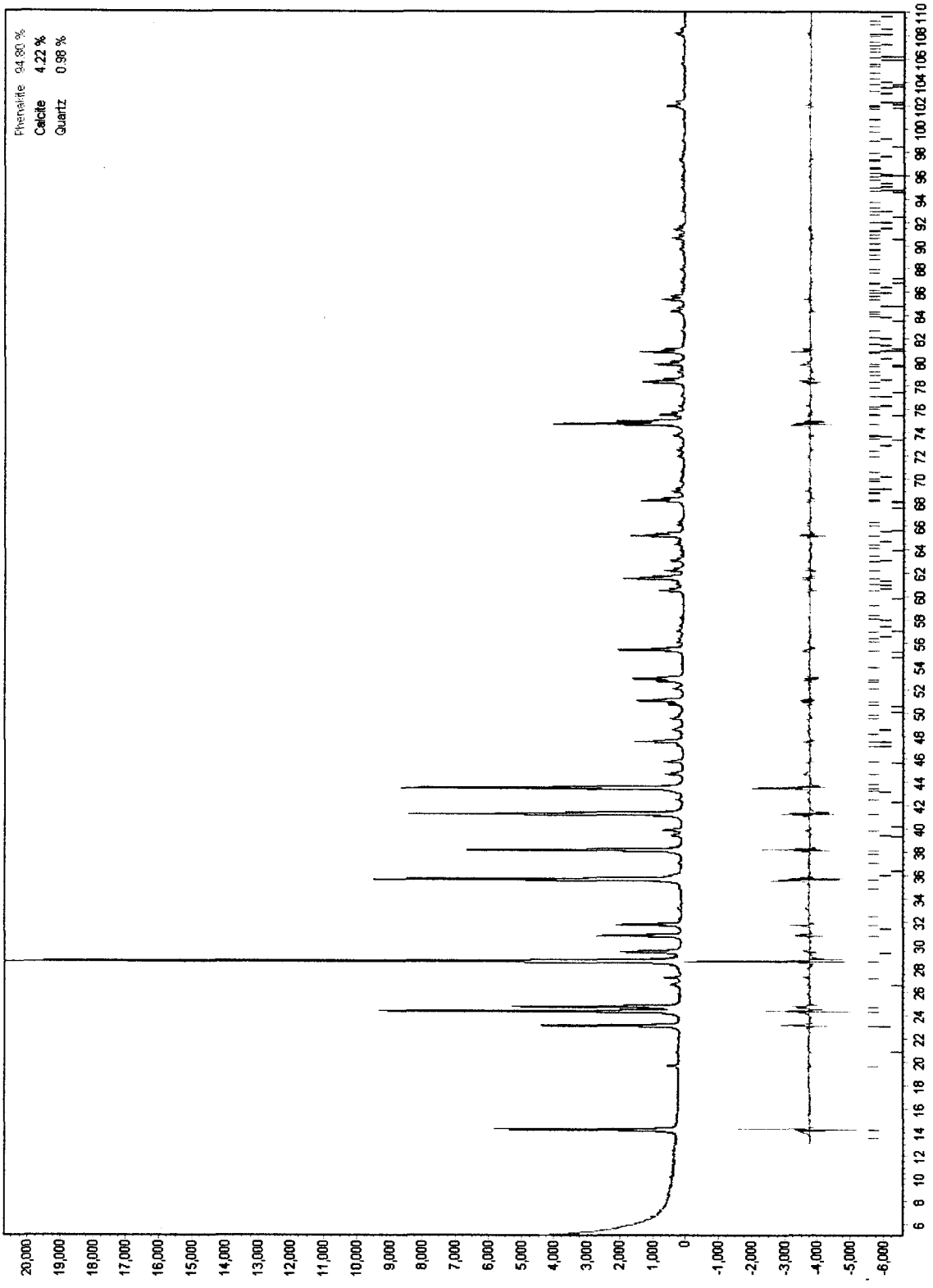

Figure 2.40: Powder X-ray diffraction pattern of Deadhorse Creek phenakite displayed in a total counts vs. 2θ diagram. The difference between the database file and actual pattern is shown below the scan in gray.

During late hydrothermal conditions, phenakite must form under relatively silica- and aluminum-poor conditions (relative to beryllium). Otherwise, the crystallization of beryl [$Be_3Al_2Si_6O_{18}$] would probably occur (Beus, 1966). These considerations are reinforced by log activity versus temperature plots taken from Barton (1986) (Figures 2.41 and 2.42). The plots were calculated from the thermodynamic model using the relation $\Delta G°_{T.P.} = -RT \ln a_i$, where a_i is the activity of the desired phase. In Figure 3.41, the log activity Al_2O_3 – temperature plot illustrates the low activity of Al_2O_3 required for the formation of a phenakite plus quartz assemblage. Also illustrated in this diagram are the lower temperature limit of phenakite (245°C) and the muscovite - potassium feldspar buffer. Under conditions of low Al_2O_3 activity, phenakite and quartz are the dominant phases above 245°C. Below, this point, bertrandite replaces phenakite in the assemblage. Illustrated in Figure 3.42 is the limited range of activity of H_4SiO_4 required in the formation of phenakite. If the activity is too low, bromellite preferentially crystallizes, while if too high, chrysoberyl begins to form, leading to the reaction: phenakite + chrysoberyl = beryl. In summary, Figure 3.43 illustrates the phase relations for the system at 600 °C. These are important constraints with respect to Deadhorse Creek complex due to the abundance of silicates and aluminum-bearing minerals. See the discussion in Chapter 4 for further details.

Table 2.10: Abbreviations used in diagrams.

Name	Abbreviation	Formula	Name	Abbreviation	Formula
Andalusite	And	Al_2SiO_5	Euclase	Eu	$BeAlSiO_4(OH)$
Bertrandite	Bt	$Be_4Si_2O_7(OH)_2$	Kaolinite	Ka	$Al_2Si_2O_5(OH)_4$
Beryl	Be	$Be_3Al_2Si_6O_{18}*nH_2O$	K-feldspar	Kspr	$KalSi_3O_8$
Bromellite	Br	BeO	Muscovite	Mu	$KAl_2(AlSi_3O_{10})(OH)_2$
Chrysoberyl	Ch	$BeAl_2O_4$	Phenakite	Ph	Be_2SiO_4
Corundum	Co	Al_2O_3	Pyrophyllite	Py	$Al_2Si_4O_{10}(OH)_2$
Diaspore	Di	AlO(OH)	Quartz	Qtz	SiO_2

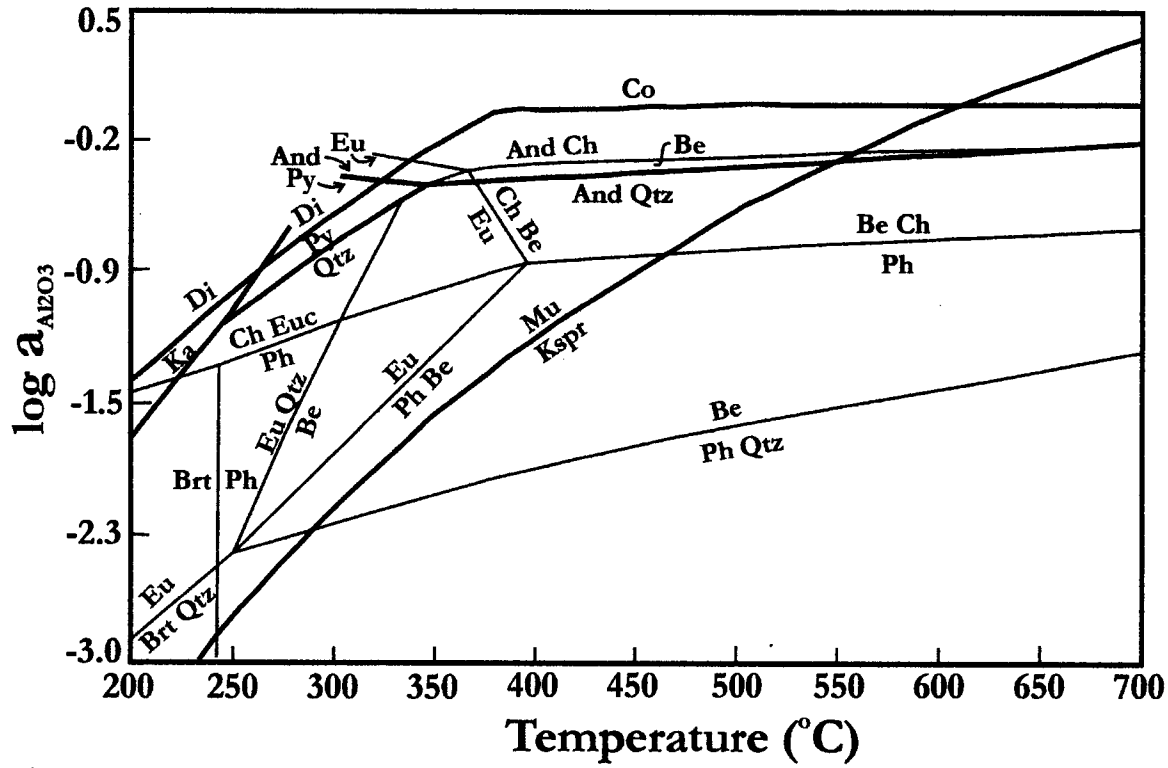

Figure 2.41: Log a_{Al2O3}-temperature projection for BASH system phase relations at 1 kbar. From Barton (1986). See Table 2.10 for abbreviations.

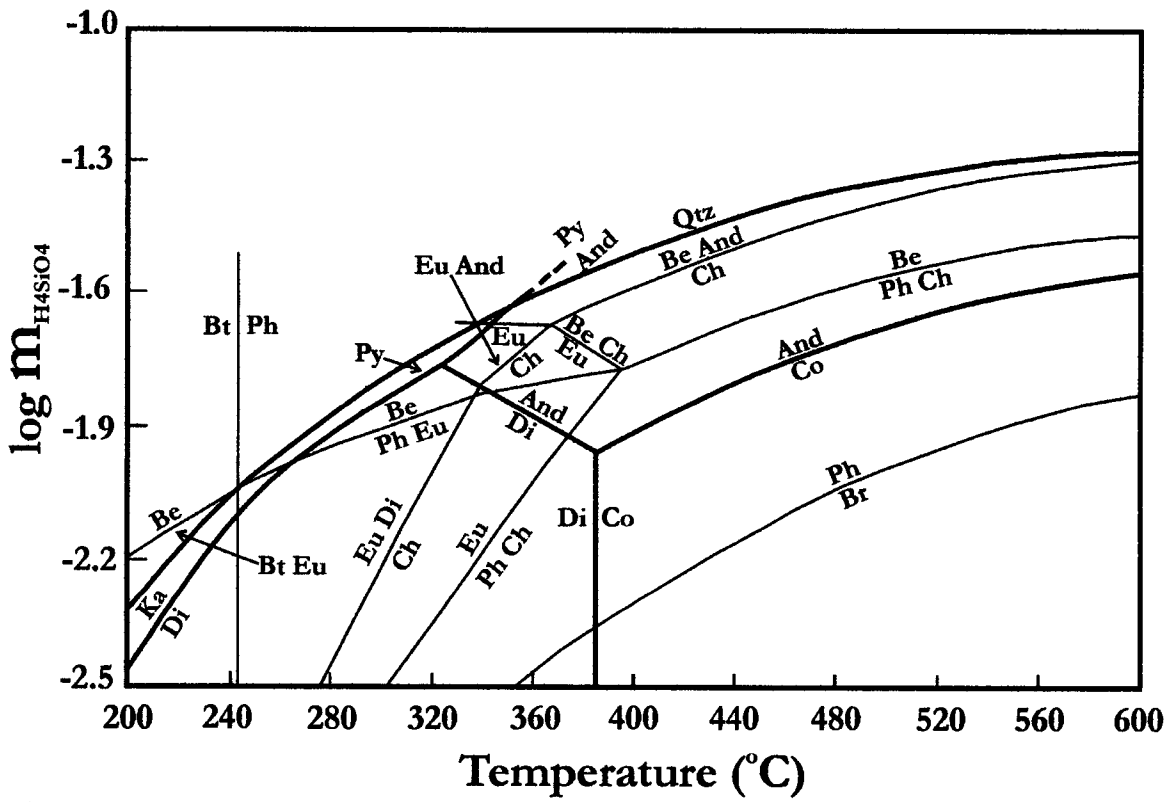

Figure 2.42: Log m_{H4SiO4} –temperature plot of BASH phase relations at 1 kbar. From Barton (1986). See Table 2.10 for abbreviations.

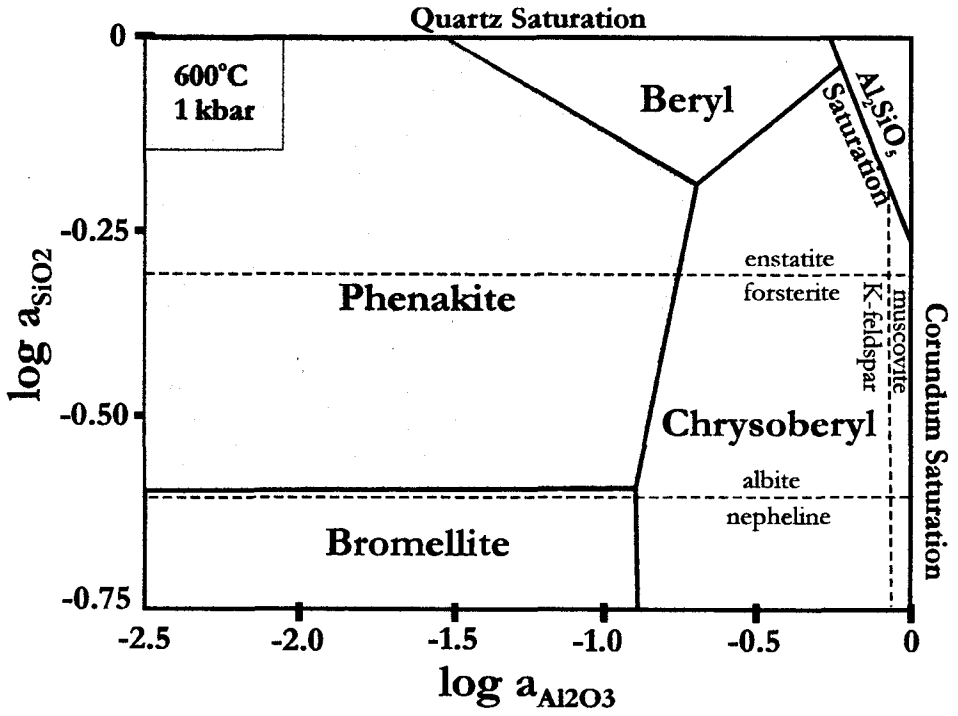

Figure 2.43: Phase relations at 600°C and 1 kbar in hydrothermal systems as a function of the activity of Al_2O_3 versus SiO_2. After Barton and Young (2002).

2.12 Pyroxene

Aegirine [$NaFeSi_2O_6$], is present in the main mineralized zone in two separate varieties: vanadium-bearing and scandium-enriched. These varieties are occur in two distinct habits: up to 150 μm in length, euhedral-to-subhedral laths set preferentially in quartz-(I); and smaller anhedral-to-subhedral fragments associated preferentially with biotite and quartz-(II). The vanadium-bearing compositions are found in both habits, whereas the scandium-bearing aegirine only occur as smaller euhedral-to-subhedral laths set preferentially in quartz, or to a lesser extent calcite.

In terms of composition, the aegirine at Deadhorse Creek consists of two separate populations, although there appears to be a limited solid solution between them. The populations were separated on the basis of scandium content, where aegirines containing greater than 2.5 wt.% Sc_2O_3 are termed Sc-enriched. The vanadium-bearing aegirine contains some of the highest recorded contents of V_2O_3 (as great as 13.5 wt.%) to date. Other substituting cations include (in decreasing abundance): Cr_2O_3, MgO, TiO_2, Al_2O_3, Sc_2O_3 and CaO (Table 2.11 for complete data and Figures 2.44 and 2.45 for images). The scandium-bearing aegirine also contains some of the highest reported contents of Sc_2O_3, with values reaching as much as 16.5 wt.%. These aegirine grains also contain appreciable amounts of vanadium (4.5 to 10.2 wt.%) with lesser amounts of: MgO, Cr_2O_3, Al_2O_3, TiO_2, and CaO. See Figures 2.46 and 2.47 for images. As illustrated in Figure 2.48, these minerals are more appropriately termed aegirine-natalyite for the V-rich members and aegirine-jervisite for the Sc-rich members. A listing of the molecular percentages of relevant end-members is attached to Table 2.11. The other reported occurrences of V- and Sc-bearing aegirines have been described from alkaline metasomatites associated with banded-iron ore deposits in Ukraine (Valter *et al.*, 1994; Pavlishin *et al.*, 2000; Valeyev 1996). In these occurrences, the aegirines were reported to contain 3 to 8 wt.% V_2O_5 and as much as 3 wt.% Sc_2O_3. Jervisite ($NaScSi_2O_6$) was reported from within a geode in granite by Mellini *et al.* (1982), but the sample contains calcium, magnesium and iron in enough concentrations that the authors propose that it is actually an intermediate in the $Ca(Mg,Fe)Si_2O_6$ – $NaScSi_2O_6$ series. Although the Deadhorse Creek aegirine-jervisite is closer to the jervisite end-member, the substitution of

vanadium, chromium and iron in place of scandium indicates that the grains are an intermediate between aegirine, jervisite and natalyite. Thus, discovery of an ideal end-member in nature remains elusive. As stated by Mellini *et al.* (1982), the rarity of scandium minerals is a result of its crystal chemical behaviour. This was first noted by Goldschmidt and Peter (1931) whom emphasized that the bulk of the element is partitioned in very small amounts in minerals formed in the early stages of magmatic differentiation; mainly pyroxenes, amphiboles and biotite. Only a miniscule amount passes through the magmatic stage and enters pegmatitic, pneumatolitic or hydrothermal deposits. Relatively pure natalyite ($NaVSi_2O_6$), has been described from the Sludyanka complex in Russia by Reznitskii *et al.* (1985), but the majority of these samples also contain appreciable amounts of Cr, Ca and Mg and are best expressed in terms of a natalyite-kosmochlore-diopside diagram. In order to balance charges, the $(V^{3+},Cr^{3+}) \leftrightarrow Mg^{2+}$ substitution at the M1-site is counterbalanced by $Na^{+} \leftrightarrow Ca^{2+}$ substitution at the M2-site (Secco *et al.* 2002).

Not surprisingly, the transitional metals in the Deadhorse Creek aegirine appear to substitute into the M1-site (iron) of aegirine. What is noteworthy is the apparent contrast in the substitution of transition metals between the Sc-enriched and V-bearing aegirine populations. For the vanadium-aegirine grains, with the exception of TiO_2, the transition metals exhibit negative correlations when plotted against iron concentrations. However, apart from the plot of Sc_2O_3 versus FeO_{Total}, the scandium-dominated grains do not exhibit any well-defined correlations. The sole exception, Sc_2O_3 versus FeO_{Total}, shows a slight negative correlation, which trends away from the vanadium-dominated population. These trends are illustrated in Figures 2.49: a-e.

Table 2.11: Representative compositions of Deadhorse Creek aegirines.

	1	2	3	4	5	6	7	8
Na_2O	12.9	13.2	13.7	13.6	12.9	12.8	12.3	12.8
MgO	1.5	1.1	1.3	0.8	0.5	1.3	0.9	0.9
Al_2O_3	0.4	-	0.2	-	0.3	0.6	0.8	0.6
SiO_2	53.0	52.9	53.9	53.7	52.5	52.9	50.5	52.3
CaO	0.4	0.3	0.3	0.1	0.4	0.3	0.6	0.5
Sc_2O_3	14.7	15.5	14.6	14.7	0.6	0.6	0.5	0.6
TiO_2	1.8	3.0	3.5	2.2	1.3	2.0	4.2	1.4
V_2O_3	6.3	5.4	4.8	6.3	16.5	7.9	8.3	6.6
Cr_2O_3	1.2	1.5	1.3	1.6	3.9	3.1	2.8	2.8
FeO	2.5	2.6	1.4	2.0	2.9	3.6	4.9	2.5
Fe_2O_3	4.8	3.6	5.2	5.9	7.1	13.5	13.2	18.8
ZrO_2	0.5	-	0.1	0.4	0.5	0.8	0.6	0.4
Totals	100.0	99.1	100.3	101.3	99.4	99.4	99.6	100.2
			Cation Proportions					
Na^{+}	0.9	1.0	1.0	1.0	1.0	0.9	0.9	0.9
Mg^{2+}	0.1	0.1	0.1	-	-	0.1	0.1	0.1
Al^{3+}	-	-	-	-	-	-	-	-
Si^{4+}	2.0	2.0	2.0	2.0	2.0	2.0	1.9	2.0
Ca^{2+}	-	-	-	-	-	-	-	-
Sc^{3+}	0.5	0.5	0.5	0.5	-	-	-	-
Ti^{4+}	0.1	0.1	0.1	0.1	-	0.1	0.1	-
V^{3+}	0.2	0.2	0.1	0.2	0.5	0.2	0.3	0.2
Cr^{3+}	-	-	-	-	0.1	0.1	0.1	0.1
Fe^{2+}	0.1	0.1	-	0.1	0.1	0.1	0.2	0.1
Fe^{3+}	0.1	0.1	0.1	0.2	0.2	0.4	0.4	0.5
Zr^{4+}	-	-	-	-	-	-	-	-
Totals	4.0	4.1	3.9	4.1	3.9	3.9	4.0	3.9

Note: Cation proportions calculated based on 6 oxygens. [-]= not detected. Analysis #1-4: Sc-enriched; 5-8: V-enriched.

Table 2.11: continued

Mol.% End-members

	1	2	3	4	5	6	7	8
$CaMgSi_2O_6$	1.5	1.1	1.2	0.4	1.6	1.4	2.7	2
$Mg_2Si_2O_6$	-	-	-	-	0.7	3.4	1.4	1.7
$Fe_2Si_2O_6$	4.1	4.3	2.4	3.1	4.8	6.4	8.1	4.2
$NaScSi_2O_6$	50.8	53.4	50.7	49.1	2.2	2.2	1.5	2
$NaCrSi_2O_6$	3.8	4.6	4.1	4.7	12.4	10.4	8.6	8.8
$NaTiSi_2O_6$	5.4	8.9	10.5	6.4	3.9	6.4	12.3	4.1
$NaVSi_2O_6$	20.2	17.1	15.4	19.3	53.0	26.7	26.2	21.1
$NaFeSi_2O_6$	14.2	10.6	15.8	17.1	21.4	43.0	39.2	56.2
Totals	100	100	100	100	100	100	100	100

Figure 2.44: BSE-image of aegirine-natalyite grains and the hydrated calcium zirconosilicate set in quartz.

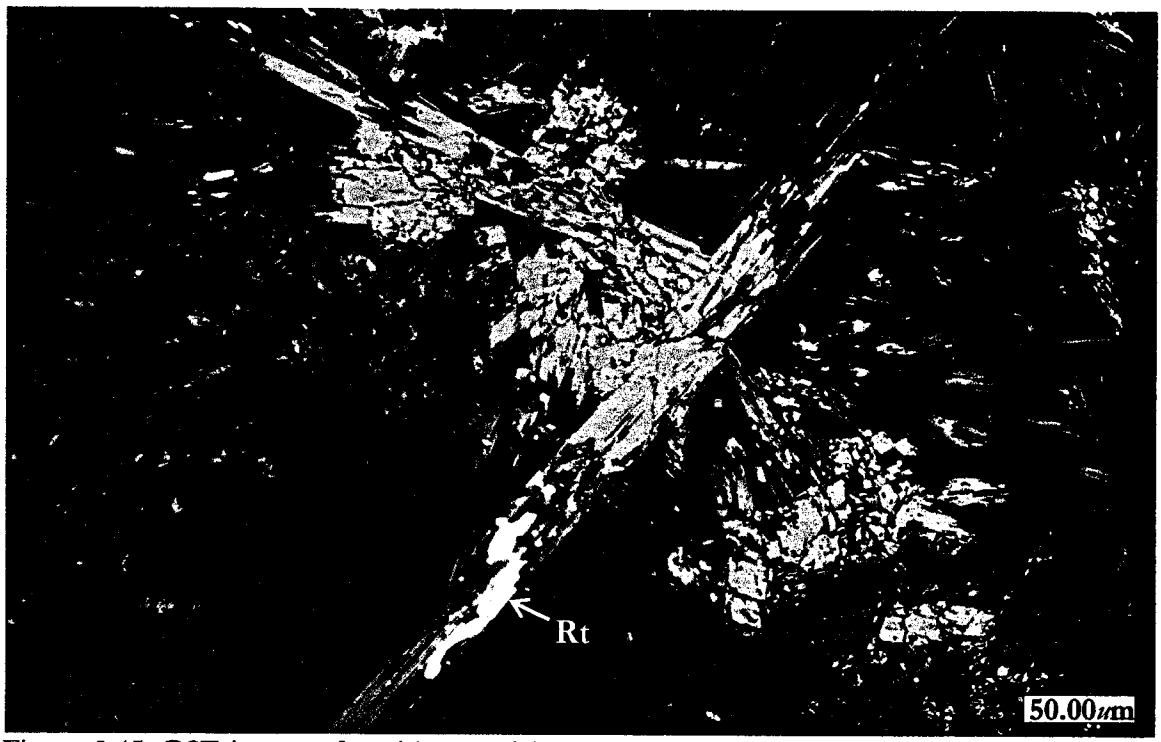

Figure 2.45: BSE-image of aegirine-natalyite grains set in quartz, with accessory subhedral rutile (Rt).

Figure 2.46: False-colored BSE-image of aegirine-jervisite grains set in quartz.

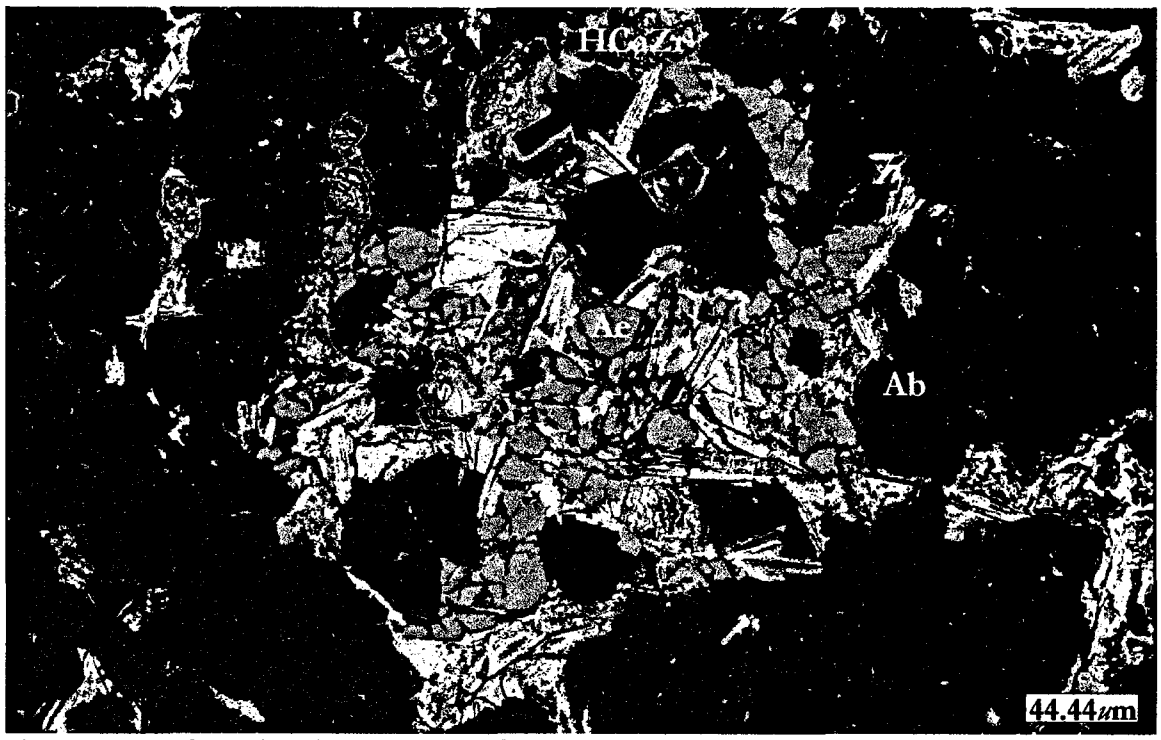

Figure 2.47: False-colored BSE-image of aegirine-jervisite grains (green) set in albite (Ab) and associated with biotite (Bio). Also shown are anhedral grains of the hydrated calcium zirconosilicate (HCaZr).

Aegirine is also present in the unmineralized diatreme breccia, although it lacks enrichment in vanadium or scandium. However, due to the presence of aluminum, magnesium and calcium, the diatreme breccia aegirine is better termed aegirine-augite. It occurs in a variety of habits, ranging from large euhedral laths to anhedral grains. Aegirine-augite and potassium feldspar form a cementing matrix, holding together the comminuted rock debris that forms the breccia.

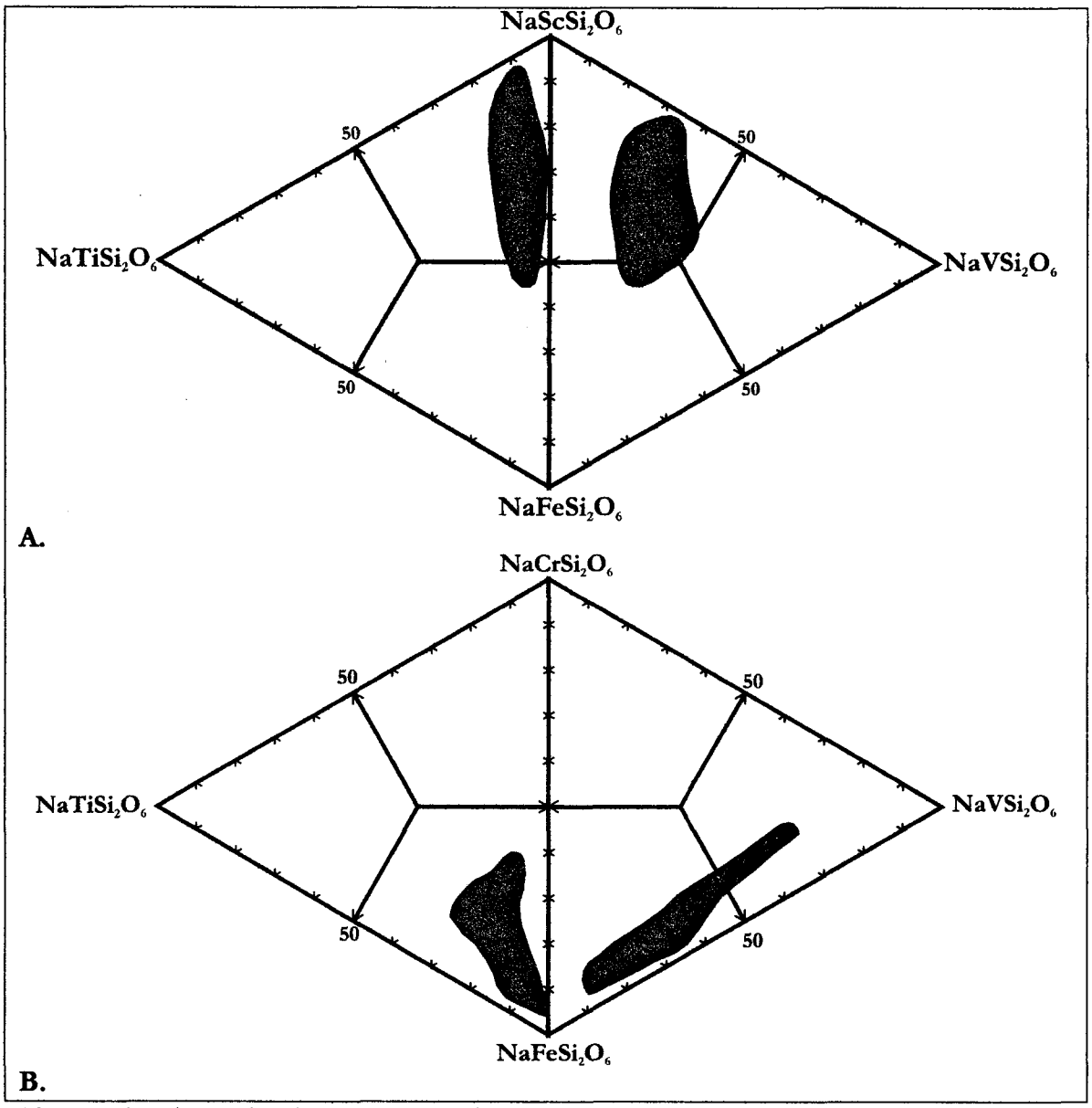

Figure 2.48: A: Molecular percentage plot of the Sc-rich members in terms of a (clockwise from top): jervisite, natalyite, aegirine and $NaTiSi_2O_6$ graph. B: Plot of V-rich members in terms of a (clockwise from top): kosmochlore, natalyite, aegirine and $NaTiSi_2O_6$ graph.

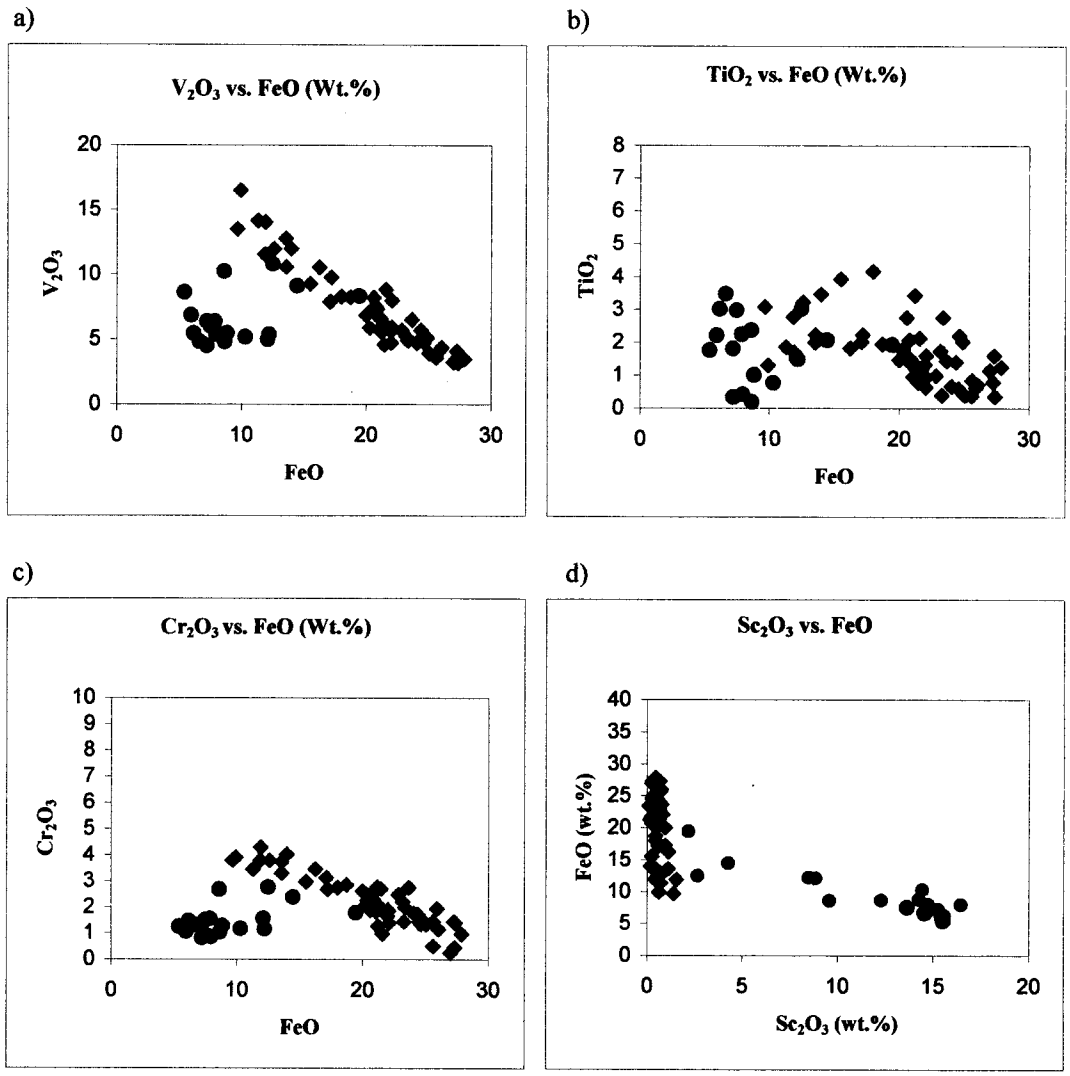

Figures 2.49a-d: Weight percent graphs of first-order transition metals against total iron from the Deadhorse Creek pyroxenes. Blue circles represent the Sc-pyroxenes and red/black diamonds represent the V-pyroxenes.

2.13 Rutile

Within the main mineralized zone, rutile is present in two varieties: stoichiometric rutile and niobium-vanadium-rich rutile. Texturally, these phases occur primarily in three habits: extensively-corroded subhedral laths; relatively-unaltered subhedral-to-anhedral grains; and 'nodules' of intergrown rutile and ilmenite. The 'pure' rutile occurs as extensively-corroded laths, set preferentially in a calcite groundmass or within calcite veins. The rutile laths range from 10 to 100 μm in length. The alteration of 'pure' rutile creates an interlocking mosaic of rutile and titanite. To a lesser degree, such rutiles are also found within quartz 'clots' enclosed in a calcite groundmass, which is possibly associated with the extensive quartz veining. The second type of rutile includes niobium-vanadium-rich compositions. These subhedral-to-anhedral grains are directly associated with the 'purer', corroded rutile described above, yet have not experienced the same degree of alteration to titanite. These small (<10 μm) grains range from anhedral, rounded blebs to subhedral angular grains. Textural evidence suggests that these rutiles formed secondarily to the corroded laths, which may have acted as sources of titanium. The third textural form of rutile, observed only in two samples, consists of a "nodule" or fragment of intergrown rutile and ilmenite forming a coarse trellis interspersed with minor titanite. The rutile is essentially stoichiometric TiO_2, whereas the ilmenite contains minor amounts of MnO (3-4 wt.%) replacing Fe.

In terms of composition, the Deadhorse Creek Nb-V-rutile is also enriched in chromium (Table 2.12). As previously noted by Platt and Mitchell (1996), the enrichment in Nb and Cr (with contents as great as 29.3 and 9.3 wt.% respectively) is similar to that of rutiles reported from alkaline igneous rocks and plots within this field as defined by Haggerty (1991) (Figure 2.50).

Compositions similar to those of the niobium-vanadium-rich rutiles have been reported from xenoliths in kimberlites. Tollo and Haggerty (1987) reported rutiles from Orapa containing a maximum of 20.9 wt.% Nb_2O_5 and 8.2 wt.% Cr_2O_3, with minor amounts of FeO, Ta_2O_5 and ZrO_2. However, the enrichment of vanadium in the Deadhorse Creek rutile is unique and reaches a maximum of 10.52 wt.% V_2O_3. Regardless of the extent of vanadium

enrichment, the niobium-vanadium rutiles plot within the region defined for rutile in alkaline igneous suites, as defined by Haggerty (1991) (Figure 2.50). Apart from the presence of vanadium and lack of tantalum, the Nb-V-rich rutiles are also very similar to the composition of ilmenorutiles $(Ti,Nb,Fe^{3+})O_2$ reported principally from pegmatites. Yet, the Deadhorse Creek rutiles plot outside the field containing pegmatitic rutile, as defined by Tollo and Haggerty (1987) (Figure 2.51). See Figures 2.52 and 2.53, for comparison of energy-dispersion X-ray spectra (EDS) of Nb-V-rutile and ilmenorutile. Furthermore, some of these mineral assemblages associated with ilmenorutile are similar to those observed in the mineralized zone of Deadhorse Creek. Černý *et al.* (1999) describe ilmenorutile from the McGuire pegmatite, associated with potassium feldspar, quartz, biotite, ilmenite and monazite-(Ce); all minerals that are present in the mineralized zone of the Deadhorse Creek diatreme. Historically, ilmenorutile has been considered as a rare mineral found only in a few categories of rare-element pegmatites. However, as Černý *et al.* (1999) note, recent research has shown that ilmenorutile has been "recognized as a significant accessory minerals in peraluminous-to-peralkaline granitic rocks and as substantial components of hydrothermal assemblages associated with alkaline intrusions." Although many of the aspects of ilmenorutile genesis and stabilities remain unknown, some are becoming more apparent. For instance, rutile that contains significant amounts of Nb is unstable at low temperatures. Thus, niobian rutile in which Fe^{2+} dominants over Fe^{3+} will exsolve titanian columbite or ixiolite, resulting in the depletion of Nb, Ta, Fe and Mn in the rutile (Černý *et al.*, 1964, 1981, 1986, 1999; Sahama, 1978). As a consequence of the predominance of ferric iron, substitution of vanadium, and the lack of detectable levels of tantalum, titanian columbite or ixiolite were not found at Deadhorse Creek.

Table 2.12: Representative compositions and cation proportions of the Nb-V rich rutiles

	1	2	3	4	5	6	7	8
Al_2O_3	0.2	0.1	0.1	0.1	0.2	0.2	0.2	0.4
SiO_2	0.8	0.3	0.5	1.1	0.7	1.0	1.0	2.0
CaO	1.0	0.7	0.8	1.1	0.8	1.2	4.5	4.1
TiO_2	64.5	63.4	62.4	57.3	60.0	58.8	53.5	58.3
V_2O_5	8.5	8.4	8.5	10.4	10.0	9.1	10.5	9.3
Cr_2O_3	4.3	4.9	4.9	4.6	4.6	4.6	4.4	4.0
MnO	0.3	-	0.1	-	0.2	0.1	0.1	-
FeO_T	0.1	0.2	0.3	0.5	0.2	0.2	0.7	0.4
SrO	0.2	0.2	0.2	0.2	0.1	0.4	0.3	0.2
Nb_2O_5	21.1	22.4	22.2	24.4	23.8	23.9	25.8	21.2
Totals	101.0	100.6	100.0	99.7	100.6	99.5	101.0	99.9
				Cation Proportions				
Al^{3+}	-	-	-	-	-	-	-	0.01
Si^{4+}	0.01	-	0.01	0.02	0.01	0.02	0.01	0.03
Ca^{2+}	0.02	0.01	0.01	0.02	0.01	0.02	0.07	0.06
Ti^{4+}	0.70	0.69	0.68	0.63	0.66	0.65	0.58	0.63
V^{3+}	0.10	0.10	0.10	0.12	0.12	0.11	**0.11**	**0.10**
Cr^{3+}	0.05	0.06	0.06	0.05	0.05	0.05	0.05	0.05
Mn^{2+}	-	-	-	-	-	-	-	-
Fe^{3+}	-	-	-	0.01	-	-	0.01	-
Sr^{2+}	-	-	-	-	-	-	-	-
Nb^{5+}	0.14	0.15	0.15	0.16	0.16	0.16	0.17	0.14
Totals	1.02	1.01	1.01	1.01	1.01	1.01	1.00	1.02

* Total Fe recalculated as Fe_2O_3. Cation proportions include an extra significant digit to illustrate the differences in vanadium valency. V_2O_3 cation proportions written in **bold are recalculated as VO_2**. Structural formulae calculated based on 2 oxygen. [-] = not detected.

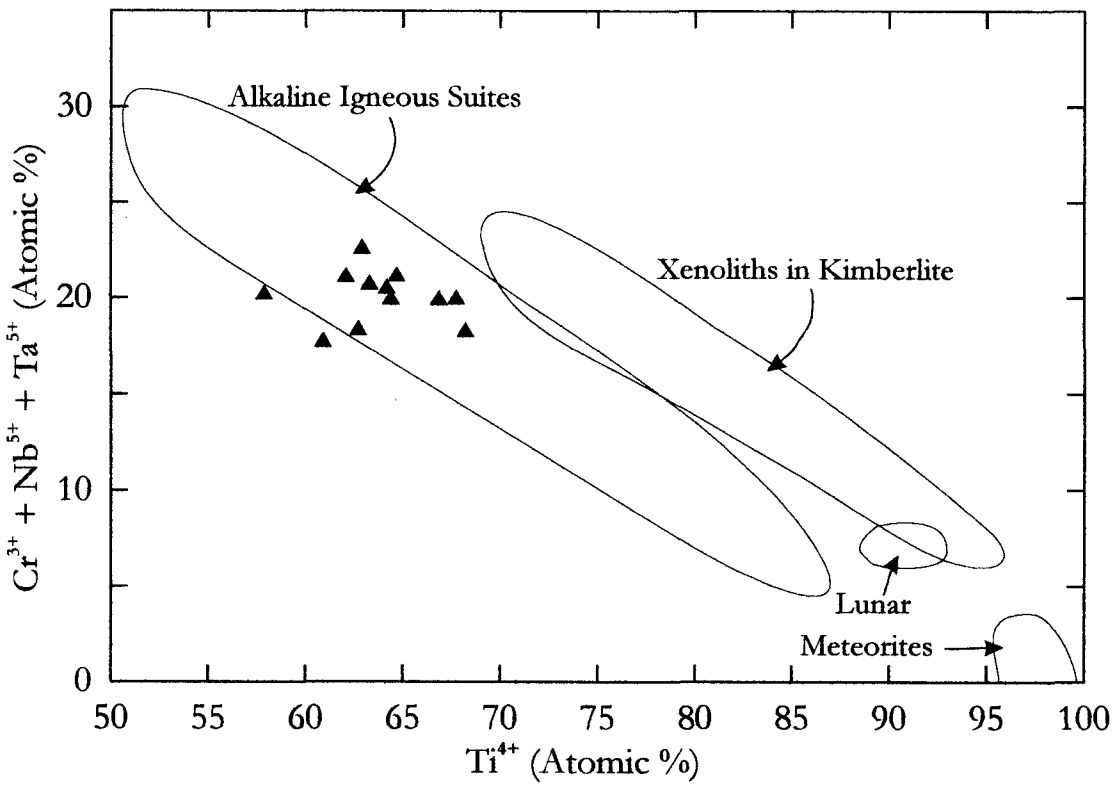

Figure 2.50: Plot of Nb^{5+} + Cr^{3+} +Ta^{5+} against TiO_2 for rutiles of various origins Note: Triangles = Nb-V rich rutiles; Circles = V-Fe rich rutiles. After Haggerty (1991).

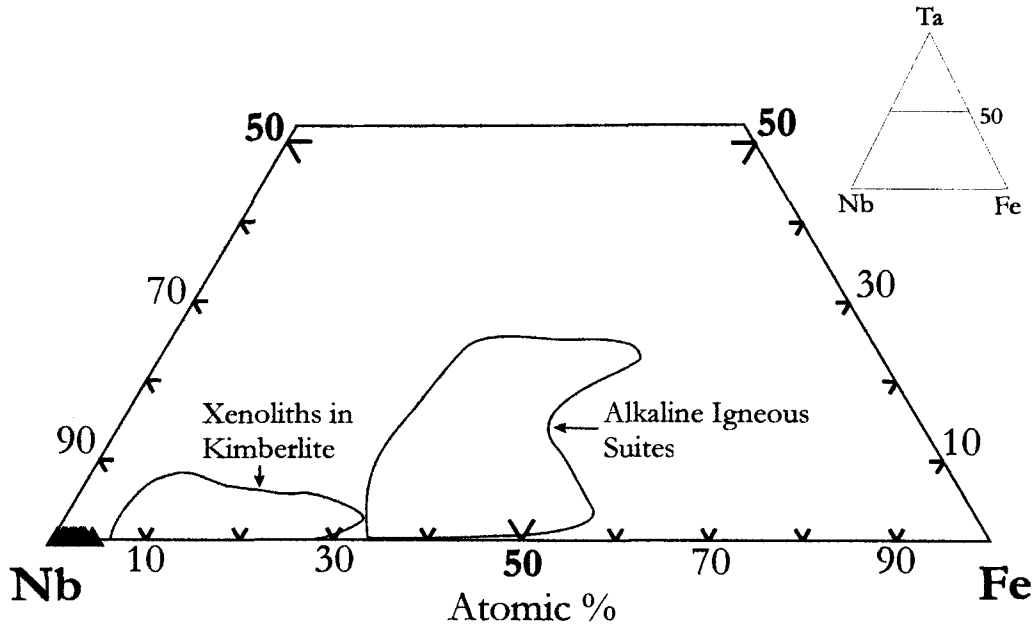

Figure 2.51: Atomic percent plot of Ta-Nb-Fe, after Tollo and Haggerty (1987). Deadhorse Creek rutile illustrated as black triangles. The area labelled alkaline igneous suites consists of two overlapping populations: rutile from granitic pegmatites and related rocks (higher Ta/Nb values); and rutile from carbonatites and associated intrusive bodies (lower Ta/Nb values).

When plotted against TiO_2, the V_2O_3, Nb_2O_5 and FeO contents of the enriched rutiles exhibit inverse correlations. Although there is a significant amount of scatter in the data, variations of Cr_2O_3 with respect to TiO_2 and FeO versus V_2O_3, illustrated slight positive correlations. Plotting Nb_2O_5 concentrations against FeO_{Total}, also illustrates a positive correlation (Figures 2.52a-e).

As indicated by the bold font in Table 2.12, some of the Nb-V rich rutiles contain VO_2 in the structural formulae calculations. As noted by Platt and Mitchell (1996): "the fundamental unknown of these unusual rutiles is the valency of the transition metals." Whereas Cr and Nb are traditionally thought to exist in both tri- and pentavalent states, the valency of vanadium remains somewhat ill-defined. Yet, as noted by Waychunas (1991), vanadium is commonly considered as a pentavalent cation in the charge-coupled substitution $M^{3+} + M^{5+} = 2Ti^{4+}$. However, based on charge and compositional difficulties arising from the incorporation of V^{5+} in the rutile lattice, it is suggested that the vanadium contained in the Nb-V-rich rutiles exists in the tri- and tetravalent states. This is in agreement with data presented by Platt and Mitchell (1996). Recent studies concerning the valency of vanadium suggest that vanadium exists as tri- tetra-and pentavalent states in melts at terrestrial fO_2, although the abundance of tetra- and pentavalent vanadium is small. However, experiments indicate that the proportion of trivalent vanadium ($V^{3+}/\sum V$) decreases with increasing fO_2 (Canil, 2002).

With the introduction of the significant amounts of Nb^{5+} into the rutile, there is a large positive charge on the structure, assuming that vanadium remains in the pentavalent state. Since the small iron concentrations were determined to consist entirely of Fe^{3+}, using the methods of Droop (1987), the only other multivalent cations present were chromium and vanadium. Chromium however, does not occur in significant enough quantities to balance the large positive charge in the structure. Thus, only vanadium is left to balance the large positive charge. In roughly half the cases, trivalent vanadium fits the structural formula better than tetravalent vanadium; the remainder of the sites being preferentially-filled with tetravalent vanadium, suggesting the possibility of the existence of both valencies within these rutiles. In terms of composition, there is a deficiency of cations in the Nb-V-rich rutiles when the atomic proportions are calculated with only pentavalent vanadium. In roughly half of the samples,

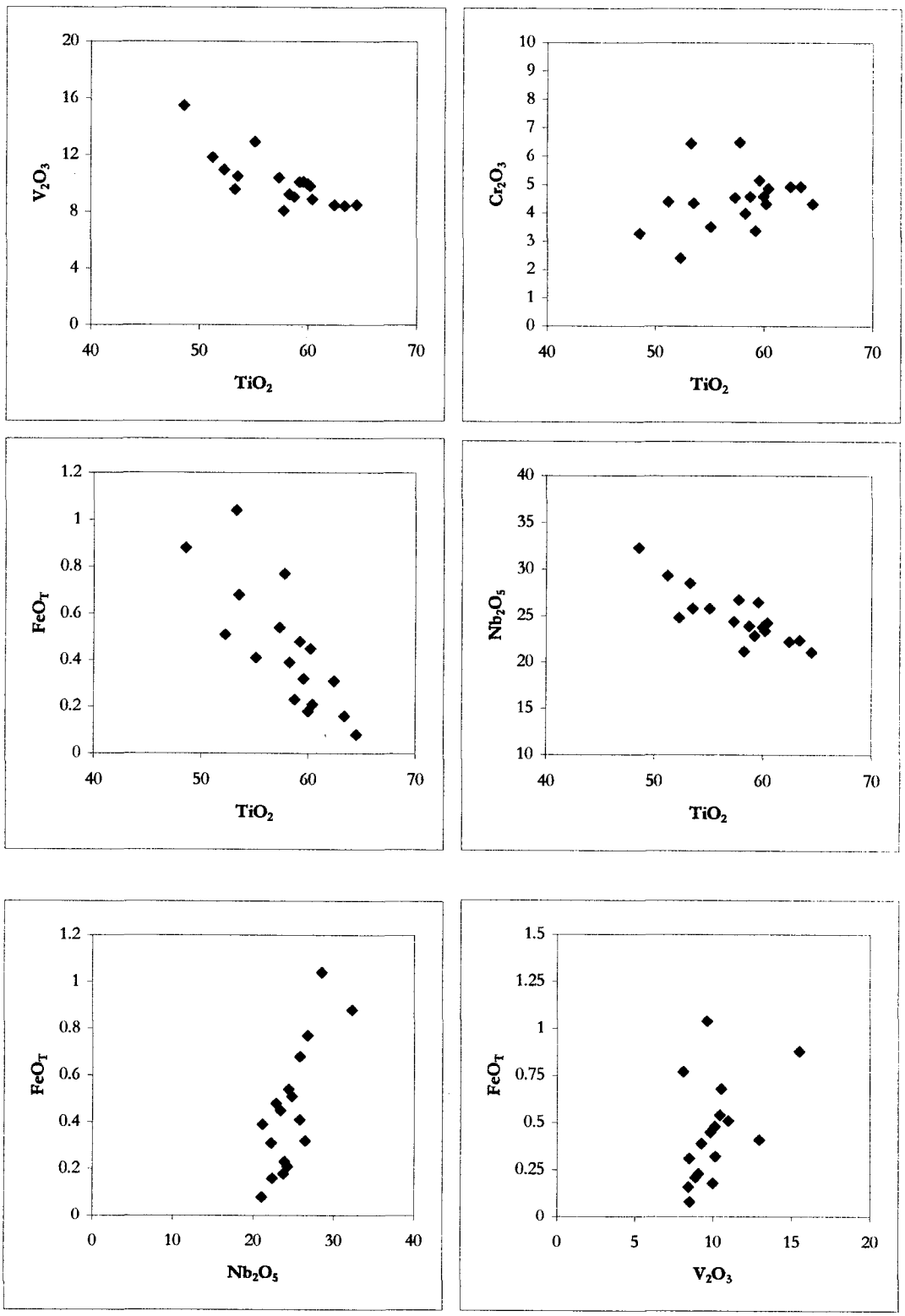

Figures 2.52 a-e: (a-d):Variations in V_2O_3, Cr_2O_3, FeO_T and Nb_2O_5 with respect to TiO_2, (e): Nb_2O_5 versus FeO_{Total}; (f) FeO versus V_2O_3.

this deficiency was most easily balanced by the introduction of tetravalent vanadium into the structure, where the substitution of trivalent vanadium resulted in an excess of cations. With the remaining Nb-V-rich rutiles, the incorporation of trivalent vanadium effectively balanced the charge within the lattice, although partial substitution of tetravalent vanadium would result in completely balancing the cations. This partial substitution of tetravalent vanadium also had little effect on the charge of the structure. Images of enriched rutile from the main mineralized zone are shown in Figures 2.54-2.57.

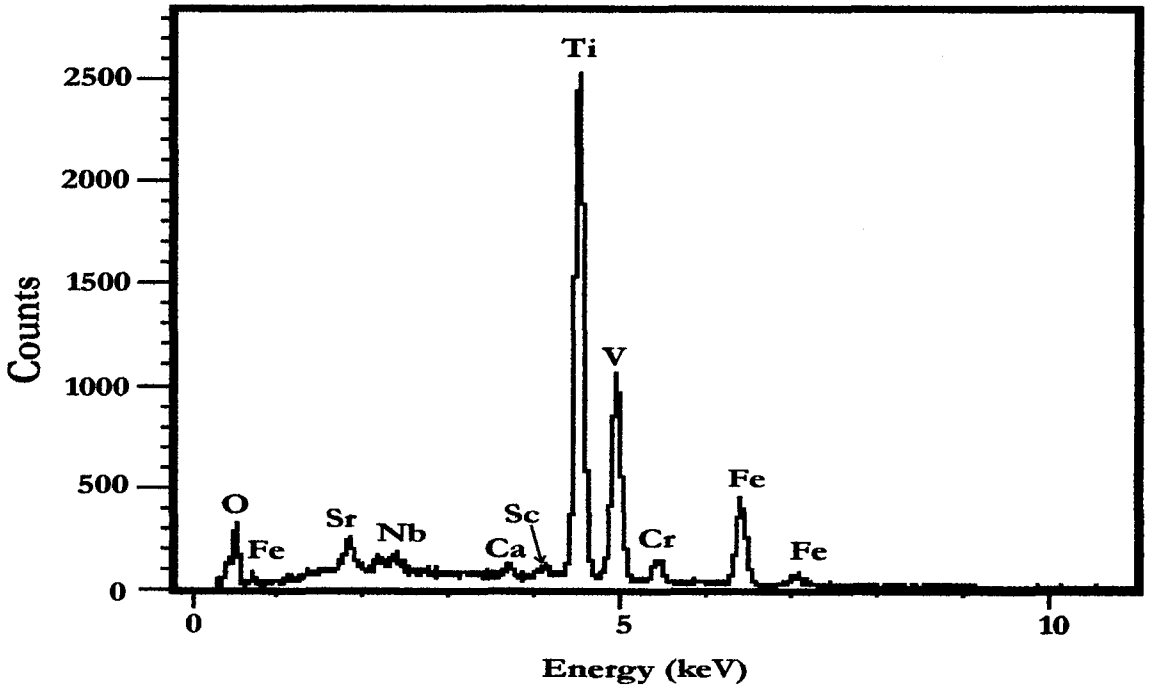

Figure 2.53: EDS spectrum of Nb-V-rutile from the main mineralized zone. Note: Tikβ1 and Vkα1 peaks overlap, giving the appearance of more V_2O_3 than actually present.

Outside the main mineralized zone, rutile is present in trace amounts within the diatreme breccia. Here, rutile occurs either as small anhedral 'clots' of trellis-type pattern exsolved Mn-ilmenite and Nb-Fe-rutile (ilmenorutile) within a stoichiometric rutile host, or anhedral grains associated with titanite and baotite $[Ba_4(Ti,Nb)_8Si_4O_{28}Cl]$. Apart from the exsolved ilmenorutile within the clots, all the remaining rutile grains found within the breccia are essentially pure TiO_2. As the nomenclature suggests, the exsolved ilmenorutile contains between 19.2 and 24.64 wt.% Nb_2O_5 and between 6.15 to 7.53 wt.% total FeO (before Fe^{2+}:Fe^{3+} recalculation). As with rutile from the main mineralized zone, the exsolved

ilmenorutile does contain some V_2O_3, ranging between 1.5 to 2.56 wt.%. As illustrated by the EDS spectrum (Figure 2.54), the ilmenorutile located in the diatreme breccia is unlike pegmatitic ilmenorutile in that is does not contain any tantalum, tungsten or tin. Representative compositions are given in Table 2.13.

Table 2.13: Representative Cr-poor, Nb-rutile compositions from the diatreme breccia

	1	2	3	4	5	6	7	8
SiO_2	0.5	0.9	1.2	0.3	0.6	0.5	0.7	0.8
TiO_2	65.3	67.7	66.5	68.5	71.6	69.5	65.7	67.9
V_2O_3	2.0	1.7	1.8	2.6	1.7	1.8	2.1	1.8
Cr_2O_3	0.2	0.1	0.3	-	0.2	0.3	0.2	0.2
MnO	0.1	0.1	0.3	0.8	-	0.9	0.1	0.2
FeO	3.2	3.3	2.8	0.6	2.2	0.7	3.5	2.6
Fe_2O_3	4.8	3.8	4.5	6.6	4.4	6.3	4.0	4.6
Nb_2O_5	24.0	22.4	22.7	20.7	19.2	20.4	24.3	21.6
Totals	100.1	100.0	100.1	100.1	99.9	100.4	100.6	99.7
				Cation Proportions				
Si^{4+}	0.01	0.01	0.02	-	0.01	0.01	0.01	0.01
Ti^{4+}	0.72	0.74	0.72	0.74	0.77	0.75	0.72	0.74
V^{3+}	0.02	0.02	0.02	0.03	0.02	0.02	0.02	0.02
Cr^{3+}	-	-	-	-	-	-	-	-
Mn^{2+}	-	-	-	0.01	-	0.01	-	-
Fe^{2+}	0.04	0.04	0.03	0.01	0.03	0.01	0.04	0.03
Fe^{3+}	0.05	0.04	0.05	0.07	0.05	0.07	0.04	0.05
Nb^{5+}	0.16	0.15	0.15	0.13	0.12	0.13	0.16	0.14
Totals	1.00	1.00	0.99	0.99	1.00	1.00	0.99	0.99

Note; [-]= not detected. Cations calculated based on 2 oxygens and include an extra significant digit to illustrate the valency differences as compared to the V-rich ilmenorutile.

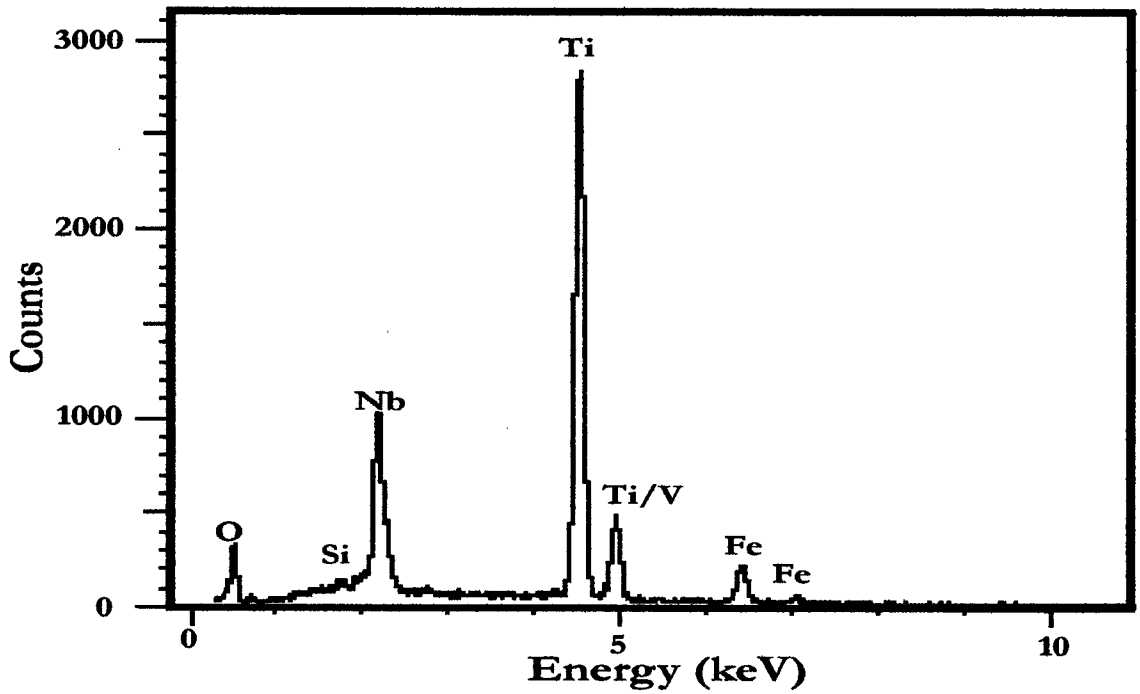

Figure 2.54: EDS spectrum of Cr-poor, Nb-rutile from the unmineralized breccia. Note: TiKβ1 and VKα1 peaks overlap, giving the appearance of more V_2O_3 than actually present.

Figure 2.55: BSE-image of corroded and altered rutile laths set in a calcite (Ct) plus albite (Ab) groundmass. White blebs are hematite grains.

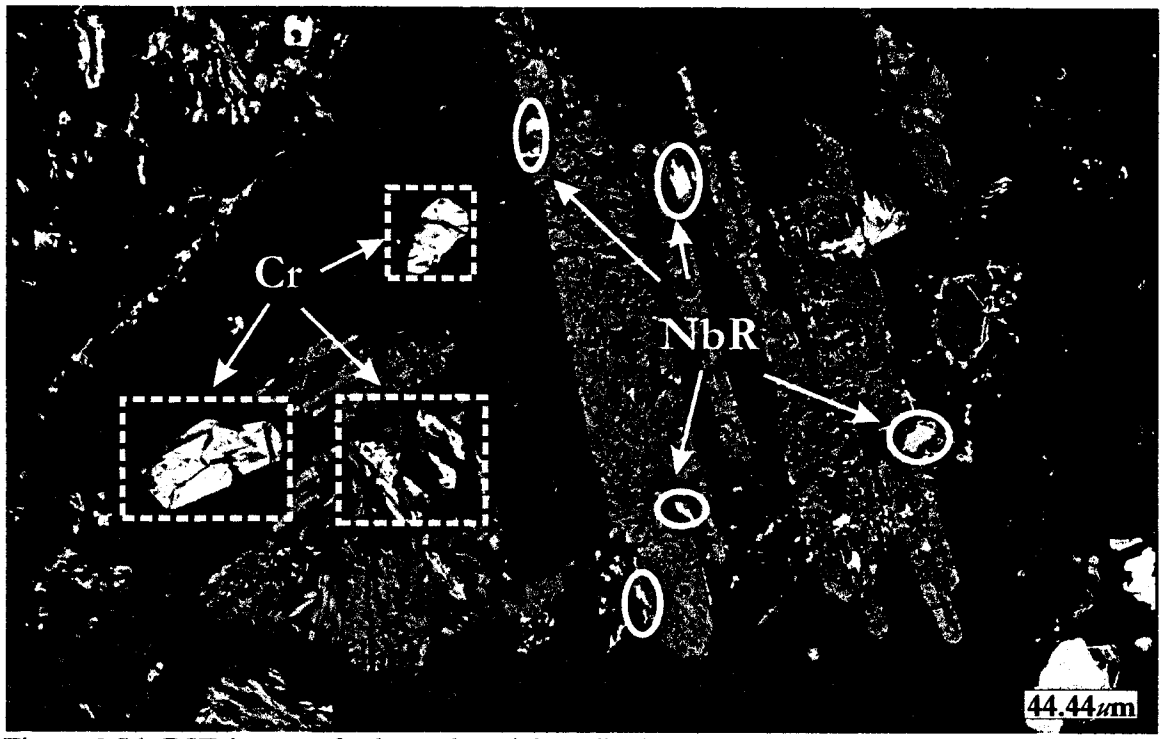

Figure 2.56: BSE-image of Nb- and V-rich rutile (NbR, solid ellipses), associated corroded rutile laths and crichtonite grains (Cr, dashed squares).

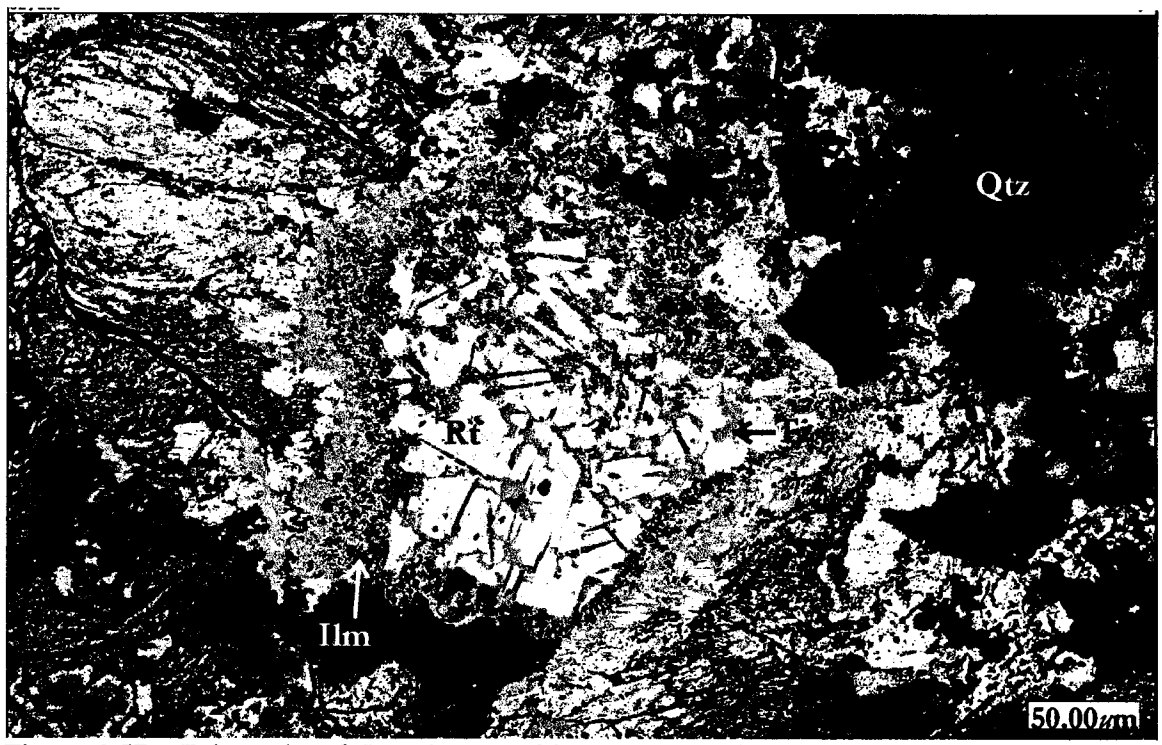

Figure 2.57: False-colored BSE-image of intergrown rutile (Rt-yellow), titanite (Ti-green) and ilmenite (Ilm-red) nodule. Nodule and fractured potassium feldspar grains (Kspr) are hosted in quartz (Qtz).

2.14 Thorite and thorogummite

Thorite [(Th,U)SiO_4] is present in the main mineralized zone, diatreme breccia, and the crosscutting carbonatite dike. In all but a few instances, thorite has become metamict, producing thorogummite [$Th(SiO_4)_{1-x}(OH)_{4x}$]. Both phases are referred to as thorogummite in this section. Although present in all three units, the greatest concentrations of thorogummite are observed in the main mineralized zone, with lesser amounts present in the diatreme breccia and carbonatite dike. Outside the main mineralized zone, thorogummite is compositionally close to the ideal formula, with small amounts of uranium present.

Within the main mineralized zone, three separate compositions of thorogummite were noted: calico-thorogummite; vanadium-rich calcio-thorogummite; and yttrium-bearing thorogummite. Calcio-thorogummite, the most abundant of the three varieties, occurs in trace amounts as dispersed, small (10 μm), rounded, anhedral grains set in quartz and calcite. In one thin-section, the thorogummite grains commonly mantle zoned-zircon grains and fragments. Apart from small amounts of calcium and vanadium (maximum of 3.6 and 0.87 wt.% respectively), these grains consist of essentially ThO_2 and SiO_2. Figures 2.58 and 2.59 illustrate the forms and textures present in these grains.

The vanadium-rich calcio-thorogummite occurs as relatively large, anhedral, sub-rounded grains concentrated together to form chains. These grains were large in comparison to the calico-thorogummite grains and were homogeneous; albeit with some V_2O_3 variation. Representative compositions are given in Table 2.14 and an EDS in Figure 2.60. Figure 2.61 illustrates that V_2O_3 variation is inversely proportional to the SiO_2 content. Images of the grains are given in Figures 2.62 and 2.63.

Table 2.14: Representative compositions of the V-rich calciothorogummite.

Al_2O_3	0.6	0.6	0.5	0.8	1.0	1.0	0.7	0.9
SiO_2	19.5	18.2	17.2	16.5	16.7	14.8	14.3	12.5
CaO	5.5	5.1	4.7	5.3	5.3	6.1	6.5	6.6
V_2O_3	3.0	4.2	4.9	6.2	7.2	9.6	10.3	12.2
MnO	0.2	0.2	0.4	0.1	0.1	-	-	-
FeO	0.2	0.1	0.2	0.2	0.9	-	-	0.2
ZrO_2	1.5	-	-	0.7	0.8	0.7	0.8	0.5
BaO	0.2	0.2	0.1	0.6	-	0.5	0.3	0.2
ThO_2	57.2	57.2	58.0	55.8	55.3	54.2	52.3	51.6
UO_2	2.0	3.6	2.6	3.1	2.5	3.0	3.5	5.2
Totals	89.9	89.4	88.6	89.3	89.8	89.9	88.7	89.9
			Cation Proportions					
Al^{3+}	-	-	-	-	0.1	0.1	-	0.1
Si^{4+}	1.0	1.0	0.9	0.9	0.9	0.8	0.8	0.7
Ca^{2+}	0.3	0.3	0.3	0.3	0.3	0.3	0.4	0.4
V^{3+}	0.1	0.2	0.2	0.3	0.3	0.4	0.4	0.5
Mn^{2+}	-	-	-	-	-	-	-	-
Fe^{3+}	-	-	-	-	-	-	-	-
Zr^{4+}	-	-	-	-	-	-	-	-
Ba^{2+}	-	-	-	-	-	-	-	-
Th^{4+}	0.7	0.7	0.7	0.7	0.6	0.6	0.6	0.6
U^{4+}	-	-	-	-	-	-	-	0.1
Totals	2.1	2.2	2.1	2.2	2.2	2.2	2.2	2.4

Note: Cation proportions calculated based on 4 oxygens.

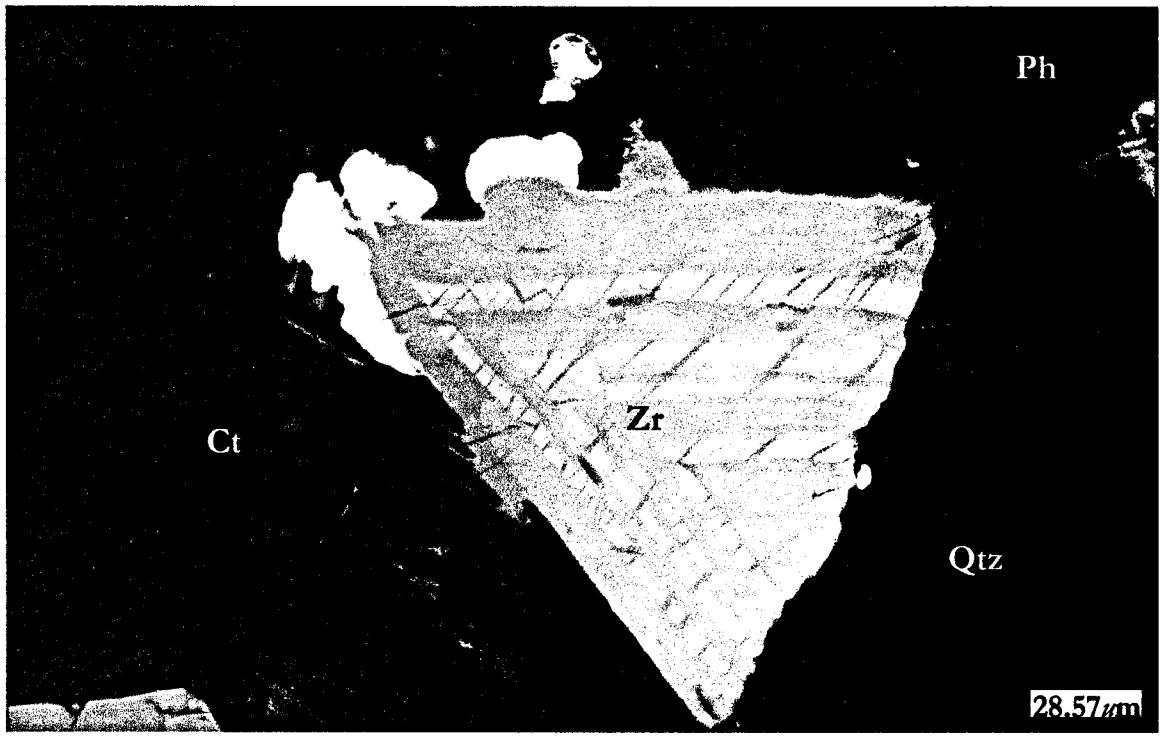

Figure 2.58: BSE-image of thorogummite (white) mantling a zoned zircon fragment (Zr), set in a quartz (Qtz) plus calcite (Ct) matrix along with phenakite (Ph).

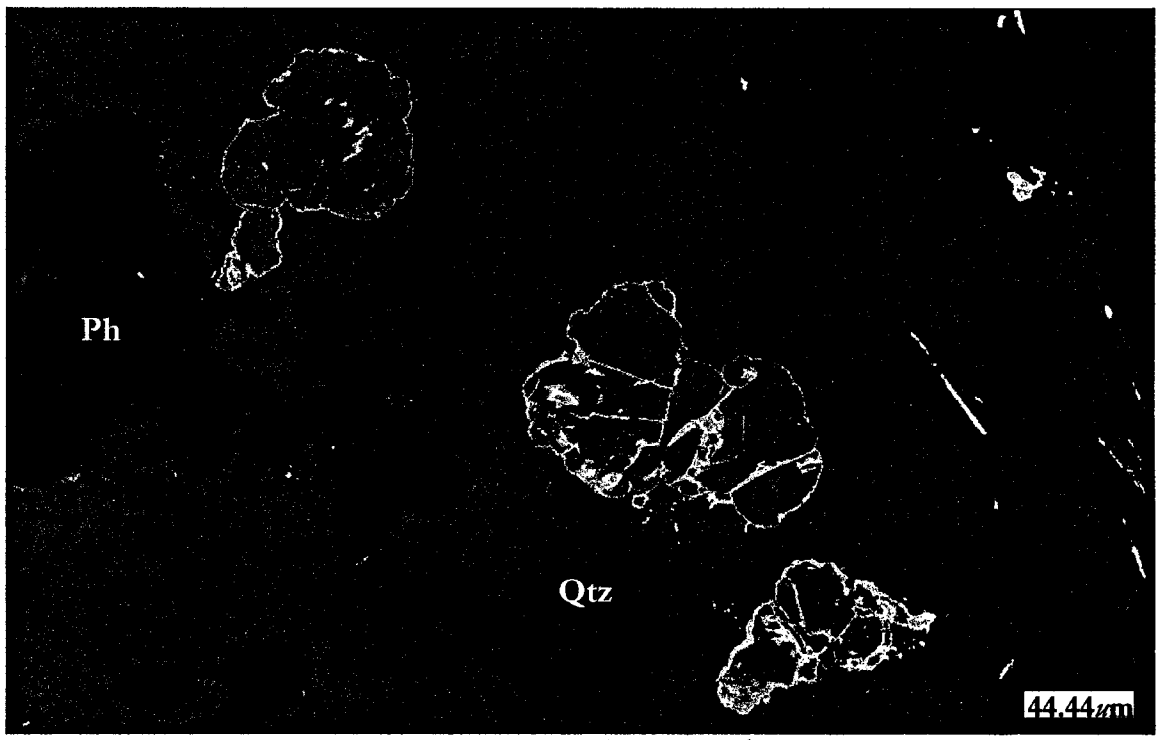

Figure 2.59: False-colored BSE-image of anhedral thorite/thorogummite grains (Th) set in quartz (Qtz), which also contains phenakite (Ph).

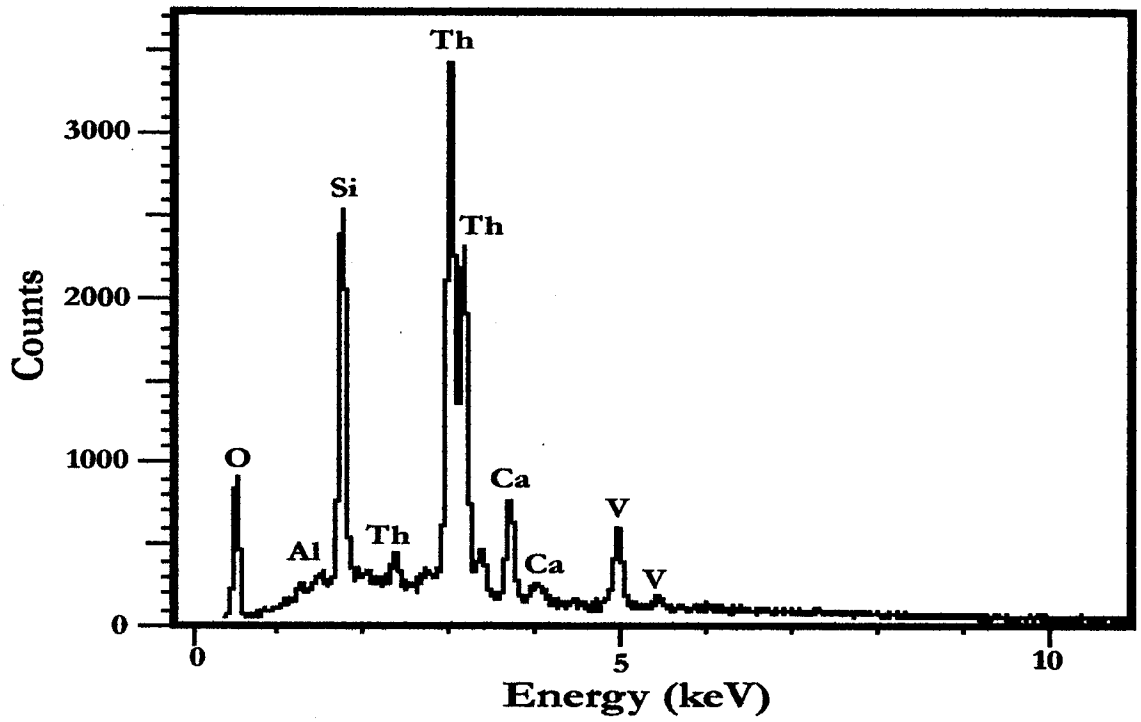

Figure 2.60: An EDS of the vanadium-rich calico-thorogummite from Deadhorse Creek.

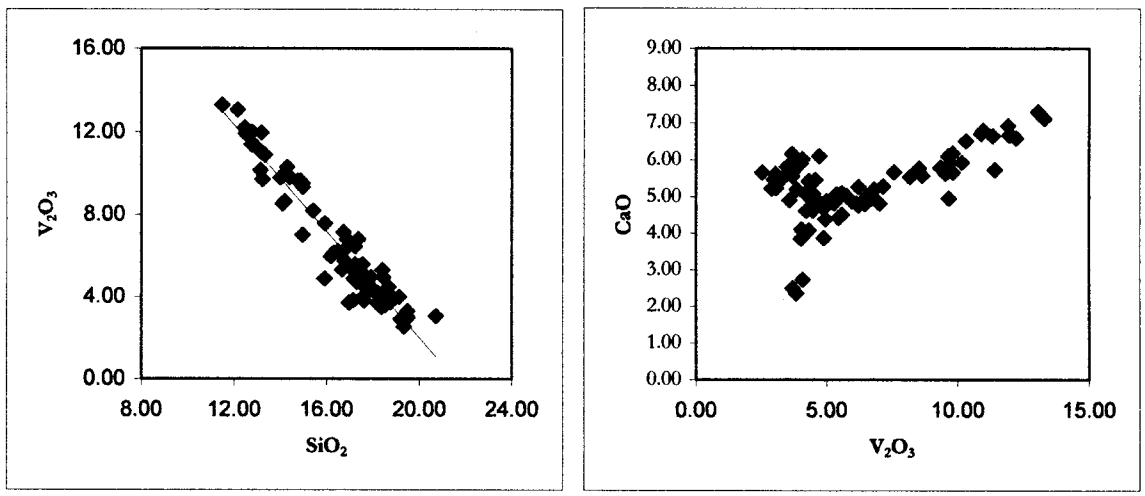

A. B.

Figure 2.61: (A) SiO_2 versus V_2O_3 plot illustrating an inverse relationship for the V-rich calciothorogummite. (B) V_2O_3 versus CaO plot from the same grains.

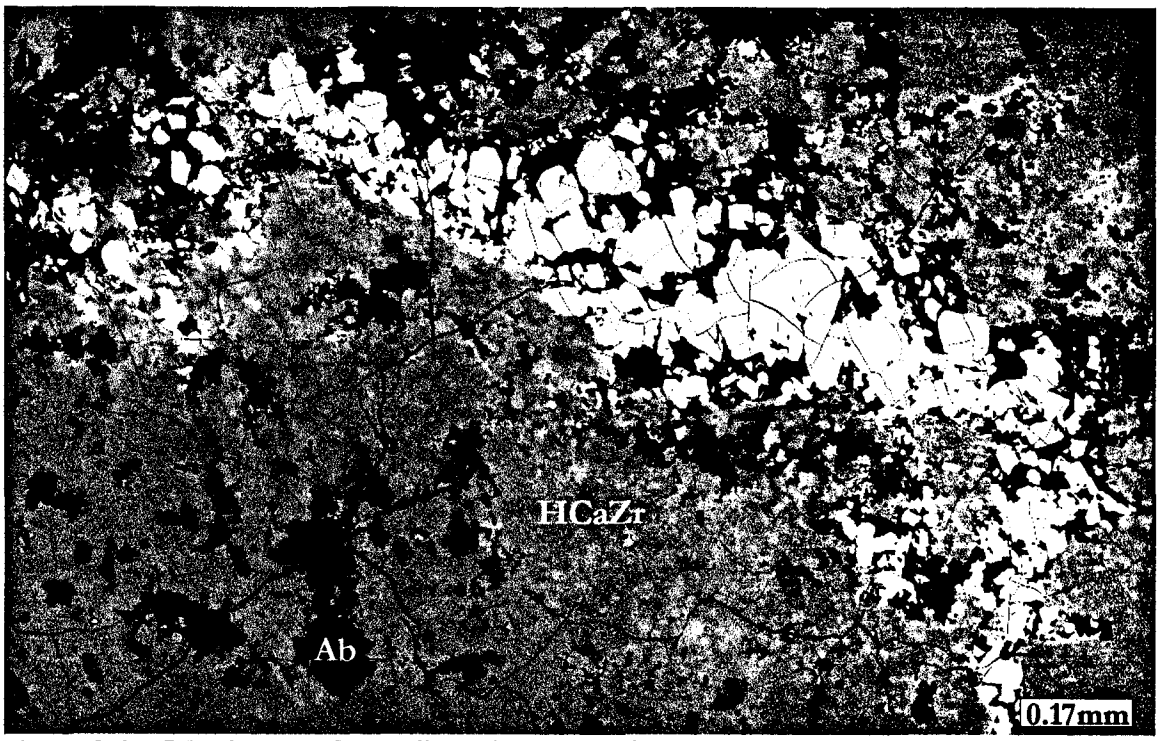

Figure 2.62: BSE-image of vanadium-rich calico-thorogummite (white) set in matrix of the hydrated calcium zirconosilicate (HCaZr) and albite (Ab).

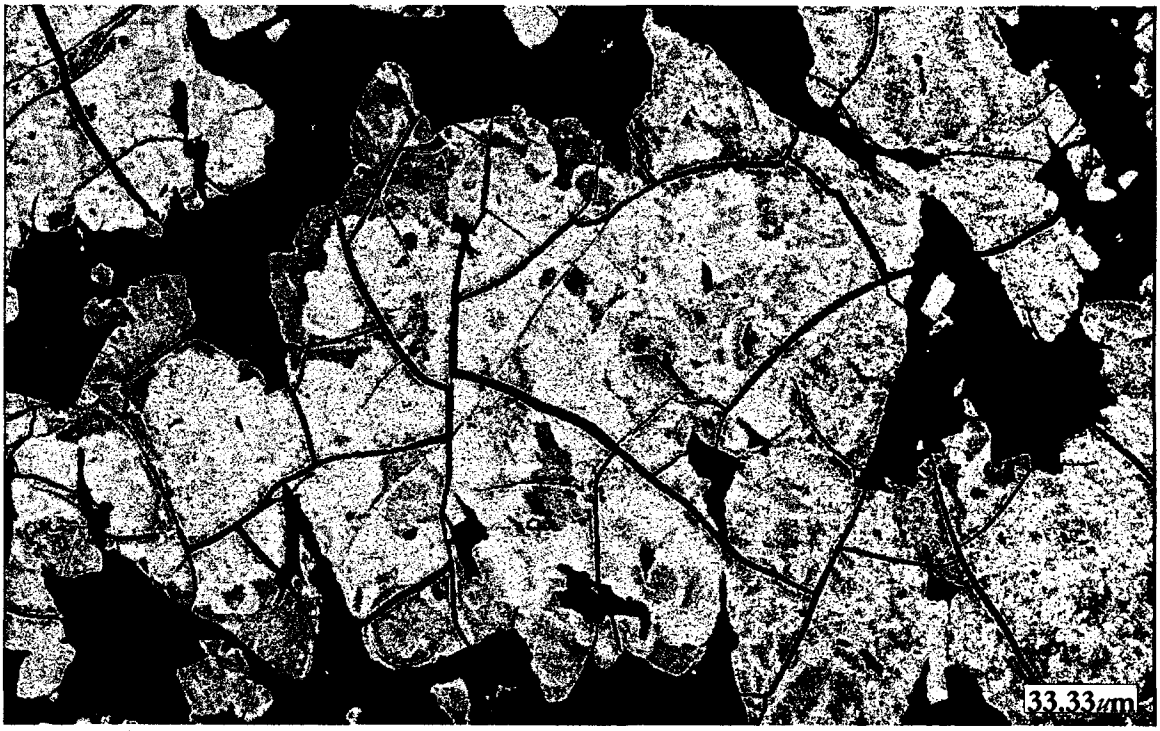

Figure 2.63: False-colored BSE-image of the V- and Ca-rich thorogummite. Thorium-enriched zones indicated by the red colors.

The third 'variety' of thorogummite is enriched in yttrium and uranium compared to the other two varieties present. It occurs as rounded, anhedral grains associated with, and commonly intergrown with xenotime-(Y), monazite-(Ce) and pyrite. The intergrowths made analysis difficult as impurities were detected in most samples and several attempts were often required to obtain a single analysis. Nonetheless, the compositional data presented in Table 2.15 illustrates the variation in composition and low analytical totals due to metamictization. In addition, an EDS (Figure 2.64) illustrates the elements present. Images of the yttrium-rich thorogummite are given in Figures 2.65 and 2.66.

Table 2.15: Composition of yttrium-rich thorite and thorogummite from Deadhorse Creek.

	1	2	3	4	5	6	7	8
MgO	0.3	0.2	0.1	0.1	0.2	0.4	0.4	0.3
SiO_2	20.4	19.8	18.9	18.6	18.5	17.9	17.3	17.5
CaO	1.2	1.3	0.8	1.4	1.0	0.9	0.9	1.0
FeO	0.5	0.4	0.6	0.6	1.1	2.1	2.1	0.6
Y_2O_3	4.6	4.4	6.1	6.1	6.1	8.5	7.3	7.0
ZrO_2	1.2	1.2	1.1	1.6	1.2	0.9	1.2	0.4
La_2O_3	0.6	0.9	0.4	0.7	-	0.1	-	0.3
Ce_2O_3	2.9	3.0	2.8	1.8	1.7	1.3	1.3	1.4
ThO_2	63.2	62.7	56.8	57.4	55.1	52.0	52.6	50.8
UO_2	5.2	4.0	6.6	2.0	3.4	2.0	1.2	3.4
Totals	100.1	97.9	94.2	90.3	88.3	86.1	84.3	82.7
Mg^{2+}	-	-	-	-	-	-	-	-
Si^{4+}	1.0	1.0	1.0	1.0	1.0	1.0	1.0	1.0
Ca^{2+}	0.1	0.1	-	0.1	0.1	0.1	0.1	0.1
Fe^{2+}	-	-	-	-	-	0.1	0.1	0.0
Y^{3+}	0.1	0.1	0.2	0.2	0.2	0.2	0.2	0.2
Zr^{4+}	-	-	-	-	-	-	-	-
La^{3+}	-	-	-	-	-	-	-	-
Ce^{3+}	0.1	0.1	0.1	-	-	-	-	-
Th^{4+}	0.7	0.7	0.7	0.7	0.7	0.7	0.7	0.7
U^{4+}	0.1	-	0.1	-	-	-	-	-
Totals	2.1	2.0	2.1	2.0	2.0	2.1	2.1	2.0

Note: column 1 thorite; columns 2-8 becoming progressively more metamict, i.e., (thorogummite).

Relatively little literature exists on the occurrence and genesis of thorogummite. Of the reported occurrences, few have presented analytical data and most only note the presence of a complex hydrated thorium silicate that forms from various primary Th and U silicates and oxides (Farges and Calas, 1991). Some of the earliest reports suggests the formation of thorogummite from weathering and alteration of thorian yttrialite [$(Y,Th)_2Si_2O_7$] (Iimori and Hata, 1938), while more recent work by McCready *et al.* (2003) suggests the formation of coffinite-thorogummite and a hydrated Th-Y-Si-P phase from antecedent monazite. With the exception of phosphate, these occurrences are the closest in composition to the thorogummites at the Deadhorse Creek complex.

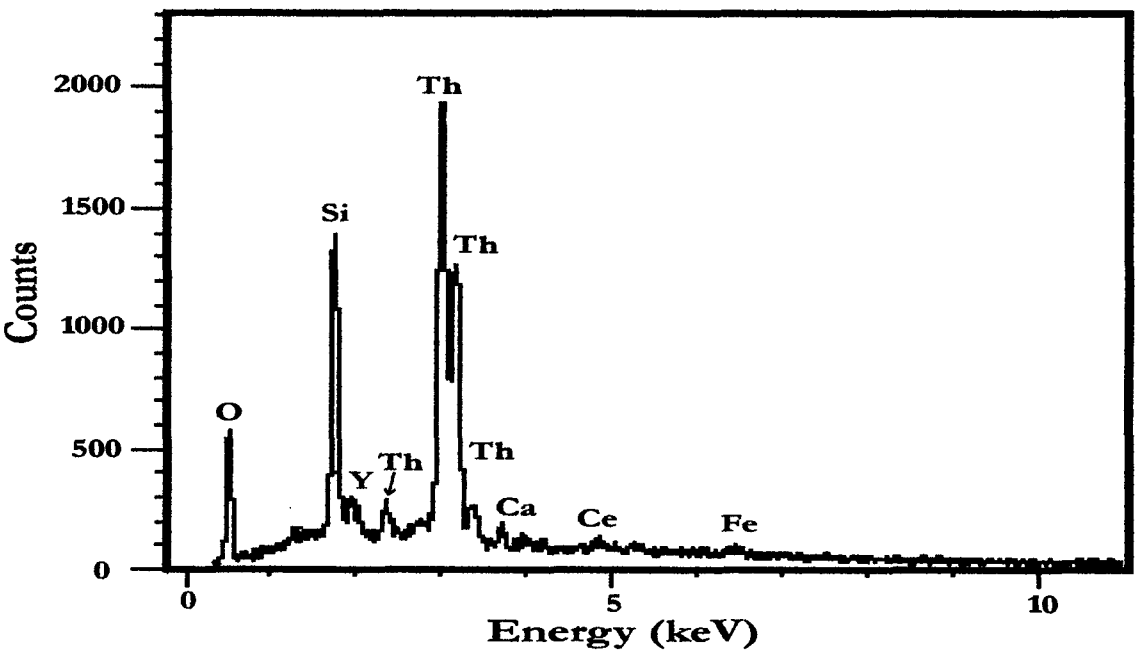

Figure 2.64: An EDS of yttrium-bearing thorogummite from Deadhorse Creek.

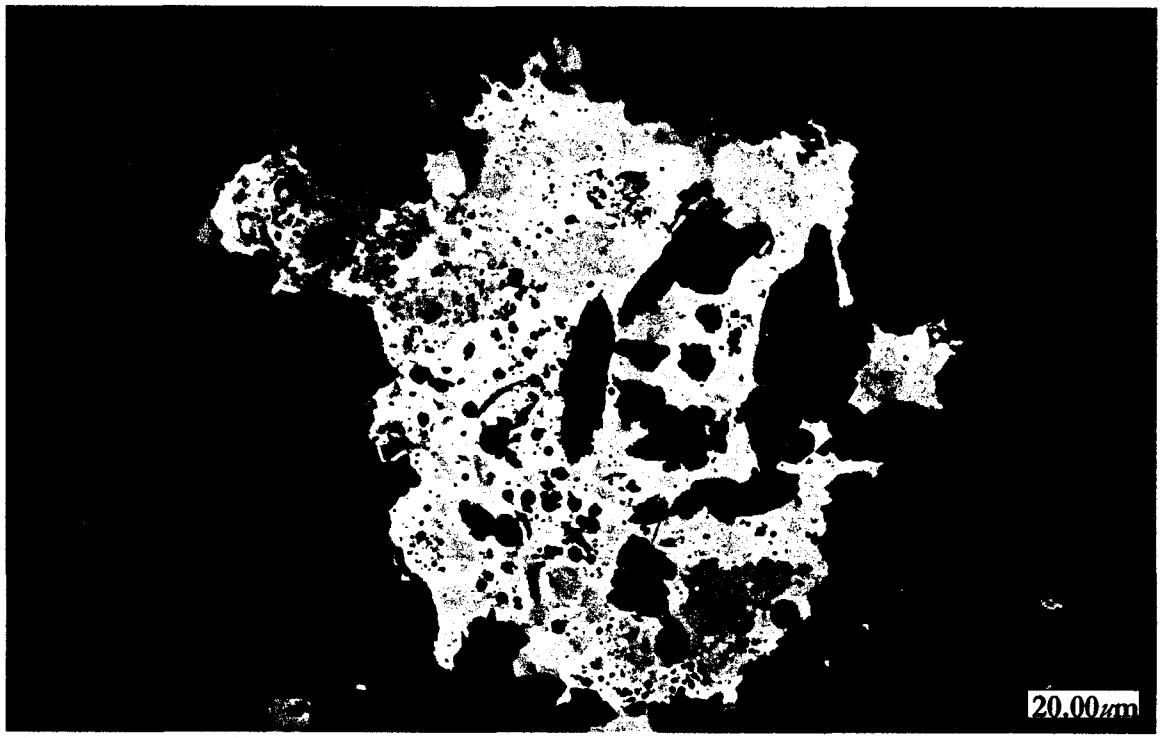

Figure 2.65: BSE-image of weathered yttrium-rich thorogummite grain set in apatite.

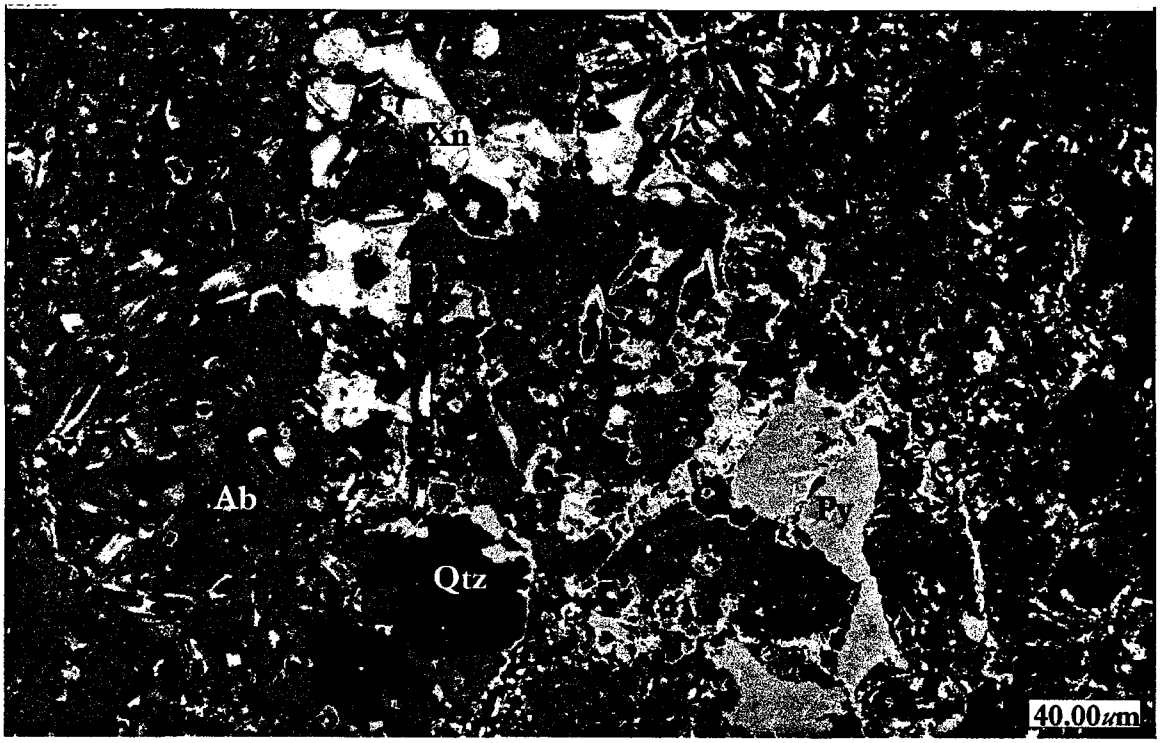

Figure 2.66: False-colored BSE-image of yttrium-rich thorogummite (Th), intergrown with xenotime (Xn) and pyrite (Py), set in an albite (Ab) plus quartz (Qtz) groundmass.

2.15 Thortveitite

Thortveitite [$Sc_2Si_2O_7$] is present within the main mineralized zone of the complex. This rare scandium silicate occurs within calcite and quartz. Regardless of the host, the habit of the thortveitite is that of tiny (<10 μm), anhedral grains (Figures 2.67 and 2.68). The grains are so small that accurate analysis is not possible as background matrix activation cannot be avoided. An EDS illustrates the composition of the phase (Figure 2.69). As a result, excess silica was present in all quartz-hosted grains and anomalously high calcium was present in all calcite-hosted grains. Although calcium has been reported in notable amounts in thortveitite (up to 1.6 wt.% CaO by Gramaccioli *et al.* (2000*a*)), the calcium content in the Deadhorse Creek thortveitite were heterogeneous, anomalously high (up to 8 wt.%) and when hosted in quartz, the thortveitite was free of calcium. Generally, the main substituting elements in place of Sc in thortveitite are Y, Zr and REE (Gramaccioli *et al.* 2000*a*). However, semi-quantitative analysis of thortveitite from Deadhorse Creek indicates only negligible amounts of Y_2O_3, CaO, V_2O_3 and FeO (less than 1 wt.%) replacing Sc_2O_3. In other samples, containing limited amounts of Y_2O_3, CaO and MnO are notably high (1.6 and 2.8 wt.%, respectively), owing to replacement of Y_2O_3 (Gramaccioli *et al.* 2000*a*).

The ability of the thortveitite structure to host notable quantities of other elements such as Y, Zr, HREE, Ca and Mn without extensive re-arrangement, and the existence of natural and synthetic REE- or Zr-dominant equivalents of the mineral (Smolin and Shepelev, 1970; Voloshin *et al.* 1983, 1985; Roelofsen-Ahl and Petersen, 1989) implies that the relatively purity of some thortveitite samples cannot be attributed to crystal-chemical reasons alone. Therefore, the compositions must reflect the chemistry of the depositing solutions (Gramaccioli *et al.* 2000*a*). A note of caution however, as the authors further state that a "general picture concerning the formation of scandium-rich minerals and their geological significance has not been established yet, owing to the scarcity of reliable physical-chemical data and of natural samples." Furthermore, the peculiar and apparent contradictory geochemical behavior of scandium complicates matters. In igneous rocks, Sc is usually concentrated in ferromagnesian minerals and thus preferentially found in mafic assemblages. Yet, notable exceptions are found in some carbonatites, where the accessory minerals are the major hosts of Sc (Gramaccioli *et al.* 2000*a*; Eby, 1973). Other important occurrences of

scandium are in hydrothermal or pneumatolitic veins in granitic rocks, in association with fluorine-rich minerals (e.g. zinnwaldite, fluorite and topaz) (Gramaccioli *et al.* 2000*a*). This close association with fluorine has led many researchers to suggest that fluorine complexes could be important in migration and concentration of scandium (Kalenov, 1961). More recently, Montero *et al.* (1998) consider the formation and breakdown of complexes with fluorine and other ligands to be essential in the enrichment of rare-earth elements and high-field strength elements and in the resultant deposition of their minerals. Indeed, Gramaccioli *et al.* (2000*b*) have shown that the stability constants of scandium fluoride complexes are much higher than most other elements, especially rare-earth elements. As a result, the authors propose that the presence of fluorides should easily lead to differentiation between scandium and other elements including rare-earth elements; giving rise to specific minerals. For example, if a fluoride-and scandium-bearing solution were to begin depositing fluorite and other fluorine-rich minerals, the activity of the fluorine ion in the solution will be consequently reduced. After deposition, the ratio $[Sc^{3+}]/[Yb^{3+}]$ in the crystals of thortveitite at equilibrium should increase by several orders of magnitude, thereby giving rise to a mineral very enriched in scandium, such as REE-free thortveitite (Gramaccioli *et al.* 2000*b*). Such a process may apply to the thortveitite at Deadhorse Creek, as the thortveitite is REE-poor and fluoride-bearing minerals fluorite and apatite are present within the complex. The proximity of fluorapatite to thortveitite is shown below in Figures 2.67 and 2.68. Unfortunately, the composition of fluorapatite and fluorite from Deadhorse Creek offer no evidence in support of the above hypothesis, as no Sc_2O_3 is detected spectroscopically. An EDS of fluorite from the main mineralized zone is shown in Figure 2.70, with Figures 2.71 and 2.72 illustrating the two habits of fluorite present. Quantitatively, Sc_2O_3 contents in the fluorite were less than 0.3 wt.% and when coupled with the lack of spectroscopic evidence, its presence appears doubtful.

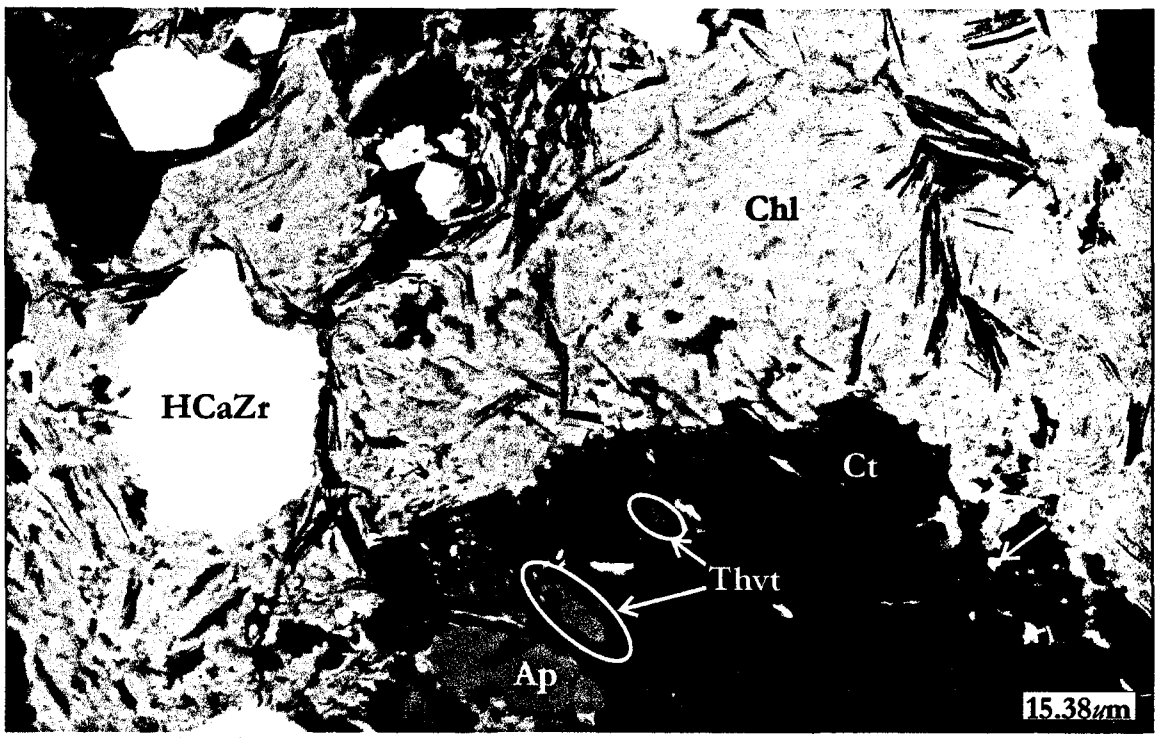

Figure 2.67: BSE-image of thortveitite (Thvt), hydrated calcium zirconosilicate (HCaZr), chlorite (Chl) and galena (Gl) set in a calcite (Ct) plus apatite (Ap) groundmass.

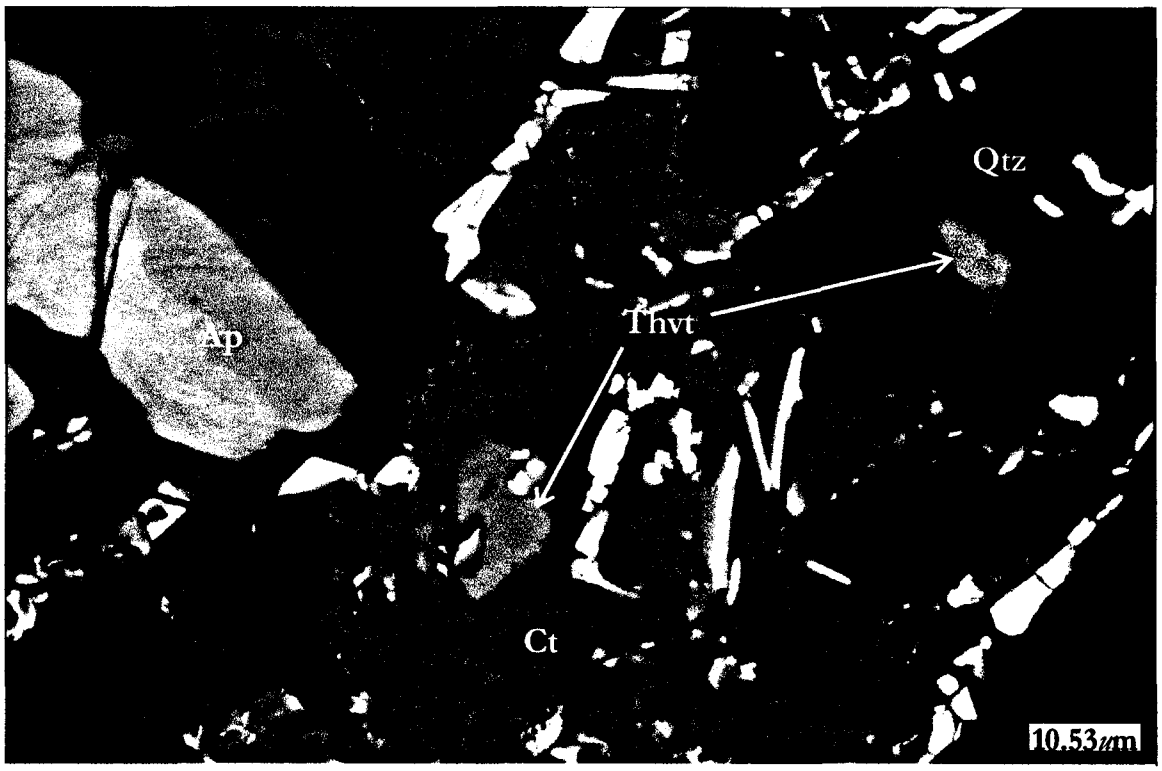

Figure 2.68: BSE-image of thortveitite (Thvt) set in both quartz (Qtz) and calcite (Ct). Also shown: associated Fe-Cr-V-oxide (white) and apatite (Ap).

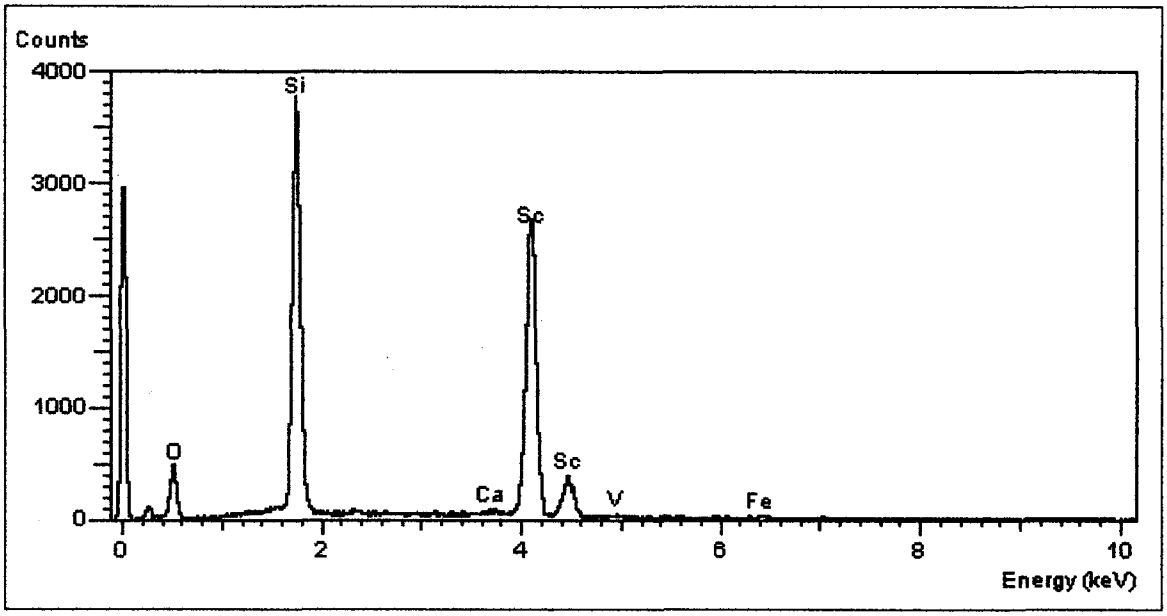

Figure 2.69: Energy-dispersive spectrum of thortveitite from the Deadhorse Creek complex. Shown are the minor amounts of Ca, V/Ti and Fe.

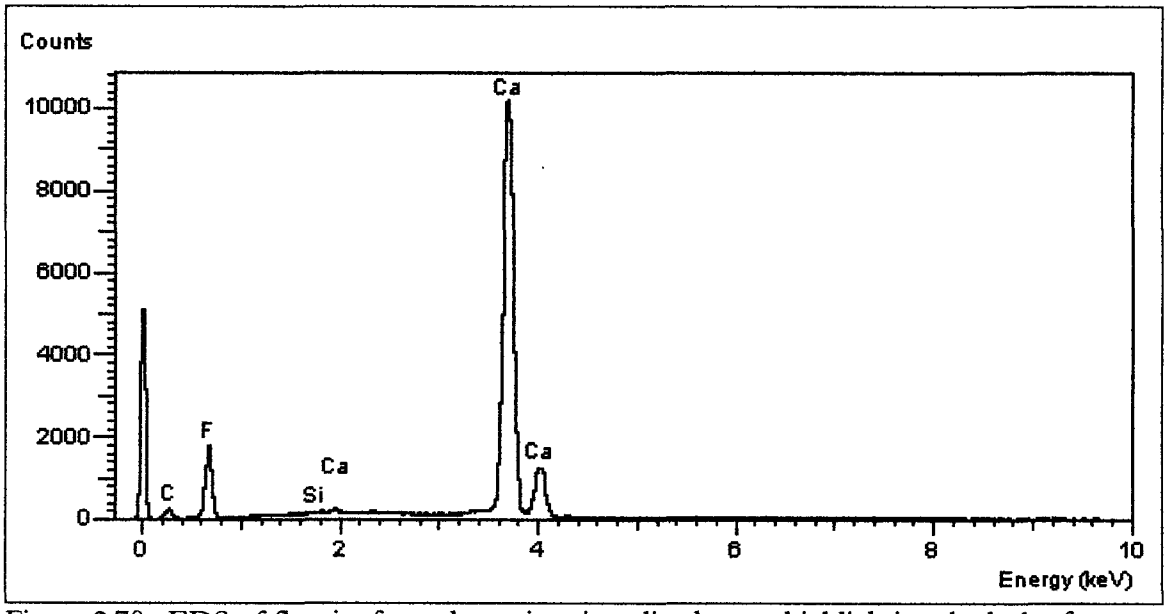

Figure 2.70: EDS of fluorite from the main mineralized zone, highlighting the lack of detectable Sc_2O_3.

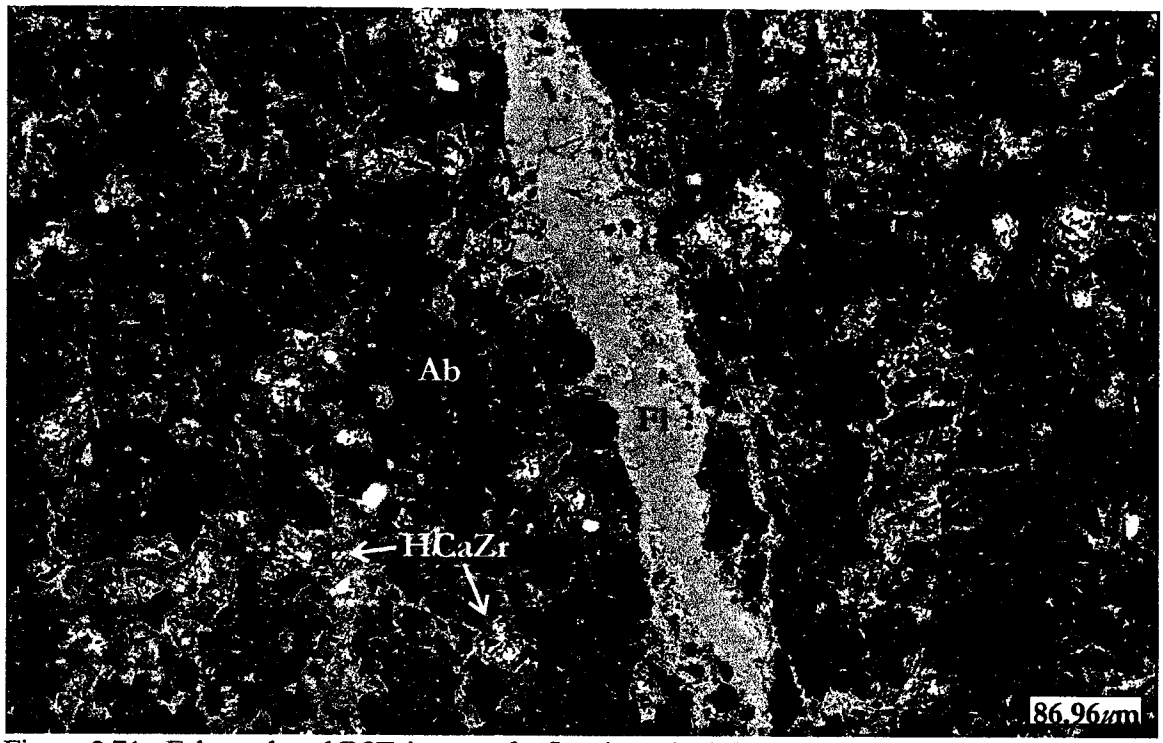

Figure 2.71: False-colored BSE-image of a fluorite vein (Fl) crosscutting an albite (Ab) groundmass, which also hosts abundant hydrated calcium zirconosilicate (HCaZr).

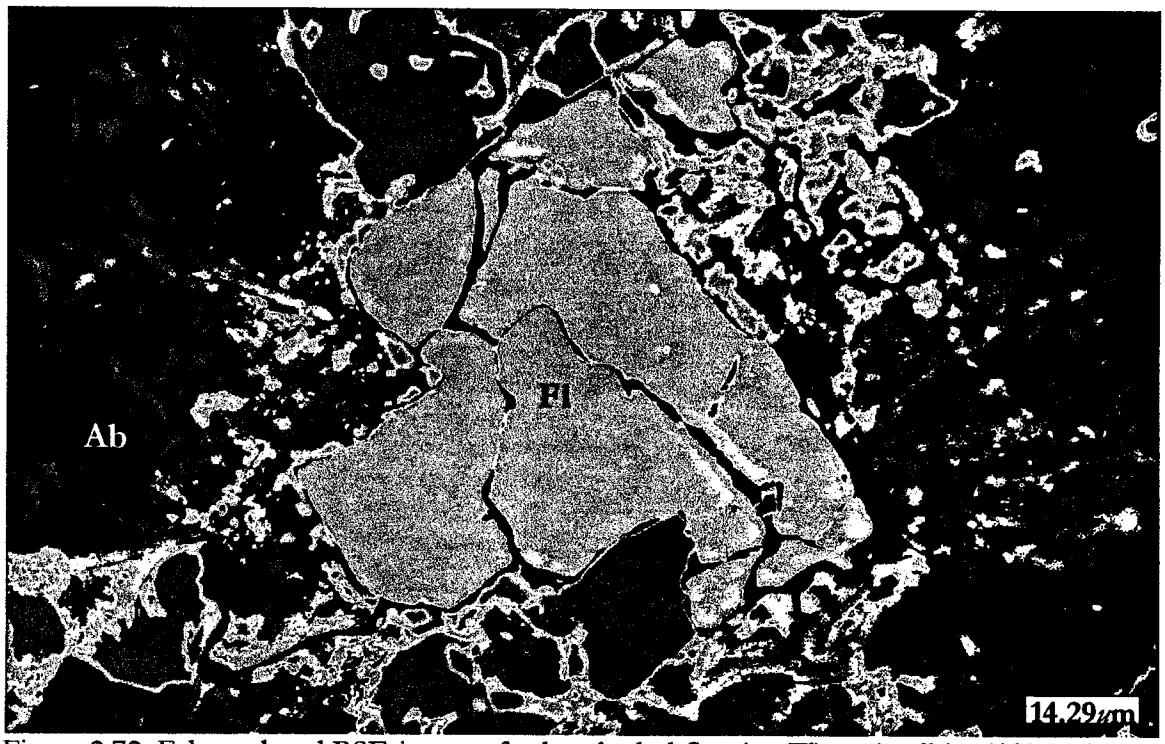

Figure 2.72: False-colored BSE-image of sub-euhedral fluorite (Fl) set in albite (Ab) and associated with the hydrated calcium zirconosilicate (HCaZr).

2.16 Tyuyamunite and Metatyuyamunite

Tyuyamunite [$Ca(UO_2)_2V_2O_8$*5-8H_2O] and metatyuyamunite [$Ca(UO_2)_2V_2O_8$*3H_2O] occur within the main mineralized zone of the complex in narrow, late-stage calcite veinlets and as anhedral grains less than 10 μm in diameter. The small veinlets cross-cut all features along their strike, while the smaller anhedral grains appear interstitial. Unfortunately, the veinlets are not abundant and do not intersect the other late-stage veinlets of barite or hollandite. However, the tyuyamunite mineralization is hosted by calcite veins, similar to the barite and hollandite veins and some analyses indicate the presence of barium. The greatest concentration of BaO measured was 12.7 wt.%, accompanied by reduced amounts of CaO (1.1 wt.% versus ~6 wt.%). Unfortunately, the small size of the veinlets and anhedral grains prevented accurate analysis. Further investigation of the textures suggests in part that the phase may have formed in open-space fractures, along which earlier calcite had crystallized. In the majority of grains, background silica, potassium and aluminum were detected, creating poor analytical totals. Therefore, no quantitative data are presented. An EDS is shown in Figure 2.73, illustrating the composition of the phases. Backscattered-electron images in Figures 2.74 and 2.75 illustrate the two separate habits. Platt and Mitchell (1996) also positively identified the phase as metatyuyamunite by X-ray diffraction.

Although the Deadhorse Creek tyuyamunite and metatyuyamunite have experienced weathering, uranyl vanadates are considered the most insoluble of uranyl minerals (Garrels and Christ, 1959; Langmuir, 1978; Smith, 1984). In fact, the minerals are so stable that it is likely that they will form wherever dissolved uranium comes in contact with waters containing dissolved vanadate ions. As a result, uranyl vanadates commonly occur where reduced uranium minerals (i.e. uraninite, coffinite or brannerite) and reduced vanadium minerals (i.e. montroseite) undergo oxidation (Finch and Murakami, 1999). As Evans and Garrels (1958) first noted, when vanadium reaches the pentavalent state in the presence of uranyl ions (UO_2^{2+}), the insoluble carnotite or slightly soluble tyuyamunite becomes the stable phase at pH values > 2.2. Within this range, all other vanadium minerals become metastable with respect to the uranium complex (shown as shaded area in Figure 2.76).

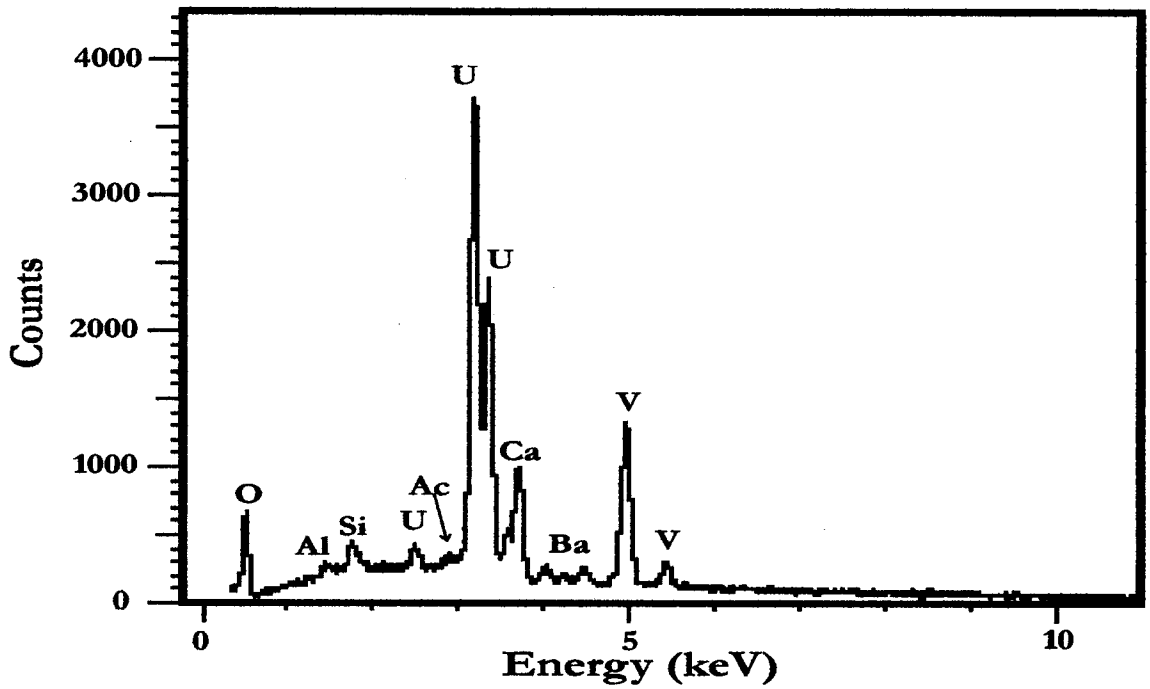

Figure 2.73: EDS of metatyuyamunite from Deadhorse Creek. Note the presence of barium, silica, aluminum and possibly actinium (Ac).

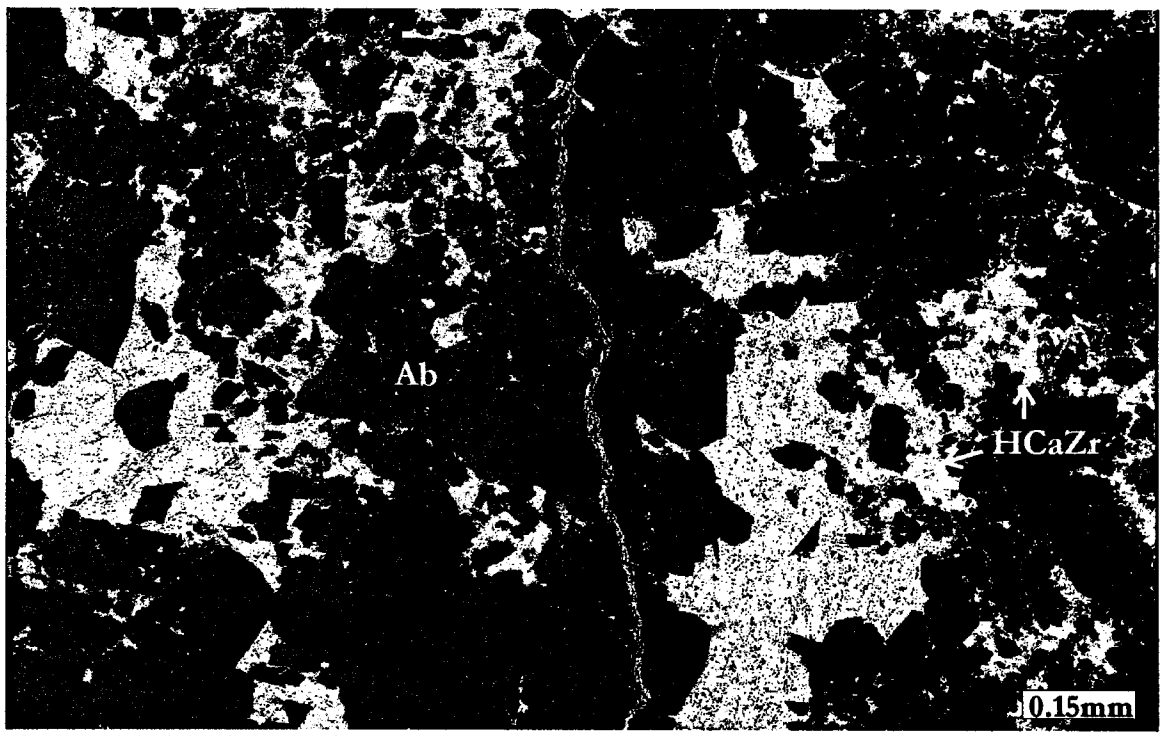

Figure 2.74: BSE-image of metatyuyamunite (red) crosscutting albite (Ab), calcite (Ct) and a hydrated calcium zirconosilicate (yellow).

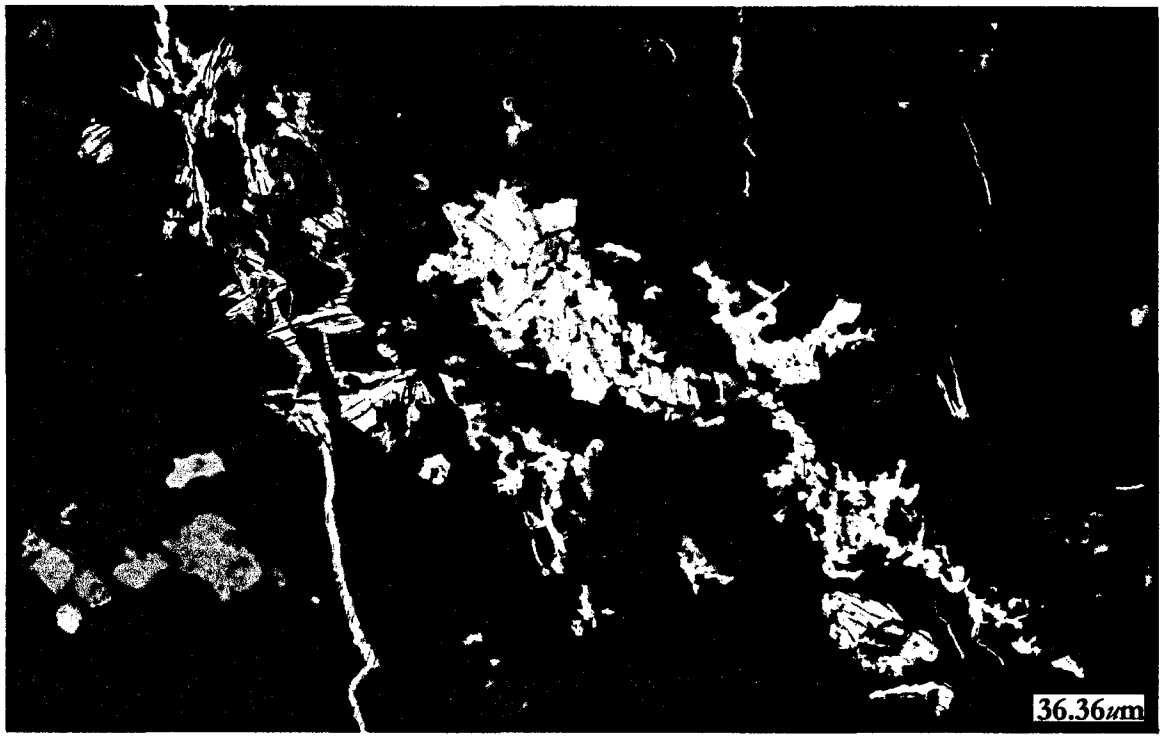

Figure 2.75: BSE-image of metatyuyamunite set in orthoclase. Also shown is the hydrated calcium zirconosilicate (lighter gray).

The hypotheses of Evan and Garrels (1958) were confirmed by Langmuir (1978), who found that carnotite is stable over pH-Eh ranges of 4.5-8.0 and 1.0-0.0 V, respectively. Furthermore, the authors illustrated that depending on the partial pressure of CO_2, the minimal solubility of carnotite is between pH values of 6 and 8. Figures 2.77 and 2.78 present the stabilities of aqueous vanadium and uranium species in terms of Eh-pH and $\log f_{H2}$-pH diagrams. From Figure 2.77, Wanty and Goldhaber (1992) note that the vanadyl species are stable thermodynamically only at low pH conditions (<6). One would therefore expect not to find vanadyl ions or complexes in solutions with pH values > 6. However, as Breit and Wanty (1991) state, solutions with pH > 6 may contain vanadyl due to kinetic hindrances to oxidizing, reducing or disproportionation of the vanadyl ion, or due to the formation of stable complexes. Hexavalent aqueous uranium is also stable at low pH values, with UO_2^{2+} being the predominant species at pH < 5 and at low $\log f_{H2}$ values (< -10). Ideally, these aqueous species should not be considered separately, but together as uranyl-vanadate species. Unfortunately, no data other than Figure 2.76 are reported in the literature.

Other hypotheses regarding the formation of tyuyamunite include the interaction of uraniferous groundwater with H_2S from migrating hydrocarbons or from the reduction of sulphates by the hydrocarbons (Allen and Thomas, 1984). Up-welling H_2S-bearing fluids are also believed to have formed at least some of the occurrences of metatyuyamunite within solution caves (Onac *et al.* 2001; Polyak and Mosch, 1995).

A variation of one of the above processes may have resulted in tyuyamunite mineralization at the Deadhorse Creek complex. As Shock *et al.* (1997) state, transport of uranium as the more soluble U^{6+} species can occur if: the pH is considerably below neutral; complexing ligands stabilize U^{6+} to higher values of $\log f_{H2}$; or if geologic processes lead to large degrees of disequilibrium with respect to coupled redox reactions. The latter process likely accounts for near-surface occurrences of uranium transport where oxidizing surface waters or groundwater could be involved (Shock *et al.* 1997).

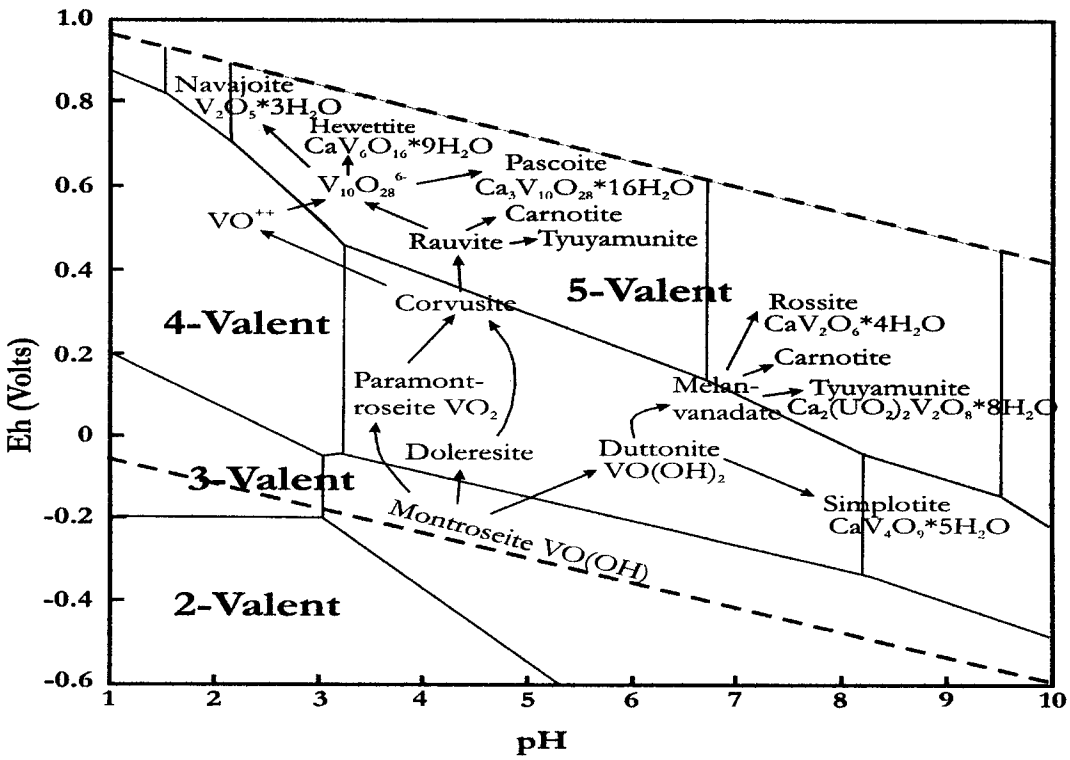

Figure 2.76: Aqueous equilibrium diagram for vanadium, illustrating the stability regions of various species. After Evans and Garrels (1958).

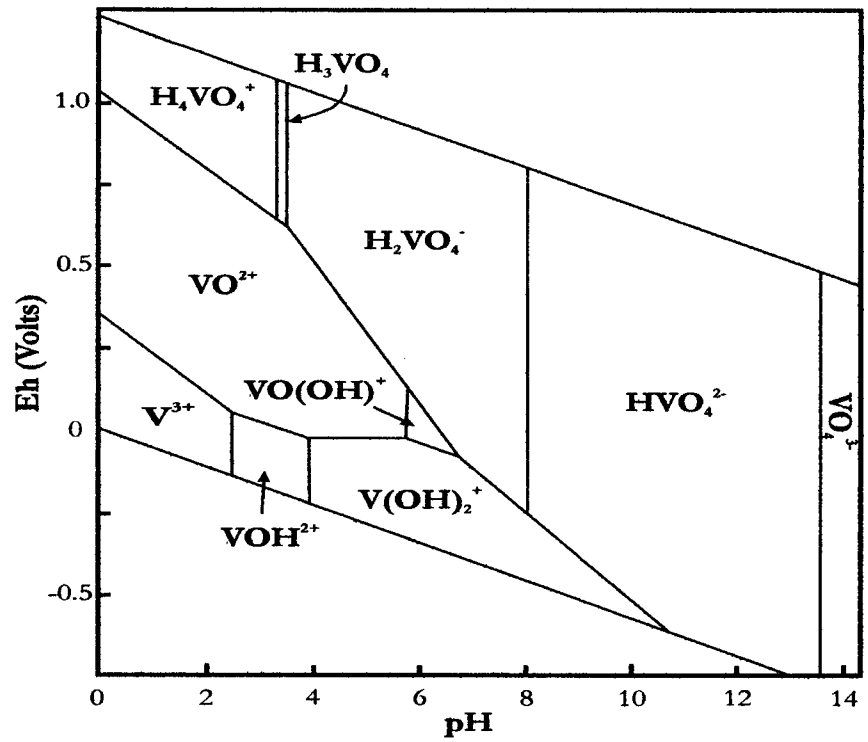

Figure 2.77: Plot of Eh versus pH at 25°C and 1 bar for aqueous vanadium species in the system V-O-H. Total V concentration is 10 μM; hence, no polymer species are stable (Wanty and Goldhaber, 1992).

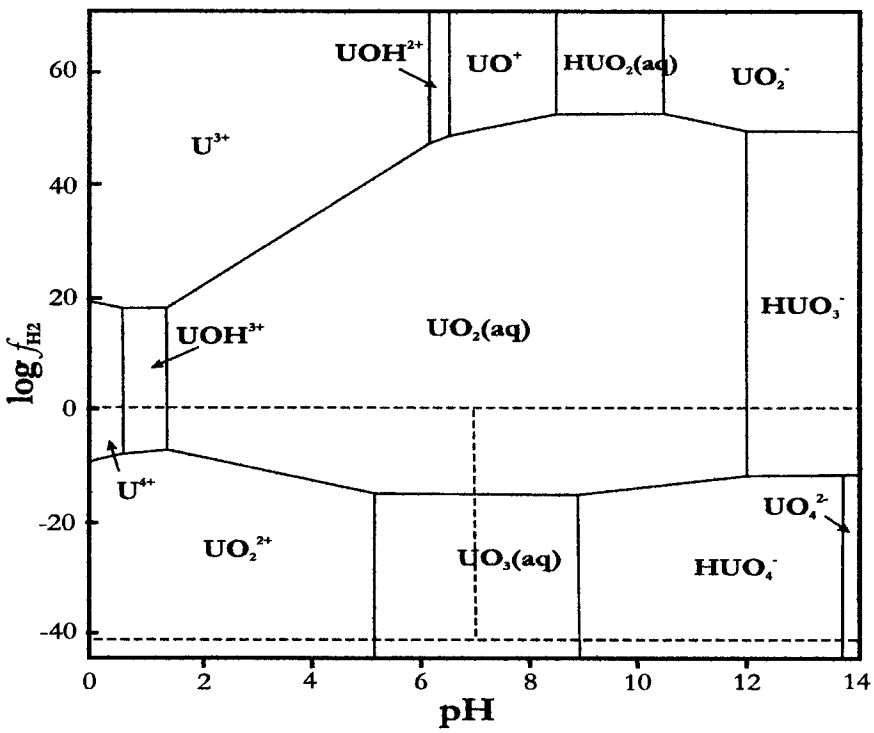

Figure 2.78: Plot of $\log f_{H2}$ versus pH at 25°C and 1 bar illustrating the relative predominance of aqueous uranium species (Shock *et al.* 1997).

Metatyuyamunite forms by dehydration of tyuyamunite, a process that is irreversible in most uranyl minerals. The removal of structurally-bound H_2O groups requires significant re-adjustment of local bonding arrangements and often results in phase transformations or even complete structural decomposition (Finch and Murakami, 1999). As noted by Čejka (1999), most uranyl vanadate minerals and synthetic phases exhibit a layer structure with $[(UO_2)_2V_2O_8]n^{2n-}$ units. Structurally bound H_2O groups most often occur in the 'interlayer' sites in the mineral structures where they may be bonded to an interlayer cation or occupy sites in which H_2O groups act as an H-bond 'bridge' only. Although H_2O groups that are H-bonded only appear to be lost most readily, the ease in which the interlayer bonded groups may be removed depends on the bonding environment (Finch *et al.*, 1998). As shown by Stern *et al.* (1956), equilibrium between tyuyamunite and metatyuyamunite was shown to be a function of partial pressure of water vapour at 24°C. Thermogravimetry experiments illustrate that tyuyamunite dehydrates in two steps, 6 H_2O (40-110°C) and 2 H_2O (200-300°C) characterized by two endotherms (110-140°C and 270-280°C) on a differential thermal analysis curve. Although a lower hydrate was not found with continued thermal decomposition of tyuyamunite, an exotherm at 500°C on the curve is associated with crystallization of a new phase, an anhydrous calcium uranyl vanadate (Čejka, 1999; Ambartsumyan *et al.*, 1961). Although existence of this anhydrous phase has not yet been identified in nature, some of the analytical totals from the metatyuyamunte at Deadhorse Creek may indicate at least a less-hydrated occurrence of metatyuyamunite; possibly grading into an anhydrous phase. However, poor standardization to uranium and the small size of the grains creating background contamination are more likely the cause of the high analytical totals.

2.17 Xenotime

Xenotime [YPO_4] is present in the main mineralized zone and the cross-cutting carbonatite dike. In addition, Dy-Gd-Th-bearing xenotime is present within the main mineralized zone. Xenotime is a fairly common accessory mineral in granite, granodiorite, syenite, granitic pegmatite, migmatites and low-to high-grade metamorphic rocks. The xenotime structure consists of PO_4^{3-} tetrahedra bonded by Y^{3+} in strongly-distorted cubic coordination (8-fold) (Nesse, 2000). The MO_8 polyhedron preferentially accommodates Y and the heavy rare earth elements due to their small ionic radii (Förster, 1998*b*).

Within the main mineralized zone, the xenotime ranges from small (>5 μm), anhedral grains up to ~10 μm large, subeuhedral-to-euhedral grains, both of which are set in calcite. The Dy-Gd-Th-bearing xenotime occurs as larger 'atoll grains' intimately associated with thorite and set in a quartz plus phenakite matrix. The stoichiometric xenotime located within the carbonatite dike forms large, cubic sub-euhedral- to -euhedral grains, which have been partially-corroded and fractured (Figures 2.79, 2.80 and 2.81).

In terms of composition, all but the Dy-bearing xenotime are essentially YPO_4. Although dysprosium and gadolinium were detected spectrospically, the lack of standard materials precluded quantitative analyses. Energy-dispersion X-ray spectra are shown in Figures 2.83 and 2.84, illustrating the presence of Dy, Gd and variability of Th.

While xenotime-(Y) commonly contains low amounts of heavy rare-earth elements and negligible amounts of the light counterparts, increased quantities of individual heavy rare-earths are exceptional (Masau *et al.* 2000*a*). Significant enrichment of heavy rare-earths have been noted from: granites (Förster, 1998*b*), alkaline granites (Jefford, 1962) and granitic pegmatites (Voloshin and Pakhomovoskii, 1986; Belolipetskii and Voloshin, 1996; Buck *et al.* 1999; Masau *et al.* 2000*a*). While not common, moderate enrichment of Yb, Dy and Gd has also been reported from: alpine veins (Demartin *et al.* 1991), metasediments (Franz *et al.* 1996) and granites (Förster, 1998*b*).

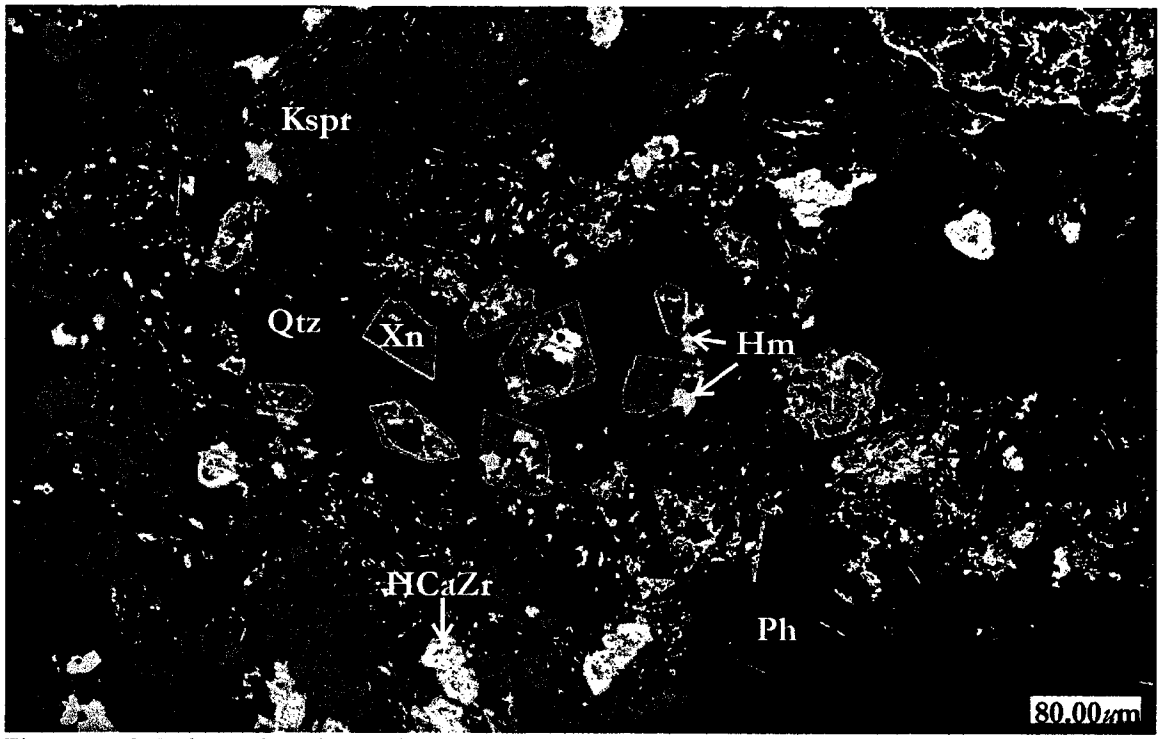

Figure 2.79: False-colored BSE-image of Dy-xenotime (Xn-red), hematite (Hm), the hydrated calcium zirconosilicate (HCaZr) and phenakite (Ph) set in quartz (Qtz) and potassium feldspar (Kspr).

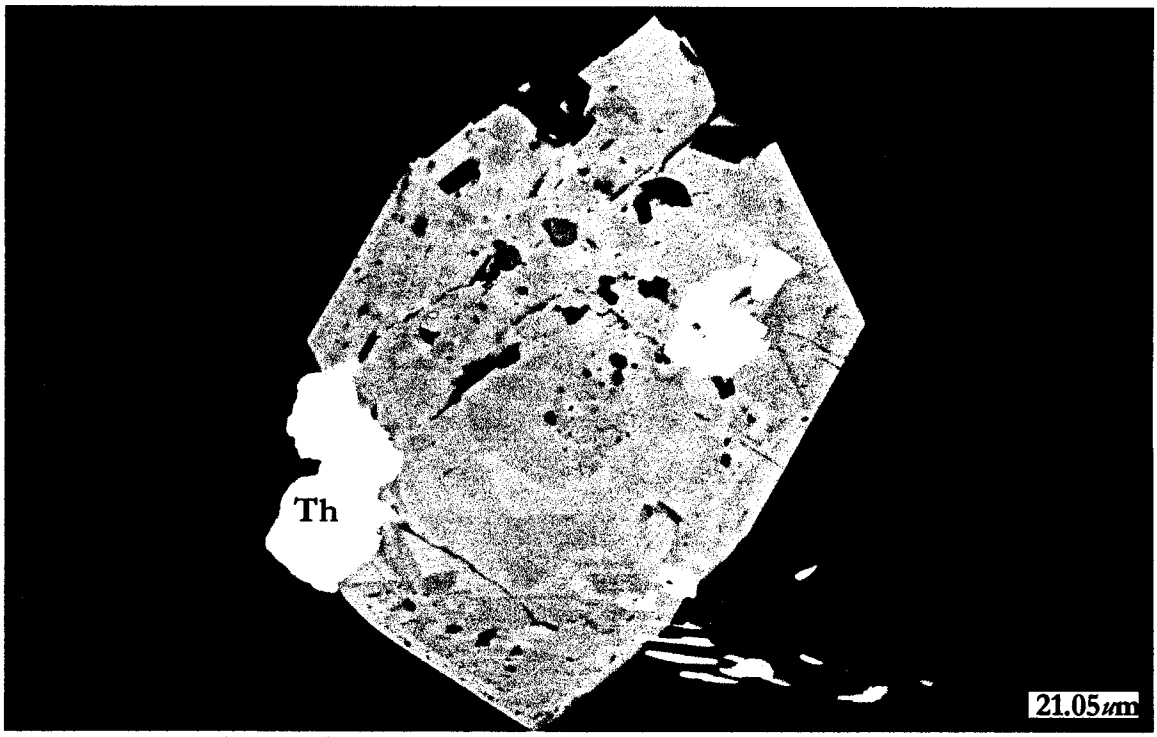

Figure 2.80: BSE-image of Dy-Th-xenotime, thorite (Th) and hematite (light gray) from the main mineralized zone. Brighter areas in the xenotime are enriched in thorium.

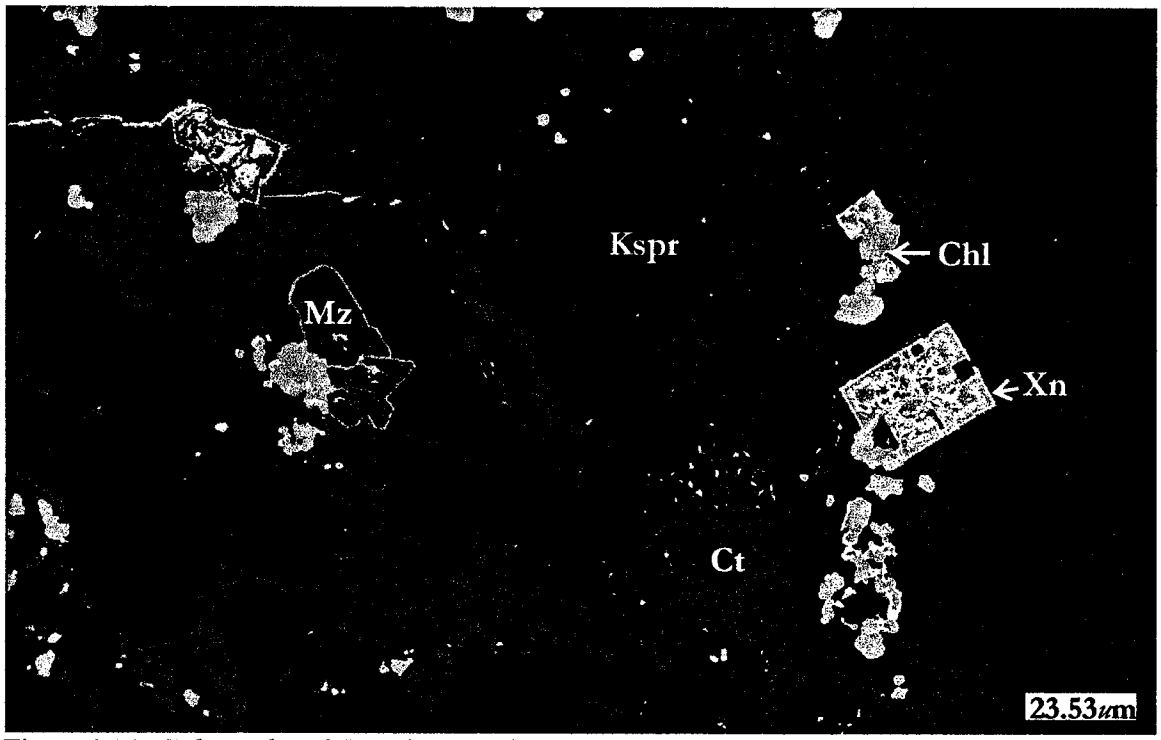

Figure 2.81: False-colored BSE-image of xenotime-(Y) (Xn-orange), chlorite (Chl), and monazite-(Ce) (Mz) from the carbonatite dike; all set in potassium feldspar (KSpr) and calcite (Ct).

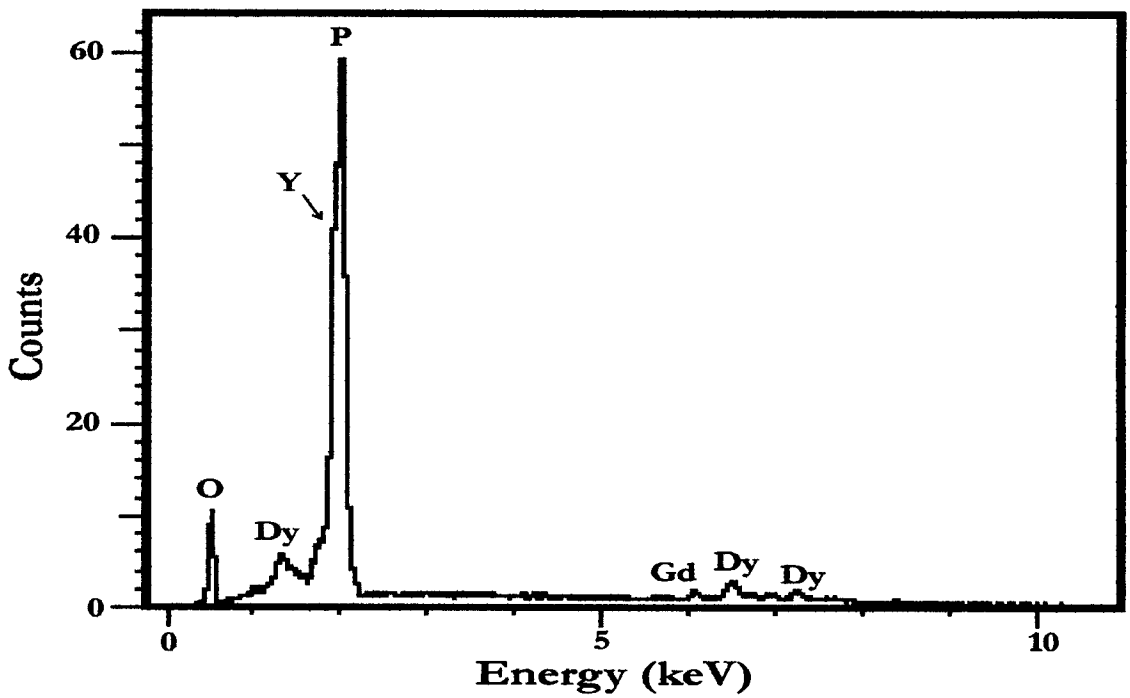

Figure 2.82: EDS of Dy-bearing xenotime from the main-mineralized zone.

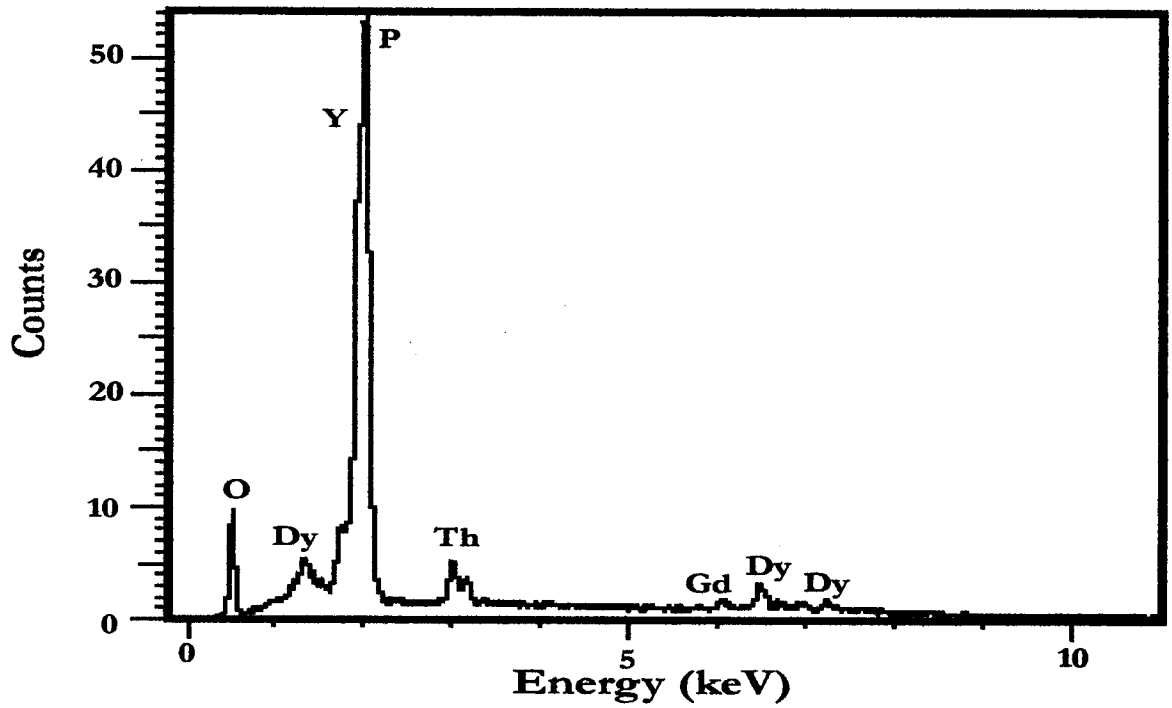

Figure 2.83: EDS of Dy- and Th-bearing xenotime from the main mineralized zone.

2.18 Zircon and Hydrated Calcium Zirconosilicate

A hydrated calcium zirconosilicate (HCaZr) is ubiquitous throughout the main mineralized zone. It occurs primarily as cryptocrystalline aggregates, which are commonly associated with phenakite, crichtonite and quartz. On a lesser scale, the HCaZr also forms concentric zones within large euhedral zircon grains, creating discontinuously zoned zircon crystals (Figure 2.84). Such zoned zircons were found almost exclusively within a calcite plus quartz groundmass. In thin section, the zoned zircons were large enough to be identified by the naked eye. Table 2.16 gives representative compositions of the zircon grains from the main mineralized zone.

The crystalline HCaZr is also closely-associated with unzoned zircon. Throughout all samples, small subhedral relict fragments of zircon can be distinguished within the HCaZr. These textures suggest that the HCaZr was formed by decomposition or metamictization of zircon. Although zircon is extremely stable during most hydrothermal alteration events, recent experiments have shown that the dissolution of zircon occurs at 650°C in 2M Na_2CO_3 solution, and precipitation of an Zr-Na-silicate phase forms on crystalline zircon at 700 °C (Rizvanova *et al.* 2000). Such alkaline-rich fluids may have interacted with the zircon during alkaline metasomatism of the main mineralized zone. Another possibility as to the origin of the HCaZr is related to the uranium and thorium content of the zircon. Radioactive decay of uranium and thorium damages the zircon structure and transforms the zircon to a metamict state. Alteration of zircon to the metamict state increases the solubility of zircon and the mobility of trace elements (Rizvanova *et al.* 2000). Despite experimental evidence of limited solid solution between zircon and its tetragonal isotypes thorite, coffinite and xenotime (Mumpton and Roy, 1961; Ushakov *et al.* 1999), data has been accumulating over the past few decades for the presence of intermediate compositions (Masau *et al.* 2000*b*). These culminated in the recent work of Förster (2001), who considers that zircon can incorporate as much as 32 wt.% ThO_2 and 8.7 wt.% UO_2, while thorite can contain up to 16.1 wt.% ZrO_2 and 23.3 UO_2 wt.% in evolved granites; indicative of significant solid solution between zircon, coffinite and thorite. As Förster (2001) states that compositions deviating from the end members were distinguished by low analytical totals (suggestive of significant H_2O), increased contents of P, Ca, Fe, Al and F, depletion of radiogenic Pb, and textures indicative

of alteration. These compositional extremes are thought to have taken place in connection with metamictization and severe fluid-mineral interaction, similar to the compositions, processes and textures proposed to have caused the formation of the HCaZr at Deadhorse Creek.

Selected compositions of the HCaZr are given in Table 2.17, an EDS of the HCaZr is shown in Figure 2.85 and Figures 2.86 and 2.87 illustrate the textures.

Table 2.16: Representative zircon compositions from the main mineralized zone.

	1	2	3	4	5	6	7	8
SiO_2	32.0	31.7	32.2	31.5	32.1	32.6	32.1	31.3
CaO	0.2	0.4	0.3	0.4	0.5	0.3	0.4	0.3
TiO_2	0.4	0.4	0.3	0.6	0.4	0.5	0.5	0.6
MnO	-	-	-	-	-	0.1	0.1	-
FeO	-	0.2	0.2	0.3	0.2	0.2	0.3	0.5
Fe_2O_3	0.1	0.1	0.1	0.1	0.1	0.1	0.1	0.1
ZrO_2	65.8	65.5	65.6	65.1	65.1	65.2	65.0	65.9
Hf_2O_3	1.6	1.4	1.6	1.6	1.8	1.6	1.2	1.5
Th_2O_3	0.2	-	-	0.3	0.1	-	0.1	-
U_2O_3	0.5	-	-	0.7	0.3	-	-	0.1
Totals	100.8	99.7	100.3	100.6	100.6	100.6	99.8	100.3

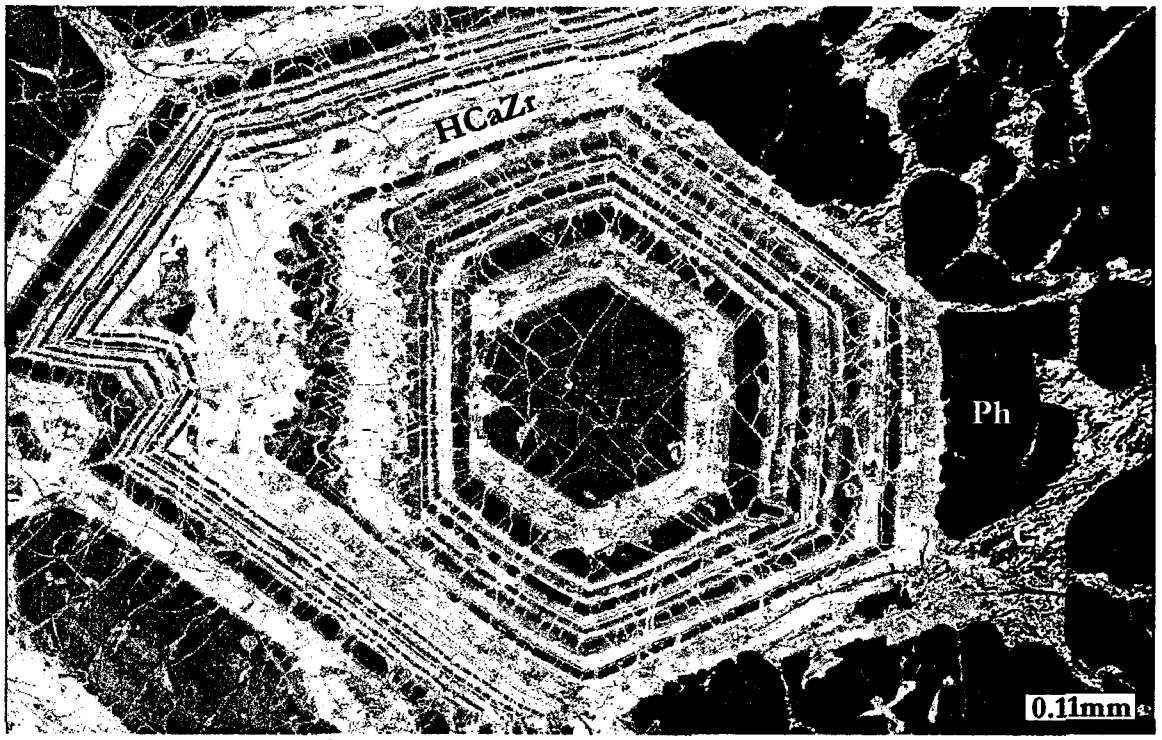

Figure 2.84: False-colored BSE-image of the zoned zircons (zircon = red, HCAZr = yellow) from the main mineralized zone. The groundmass consists of phenakite (Ph) cemented by calcite.

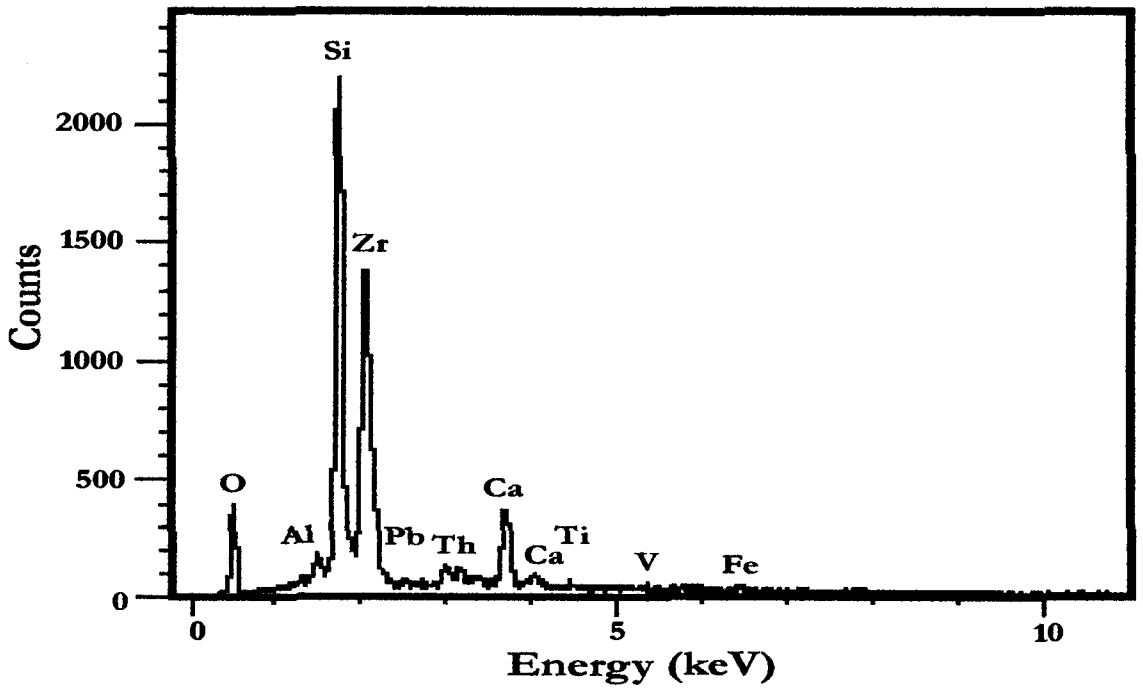

Figure 2.85: EDS spectrum of HCaZr from the main mineralized zone.

Table 2.17: Representative compositions of the HCaZr taken from the main mineralized zone.

	1	2	3	4	5	6	7	8
Al_2O_3	0.7	0.6	0.6	0.9	0.9	0.5	0.8	0.9
SiO_2	29.0	29.2	29.0	29.3	29.2	27.4	30.0	29.7
CaO	6.3	6.5	6.0	6.1	6.0	5.9	6.0	6.0
TiO_2	-	0.3	0.2	-	0.1	-	0.2	-
MnO	0.6	0.5	0.5	0.6	0.7	0.7	0.5	0.5
FeO	0.4	0.4	0.3	0.2	0.2	0.1	0.3	0.7
ZrO_2	41.5	42.3	41.8	41.8	42.1	43.5	42.9	42.5
HfO_2	1.0	1.1	0.3	0.9	1.1	0.9	0.8	0.6
ThO_2	-	0.3	-	0.1	0.6	0.4	0.6	0.8
UO_2	1.8	1.7	2.3	1.2	2.3	2.0	0.9	1.7
H_2O	18.7	17.1	19.0	18.9	16.8	18.6	17.0	16.6
Totals	100.0	100.0	100.0	100.0	100.0	100.0	100.0	100.0

Note: H_2O calculated by difference.

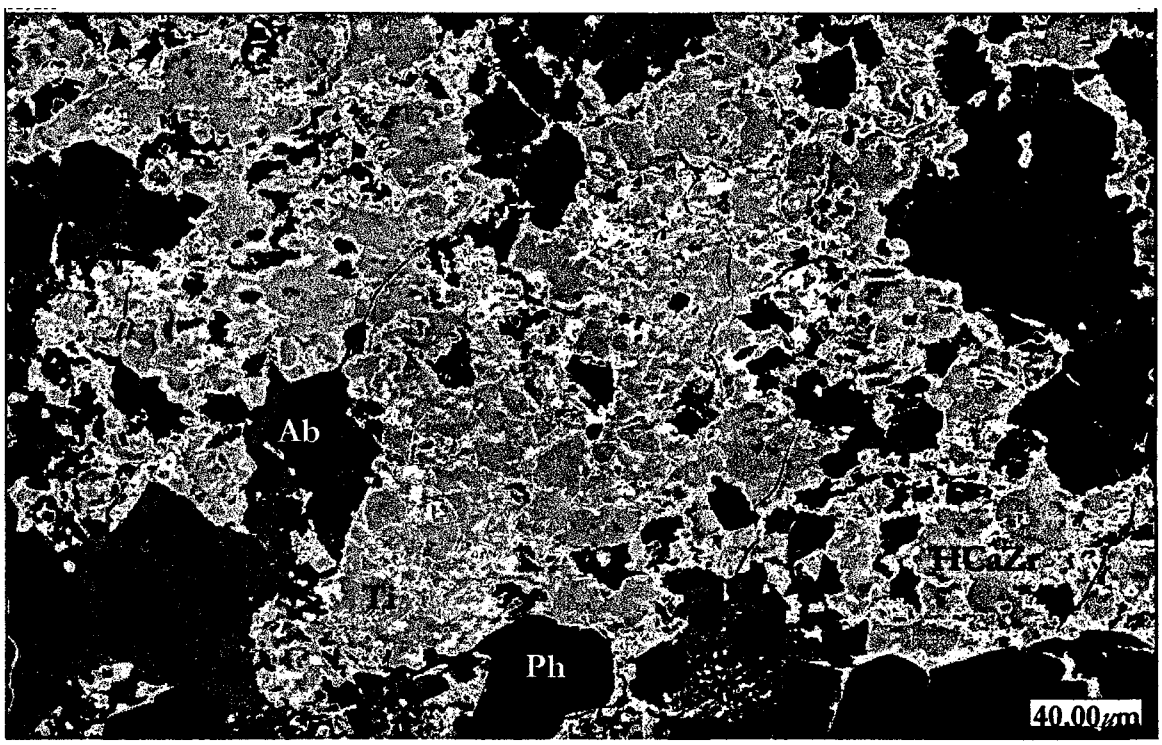

Figure 2.86: False-colored BSE-image of the hydrated calcium zirconosilicate (HCaZr), set in a potassium feldspar groundmass (light blue) with phenakite (Ph) and albite (Ab).

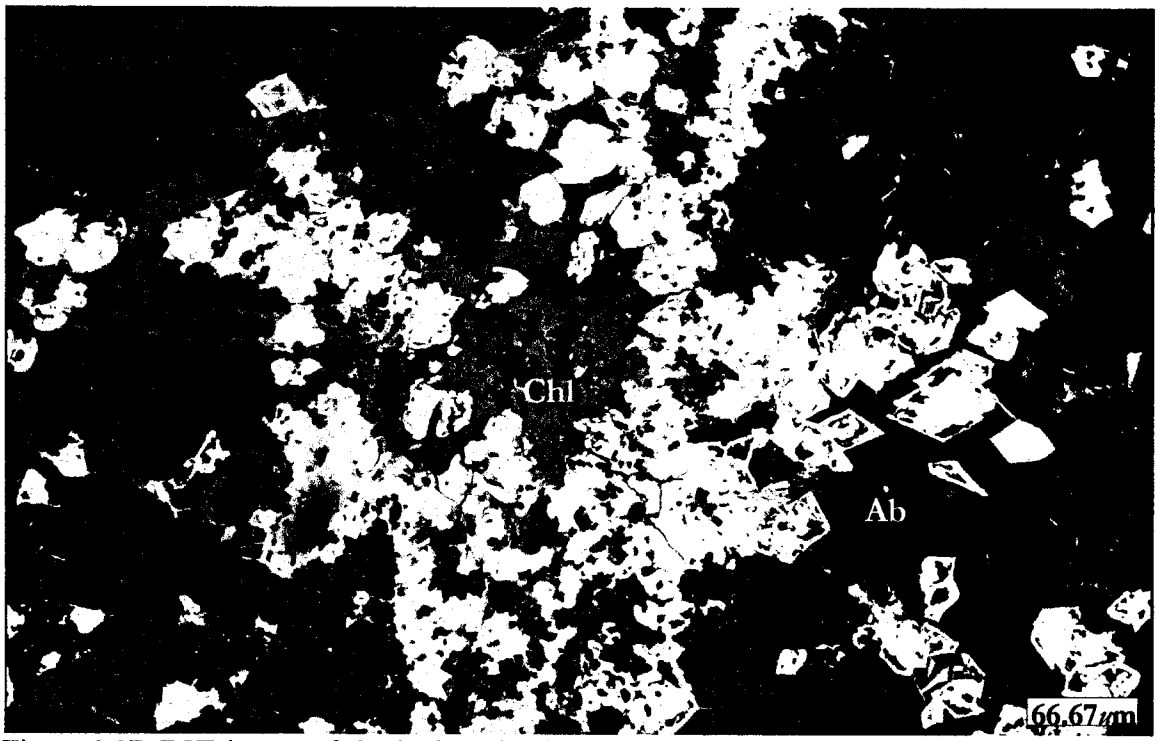

Figure 2.87: BSE-image of the hydrated calcium zirconosilicate that is pseudomorphic after zircon, and is set in an albite groundmass with V-bearing chlorite (Chl).

In addition to the compositions given in Table 2.17, selected grains of the HCaZr are enriched in ThO_2 and UO_2 where the mineral is associated with uraninite or thorite. As illustrated by Figure 2.88, ThO_2 and UO_2 are incorporated into the mineral at the expense of ZrO_2. The ThO_2 contents in the mineral reach a maximum of 23 wt.%., while UO_2 contents reach 29 wt.% before the phase become less hydrated and grades essentially into coffinite (82 wt.% UO_2). These compositions are listed in Table 2.18, and are plotted in an atomic percent Th-U-Zr ternary diagram in Figure 2.89. Images of the 'enriched' grains are shown in Figures 2.90 and 2.91. As Finch and Murakami (1999) point out, zircon is isostructural with both thorite and coffinite, indicating the potential of a solid solution between zircon and the actinide-dominated species. The uranium and thorium silicates form a complete series of anhydrous and hydrous compounds, with generalized formulas of $(Th,U)SiO_4$ and $(Th,U)SiO_4{*}nH_2O$ ($n<4$). The series is manifested in three minerals: thorite, the anhydrous end member with Th>U; thorogummite, the hydrous end member with Th>U; and coffinite, the hydrated and anhydrous end member with U>Th (Finch and Murakami, 1999). The data presented in Table 2.18 is indicative of an extensive solid solution between

metamict zircon and coffinite, and to a lesser extent, between zircon and thorite. The lack of intermediate members between coffinite and thorite is possibly a result of the grain associations before metamictization or metasomatism; zircons associated with thorite contain significant amounts of ThO_2, whereas those grains associated with coffinite incorporate UO_2.

As noted by Förster (2001), the relatively few experimental studies suggest that these enriched compositions are unlikely to be thermodynamically stable. Rather they represent metastable phases produced by residual melts or fluids containing abundant Th, U, Zr, Y and other elements that were mobilized during decomposition of other phases in the vicinity.

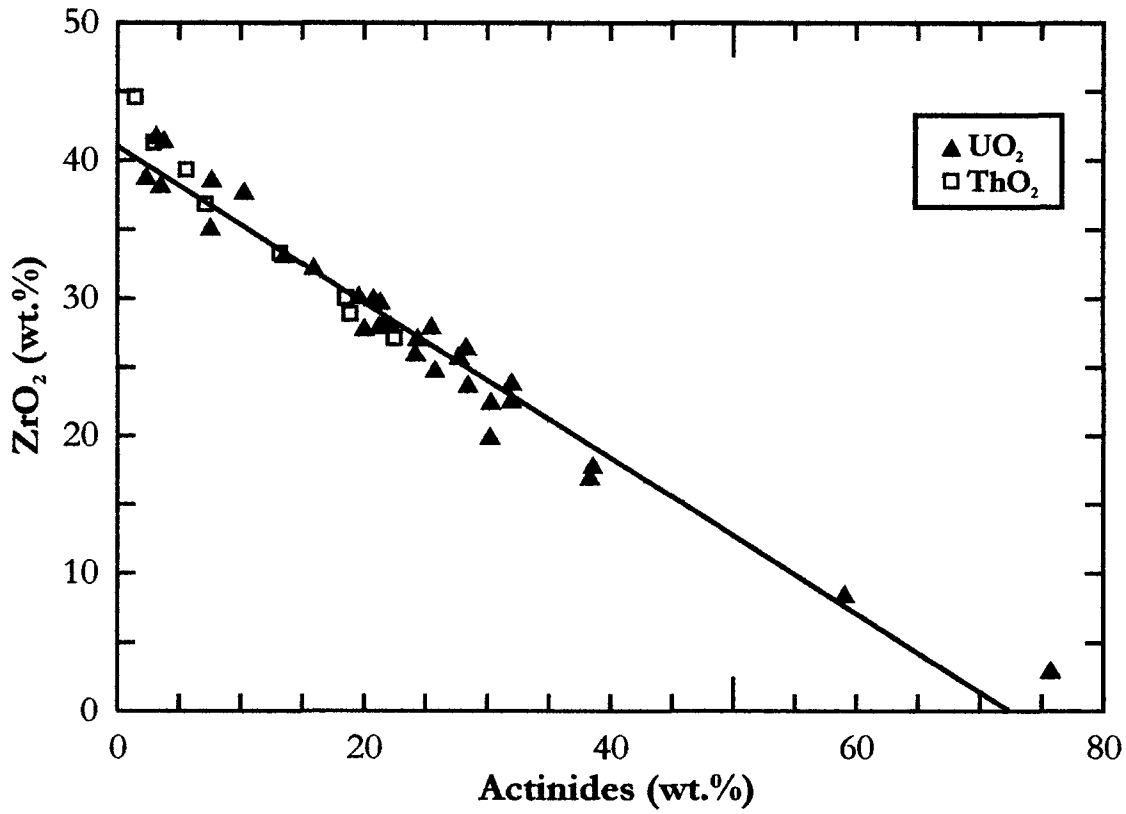

Figure 2.88: Weight percentage plot of ThO_2 and UO_2 versus ZrO_2, illustrating the negative correlation in the enriched HCaZr.

Table 2.18: Representative compositions of Th- and U-bearing HCaZr.

	1	2	3	4	5	6	7	8
Al_2O_3	1.2	1.3	1.4	0.9	0.8	1.7	1.1	0.6
SiO_2	28.3	28.5	30.7	24.6	24.8	25.4	19.0	7.8
CaO	8.5	8.2	8.4	7.8	8.6	8.5	6.5	4.4
TiO_2	0.2	0.1	0.1	-	0.2	-	0.2	0.1
V_2O_5	0.1	0.2	-	0.9	0.8	1.3	1.0	1.7
MnO	0.5	0.6	0.5	0.3	0.3	0.3	0.3	0.3
FeO	0.3	-	0.5	-	-	-	-	-
ZrO_2	**27.1**	**28.9**	**33.3**	**25.3**	**25.1**	**16.8**	**8.3**	**-**
BaO	0.2	0.5	0.3	-	0.1	1.4	2.6	2.8
ThO_2	**22.5**	**18.9**	**13.2**	**0.2**	**1.5**	**0.4**	**0.3**	**-**
UO_2	**0.9**	**1.1**	**0.9**	**29.7**	**27.1**	**38.3**	**59.1**	**81.6**
H_2O	10.2	11.7	10.7	10.3	10.7	5.9	1.6	-
Total	100.0	100.0	100.0	100.0	100.0	100.0	100.0	99.3

Note: the H_2O contents are calculated by difference.

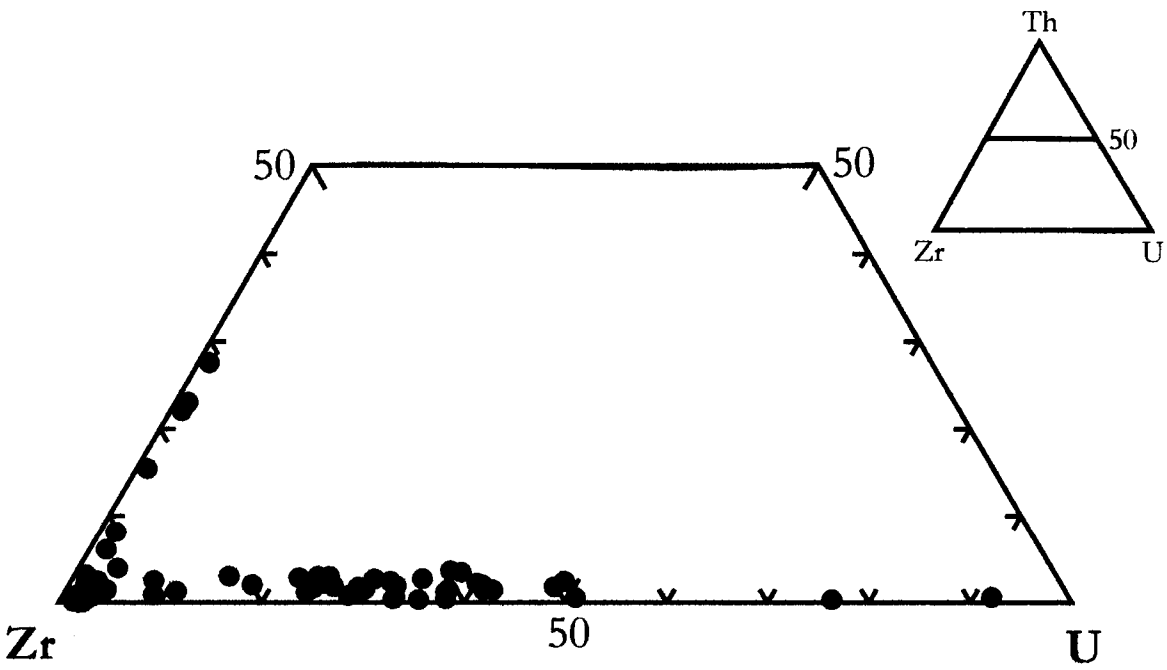

Figure 2.89: Composition of the 'enriched' HCaZr plotted in terms of atomic percent Th-Zr-U.

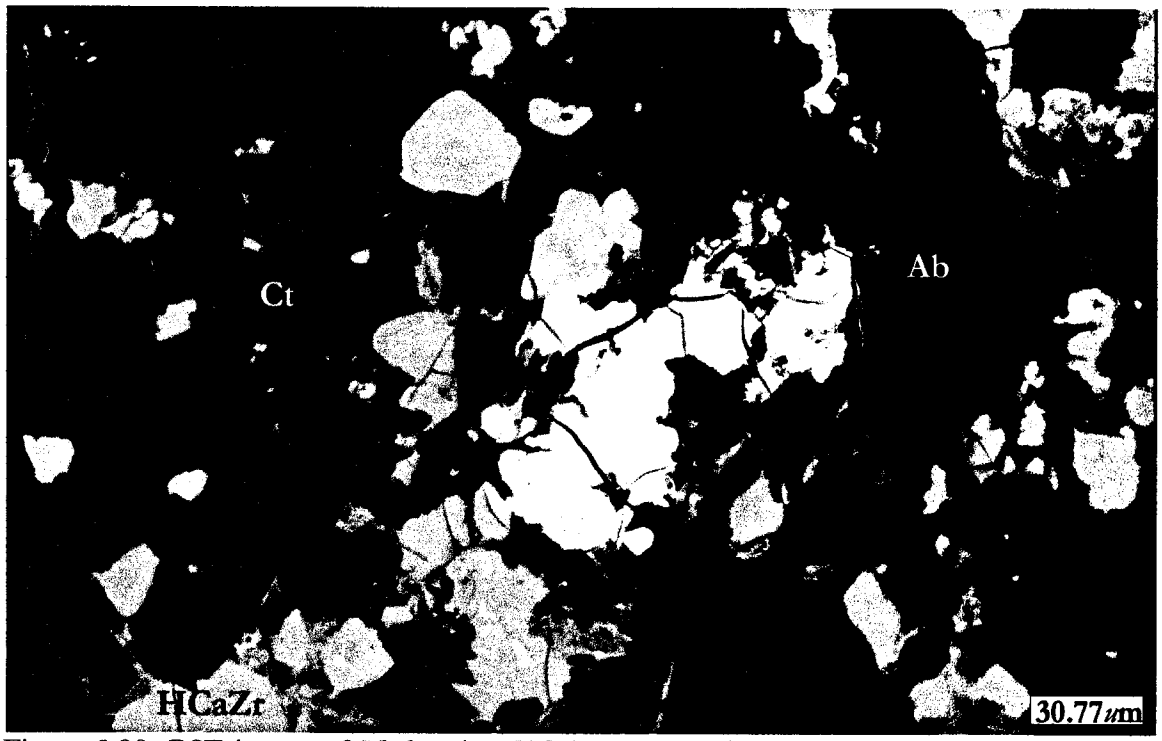

Figure 2.90: BSE-image of Th-bearing HCaZr. Increasing ThO_2 content represented by whiter colors. The groundmass consists of calcite (Ct) with albite phenocrysts (Ab).

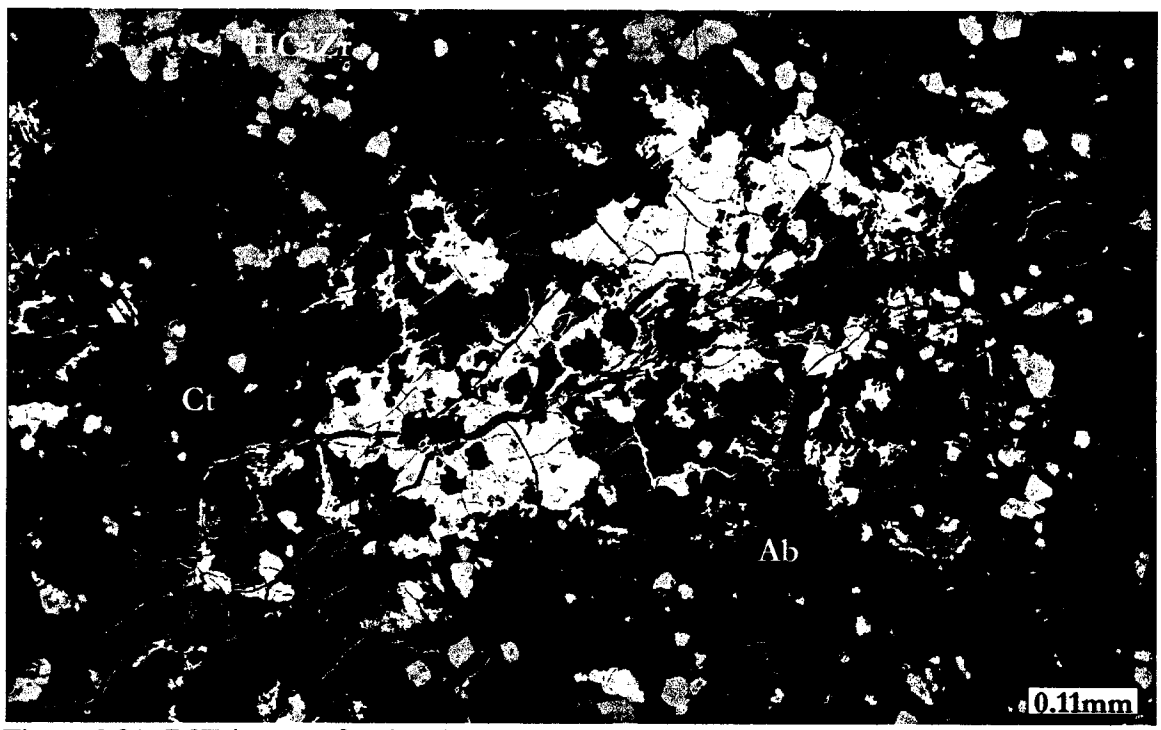

Figure 2.91: BSE-image of U-bearing HCaZr with increasing UO_2 content represented by whiter colors. Groundmass consists of calcite (Ct) with albite phenocrysts (Ab).

3.1 Diatreme Breccia

The diatreme breccia consists of comminuted rock debris cemented in place by secondary potassium feldspar and aegirine-augite (Figures 3.1 and 3.2). Attempts were made to identify mineral phases present in the original material, but only fragments of hematitized quartz and potassium feldspar could be identified conclusively. Although not quite as mineralogically complex as the main mineralized zone, approximately 31 mineral species were identified in the samples. While the majority of these phases are thought to represent 'primary' minerals formed during cementation of the rock debris, subsequent events have produced an array of usual phases such as barian feldspars, baotite and ilmenorutile.

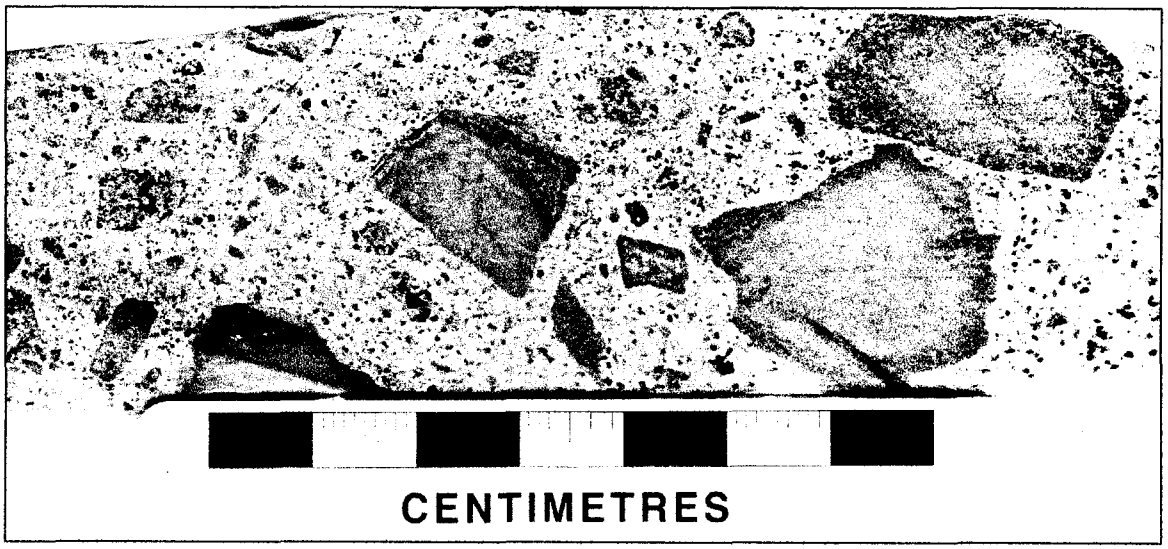

Figure 3.1: Photograph of hematitized quartz and potassium feldspar fragments cemented by the potassium feldspar groundmass.

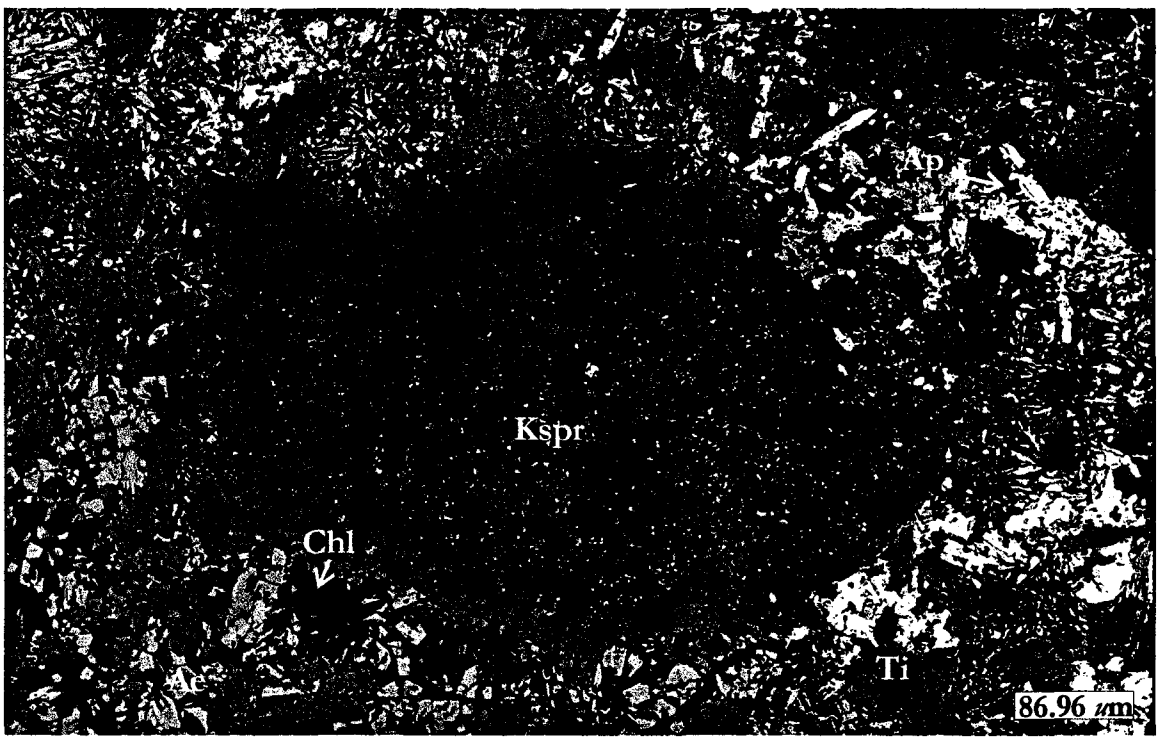

Figure 3.2: BSE-image of hematitized potassium feldspar fragment (Kspr) set in secondary potassium feldspar and aegirine-augite (Ae) and surrounded by titanite (Ti), apatite (Ap) and chlorite (Chl).

As noted above, potassium feldspar forms the groundmass of the breccia, creating a porous, interlocking mosaic of anhedral grains. The earliest of the accessory minerals to form were large, euhedral-to-subeuhedral grains of aegirine-augite and apatite (Figure 3.3). Whereas the aegirine-augite grains are relatively-intact, the larger apatite grains show some signs of corrosion. Compositionally, the apatite contains minor amounts of fluorine, strontium, cerium and iron (see section 2.8). Aegirine-augite is the dominant pyroxene composition, with only a minor percentage of the population trending towards the diopside end-member. Euhedral grains of enstatite were also found amongst grains of aegirine-augite near pore spaces. In addition to the angular fragments of quartz, smaller anhedral grains were found interstitial to the potassium feldspar groundmass. Similar textures found in the crosscutting carbonatite dike imply that this quartz (and the abundant biotite within the dike) may be related to thermal metamorphism associated with the intrusion of the Coldwell Alkaline Complex. The majority of the accessory phases are hosted in the potassium feldspar matrix; only small amounts of barite, titanite, thorite and zircon occur in quartz. The subeuhedral-to-euhedral grains of aegirine-augite do not host any other phases.

Figure 3.3: BSE-image of subhedral apatite (Ap) and aegirine-augite (Ae) set in potassium feldspar (Kspr).

The majority of the accessory phases exhibit anhedral habits, except for monazite-(Ce), baotite, and pyrite. Pyrite is the most abundant, commonly occurring as relatively large (up to 0.6 mm), rounded anhedral grains that are partially-altered to hematite (Figure 3.4). Zircon present within the breccia also shows signs of alteration to the hydrated calcium zirconosilicate found in the main mineralized zone. The resultant hydrated phase occurs as round, anhedral grains set in potassium feldspar. Minerals associated with zircon include monazite-(Ce) and hematite.

As in the main mineralized zone, monazite-(Ce) is the dominant rare-earth element bearing mineral, although it is present in greater amounts. In the breccia, it occurs in two habits: large, subeuhedral grains up to 0.1 mm in length; and smaller (~50 μm) anhedral grains interstitial to aegirine-augite. Although the larger grains are subhedral in habit, they are intensely fractured and are locally concentrated in the breccia, forming enriched zones.

Figure 3.4: BSE-image of anhedral pyrite partially-altered to hematite, set in potassium feldspar (dark) together with augite-diopside (light gray).

Molybdenite is present in trace amounts within the breccia and occurs as subhedral grains set in potassium feldspar interstitial to subhedral augite-diopside grains. Most crystals are lath-like in habit, reaching 40 μm in length and were impinged by augite-diopside (Figure 3.5). Typically, molybdenite occurs as an accessory phase in granites, pegmatites, aplites, quartz veins in silicified granites and associated with porphyry copper deposits. In several of these occurrences, it is associated with scheelite (Klein, 2002). Although it was not found in direct contact with the molybdenite grains, scheelite was found within the samples, in the same potassium feldspar plus augite-diopside groundmass. Ideally, these phases should be associated with the granitic fluids that initially formed the main mineralized zone, but neither mineral was found within the main mineralized zone. Other possible sources include the country rocks or quartz veins that were incorporated into the breccia during intrusion.

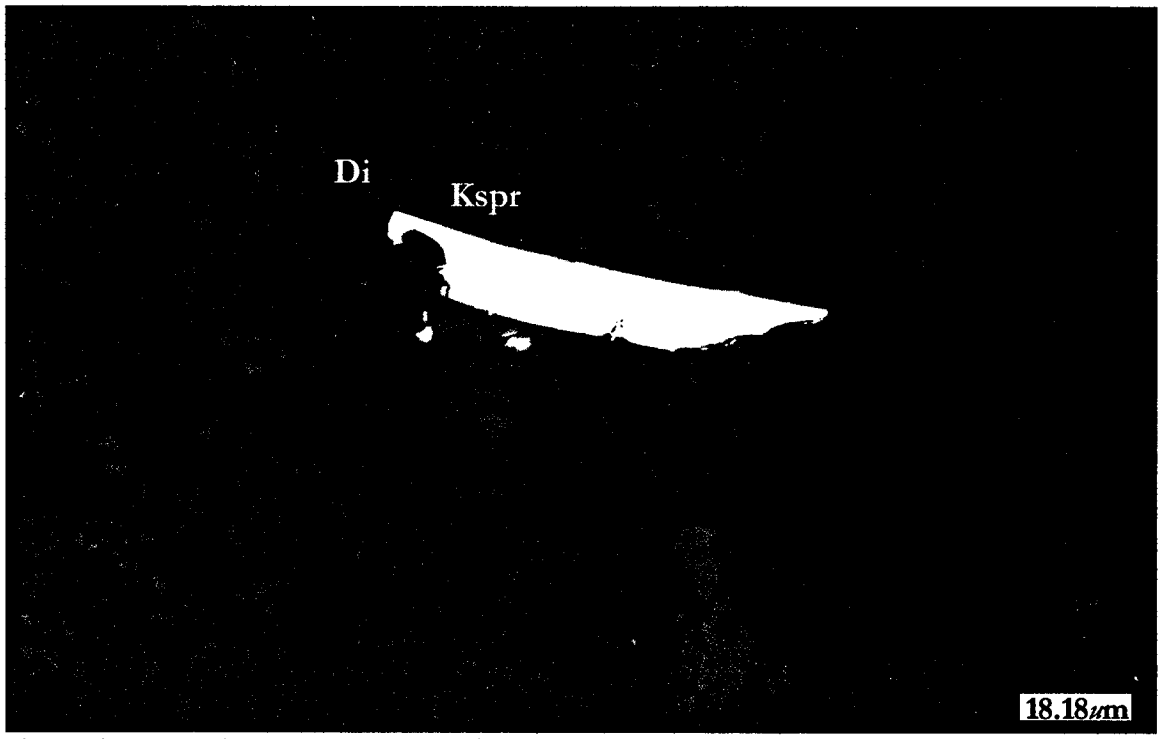

Figure 3.5: BSE-image of molybdenite grain set in potassium feldspar and impinged by augite-diopside grains.

The 'unmineralized' diatreme is host to several barium minerals: baotite, barian feldspars and barite. Interestingly, baotite and the barian feldspars occur in greater concentrations than the barite and are found only in the breccia. Baotite, a rare Ba-Ti-Nb chlorosilicate, occurs as anhedral grains poikilitically-enclosed in: titanite; titanite plus rutile; and as an exsolved phase with Mn-ilmenite and ilmenorutile within a rutile host (Figure 3.6). The rutile and titanite hosts are distinguished from the exsolved phases by their stoichiometric composition. Mn-ilmenite typically contains less than 23 wt.% MnO, while the baotite is close to the ideal formula $[Ba_4(Ti,Nb)_8Si_4O_{28}Cl]$, with minor amounts of calcium, iron and vanadium. The host rutile or titanites occur interstitial to the aegirine-augite grains within the porous potassium feldspar matrix. Thorite is commonly associated with exsolved baotite hosted by rutile, forming anhedral, fractured grains generally less than 0.1 mm in diameter.

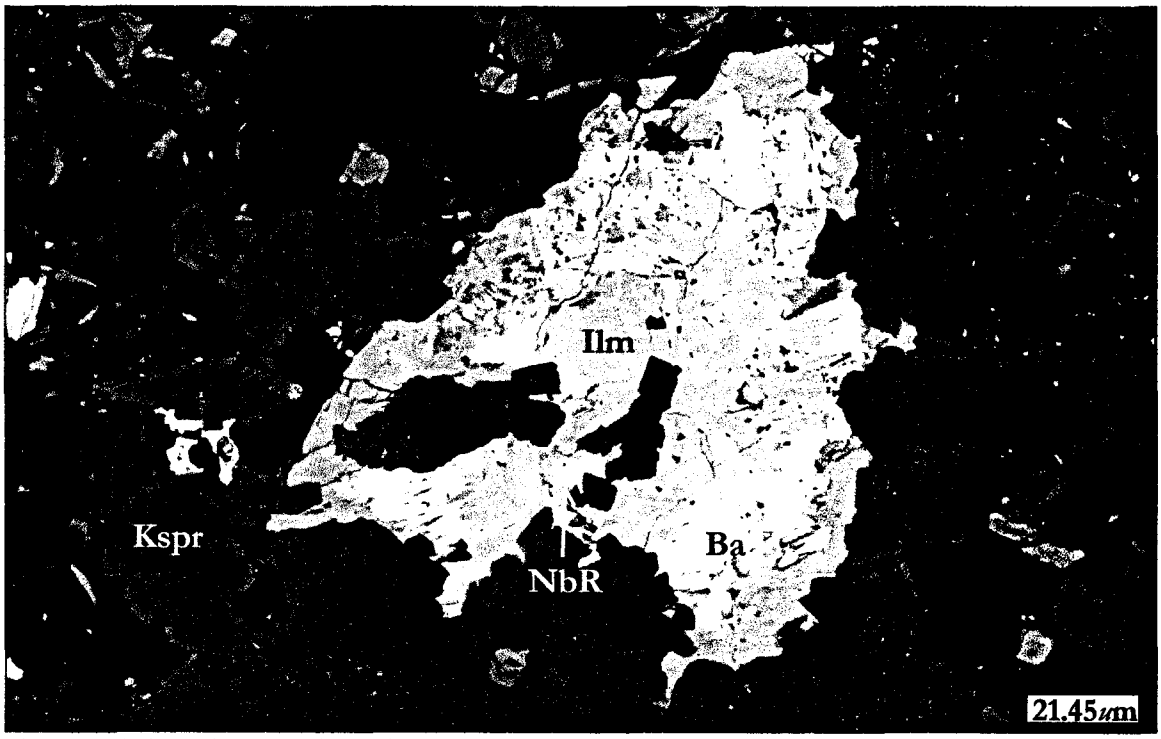

Figure 3.6: BSE-image of exsolved baotite (Ba) and ilmenorutile (NbR) set in a Mn-ilmenite host (Ilm). Also shown is the porous potassium feldspar (Kspr).

The barian feldspars, when expressed in terms of the ternary system celsian-albite-orthoclase, exhibit a range in composition from $Cn_{0\text{-}86}Ab_{0\text{-}11}Or_{13\text{-}100}$. The barium-enrichment occurs in zoned, angular grains of feldspar cemented in place by the stoichiometric potassium feldspar groundmass and augite-diopside grains. As illustrated by Figure 3.7, the grains are aggregated in a fashion that is suggestive of interaction with a wave of Ba-enriched fluids acting upon the otherwise stoichiometric potassium feldspar. Closely associated with the barian feldspars are small anhedral grains of barian biotite, containing approximately 3 wt.% BaO. Larger grains of biotite concentrated near pores spaces in the breccia are devoid of any barium enrichment.

Figure 3.7: BSE-image of the barian feldspars (white) set in a potassium feldspar and augite groundmass.

The least abundant barium-bearing mineral present in the breccia is barite, which occurs in very minor amounts (<5 modal %) as small (~10 μm), anhedral grains set in the potassium feldspar groundmass. On the basis of abundance, habit and texture, the barite in the diatreme breccia is considered to represent 'primary' mineralization in the formation of the breccia.

The porous nature of the breccia also permitted circulation of hydrothermal fluids enriched in Fe, Cu and S. Interaction of these fluids with the diatreme breccia resulted in the formation of banded vugs filled by chalcopyrite and hematite interspersed with minor amounts of silica and galena (Figure 3.8).

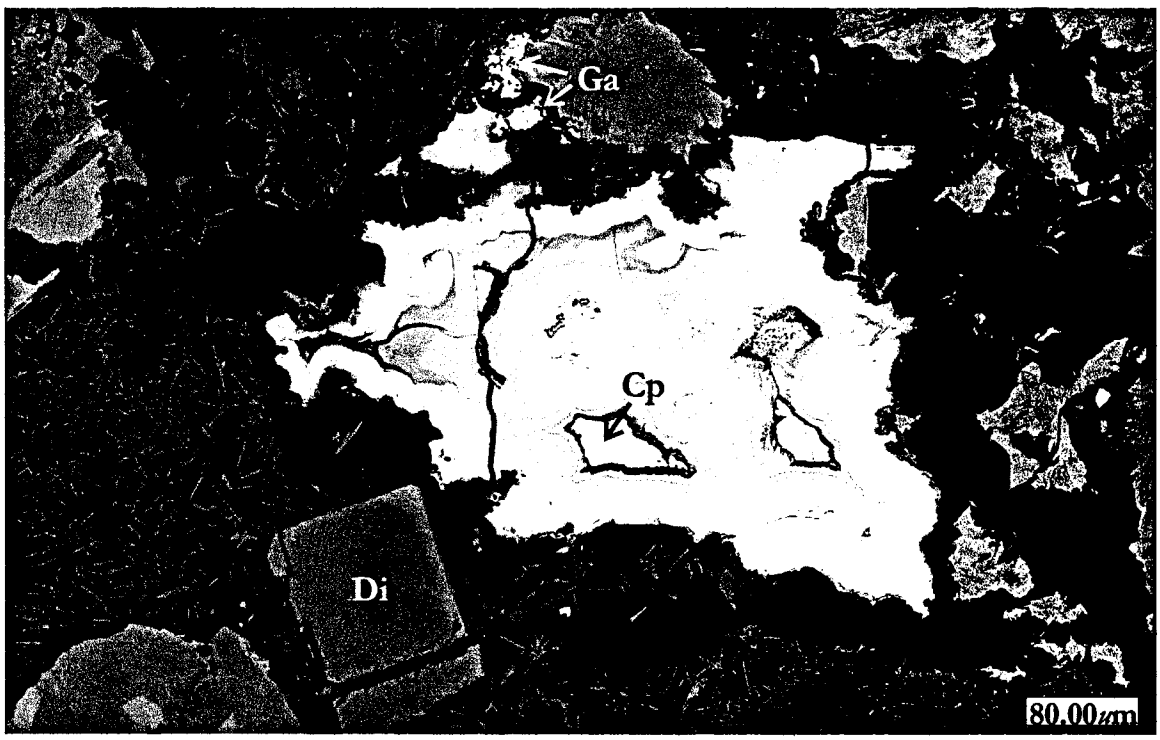

Figure 3.8: BSE-image of banded hematite-chalcopyrite (Cp) in a pore space within the breccia. Also shown: needles of augite-diopside; euhedral tabular augite-diopside (Di); and galena (Ga).

To facilitate discussion, the paragenetic relationships are summarized in Figure 3.9. Whereas the majority of the minerals are considered to represent "primary" mineralization formed during the cooling of the igneous breccia, several of the more exotic species are attributed to thermal metamorphism. During the metamorphism, fluids enriched in Ba, Nb and Si might have traveled along the strike of the foliation of the country rocks and reacted with the parent phases to produce the barian feldspars, Ba-biotite, baotite and ilmenorutile. Although similar vanadium and barium minerals have been described by Pan and Fleet (1991,1992), the authors propose that these phases occurred as a result of regional metamorphic events that occurred between 2672-2670 Ma at 450-500°C and were remobilized during later hydrothermal events (Pan and Fleet, 1995). Unfortunately, these ages predate the Deadhorse Creek Complex, although subsequent thermal metamorphism associated with the Coldwell Alkaline Complex may have remobilized these elements. For a complete listing of minerals present within the breccia and approximate modal percentages, refer to Appendix C.

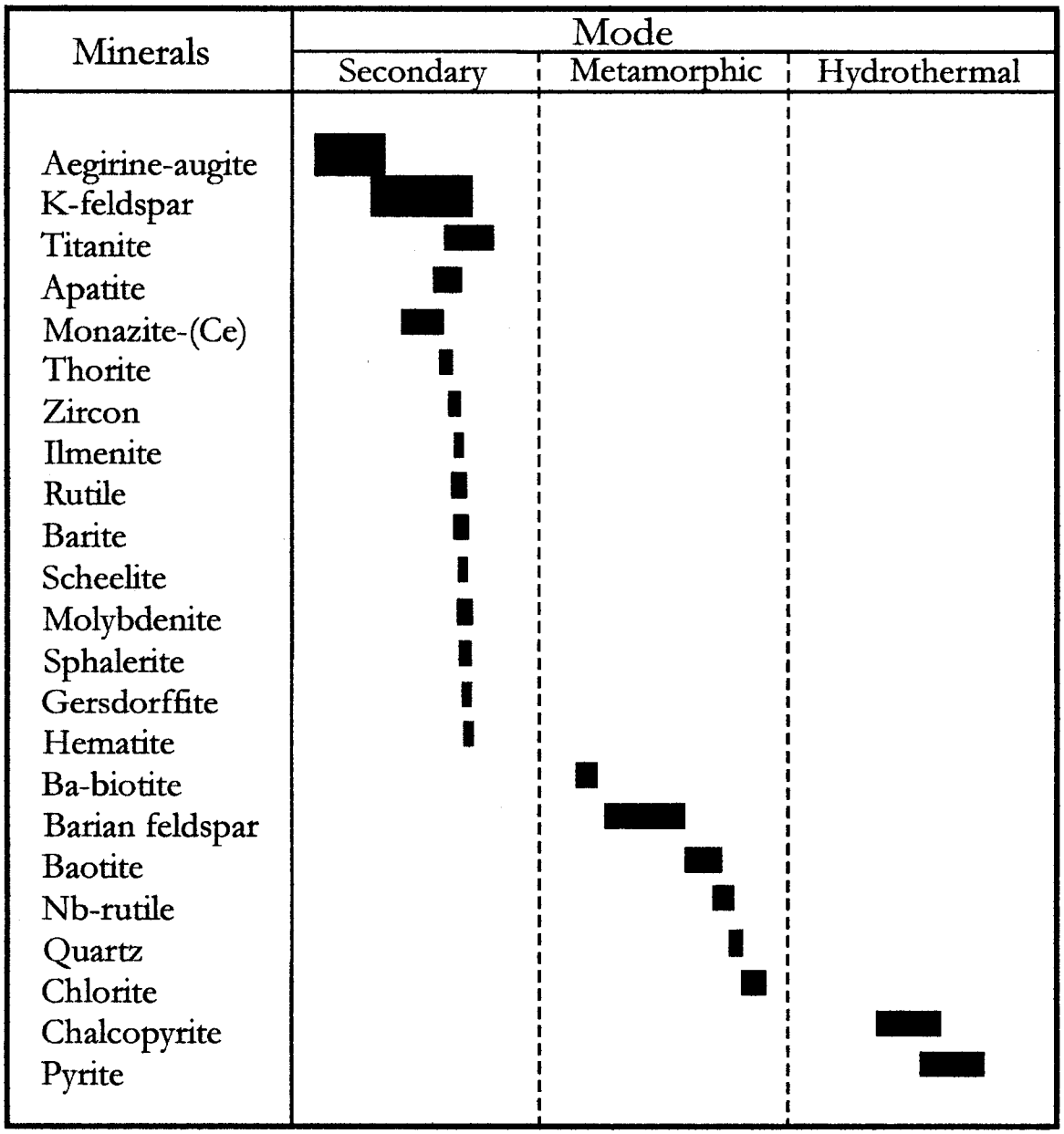

Figure 3.9: Generalized paragenetic scheme for the Deadhorse Creek diatreme breccia.

3.2 Main Mineralized Zone

At Deadhorse Creek, the main mineralized zone is emplaced in the diatreme breccia, which is situated along a proposed fault system, providing a plumbing system for the mineralizing fluids (Sage, 1982; Smyk *et al.* 1993; Platt and Mitchell, 1996). Initial investigations indicated that the mineralogy of the three geological units was diverse, signifying that the three units represented three separate events. The chondrite-normalized REE distribution patterns further supported this initial hypothesis (Figure 1.4). Further mineralogical investigation of the main mineralized zone revealed an extremely complex mineralogy with at least 54 distinct mineral species identified. Four events were involved in the formation of the main mineralized zone, in order, these are: intrusion of A-type granitic fluids, alkaline metasomatism, thermal metamorphism due to the emplacement of the Coldwell Complex, and supergene mineralization.

The main mineralized zone consists predominantly of a granitic mineral assemblage: potassium feldspar, albite, quartz-(I), together with calcite. In addition, phenakite and an unknown hydrated calcium zirconosilicate can be considered as significant minor minerals, which form 10-15 modal % of the unit, but locally can form up to 80 volume % of the sample.

The earliest of these phases to crystallize was albite, which commonly forms euhedral platy grains, reaching 0.5 mm in length (Figure 3.10). For the most part, these euhedral grains contain the least amount of accessory minerals and are set in a quartz-(I), potassium feldspar or calcite matrix. Later, anhedral albite grains are host to notably more accessory mineralization. However, both albite populations combine to make approximately 35 modal % and are essentially stoichiometric $NaAlSi_3O_8$ in composition, with only trace amounts of iron and potassium detected (<0.3 wt.%). Next to crystallize was potassium feldspar and quartz-(I). Both of these phases are major hosts of similar accessory minerals, are typically anhedral in habit and each form approximately 20 modal % of the rock. The potassium feldspar and quartz are believed to have formed at approximately the same time, as the potassium feldspar occurs interstitial to quartz grains and fragments in certain sections. Early-formed quartz-(I) is not to be confused with the late-stage quartz-(II) veins and vein-breccias that are generally barren of any accessory mineralization, except for large anhedral

phenakite crystals and tiny euhedral barylite grains. The final major mineral to crystallize was calcite, forming approximately 5 modal % of the rock. This phase is the major host of the accessory mineralization within the complex and occurs interstitial to the albite, potassium feldspar and quartz-(I). The complex is also host to late-stage calcite veinlets that are not related to the above 'primary' calcite, but rather weathering processes.

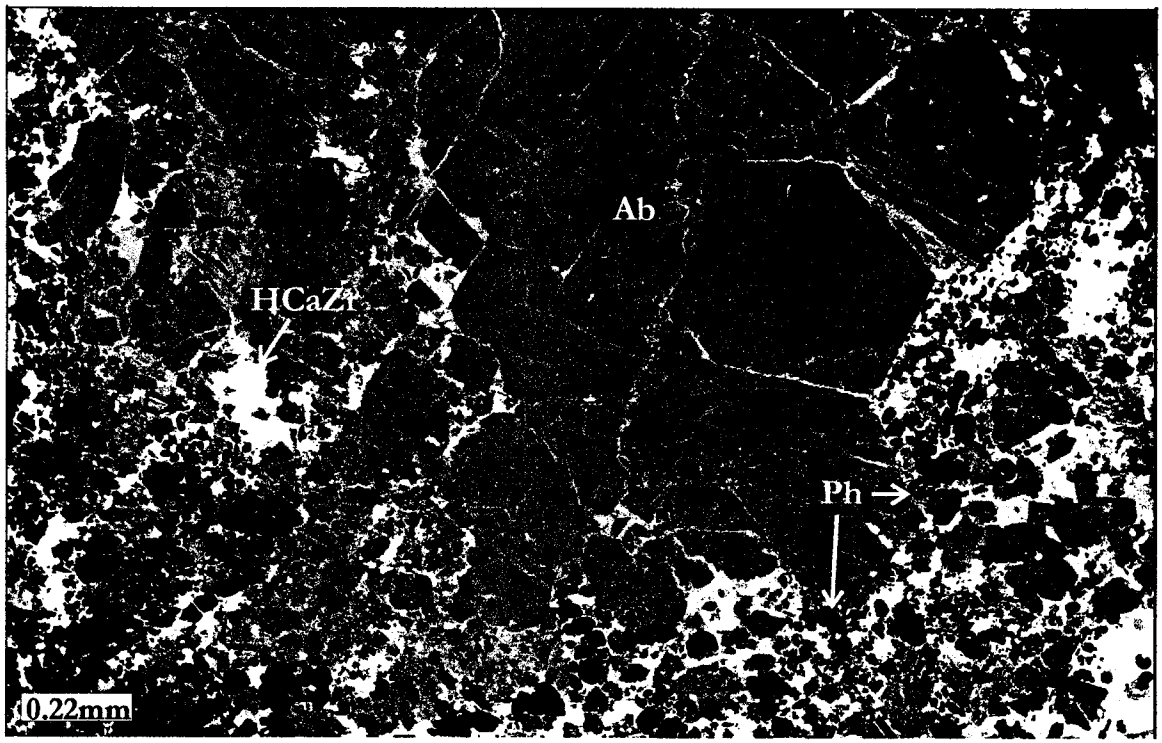

Figure 3.10: BSE-image of a platy albite grain (Ab) surrounded by phenakite (Ph) and the hydrated calcium zirconosilicate (HCaZr).

Phenakite is the most abundant accessory mineral within the main mineralized zone and occurs in two habits. Macroscopic phenakites occur as large, fractured, radiating, euhedral grains set in a quartz-(II) groundmass and commonly reaching several millimeters in length. The second habit of phenakite commonly occurs close to the radiating grains as anhedral, rounded grains, some of which have broken off the radiating grains. When not found in proximity to the radiating grains, the anhedral phenakite aggregates in large patches that are cemented by calcite and apatite. Associated minerals include: quartz-(II); a hydrated calcium zirconosilicate; and calcite. Due to extreme localized enrichment, it was possible to conclusively identify the phenakite by powder X-ray diffraction (refer to Figure 2.40 on page 58). Interestingly, the quartz-(II) associated with phenakite contains very little-to-no

accessory mineralization. As shown in Figure 3.11, most of the accessory phases are hosted within the calcite groundmass. The phenakite and associated barren-quartz (quartz-II) are considered to be derived from the same granitic fluids that generated the major rock-forming minerals; thereby implying that the overall assemblage represents late differentiates of granitic magma.

Despite the abundance of phenakite, barylite was the only other beryllium-bearing mineral identified within the complex. Barylite occurs as small (<70 μm in length), euhedral platy-to-acicular grains set entirely in quartz-(II). Unfortunately, the rarity of this mineral precluded identification by X-ray diffraction. Rather, the beryllium contents were determined by difference and agree with published data (e.g. Petersen *et al.* 1991). Although there are no other phases directly associated with the barylite grains, they form preferentially along fractures within quartz-(II), signifying a genetic association with phenakite.

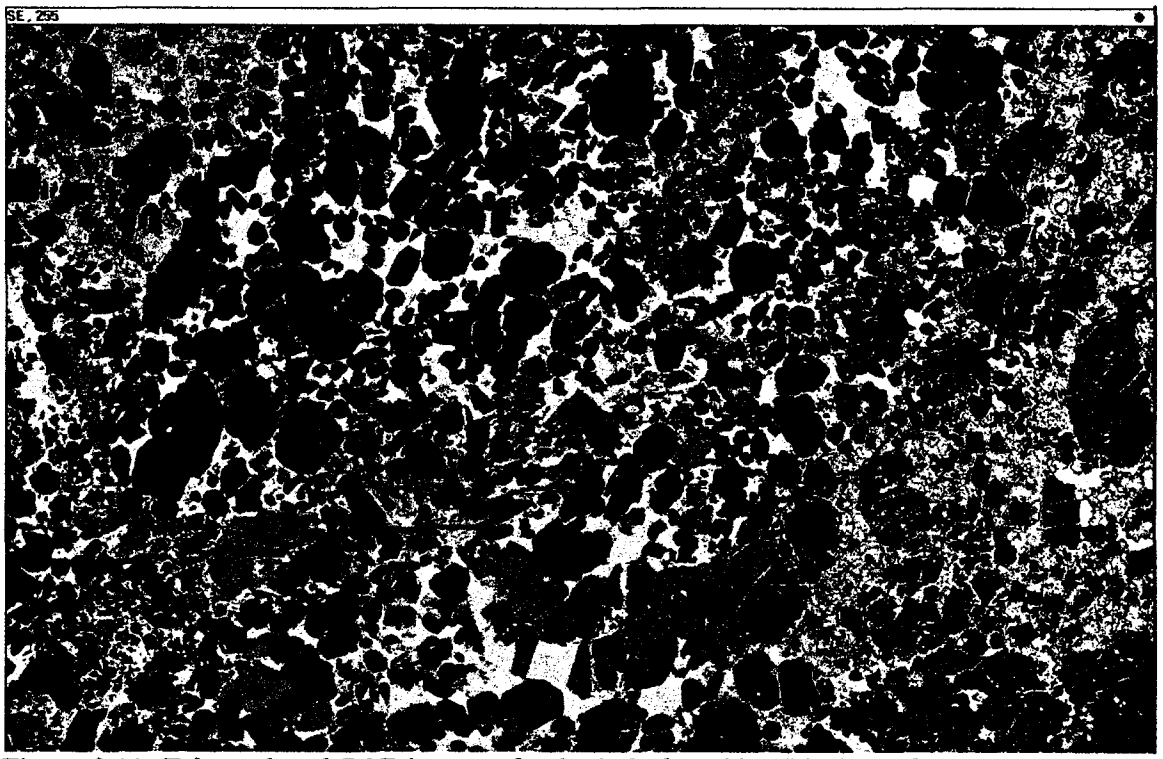

Figure 3.11: False-colored BSE-image of anhedral phenakite (black) and quartz (dark blue) cemented by calcite (light blue). Also shown: the hydrated calcium zirconosilicate (pink); apatite (yellow-green) and thorogummite (white).

The abundant hydrated calcium zirconosilicate appears to have formed by the decomposition or metamictization of zircon. Originally, the phase was identified within concentric zones in euhedral zircon grains (Figure 3.12). However, further investigation led to the identification of large patches of the cryptocrystalline phase, within the groundmass. In these, fragments of the relic zircon can be clearly distinguished within the host (Figure 3.13). Other images (such as Figure 2.88), demonstrate that the phase is pseudomorphic after euhedral zircon. The zoned zircons are preferentially-located in a calcite plus quartz and phenakite matrix, whereas the hydrated calcium zirconosilicates are situated within albite and calcite. Minerals associated with the hydrated calcium zirconosilicate include: uraninite; an unidentified Ca-Mn-silicate; thorite; and thorogummite.

An unidentified, hydrated Ca-Mn-silicate forms along the grain boundaries of a few grains as a reaction product of the hydrated calcium zirconosilicate. This rare unidentified phase is clearly replacing the hydrated calcium zirconosilicate, which is hosted by an albite groundmass veined by calcite (Figure 3.14). Although attempts were made to locate further examples of this replacement phase, only three occurrences were recognized. As a result, few analytical data were acquired along with an energy-dispersion X-ray spectrum. Hydration is assumed due to the consistently low analytical totals in the range of 86.9 to 88.5 wt.%. Associated phases include the hydrated calcium zirconosilicate, thorium, albite and calcite.

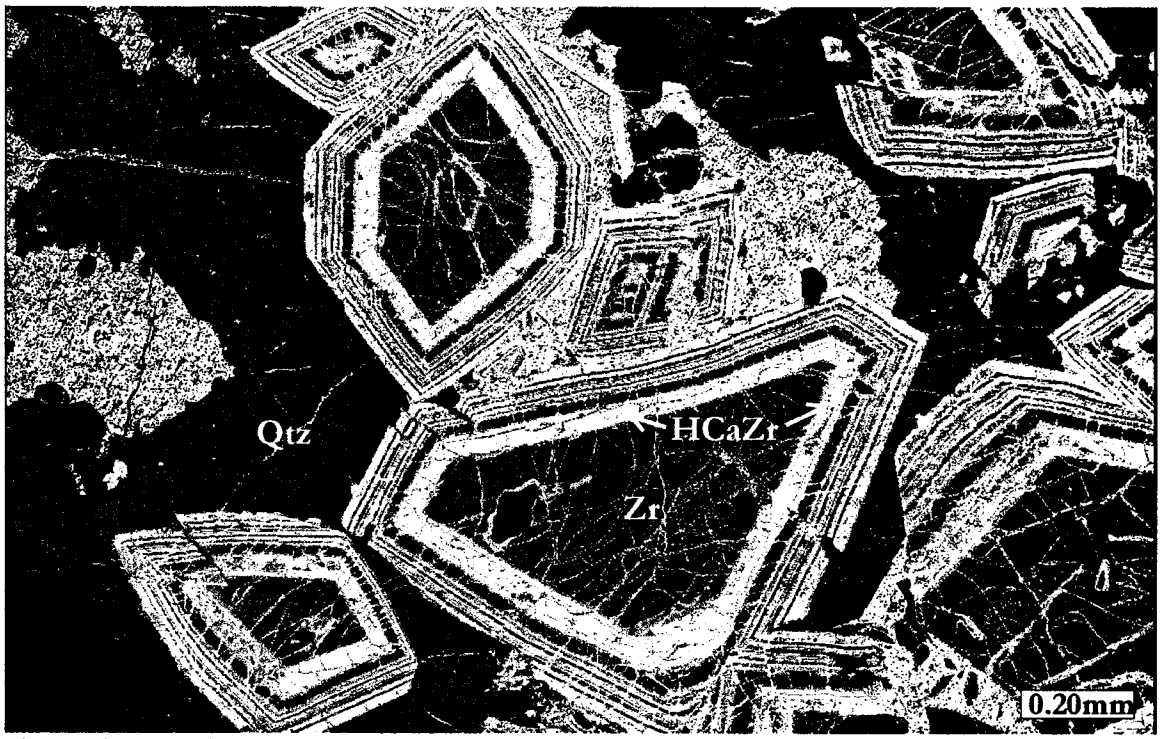

Figure 3.12: False-colored BSE-image of the hydrated calcium zirconosilicate (HCaZr) forming concentric zones within macroscopic zircon grains (Zr). The groundmass consists of quartz (Qtz) and calcite (Ct).

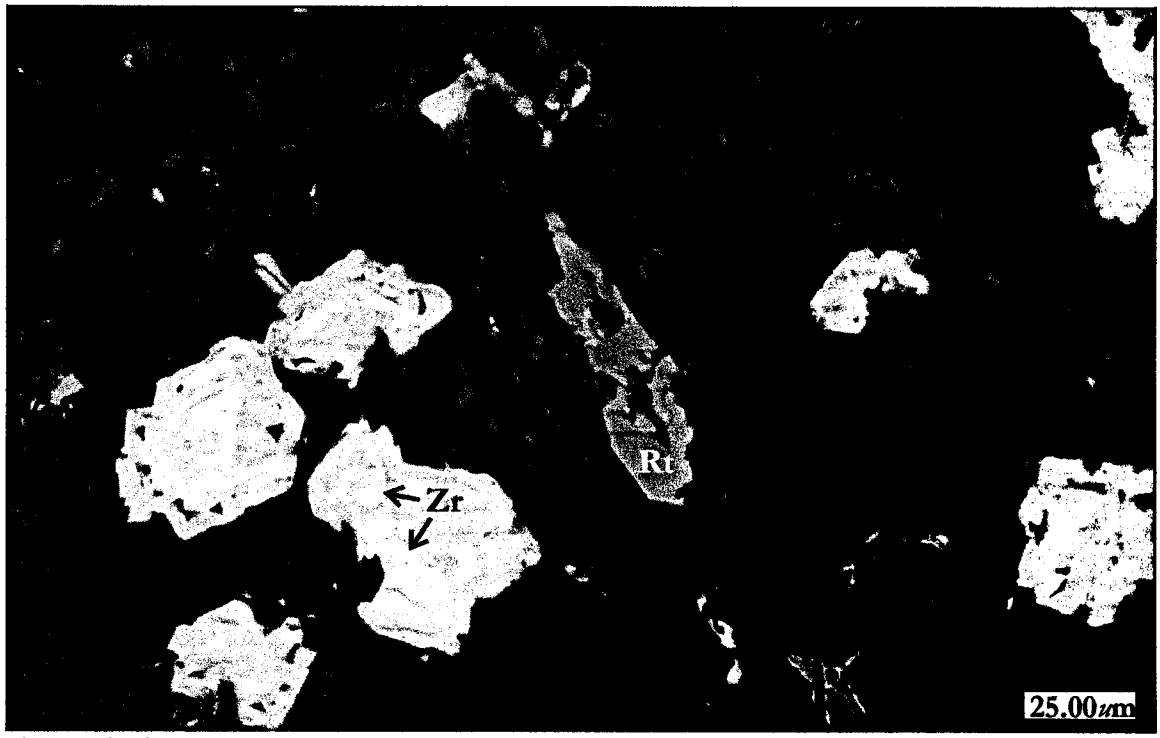

Figure 3.13: BSE-image of remnant zircon grains (Zr) set in the hydrated calcium zirconosilicate (HCaZr) and a V-rich rutile (Rt), all set in quartz.

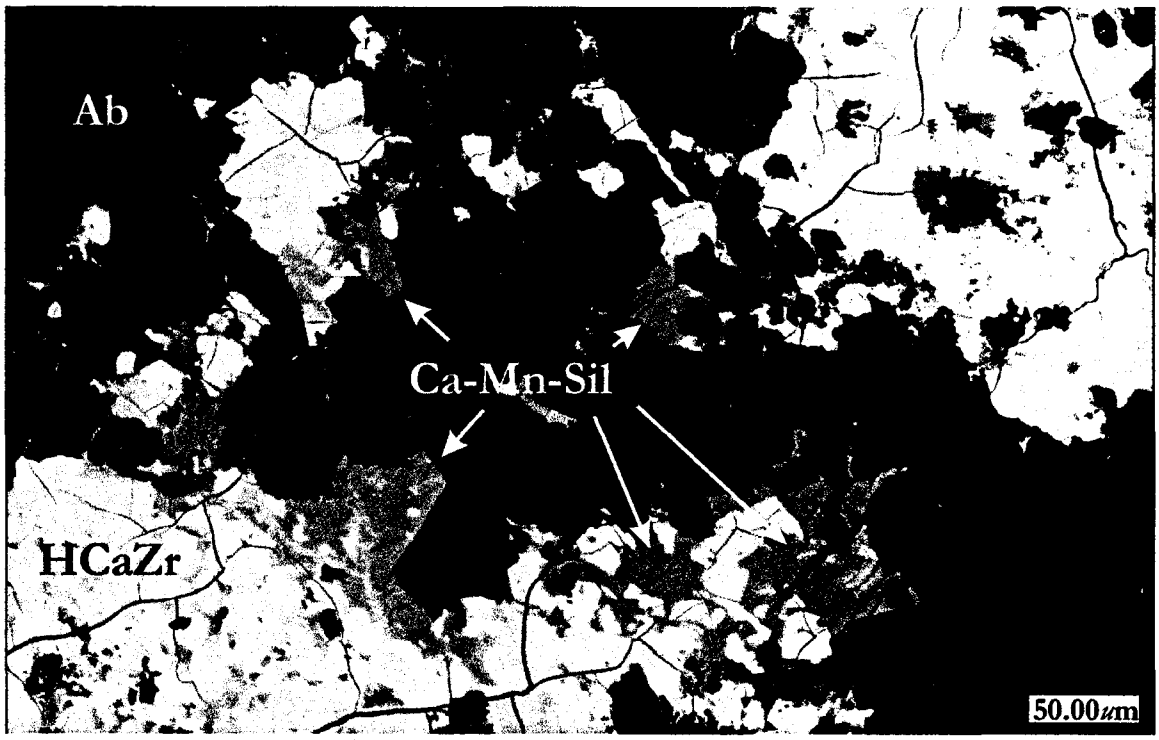

Figure 3.14: BSE-image of Ca-Mn-silicate forming as reaction product along the grain boundary of the hydrated calcium zirconosilicate (HCaZr).

Excluding hematite, which is pervasive throughout the complex, rutile is one of the more common oxide minerals within the main mineralized zone. It occurs in two generations, which are represented by differing compositions and three distinct habits; all of which are preferentially set in a calcite groundmass. The earliest generation of rutile consists of essentially stoichiometric TiO_2 forming large, corroded lath-like grains partially altered to titanite. The second generation of rutile is distinct due to the enrichment in niobium and vanadium and a smaller, anhedral habit. Due to the enrichment (up to 29.3 wt.% Nb_2O_5 and 10.5 wt.% V_2O_3), these grains are best termed ilmenorutile. The minor Cr contents and Nb-enrichment are similar to those of rutile described from xenoliths in the Orapa kimberlite (Tollo and Haggerty, 1987). The vanadium enrichment however, is unique to the Deadhorse Creek rutile. These grains occur in direct contact with the earlier rutile laths, commonly mantling relict TiO_2 (Figure 3.15). The third habit of rutile within the main mineralized consists of nodules of intergrown rutile and ilmenite, forming a coarse trellis interspersed with minor titanite. The rutile is essentially pure TiO_2, whereas the ilmenite contains minor amounts of MnO (3-4 wt.%). The first two habits are associated with, crichtonite, hematite, titanite and occur in calcite. Unfortunately, nodules of intergrown rutile, ilmenite and

titanite were only identified in two samples. In both instances, the nodules occur in a fractured potassium feldspar grain hosted in quartz.

Crichtonite, which is closely associated with rutile, is also set in a calcite groundmass. The mineral occurs primarily as large (~100 μm in length) subhedral-to-euhedral, fractured grains, which commonly display atoll-textures. The phase also occurs as smaller anhedral grains, generally less than 10 μm. in length. In common with rutile, crichtonite is preferentially set in a calcite matrix, which contains grains of anhedral-to-euhedral fluorapatite, albite and the hydrated calcium zirconosilicate. Due to the unique enrichment in vanadium (up to 15.4 wt.%), this phase is best termed a vanadium-rich analogue of crichtonite.

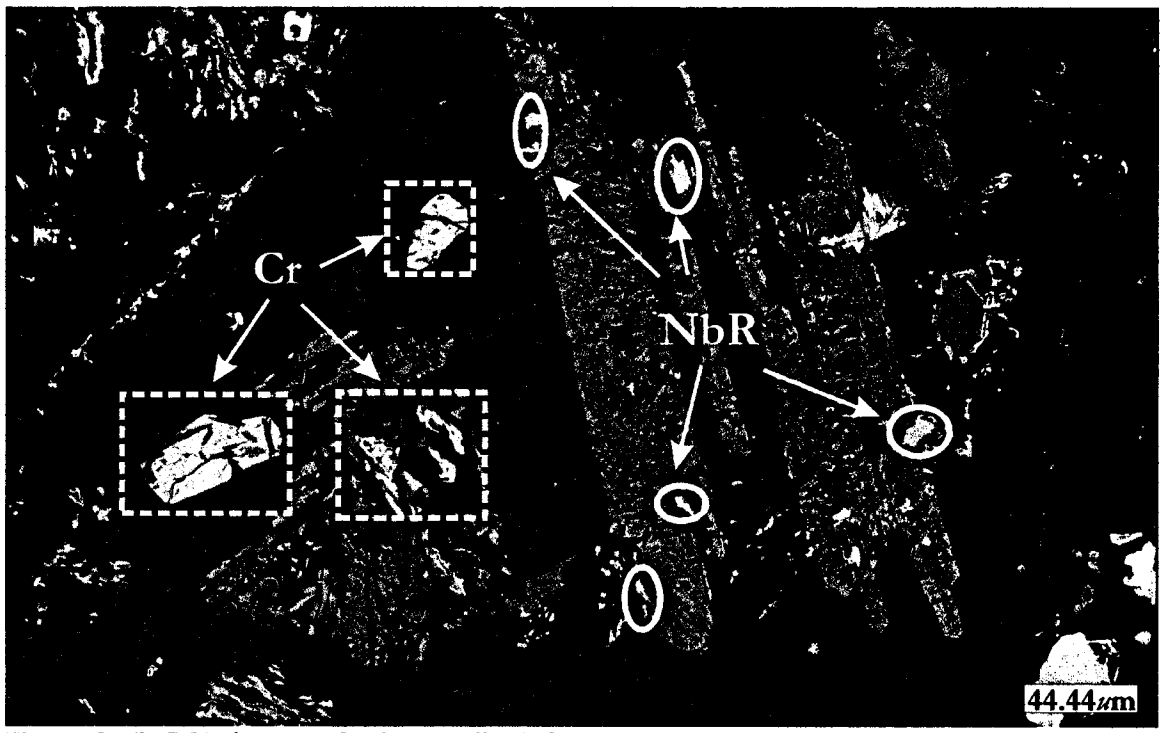

Figure 3.15: BSE-image of Nb-V-rutile (NbR) and crichtonite (Cr) with associated altered rutile laths.

Barite, the most abundant barium-mineral of the complex, is present in two generations. The older, first-generation is confined to small (<10 μm), rounded grains set in either a calcite or quartz-(I) groundmass. These grains occur throughout the entire complex and generally represent stoichiometric $BaSO_4$. The second-generation of barite occurs primarily in late-stage calcite veinlets, which are found throughout the main mineralized

zone. Similar calcite veinlets contain tyuyamunite and hollandite elsewhere in the main mineralized zone. Although the majority of barite-dominated veinlets consisted of only barite and calcite, a few veinlets contained accessory mineralization consisting of (from center to edge): barite, hematite, pyrite and biotite. Regardless of the associated phases, the veinlets cross-cut all features within the complex. In terms of composition, the veinlet-barite contains small amounts of SrO and PbO (as great as 1.45 and 1.24 wt.%, respectively).

Similar calcite veinlets are also host to tyuyamunite (Figure 3.16). However, since the small veinlets do not extend more than a few millimeters, no textural evidence of their relationship to barite or hollandite could be obtained. The veinlets cross-cut all features and are best preserved in a quartz groundmass. In a few samples, the tyuyamunite also occurs within a cementing calcite-plus-apatite groundmass, interstitial to brecciated phenakite grains. Similar textures are found within the Ba-Mn-hollandite-bearing veinlets, although they occur within calcite, interstitial to the hydrated calcium zirconosilicate and albite. A review of the literature regarding hollandite genesis indicates that the majority of hollandite occurrences are related to secondary, supergene enrichment of manganese deposits (Vasconcelos, 1999; Nicholson, 1992). Similarly, tyuyamunite, calcite and barite occurrences have been described from supergene environments.

Although clinopyroxenes are the most abundant mafic mineral within the unmineralized diatreme breccia, they only occur in trace amounts within the main mineralized zone. Aegirine-natalyite and aegirine-jervisite grains occur in trace amounts with both varieties set in a quartz groundmass, ranging in habit from large ($\leq$150 μm) euhedral-to-subhedral laths to smaller anhedral fragments. Although aegirine-natalyite occurs in both habits, aegirine-jervisite grains are only present as the smaller, anhedral grains associated with biotite and quartz. Associated phases with the aegirine-natalyite include: rutile, hydrated calcium zirconosilicate and in some instances, crichtonite. Due to the limited occurrence of aegirine-jervisite, the only associated phases noted were quartz and biotite.

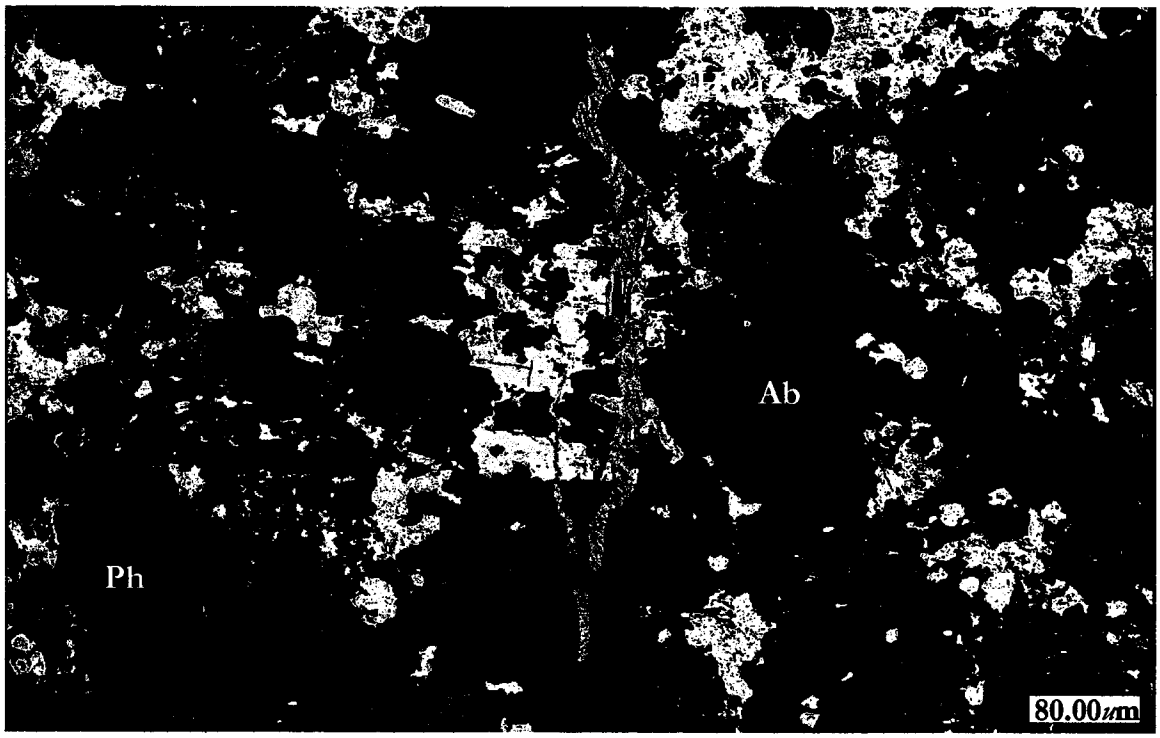

Figure 3.16: False-colored BSE-image of tyuyamunite veinlet crosscutting phenakite (Ph), albite (Ab) and the hydrated calcium zirconosilicate (HCaZr).

Thortveitite occurs within the main mineralization zone in trace amounts. Although the anhedral grains are too small for accurate analysis, they are large enough to be positively-identified spectroscopically. Due to the small size, excess silica was present in all quartz-hosted grains and anomalously high calcium was present in all the calcite-hosted grains. While thortveitite can reportedly contain minor amounts of calcium (up to 1.6 wt.%), the high amounts recorded (up to 8 wt.%) and the fact that the quartz-(II)-hosted thortveitite does not contain any calcium, suggests that the calcium represents background activation (Gramaccioli *et al.* 2000*a*). The anhedral thortveitite grains are set in calcite groundmass that contains: fluorapatite; galena; hydrated calcium zirconosilicate; an unidentified Fe-Cr-V-oxide; and chlorite. The quartz-hosted thortveitite occurs within large quartz grains, along with an unidentified Fe-Cr-V-oxide, set in a calcite groundmass. While recent work by Gramaccioli *et al.* (2000*b*) has suggested that scandium is likely to be transported as fluoride complexes, none of the associated phases including fluorapatite or fluorite contain any scandium. Furthermore, none of the fluorite grains in the Deadhorse Creek Complex occur in direct contact with the thortveitite grains.

Allanite-(Ce) occurs trace amounts within the main-mineralized zone, with only a few occurrences noted. In each instance, the anhedral grains were intergrown with titanite, set in quartz and associated with biotite. Due to the small size of the grains and the limited occurrence of the phase, no reliable quantitative data were acquired.

The primary LREE-bearing phase in the complex is monazite-(Ce). The mineral occurs in greater concentrations in the carbonatite dike and unmineralized diatreme breccia than the main mineralized zone. In addition to differences in abundance, monazite from the main mineralized zone lacks minor Nd, which is present in monazite-(Ce) from the other two units. Due to the lack of a suitable standard material, Nd contents were not quantified, although its presence was detected spectroscopically. Within the main mineralized zone, monazite occurs either as: small, rounded anhedral grains; or large acicular grains, which reach 0.14 mm in length. In both cases, the grains are set in a calcite groundmass and associated with hematite. In a few instances, the larger grains are found near chlorite.

Xenotime-(Y) is the only yttrium-dominant mineral within the complex and occurs in trace amounts within the main mineralized zone and the 'carbonatite' dike. Two varieties occur within the main mineralized zone, the more common of which are small (<10 μm) anhedral grains set in calcite and associated with hematite. Less commonly, xenotime-(Y) occurs as large, subhedral-to-euhedral grains set in quartz and associated with the hydrated calcium zirconosilicate, hematite and thorite. In addition to the difference in habit, these grains are distinguished by the presence of detectable levels of thorium, dysprosium and gadolinium. Unfortunately, lack of suitable standard materials for Gd and Dy precluded quantitative analysis of these grains.

In summary, a generalized paragenetic scheme is presented in Figure 3.17. As noted above, the majority of the phases are believed to have formed during the initial intrusion of the "granitic" fluids. Subsequent metasomatism created the niobium and vanadium species and later thermal metamorphism (from the intrusion of the Coldwell Alkaline Complex), probably resulted in the formation of pyrite, biotite, Ba-biotite and chlorite. Finally, weathering of the complex resulted in the formation of the supergene minerals, calcite, tyuyamunite, hollandite and barite. For a complete listing of the minerals present in the main mineralized zone and relative modal percentages, refer to Appendix C.

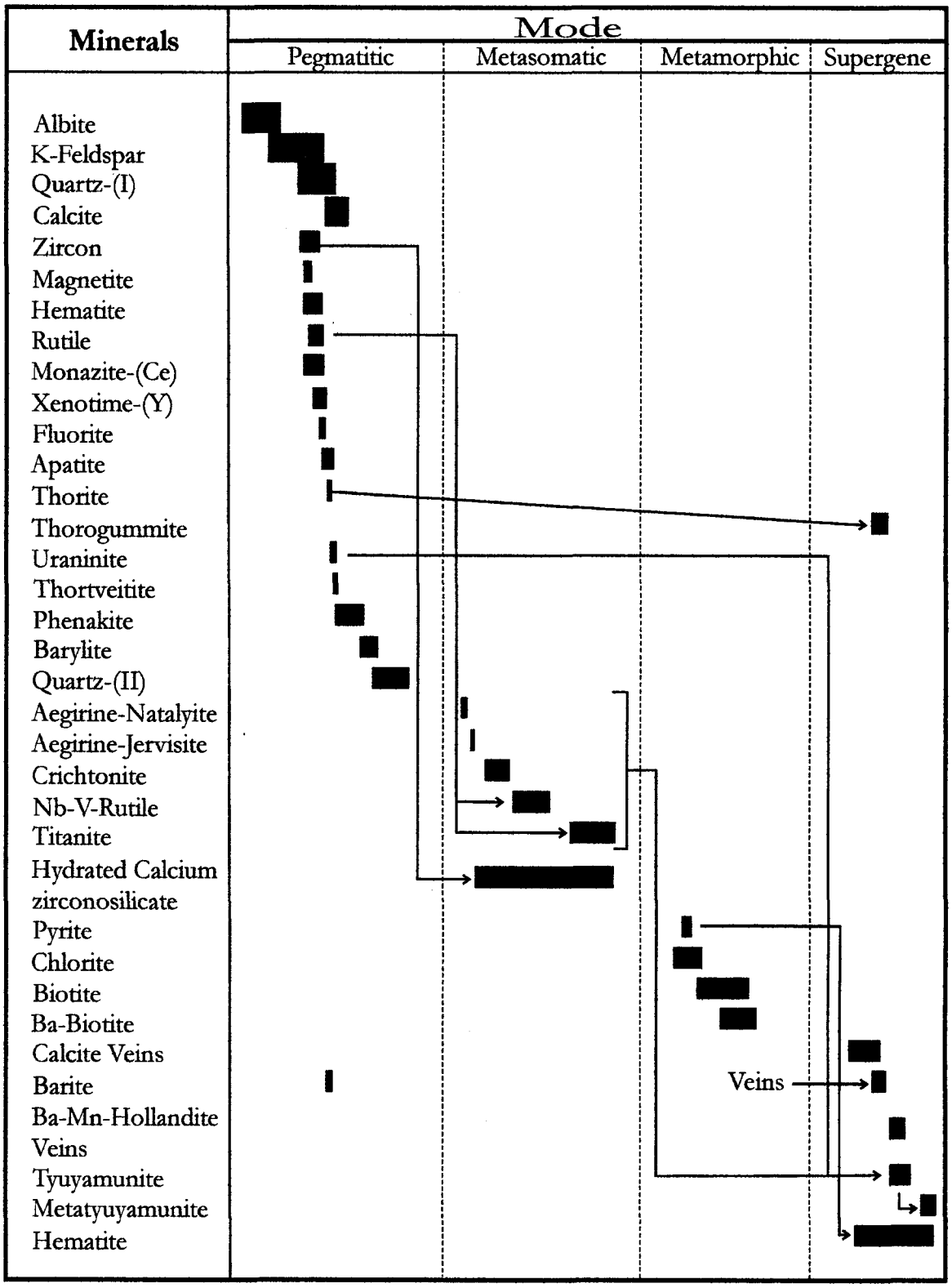

Figure 3.17: Generalized paragenetic scheme of the main mineralized zone of the Deadhorse Creek Complex. The arrows indicate alteration/reaction trends (i.e., zircon was altered to the hydrated calcium zirconosilite during metasomatism).

3.3 Carbonatite Dike

The carbonatite dike cross-cuts the diatreme breccia, pinching and swelling for its entire length of 52 m at a width of 1.52 m. The major minerals are (in decreasing abundance): dolomite-ankerite, calcite and potassium feldspar, the latter of which occurs in fragments scavenged from the diatreme breccia. Data obtained by Unocal Ltd. give average contents of 0.23% Y_2O_3 and 0.40% ZrO_2 over the entire length of the dike (Kennedy and Sherlock, 1989). These data reflect the relative abundance of xenotime-(Y) and zircon. In addition to these minerals, the dike also contains significant barite, monazite-(Ce) and thorite. Aside from the few metamorphic species noted below, the mineralization present in the dike is primary.

The dominant rock-forming mineral is rounded, anhedral grains of fractured dolomite-ankerite. These consist of approximately: 30 wt.% CaO, 18 wt.% MgO, 5 wt.% FeO and less than 1 wt.% MnO. Interstitial to the dolomite-ankerite is calcite, which is the primary host of the accessory mineralization (Figure 3.18). In a few instances, fragments of potassium feldspar and quartz were seen to be cemented in place by calcite. While not angular in habit, the potassium feldspar is fractured and pock-marked with signs of corrosion. The angular quartz grains are thought to represent fragments of the metasedimentary country rocks, whereas the most probable source of the potassium feldspar is the diatreme breccia. These quartz fragments are not to be confused with later anhedral quartz considered to be formed by thermal metamorphism associated with the intrusion of the Coldwell Alkaline Complex. The heat from the intrusion could have melted the surrounding sedimentary rocks and may have provided silica-rich fluids required to form quartz and chlorite in the carbonate-rich dike.

The most abundant accessory minerals are xenotime-(Y) and zircon. Xenotime-(Y) occurs as large euhedral grains, while zircon has been partially-altered to the hydrated calcium zirconosilicate found throughout the complex. The zircon grains aggregate to form long wisps of anhedral grains in the samples; whether the alteration caused this habit or if it is primary is unknown (Figure 3.19). Minerals associated with the anhedral zircon and euhedral xenotime-(Y) include: thorite, monazite-(Ce), pyrite, hematite and quartz.

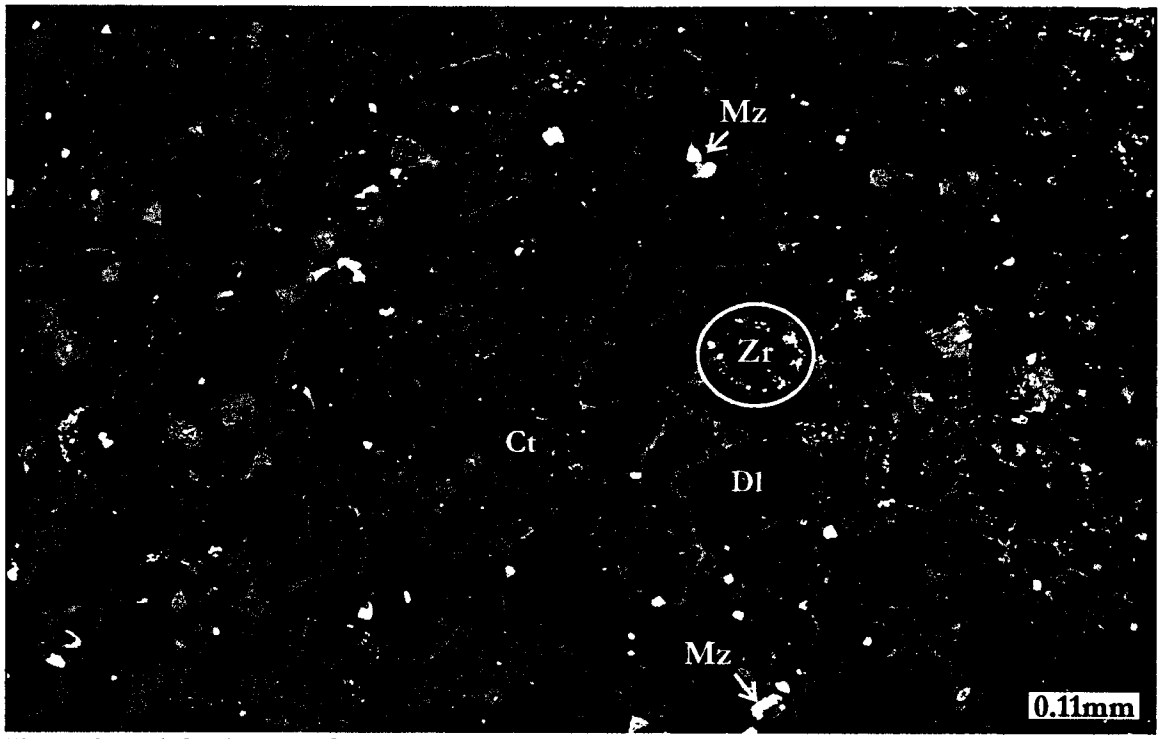

Figure 3.18: BSE-image of the dolomite-ankerite grains (Dl) set in calcite (Ct). Also shown: hematite, monazite-(Ce) (Mz) and a few zircon grains (circled Zr).

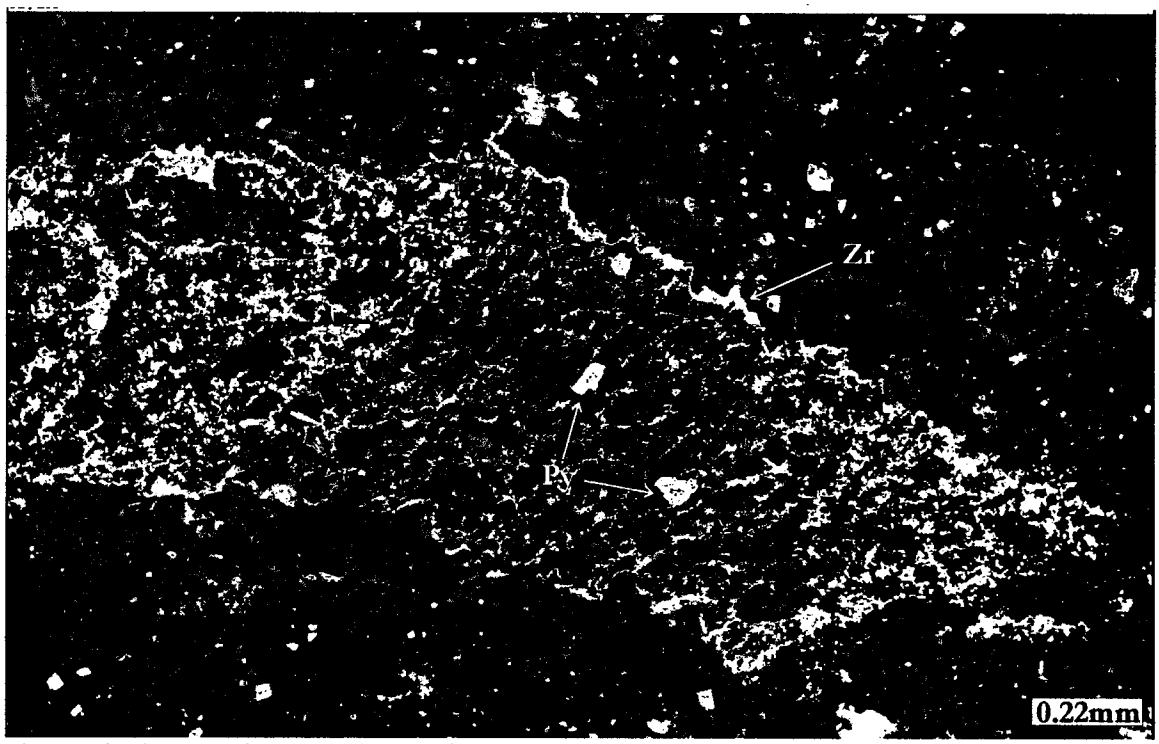

Figure 3.19: BSE-image of anhedral zircon grains aggregating to form 'wisps' in the dolomite-ankerite plus calcite matrix. Also shown are larger grains of pyrite and small grains of monazite-(Ce) (white).

In common with the diatreme breccia, monazite-(Ce) occurs in relatively high contents in two habits: small anhedral grains and larger, corroded sub-euhedral lath-like grains. In contrast to the diatreme breccia, the more abundant of these two habits are the smaller anhedral grains that are pervasive throughout the dike. The anhedral monazite-(Ce) is found in association with almost all the accessory minerals identified in the dike and occurs in dolomite-ankerite, calcite and metamorphic quartz. The larger subeuhedral grains are essentially confined to interstitial calcite and were found in association with apatite, zircon, thorite and pyrite.

Apatite is typically found as rounded, anhedral grains set in interstitial calcite. In an isolated occurrence, it was also observed rimming interstitial quartz together with zircon, monazite-(Ce), xenotime-(Y) and hematite

Thorite occurs in relatively high abundance within the carbonatite dike, when compared to the other accessory minerals. It occurs as small (<20 μm) anhedral grains set in dolomite-ankerite and calcite. Phases with which thorite is preferentially-associated include: hematite; monazite-(Ce); pyrite; and zircon. Of these, thorite was most intimately associated with monazite-(Ce) and hematite, in some instances occurring poikilitically-enclosed in the grains (Figure 3.20).

Pyrite is the most abundant sulphide mineral, followed by sphalerite, galena and barite. With the exception of pyrite, all occur as small (<20 m), anhedral grains set in groundmass dolomite-ankerite or calcite. As illustrated in Figure 3.19, pyrite primarily occurs as larger (>30 μm) anhedral grains, and to a lesser extent, as small corroded sub-euhedral grains partially replaced by hematite and chlorite.

A generalized paragenetic scheme is presented in Figure 3.21. The carbonatite dike is considered to represent the most recent event in the formation of the complex, being intruded following the alkaline metasomatism yet prior to the intrusion of the Coldwell Alkaline Complex. The subsequent intrusion of the Coldwell Complex provided the heat and silica source required for the formation of chlorite and quartz in a relatively silica-free system. A complete listing of the minerals present in the dike and approximate modal percentages are given in Appendix C.

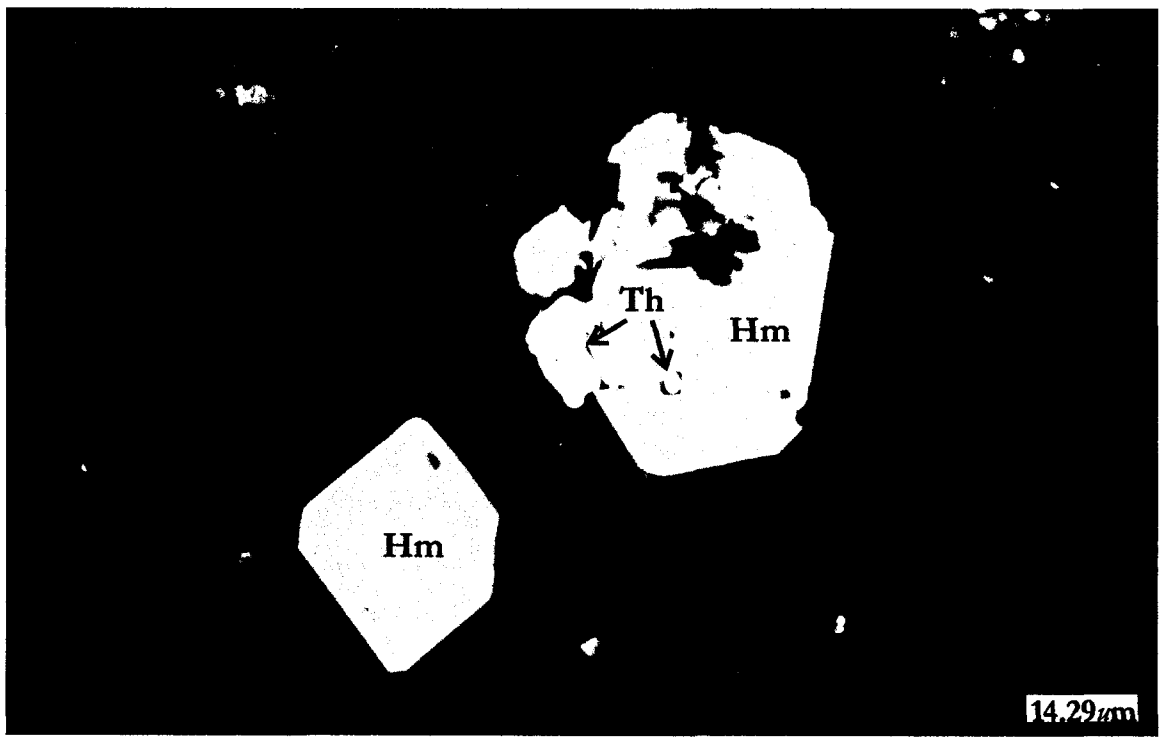

Figure 3.20: BSE-image of thorite (Th) in association with hematite (Hm). Both phases are set in a dolomite-ankerite grains.

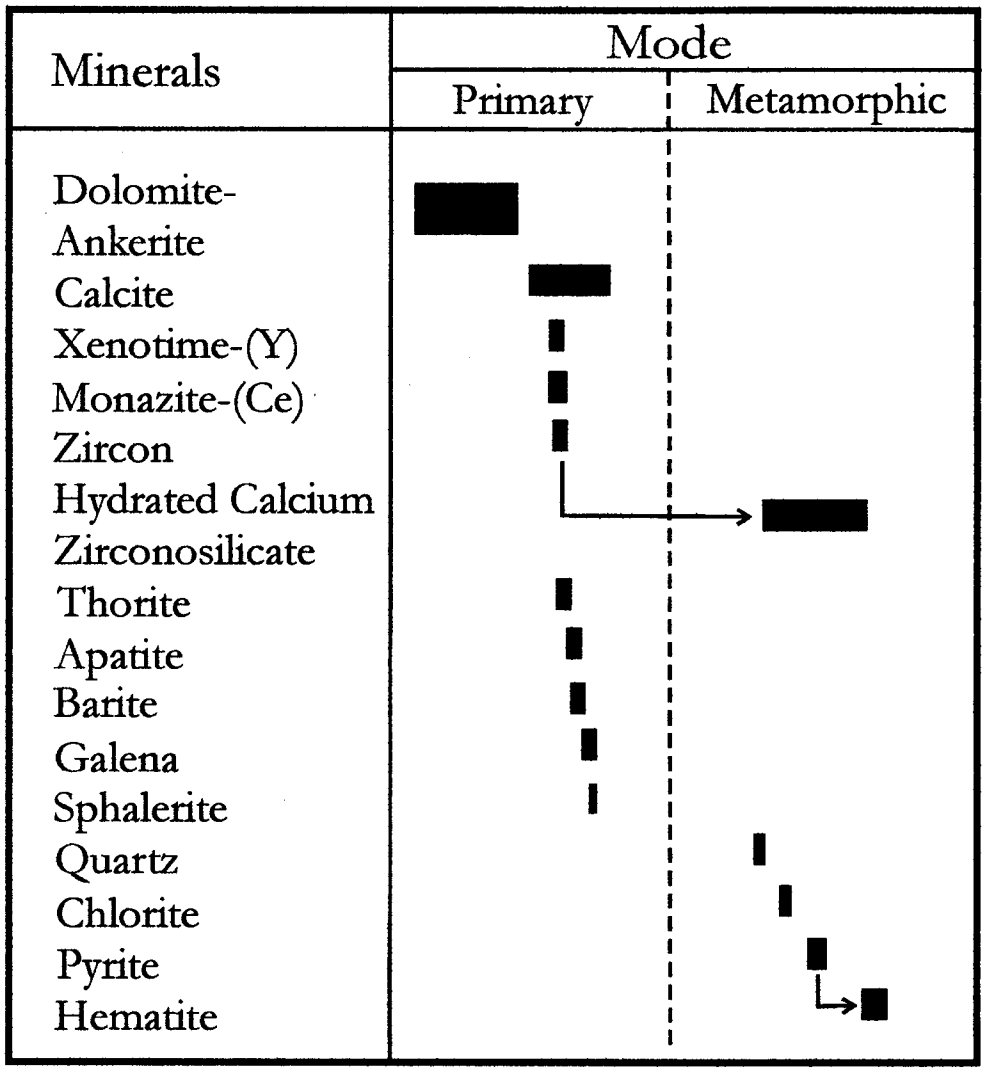

Figure 3.21: Generalized paragenetic scheme for the crosscutting carbonatite dike of the Deadhorse Creek Complex. The arrow indicates alteration/reaction trends (i.e. zircon is altered to the hydrated calcium zirconosilicate).

CHAPTER FOUR

4.1 Discussion

As noted in Chapter 1.2, the Deadhorse Creek 'diatreme' breccia is better termed an igneous vent breccia, which probably formed in response to early Keweenawan mid-continent rifting. Although the exact timing of the event is unknown, the presence of Neoarchean clasts within the breccia and a zircon U-Pb age determination of 1128.7 ±6 Ma for the main mineralized zone (M. Smyk pers. comm.) constrain the emplacement of the breccia to the Proterozoic. In the Proterozoic, the most geologically significant events affecting the region were associated with mid-continent rifting. Furthermore, the complex occurs along the proposed failed third-arm of the rift: the Thiel fault, which is the northern part of the Trans-Superior Tectonic Zone (Mitchell and Platt, 1982*a*; Weiblen, 1982; Sage, 1982; 1991). The complex mineralogy observed in the main mineralized zone of the Deadhorse Creek Complex is undoubtedly a result of several episodes of alteration. Following emplacement of the breccia, three events were involved in the formation of this occurrence, in order these are: intrusion by granitic fluids; alkaline metasomatism; and thermal metamorphism. Following these events, erosion exposed the complex, causing oxidation and leaching of minerals from the main mineralized zone. This weathering resulted in the deposition of supergene hollandite, tyuyamunite, barite and calcite. The alteration events and emplacement of a crosscutting carbonatite dike can be linked to major changes in the regional geology: emplacement of nearby carbonatite and alkaline complexes and thermal metamorphism associated with the Coldwell Complex. The timing of the events that affected the Deadhorse Creek complex has been deduced using textural and compositional information for the mineral parageneses present in the various geological units of the complex. Table 4.1 lists the radiometric ages of nearby alkaline and carbonatite complexes related to the Trans-Superior Tectonic Zone.

Table 4.1: Radiometric age determinations of nearby alkaline and carbonatite complexes.

Complex	Age (Ma)	Method	Reference
Prairie Lake	1165 ±30	Rb-Sr	Pollock, 1987
Deadhorse Creek	1128.7 ±6	U-Pb	M.C. Smyk, Unpublished
Coldwell	1108 ±1	U-Pb	Heaman and Machado, 1987
Killala Lake	1098 ±48	Rb-Sr	Bell and Blenkinsop, 1980
Chipman Lake	1029 ±31	K-Ar	Sage, 1985

Following development of the breccia, Be- and Sc-rich fluids derived from an A-type granitic source intruded the western subcomplex along an active fault system. These fluids initially caused the formation of euhedral albite grains set in a matrix of potassium feldspar and quartz (quartz-I). Following crystallization of the feldspars, the activities of Al and Si were decreased enough in the residual fluids to permit to formation of phenakite and barylite. From these residual fluids, large grains of euhedral phenakite and smaller euhedral grains of barylite crystallized in quartz that is free of any other accessory mineralization (quartz-II). As noted in Chapter Two, abundant feldspar crystallization may have depleted the Al-content of the fluids, reducing the activity of Al_2O_3 sufficiently to permit to the formation of phenakite rather than beryl. During this period, the activity of SiO_2 was narrowly constrained. According to data given in Figures 2.38 and 2.39, the log activity of Al_2O_3 fell below approximately –1.0, whereas the log activity of H_4SiO_4 ranged from –2.3 to –1.7, at temperatures great than 340°C (at 1 kbar). In contrast, Gramaccioli *et al.* (2000*a*) suggest another reason why phenakite, rather than beryl, can form in a feldspar-rich system. If equilibrium between beryl and alkali feldspar is expressed as: $Be_3Al_2Si_6O_{18} + 2K^+ + 4H^+ \rightarrow 2KAlSi_3O_8 + 3Be^{2+} + 2H_2O$ and if the activity of $KAlSi_3O_8$ is constant and the solution dilute; then $K = \exp(-\Delta G°/RT) = [a Be^{2+}]^3/([aK^+]^2[aH^+]^4[\gamma.x\ Be_3Al_2Si_6O_{18}])$, where *a* represents the activity of the corresponding element in the depositing solutions. For beryl, the product γ.x between the activity coefficient and the molar fraction in the crystal has been used in place of the activity. Under these assumptions, such a molar fraction depends strongly on the pH of the solutions and is independent of the activity of Al. In particular, a low pH value in the solutions would prevent the formation of an Al-rich member of the beryl group. Therefore, even if significant contents of Be^{2+} were present in these solutions at low pH, the formation of "common" beryl would not occur. Furthermore, if this mineral were already present, it would be destroyed to form feldspar (Gramaccioli *et al.* 2000*a*). As

phenakite crystallization neared completion, small grains of barylite formed, perhaps as a final stage of Be-mineralization. Once Be was depleted from the fluids, incompatible Sc was partitioned into small, anhedral grains of thortveitite, followed by crystallization of quartz-II. What is interesting to note from this assemblage is the presence of thortveitite, barylite and alkali feldspar without bazzite [$Be_3(Sc,Al)_2Si_6O_{18}$] or celsian [$BaAl_2Si_2O_8$]. Any Ba present was forced to combine with Be in barylite rather than appear in celsian or hyalophane. The presence of thortveitite rather than bazzite supports the hypothesis of preferential formation of potassium feldspar under low pH values, as Sc replaces Al in bazzite, and even if the activity of Al was lowered, the activity of Sc should have been high enough to form bazzite. Subsequent events described below resulted in the brecciation of the large euhedral phenakite grains, forming the anhedral-to-rounded grains.

The 'granitic' mineral assemblage was in turn, altered by alkaline metasomatic fluids enriched in V, Nb and Cr. Reaction of these fluids with rutile and albite resulted in the formation of vanadium-rich crichtonite, Nb-V-rutile (ilmenorutile), aegirine-natalyite and aegirine-jervisite. These fluids also aided in the decomposition of zircon, causing the formation of a hydrated calcium zirconosilicate. Although the source of these fluids remains enigmatic, the most probable sources are alkaline or carbonatite magma (i.e. Coldwell Complex, Prairie Lake Carbonatite, Killala Lake Complex). In her description of mineralization at the Christy Ti-V-Nb deposit, Flohr (1994) ascribes the enrichment of Ti, V and Nb to evolved alkali fluids derived from the adjacent Magnet Cove carbonatite-alkaline complex. In addition, Barkov *et al.* (1997, 2000) describe unusual Ti-, V- and Nb-minerals from a fenitized xenolith enclosed within nepheline syenite in the Khibina alkaline complex. All of these occurrences point to mobility of Ti, Nb and V in metasomatic processes. The source and mobility of Cr ,on the other hand, remains problematic.

With the exception of crichtonite, all of these minerals are present in small sub-euhedral-to-anhedral grains. The crichtonites form corroded grains, some of which are best-termed atoll grains. These textures suggest that the crichtonite grains may have formed early in the metasomatic sequence, only to be partially resorbed later, or transported in fluids before being emplaced in the breccia. Interestingly, the Deadhorse Creek crichtonites plot in the upper mantle quadrant of the $FeO + Fe_2O_3 + MgO$ versus TiO_2 diagram outlined by Haggerty (1991). However, as Platt and Mitchell (1996) suggest, this quadrant may be more appropriately termed the alkali metasomatic quadrant as the geologic environment of the

Deadhorse Creek Diatreme predicates against an ultramafic upper mantle setting. Due to the porous nature of the breccia, these fluids also percolated into the breccia surrounding the main mineralized zone. The effects of these fluids are preserved in the rock as anhedral grains of ilmenorutile that has exsolved from an Mn-bearing ilmenite. In common with ilmenorutile from the main mineralized zone, the breccia phase contains minor amounts of vanadium. In their description of vanadian silicates from the nearby Hemlo gold deposit, Pan and Fleet (1992) ascribed the formation of these phases to metasomatic fluids which had leached the required elements from local ultramafic-to-mafic units and were introduced during the waning stages of the second regional metamorphism at 2672-2670 Ma. If the V-rich minerals at Deadhorse Creek were derived from the same ultramafic-to-mafic units, a second thermal event is required to remobilize the vanadium, as no ultramafic or mafic rocks occur near the occurrence. No evidence exists in support of such a thermal event, suggesting that the fluids must have been enriched in vanadium at the source. Again, the nearby alkaline rocks are the most probable sources of the V, Cr and Nb-enriched alkaline fluids.

Next in the history of the complex, a carbonatite dike intruded the diatreme breccia. Petrographically, the dike is comprised of (modal %): 45% dolomite-ankerite, 20% calcite, 20% biotite and 15% accessory minerals. The latter consist of xenotime-(Y), monazite-(Ce), thorite, metamict zircon, galena and pyrite. As the only silicates within the dike occur as anhedral and interstitial grains, they are believed to have resulted from subsequent thermal metamorphism associated with the emplacement of the Coldwell complex (see below). The silicates present include: quartz, chlorite, biotite, potassium feldspar and pyrite. Metamictization of primary zircon resulted in the formation of a hydrated calcium zirconosilicate, a mineral common throughout the entire complex. Although similar dolomitic and ankeritic dikes have been described from Chipman Lake (Platt and Wooley, 1990), their accessory mineralization differs greatly due to the presence of sodic- and REE-carbonates. Furthermore, the significant distance between the occurrences (~150 km) eliminates any possibility of a genetic affinity. A preliminary K-Ar age determination for the Chipman Lake fenite also suggests an age of 1029 ±31 Ma (Sage, 1985), which is younger than the emplacement of the Coldwell complex.

Following the intrusion of the dike, the Deadhorse Creek complex experienced thermal metamorphism associated with the intrusion of the Coldwell Alkaline Complex.

The Coldwell complex is a composite intrusion consisting of three intrusive centers that young progressively towards the west (Mitchell and Platt, 1982*b*). Center 1 occurs along the eastern margin and consists of two phases, gabbro and the more prevalent ferroaugite syenite. Center 2 forms the central part of the complex and consists of biotite gabbros and nepheline syenites. Center 3 intrudes most other phases in the complex and forms the western sector of the complex. This unit is comprised of granites, quartz syenites and syenites (Mitchell and Platt, 1978; 1982*b*). On the basis of mineral composition and textures, Mitchell and Platt (1978, 1982*b*) and Heamann and Machado (1992) propose a relatively rapid cooling history between the temperature of initial crystallization (~850°C) and that of the residual fluids (~500°C). Furthermore, the authors suggest that the whole complex was emplaced over a relatively short period (<3Ma), that each magma batch had time to evolve and each center was almost completely solid before emplacement of the subsequent magma batches. High-resolution gravity profile modeling by Mitchell *et al.* (1983) has inferred the presence of a differentiated basic intrusion beneath the complex. The intrusion consists of a 3-5 km thick layer of gabbro, underlain by another 3 km thick layer of peridotite or pyroxenite. As noted by Walker (1967) a large thermal aureole surrounds the Coldwell complex and extends beyond the Deadhorse Creek complex, to the Middleton area. From detailed mapping, the author notes the development of hornfelsic rocks, with tuffaceous metasediments just west of the Deadhorse Creek containing clear plagioclase and randomly oriented prism of blue-green hornblende. In the basic volcanic rocks, hornblende develops in place of chlorite and actinolite, biotite forms closer to the contact, and adjacent to the contact, pyroxene appears.

Within the Deadhorse Creek breccia, the thermal metamorphism from the Coldwell Complex and the underlying basic intrusion is proposed to have resulted in the formation of barian feldspars, quartz, barian biotite and biotite. Within the main mineralized zone, the effects are preserved in barian biotite, biotite, chlorite and pyrite. Once again, similarities in mineralogy between the main mineralized zone and the Hemlo area can be drawn. Pan and Fleet (1991) describe the mineralogy of a green mica schist that contains barian feldspars and micas, located 21 km west of the Hemlo gold deposit, and ascribe the formation of these schists due to partial melting of a barite-rich layer during the second regional metamorphic event (2672-2670 Ma). Estimated pressures and temperatures are given as 530°C at 3-4 kbar. It is suggested here that the same metamorphic event also dispersed barium-rich fluids to the

west, along the foliation of the country rocks. These barium-rich fluids settled in the area and were later remobilized during emplacement of the Coldwell complex and underlying basic intrusion. In essence, heat from these events drove barium-rich fluids, which were derived from the country rocks, towards the nearby (<1 km) Deadhorse Creek complex. Interaction of these fluids with the porous diatreme breccia resulted in the formation of barian feldspars, barian biotite, quartz and biotite. Within the main mineralized zone, these fluids resulted in the formation of barian biotite, biotite, chlorite and pyrite.

Following the events associated with the mid-continental rifting and presumably post-glaciations, oxidation and leaching of the main mineralized zone resulted in the formation of the supergene minerals: hollandite, tyuyamunite, barite and calcite. These processes likely began post-glaciations, when erosion exposed the occurrence to meteoric waters and are likely continuing at present. All of these minerals occur in calcite veinlets that have precipitated in small fractures throughout the mineralized zone. Initially, slightly acidic, oxidizing groundwaters became enriched in uranyl and vanadate ions due to decomposition and leaching of the uranium and vanadium minerals. These enriched fluids were slightly acidic with pH values near 6.0. As the waters percolated down fractures within the complex, they became more alkaline and basic in nature due to the dissolution of calcium. The increase in alkalinity initially caused the precipitation of calcite, followed by tyuyamunite and hollandite. From Figures 4.1, 4.2 and 4.3 the pH of the depositing fluids is estimated to be greater than 8, under oxidizing conditions (Eh values in the range of 0.4 to 0.8 volts). The initial fluids are assumed to have been acidic in order to permit the solubility of uranyl and vanadyl ions. Typically, vanadyl ions only occur in solutions with pH<6 (Wanty and Goldhaber, 1992). However, due to kinetic hindrances to oxidizing, reduction or disproportionation of the vanadyl ion, or formation of stable complexes, solutions with pH>6 may contain vanadyl. (Breit and Wanty, 1991). As first noted by Evans and Garrels (1958), when vanadium reaches the pentavalent state in the presence of uranyl ions, carnotite and tyuyamunite become the stable phases at pH values greater than 2.2. Within this range (shaded area in Figure 4.1), all other vanadium-bearing minerals become metastable with respect to the uranium complex ions. Finch and Murakami (1999) note that these phases are so stable that they will precipitate wherever dissolved uranium encounters waters containing dissolved vanadate ions. Figures 4.2 and 4.3 illustrate the stability fields of calcite and manganese ions. As hollandite contains Mn^{4+} and Mn^{2+}, data from Figure 4.3 illustrates that

the hollandite probably formed under the same basic, oxidizing conditions as tyuyamunite (pH>8, Eh 0.4-0.8).

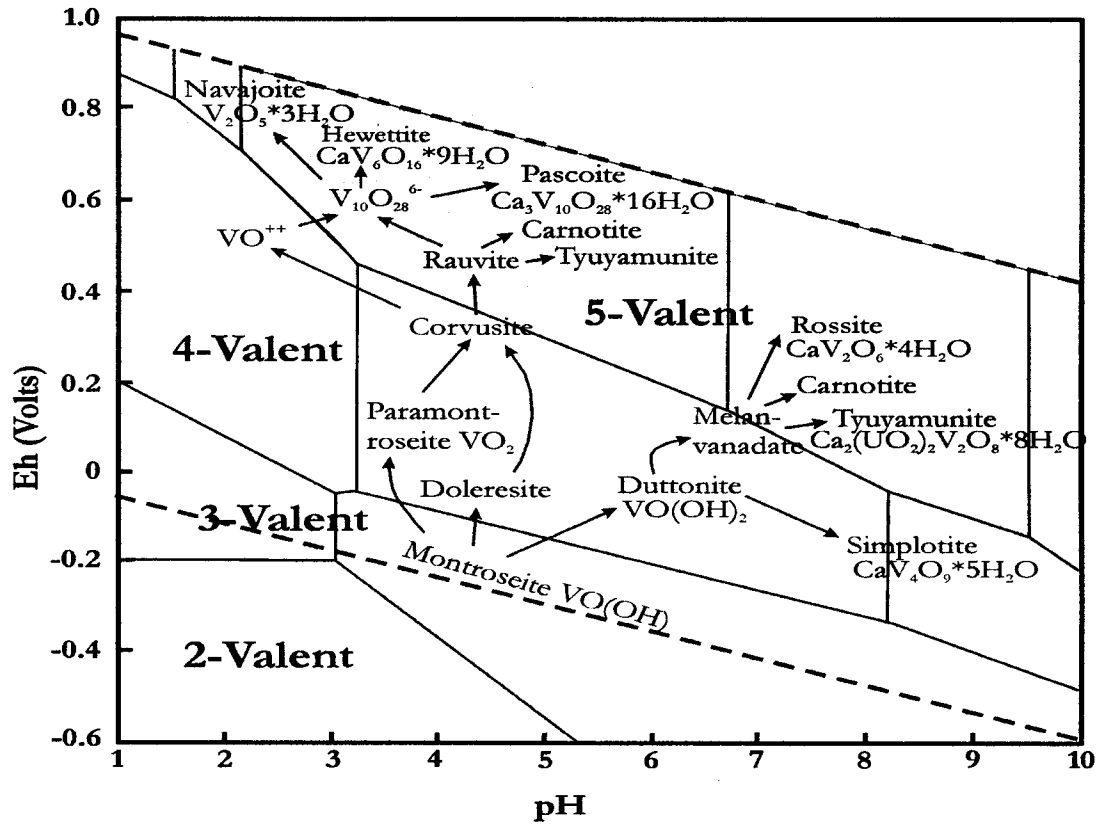

Figure 4.1: Aqueous equilibrium diagram for vanadium species, illustrating the stability regions of various minerals (after Evans and Garrels, 1958). The stability field for tyuyamunite is shaded.

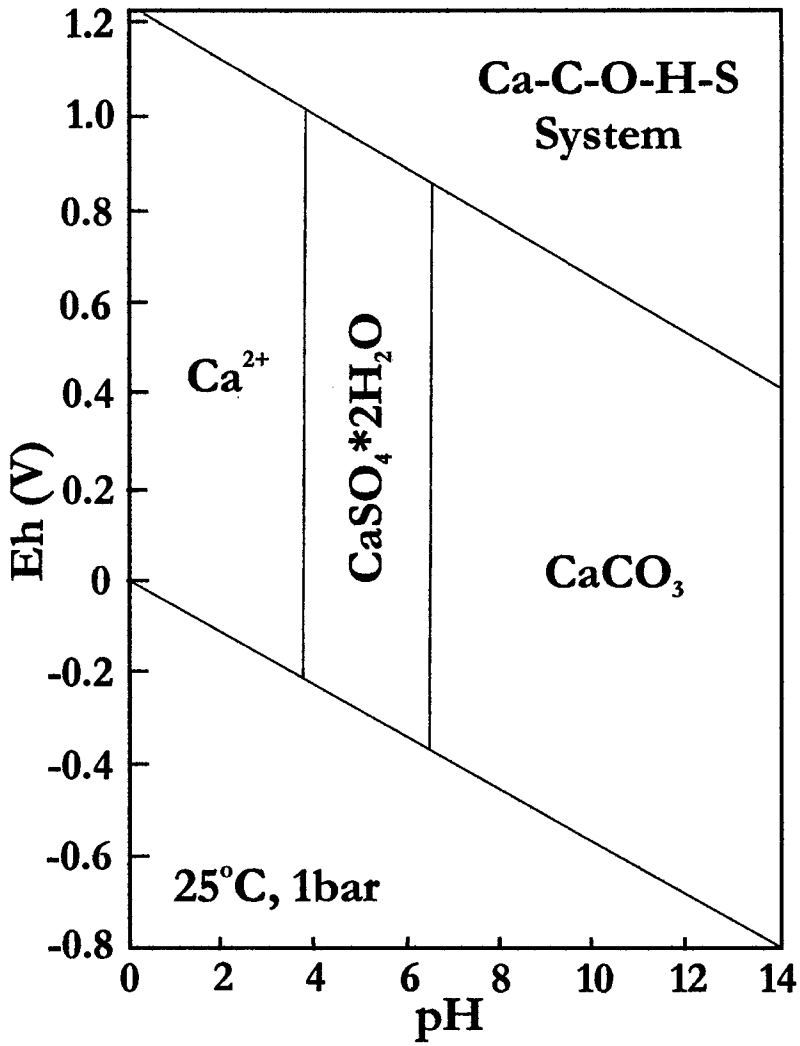

Figure 4.2: Eh-pH diagram for the Ca-C-O-H system at 25°c and 1 bar (Brookins, 1988). Activities of the dissolved species are: $Ca=10^{-2.5}$; $S=10^{-3}$; $C=10^{-3}$.

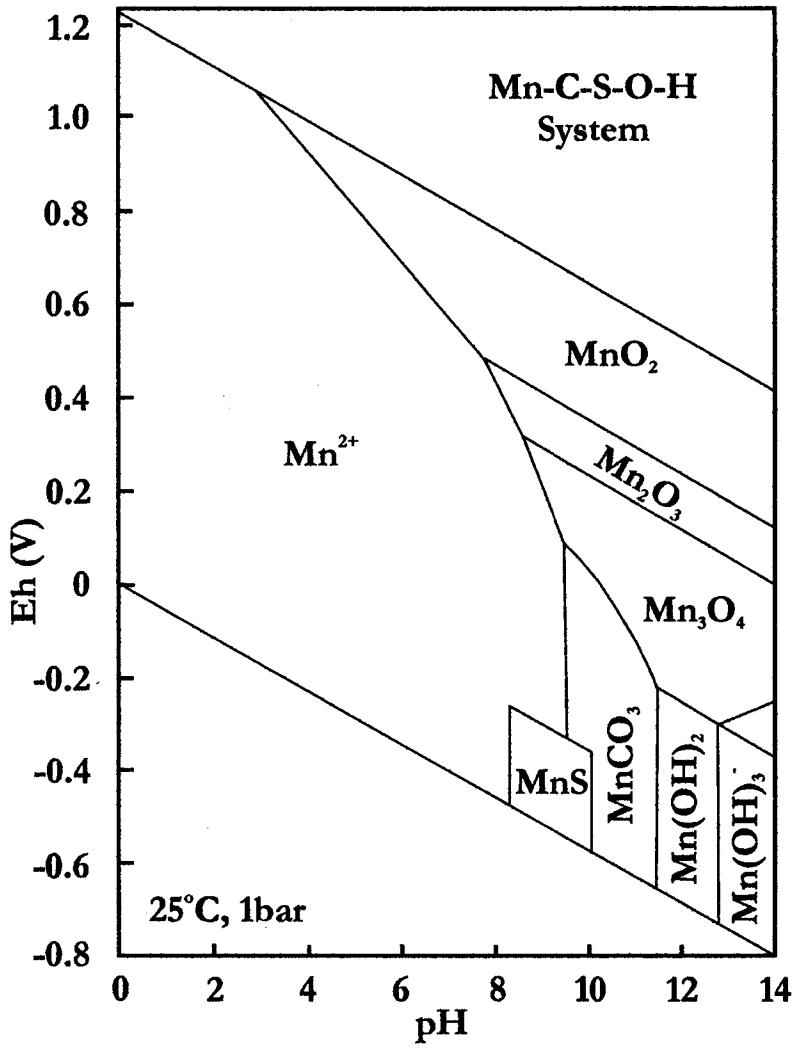

Figure 4.3: Eh-pH diagram of the Mn-C-S-O-H system at 25°C and 1 bar (Brookins, 1988). Assumed activities of the dissolved species are: $Mn=10^{-6}$; $C=10^{-3}$; $S=10^{-3}$.

4.2 Conclusions

The Deadhorse Creek is an igneous vent breccia that probably formed by unknown processes in response to early mid-continent rifting in the Proterozoic. Following development of the breccia, the complex mineralogy observed in the main mineralized zone of the western subcomplex was created by three independent events. Each event has produced a unique mineral paragenesis and the timing of each has been deduced from both textural and compositional evidence. While independent, these events made use of the same pre-existing fracture system along which the western subcomplex is situated. In order, these events were: intrusion of granitic fluids, alkaline metasomatism, and thermal metamorphism associated with the emplacement of the Coldwell alkaline complex. Following the alteration events, and presumably post-glaciations, oxidization and leaching of the main mineralized zone also produced (and currently is) a supergene paragenesis of: calcite, tyuyamunite, hollandite and barite. Due to the complex evolution, the main mineralized zone was enriched in first- and second-order transition metals, rare-earth elements, beryllium, Th and U. The resulting mineralogy is both unique and complex, with several new compositional extremes reported, (i.e. Nb-V-rutile, aegirine-jervisite, aegirine-natalyite, zircon-thorite-coffinite solid solutions, Dy-xenotime-(Y) and V-crichtonite). In addition, unique parageneses were reported, giving further insight into the geochemistry and mineralogy of Be, Ba, Sc, V, Nb, Ti and Cr and conditions of formation for phenakite, barylite, thortveitite, crichtonite, ilmenorutile and barian feldspars.

Although care has been taken to describe all textures and paragenetic relationships, the complexity and aphanitic texture of the occurrence precludes unambiguous genetic conclusions. For example, while a source of the hydrous alkaline fluids enriched in Ti, V and Nb has been attributed to the nearby alkaline complexes, the source and mobility of Cr in these fluids remains a problem. Furthermore, the source and timing of barium-rich fluids, which reacted with the breccia to form barian feldspars and barian biotite, remains vague. It is hoped that work will continue on this occurrence and the surrounding area, providing more clues to the complex geological history of the region.

REFERENCES

Allen, R.F., and Thomas, R.G. (1984): The uranium potential of diagenetically altered sandstones of the Permian Rush Springs Formation, Cement District, southwest Oklahoma. *Econ. Geol.* 79, pp. 284-296.

Ambartsumyan, Ts. L., Basalova, G.I., Gorzhevskaya, S.A., Nazarenko, N.G. and Khodzhayeva, R.P. (1961): Thermal investigations of uranium-bearing minerals, Gosatmizdat, Moscow, 148 p.

Barkov, A.Y., Laajoki, K.V.O., Men'shikov, Y.P., Alapieti, T.T. and Sivonen, S.J. (1997): First terrestrial occurrence of titanium-rich pyrrhotite, marcasite and pyrite in a fenitized xenolith from the Khibina alkaline complex, Russia. *Can. Mineral.* 35, pp. 875-885.

_____., Martin, R.F. and Poirier, G. (2000): Zoned tungsten molybdenite from a fenitized megaexenolith in the Khibina alkaline complex, Russia. *Can. Mineral.* 38, pp. 1377-1385.

Barton, M.D. (1986): Phase equilibria and thermodynamic properties of minerals in the BeO-Al_2O_3-SiO_2-H_2O (BASH) system, with petrologic implications. *Am. Mineral.* 71, pp. 277-300.

_____, and Young, S. (200): Non-pegmatitic deposits of beryllium: mineralogy, geology, phase equilibria and origin. In: *Beryllium: Mineralogy, Petrology and Geochemistry.* (E.S. Grew Ed.), Reviews in Mineralogy and Geochemistry 50, Mineral. Soc. Am. pp.

Bell, K. and Blenkinsop, J. (1980): Ages and initial $^{87}Sr/^{86}Sr$ ratios from alkalic complexes of Ontario. *In:* Geoscience Research Grant Program Summary of Research 1979-1980, Ontario Geological Survey, Miscellaneous Paper 93, pp. 16-23.

Belolipetskii, A.P. and Voloshin, A.V. (1996): Yttrium and rare earth element minerals of the Kola Peninsula, Russia. *In: Rare Earth Mineral: Chemistry, Origin and Ore Deposits.* (A.P.Jones, F. Wall and C.T. Williams Eds.) Chapman and Hall, London, U.K. pp. 311-326.

Beus, A.A. (1966): *Geochemistry of Beryllium and Genetic Types of Beryllium Deposits.* W.H. Freeman & Co., San Francisco and London, 401 p.

Bjørlykke, K.O. and Griffin, W.L. (1973): Barium feldspars in Ordovician sediments, Oslo region, Norway. *J. Sed. Petrol.* 43, pp. 461-465.

Breit, G.N. and Wanty, R.B. (1991): Vanadium accumulation in petroleum and carbonaceous rocks: a review of geochemical controls during deposition and diagenesis. *Chem. Geol.* 91, pp. 83-97.

Brookins, D.G. (1988): *Eh-pH Diagrams for Geochemistry.* Springer-Verlag, N.Y., 176 p.

Bruker, AXS (2002): EVA V8.0. Qualitative and semi-quantitative phase analysis software for powder diffraction data. User's Manual, Bruker AXS, Karlsruche, Germany.

_____, (2003): Topas V2.1: General profile and structre analysis software for powder diffraction data. User's Manual, Buker AXS, Karlsruche, Germany.

Buck, H.M., Cooper, M.A., Černý, P, Grice, J.D. and Hawthorne, F.C. (1999): Xenotime-(Yb), $YbPO_4$, a new mineral species from the Shatford Lake pegmatite group, southeastern Manitoba, Canada. *Can. Mineral.* 37, pp. 1303-1306.

Canil, D. (2002): Vanadium in peridotites, mantle redox and tectonic environments: Archean to present. *Earth and Planetary Science Letters* 195, pp. 75-90.

Čejka, J. (1999): Infrared spectroscopy and thermal analysis of the uranyl minerals. *In: Uranium: Mineralogy, Geochemistry and the Environment.* (P.C. Burns and R. Finch Eds.), Reviews in Mineralogy v. 38. Mineral. Soc. Am. pp. 521-622.

Černý, P. (2002): Mineralogy of beryllium in granitic pegmatites. *In: Beryllium: Mineralogy, Petrology and Geochemistry.* (E.S. Grew Ed.), Reviews in Mineralogy and Geochemistry 50, Mineral. Soc. Am. pp. 405-444.

_____., Čech, F. and Povondra, P. (1964): review of ilmenorutile-strüverite minerals. *Neues Jahrbuch für Mineralogie*, Abhandlungen 101, pp. 142-172.

_____., Paul, B.J., Hawthorne, F.C. and Chapman, R. (1981): A niobian rutile-disordered columbite intergrowth from the Huron Claim pegmatite, southeastern Manitoba. *Can. Mineral.* 19, pp. 541-548.

_____., Goad, B.E., Hawthorne, F.C. and Chapman, R. (1986): Fractional trends of the Nb- and Ta-bearing oxide minerals in the Greer Lake pegmatitic granite and its pegmatite aureole, southeastern Manitoba. *Amer. Mineral.* 71, pp. 501-517.

_____., Chapman, R., Simmons, W.B. and Chackowsky, L.E. (1999): Niobian rutile from the McGuire pegmatite, Park County, Colorado: solid solution, exsolution and oxidation. *Amer. Mineral.* 84, pp. 754-763.

Chabu, M. and Boulègue,J. (1992): Barian feldspar and muscovite from the Kipushi Zn-Pb-Cu deposit, Shaba, Zaire. *Can. Mineral.* 30, pp. 1143-1152.

Chakhmouradian, A.R., Reguir, E.P. and Mitchell, R.H. (2002): Strontium-apatite: new occurrences and the extent of Sr-for-Ca substitution in apatite-group minerals. *Can. Mineral.* 40, pp. 121-136.

Coats, J.S., Fortey, N.J., Gallagher, M.J. and Grout, A. (1984): Stratiform barium enrichment in the Dalaradian of Scotland. *Econ. Geol.* 79, pp. 1585-1595.

_____., Smith, C.G., Fortey, N.J., Gallagher, M.J., May, F. and McCourt, W.J. (1980): Strata-bound barium-zinc mineralization in Dalaradian schist near Aberfeldy, Scotland. *Trans. Inst. Mining Metall., Sect B: Appl. Earth Sci.* 89, pp. 110-122.

Cooper, A.F. (1996): Nb-rich baotite in carbonatites and fenites at Haast River, New Zealand. *Mineral. Mag.* 60, pp. 473-482.

Dawson, J.B and Smith, J.V. (1977): The MARID (mica-amphibole-rutile-ilmenite-diopside) suite of xenoliths in kimberlite. *Geochim. Cosmochim.* Acta. 41, pp. 390-323.

Deer, W.A, Howie, R.A, and Zussman, J. (2001): *Rock-Forming Minerals. Framework Silicates: Feldspars,* Vol. 4A, 2nd ed., The Geological Society of London, U.K., 972 p.

DeMartin, F., Pilati, T., Diella, V., Donzelli, S., Gentile, P. and Gramaccioli, C.M. (1991): The chemical composition of xenotime from alpine fissures and pegmatites in the Alps. *Can. Mineral.* 29, pp. 69-75.

Devaraju, T.C., Raith, M.M. and Spiering, B. (1999): Mineralogy of the Archean barite deposit of Ghattishosahalli, Karnataka, India. *Can. Mineral.* 37, pp. 603-617.

Droop, G.T.R. (1987): A general equation for estimating Fe^{3+} concentrations in ferromagnesian silicates and oxides from microprobe analyses, using stoichiometric criteria. *Miner. Mag.* 51, pp. 431-435.

Eby, G.N. (1973): Scandium geochemistry of the Oka carbonatite complex, Oka, Quebec. *Am. Mineral.*, 58, pp. 819-825.

van Emden, B., Thornber, M.R., Graham, J. and Lincoln, F.J. (1997): The incorporation of actinides in monazite and xenotime from placer deposits in western Australia. *Can. Mineral.* 35, pp. 95-104.

Ercit, T.S. (2002): The mess that is "allanite" *Can. Mineral.* 40, pp. 1411-1419.

Evans, H.T. and Garrels, R.M. (1958): Thermodynamic equilibria of vanadium in aqueous systems as applied to the interpretation of the Colorado Plateau ore deposits. *Geochim. Cosmochim. Acta* 15, pp. 131-149.

Farges, F. and Calas, G. (1991): Structural analysis of radiation damage in zircon and thorite: an X-ray absorption spectroscopic study. *Am. Mineral.* 76, pp. 60-73.

Ferguson, A.K. and Cundari, A. (1982): Feldspar crystallization trends in leucite-bearing and related assemblages. *Contrib. Mineral. Petrol.* 81, pp. 212-218.

Finch, R.J., Hawthorne, F.C. and Ewing, R.C. (1998): Crystallographic relations among schoepite, metaschoepite and dehydrated schoepite. *Can. Mineral.* 36, pp. 831-845.

_____. and Murakami, T. (1999): Systematics and paragenesis of uranium minerals. In: *Uranium: Mineralogy, Geochemistry and the Environment.* (P.C. Burns and R. Finch Eds.), Reviews in Mineralogy v. 38. Mineral. Soc. Am. pp. 91-180.

Flohr, M.J. and Ross, M. (1990): Alkaline igneous rocks of Magnet Cove, Arkansas: mineralogy and geochemistry of syenites. *Lithos*, 26, pp. 67-98.

_____. (1994): Titanium, vanadium and niobium mineralization and alkali metasomatism from the Magnet Cove Complex, Arkansas. *Econ. Geol.* 89, pp. 105-130.

Foley, S., Höffer, H. and Brey, G. (1994): High-pressure synthesis of priderite and members of the lindsleyite – mathiasite and hawthorneite – yimengite series. *Contrib. Mineral. Petrol.* 117, pp. 164-174.

Förster, H.J. (1998*a*): The chemical composition of REE-Y-Th-U-rich accessory minerals in peraluminous granites of the Erzgebirge-Fichtelgebirge region, Germany. Part I. The monazite-(Ce)-brabantite solid solution series. *Am. Mineral.* 83, pp. 259-272

_____. (1998*b*): The chemical composition of REE-Y-Th-U-rich accessory minerals in peraluminous granites of the Erzgebirge-Fichtelgebirge region, Germany. Part II. Xenotime. *Am. Mineral.* 83, pp. 1302-1315.

_____. (2001): Thorite-zircon-coffinite-xenotime solid solutions: composition and origin. (Abs.) European Union of Geosciences Convention XI. Physiochemical Behavior of Accessory Minerals, p. 676.

Fortey, N.J. and Beddoe-Stephens, B. (1982): Barium silicates in stratabound Ba-Zn mineralization in the Scottish Delaradian. *Mineral. Mag.* 46, pp. 63-72.

_____., Coats, J.S., Gallagher, M.J., Smith, C.G. and Greenwood, P.G. (1993): New strata-bound barite and base metals in the Middle-Dalaradian rocks near Braemar, northeast Scotland. *Trans. Inst. Mining Metall., Sect. B: Appl. Earth Sci.* 102, pp. 55-64.

Franz, G., Andrehs, G. and Rhede, D. (1996): Crystal chemistry of monazite and xenotime from Saxothuringian-Moldanubian metapelites, NE Bavaria, Germany. *Eur. J. Mineral.* 8, pp. 1097-1118.

Garrels, R.M. and Christ, C.L. (1959): Behoavior of uranium minerals during oxidation. In: *Geochemistry and Mineralogy of the Colorado Plateau Uranium Ores.* (R.M. Garrels and E.S. Larsen Eds.), US Geol. Surv. Prof. Paper 320. pp. 81-89.

Gatehouse, B.M., Grey, I.E., Campbell, L.H. and Kelly, P.R. (1978): the crystal structure of loveringtonite-a new member of the crichtonite group. *Am. Mineral.* 63, pp. 28-36.

_____., Grey, I.E. and Kelly, P.R. (1979): The crystal structure of davidite from Arizona. *Am. Mineral.* 64, pp. 1010-1017.

Gay, P. and Roy, N.N. (1968): The mineralogy of the potassium-barium feldspar series.III. Subsolidus relationships. *Mineral. Mag.* 36, pp. 914-932.

Goldschmidt, V.M. and Peter, C. (1931): Zur Geochemie des Scandium. Nachrichten von der königlichen Gesellschaft der Wissenschaffen zü Gottingen-Geologie und Mineralogie IV, pp. 257-259.

Gramaccioli, C.M, Diella, V., Demartin, F., Orlandi, P and Campostrini, I. (2000*a*): Cesian bazzite and thortveitite from Cuasso Al Monte, Varese, Italy: A comparison with the material from Baveno and inferred origin. *Can. Mineral.* 38, pp. 1409-1418.

_____, Diella, V. and Demartin, F. (2000*b*): The formation of scandium minerals as an example of the role of complexes in the geochemistry of rare earths and HFS elements. *Eur. J. Mineral.* 12, pp. 795-808.

Grew, E.S. (2002): Mineralogy, petrology and geochemistry of beryllium: an introduction and list of beryllium minerals. In: *Beryllium: Mineralogy, Petrology and Geochemistry.* (E.S. Grew Ed.), Reviews in Mineralogy and Geochemistry 50, Mineral. Soc. Am. pp. 1-76.

Grey, I.E. and Lloyd, D.J. (1976): The crystal structure of senaite. *Acta Crystallogr.* B32, pp. 1509-1513.

_____., Lloyd, D.J. and White, Jr., J.S. (1976): The crystal structure of crichtonite and its relationship to senaite. *Am. Mineral.* 61, pp. 1203-1212.

Guo, J. and Green, T.H. (1989): Barium partitioning between alkali feldspar and silicate liquid at high pressures and temperatures. *Contrib. Mineral. Petrol.*, 102, pp. 328-335.

Haggerty, S.E. (1991): Oxide mineralogy of the upper mantle. In: *Oxide Minerals: petrologic and magnetic significance.* (D.H. Lindsley Ed.), Reviews in Mineralogy 25, Mineral. Soc. Amer., pp. 335-416.

_____. and Gurney, J.J. (1984): Zircon-bearing nodules from the upper mantle, (Abs.) EOS *Trans. Am. Geophys.* Union 65, pp. 301.

Hamilton, R. and Rock, N.M.S. (1990): Geochemistry, mineralogy and petrology of a new finds of ultramafic lamprophyres from Bulljah Pool, Nabberu Basin, Yilgarn Craton, Western Australia. *Lithos*, 24, pp. 275-290.

Hawthorne, F.C. and Huminicki, D.M.C. (2002): The crystal chemistry of beryllium. In: *Beryllium: Mineralogy, Petrology and Geochemistry.* (E.S. Grew Ed.), Reviews in Mineralogy and Geochemistry 50, Mineral. Soc. Am. pp. 333-404.

Heaman, L.M. and Machado, N. (1987): Isotope geochemistry of the Coldwell alkaline complex I- U-Pb studies of accessory minerals. *In*: Program with Abstracts, Geological Association of Canada-Mineralogical Association of Canada, 12, pp. 54.

_____. and _____. (1992): Timing and origin of midcontinent rift alkaline magmatism, North America: evidence from the Coldwell Complex. *Contrib. Mineral.Petrol.* 110, pp. 289-303.

Hughes, J.M., Cameron, M. and Crowley, K.D. (1991): Ordering of divalent cations in the apatite structure: crystal structure refinements of natural Mn- and Sr-bearing apatite. *Am. Mineral.* 76, pp. 1857-1862.

Iimori, S. and Hata, S. (1938): Japanese thorogummite and its parent material. *Scientific Papers of the Institute of Physical and Chemical Research* 34, pp. 447-454.

Jakobsen, U.H. (1990): A hydrated barium silicated in unmetamorphosed sedimentary rocks of central North Greenland. *Mineral. Mag.* 54, pp. 81-89.

Jefford, G. (1962): Xenotime from Rayfield, northern Nigeria. *Am. Mineral.* 47, pp. 1467-1472.

Johan, Z. Johan, V. and Besson, M. (1991): Tungsten-bearing baotite from Pierrefitte, Pyrenes, France. *Mineral. Petrol.* 45, pp. 19-27.

Kalenov, A.D. (1961): Certain features of the accumulation of scandium. *Geokhimiya*, 3, pp. 241-251.

Kelly, P.R., Campbell, I.H., Grey, I.E. and Gatehouse, B.M. (1979): Additional data on loveringtonite (Ca,REE)(Ti,Fe,Cr)$_{21}$O$_{38}$ and mohsite discredited, *Can. Mineral.* 17, pp. 635-638.

Kennedy, M.C. and Sherlock, E.J. (1989): Northwest region industrial minerals program 1988. *In* Report of Activities 1988, Resident Geologists. Ontario Geological Survey, Miscellaneous Paper 142, pp. 157-180.

Khomyakov, A.P., Lisitsyn, D.V., Kulikova, I.M. and Rastsvetaeva, R.K. (1996): Deloneite-(Ce) NaCa$_2$SrCe(PO$_4$)$_3$F –a new minerals with a belovite-like structure. *Zap. Vser. Mineral. Obshchest.*, 125, pp. 83-94.

Klein, C. (2002): *The 22nd Edition of the Manual of Mineral Science.* John Wiley and Sons, USA, 641 p.

Knox, A.W. (1987): Geology and rare element mineralization, Dead Horse Creek yttrium property, Ontario. Unpublished report, Unocal Canada Ltd., 81 p.

van Kooten, G. (1980): Mineralogy, petrology and geochemistry of an ultrapotassic basaltic suite, central Sierra Nevada, California, U.S.A. *J. Petrol.*, 21, pp. 651-684.

Kribek, B., Hladíková, J., Zák, K., Pudilová, M. and Uhlík, Z. (1996): Barite-hyalophane sulfidic ores at Rozna, Bohemian Massif, Czech Republic: metamorphosed black-shale hosted submarine exhalative mineralization. *Econ. Geol.* 91, pp. 14-35.

Langmuir, D. (1978): Uranium solution-minerals equilibria at low temperatures with applications to sedimentary ore deposits. *Geochim. Cosmochim. Acta* 42, pp. 547-569.

Langworthy, A.P. and Black, L.P. (1978): The Mordor Complex: a highly differentiated potassic intrusion with kimberlitic affinities in Central Australia. *Contrib. Mineral. Petrol.* 67, pp. 51-62.

Larsen, J.G. (1981): Medium pressure crystallization of a monchiquitic magma - evidence from megacrysts of Drever's block, Ubekendt Ejland, West Greenland. *Lithos*, 14, pp. 241-262.

LeCheminant, A.N., Miller, A.R. and LeCheminant, G.M. (1987): Early Proterozoic alkaline igneous rocks, District of Keewatin, Canada: petrogenesis and mineralization. In: *Geochemistry and mineralization of Proterozoic volcanic rocks* (T.C. Pharaoh, R.D. Beckinsale and D. Rickard, Eds.) Geol. Soc. London Spec. Publ., 33, pp. 219-240.

Masau, M., Černý, P. and Chapman, R. (2000): Dysprosian xenotime-(Y) from the Annie claim #3 granitic pegmatite, southeast Manitoba, Canada: Evidence of the tetrad effect? *Can. Mineral.* 38, pp. 899-905.

_____., _____. and _____. (2000): Intergrowths of thorian coffinite with zircon from the Annie Claim #3 granite pegmatite, Southeastern Manitoba: Primary coprecipitation or exsolution? Annual Meeting of the Canadian Society of Exploration Geophysicists, Calgary AB. Abstracts.

Matsubara, S. (1985): The mineralogical implication of barium and strontium silicates. *Bull. Nat. Sci. Mus. Tokoyo, Ser.* C11(2), pp. 1-95.

McCready, A.J., Stumpfl, E.F. and Melcher, F. (2003): U/Th-rich bitumen in Archean granites and Paleoproterozoic metasediments, Rum Jungle Mineral Field, Australia: implications for mineralizing fluids. *Geofluids* 3, pp. 147-159.

McDonough, W.F. and Sun, S.-S. (1995): The composition of the Earth. *Chem. Geol.* 120, pp. 223-253.

McSwiggen, P.L., Morey, G.B. and Cleland, J.M. (1994): Occurrence and genetic implications of hyalophane in manganese-rich iron formation, Cuyuna Iron Range, Minnesota, USA. *Mineral. Mag.* 58, pp. 387-399.

Mellini, M., Merlino, S., Orlandi, P. and Rinaldi, R. (1982): Cascandite and jervisite, two new scandium silicates from Baveno, Italy. *Am. Mineral.* 67, pp. 599-603.

Mitchell, R.H. and Platt, R.G. (1977): *Field guide to aspects of the geology of the Coldwell alkaline complex.* Institute on Lake Superior Geology, 23rd Annual Meeting, Thunder Bay. Guide Book, 35 p.

_____. and _____. (1978): Mafic mineralogy of ferroaugite syenites from the Coldwell alkaline complex, Ontario, Canada. *J. Petrol.*, 19. pp. 627-651.

_____. and _____. (1982*a*): The Coldwell alkaline complex. *In: Proterozoic geology of the Northern Lake Superior area.* J.M. Franklin Ed., Geological Association of Canada, Field Trip Guide Book 4, pp. 42-61.

_____. and _____. (1982*b*): Mineralogy and petrology of nepheline syenites from the Coldwell alkaline complex, Ontario, Canada. *J. Petrol.*,23, p. 183-214.

_____., _____. and Cheadle, S.P. (1983): A gravity study of the Coldwell Complex, northwestern Ontario and its petrological significance. *Can. J. Earth Sci.*, 20, pp. 1631-1638.

_____., Yakovenchuk, V.N., Chakhmouradian, A.R., Burns, P.C. and Pakhomovsky, Y.A. (2000): Henrymeyerite, a new hollandite-type Ba-Fe titanate from the Kovdor Complex, Russia. *Can. Mineral.* 38, pp. 617-626.

Montero, P., Floor, P. and Corretgé, G. (1998): The accumulation of rare-earth and high-field strength elements in peralkaline granitic rocks: the Galineiro orthogneissic complex, Northwestern Spain. *Can. Mineral.*, 36, pp. 683-700.

Moro, M.C, Cembranos, M.L. and Fernandez, A. (2001): Celsian, (Ba,K)-feldspar from Sedex barite deposits of Zamora, Spain. *Can. Mineral.* 39, pp. 1039-1051.

_____., Perez Del Villar, L. and Cembranos, M.L. (1994): Stratiform barite ore deposits in Paleozoic rocks, Provincce of Zamora (Spain). *In: Metallogeny of Collisional Orogens* (R. Seltmann, H. Kämpf and P. Möller, eds.). Czech Geological Survey, Prague, Czech Republic, pp. 376-382.

Mumpton, F.A. and Roy, R. (1961): Hydrothermal stability of the zircon-thorite group. *Geochim. Cosmoschim. Acta* 21, pp. 217-238.

Nakamura, Y and Yoder, H.S. Jr. (1973): Analcite, hyalophane and phillipsite from the Highwood Mountains, Montana. *Carnegie Inst. Wash. Yearbook*, 72, pp. 354-358.

Neese, W.D. (2000): *Introduction to Mineralogy.* Oxford University Press, New York. 442 p.

Nekarsov, Y.V., Ponomarev, V.I., Simonov, V.I. and Kheiker, D.M. (1970): Refinement of the atomic structure of baotite and the isomorphic relationships in this mineral. *Sov. Phys. Crystallogr.*,, 14, pp. 508-514.

Nemec, D. (1987): Baotite- a rock-forming mineral of Ba-rich hyperpotassic dyke rocks. *Neues Jahrb. Mineral, Mh.* pp. 31-42.

Nicholson, K. (1992): Contrasting mineralogical-geochemical signatures of manganese oxides: guides to Metallogenesis. *Econ. Geol.* 87, pp. 1253-1264.

Onac, B.P. Veni, G. and White, W.B. (2001): Depositional environment of metatyuyamunite and related minerals from Caverns of Sonora, TX. *European Jour. of Mineral.* 13, pp. 135-143.

Orlandi, P., Pasero, M., Duchi, G. and Olmi, F. (1997): Dessauite, $(Sr,Pb)(Y,U)(Ti,Fe^{3+})_{20}O_{38}$, a new mineral of the crichtonite group from Buca della Vena mine, Tuscana, Italy. *Amer. Mineral.* 82, pp. 807-811.

Ossa, A.C. (1970): Genesis of manganese deposits in northern Chile, *Econ. Geol.* 65, pp. 681-689.

Pan, Y. and Fleet, M.E. (1990): Metamorphism, geochemistry, skarn development and gold mineralization in the White River gold prospect, Hemlo area. *Ont. Geol. Surv., Misc. Pap.* 150, pp. 13-26.

___. and _____. (1991): Barian feldspar and barian-chromian muscovite from the Hemlo area, Ontario. *Can. Mineral.* 29, pp. 481-498.

___. and _____. (1992): Mineral chemistry and geochemistry of vanadian silicates in the Hemlo gold deposit, Ontario, Canada. *Contrib. Mineral. Petrol.* 109, pp. 511-525.

___. and _____. (1995): The late Archean Hemlo fold deposit, Ontario, Canada: a review and synthesis. *Ore Geology Reviews* 9, pp. 455-488.

Pavlishin, V.I., Baklan, F.G., Bugaenko, V.M., Voznyak, D.K., Galaburda, Yu, A., Dekhtulins'ky, E.S., Donskey, O.M., Krivdik, S.G., Kulchic'ka, G.O., Mel'nikov, V.S., Radzivill, A, Ya. and Zimbal, S.M. (2000): Science-based perspectives of improvement of mineral resources or rare metals in Ukraine. *Mineral. Journal* 22, pp.5-20. (in Russian)

Peishan, Z., Zhuming, Y., Kejie, T. and Xueming, Y. (1995): *Mineralogy and Geology of Rare Earths in China.* Science Press, Beijing, China. 209 p.

Peng, Ch'i-Jui (1950): The discovery of several new minerals of rare elements. *Amer. Mineral.* 45, p. 745.

Petersen, O.V., Randløv, J., Leonardsen, E.S. and Rønsbo, J.G. (1991): Barylite from the Ilímaussaq alkaline complex and associated fenites, South Greenland. *N. Jahrb. Mineral. Monatsh.* 1991, pp. 212-216.

Platt, R.G. and Mitchell, R.H. (1996): Transition metal rutiles and titanates from the Deadhorse Creek Diatreme complex, northwestern Ontario, Canada. *Miner. Mag.* 60, pp. 403-413.

_____. and Wooley, A.R. (1990): The carbonatites and fenites of Chipman Lake, Ontario. *Can. Mineral.* 28, pp. 241-250.

Pointer, C.M., Ashworth, J.R. and Ixer, R.A. (1988*a*): The zircon-thorite group in metasomatized granite, Ririwai, Nigeria 2. Zoning, alteration and exsolution of zircon. *Mineral. Petrol.* 38, pp. 21-37.

_____., _____. and _____. (1988*b*): The zircon-thorite mineral group in metasomatized granite, Ririwai, Nigeria 1. Geochemistry and metastable solid solution of thorite and coffinite. *Mineral Petrol.* 38, pp. 245-262.

Pollock, S.J. (1987): The isotopic geochemistry of the Prairie Lake carbonatite, Ontario. Unpublished MSc thesis, Carleton University, Ottawa, Ontario, 71 p.

Polyak, V.J. and Mosch, C.J. (1995): Metatyuyamunite from Spider Cave, Carlsbad Caverns National Park, New Mexico. *NSS Bulletin* 57, no. 2, pp. 85-90.

Potter, R.W., II and Brown, D.L. (1977): The volumetric properties of aqueous sodium chloride solutions from 0 to 500 °C at pressures up to 2000 bars based on a regression of available data in the literature. *U.S. Geol. Surv. Bull.* 1421-C.

_____, Clynne, M.A. and Brown, D.L. (1978): Freezing point depression of aqueous sodium chloride solutions. *Econ. Geol.* 73, pp. 284-285.

Pouit, G. and Bois, J.P. (1986): Arrens Zn(Pb), Ba Devonian deposits, Pyrénées, France: an exhalative-sedimentary type deposit similar to Meggen. *Mineral. Deposita* 21, pp. 181-189.

Pushcharovskii, D.Yu., Nadezhina, T.N. and Khomyakov, A.P. (1987): Crystal structure of strontium-apatite from Khibiny. *Sov. Phys. Crystallogr.*, 32, pp. 524-526.

Quandt, U. and Herr, W. (1974): Beryllium abundance in meteorites determined by 'non-destructive" photon activation. *Earth Planet Sci. Lett* 24, pp. 53-58.

Rapp, R.P. and Watson, E.B. (1986): Monazite solubility and dissolution kinetics: implications for the thorium and light rare earth chemistry of felsic magmas. *Contrib. Mineral. Petrol.* 94, pp. 304-316.

Rakovan, J.F. and Hughes, J.M. (2000): Strontium in the apatite structure: strontian fluorapatite and belovite-(Ce). *Can. Mineral.*, 38, pp. 839-845.

Reinecke, T. (1982): Cymrite and celsian in manganese-rich metamorphic rocks from Andros Island, Greece. *Contrib. Mineral. Petol.* 79, pp. 333-336.

Reznitskii, L.Z., Sklyarov, E.V. and Ushchapovskaya, Z.F. (1985): Natalyite $Na(V,Cr)Si_2O_6$, a new chromian-vanadian pyroxene from Sludyanka. *Proceeding Russian Mineralogical Society,* 114, pp. 630-635.

Ringwood, A.E., Kesson, S.E., Ware, N.G., Hibberson, W. and Major, A. (1979): Immobilisation of high level nuclear reactor wastes in SYNROC. *Nature* 278, pp. 219-223.

Rizvanova, N.G., Levchenko, O.A., Belous, A.E., Bezman, N.I., Maslenikov, A.V., Komarov, A.N., Makeev, A.F. and Levisky, L.K. (2000): Zircon reaction and stability of the U-Pb isotope system during interaction with carbonate fluid: experimental hydrothermal study. *Contrib. Mineral. Petrol.* 139, pp. 101-114.

Roelofsen-Ahl, J.N. and Petersen, R.C. (1989): Gittinsite: a modification of the thortveitite structure. *Can. Mineral.* 27, pp. 703-708.

Rouse, R.C. and Peacor, D.R. (1968): The relationship between senaite, magnetoplumbite and davidite. *Am. Mineral.* 53, pp. 869-879.

Sage, R. P. (1982): Mineralization in diatreme structures north of Lake Superior. Ontario Geological Survey Study 27, Ontario Ministry of Natural Resources, Toronto, 79 p.

_____. (1985): geology of carbonatite-alkalic rock complexes of Ontario, Chipman Lake area, districts of Thunder Bay and Cochrane. Ontario Geological Survey, Study 44, 40 pp.

_____. (1991): Alkalic rock, carbonatite and kimberlite complexes of Ontario, Superior Province. *In: Geology of Ontario*, Ontario Geological Survey, Special Volume 4, pp.683-709.

Sahama, T.G. (1978): Niobian rutile from Miuane, Mozambique. *Jornal de Mineralogia Recife* 7, pp. 115-118.

Sarp, H., Bertrand, J., Deferne, J. and Liebich, B.W. (1981): A complex rhenium-rich titanium and iron oxide of the crichtonite-senaite group. *Neues Jahrbuch für Mineralogie Mh.* 10, pp. 433-443.

Schneiders, B.R. and Smyk, M.C. (1989): Scheiber-Hemlo resident geologists district. *In:* Report of Activities 1988, Resident Geologists. Ontario Geological Survey, Miscellaneous Paper 142, pp. 133-156.

Shock, E.L., Sassani, D.C. and Betz, H. (1997): Uranium in geologic fluids: estimates of standard partial molal properties, oxidation potentials and hydrolysis constants at high temperatures and pressures. *Geochim. Cosmochim. Acta* 61, pp. 4245-4266.

Secco, L., Martignago, F., Dal Negro, A., Reznitskii, L.Z. and Sklyarov, E.V. (2002): Crystal chemistry of Cr^{3+}-V^{3+}-rich clinopyroxenes. *Am. Mineral.*, 87, pp. 709-714.

Semenov, E.I., Khun, Ven-Sin, and Kapitonova, T.A. (1961): Baotite, a new niobian mineral. *Dokl. Akad. Nauk* USSR. 136, pp. 915-916.

Shurgia, T.N., Piabeva, E.G. and Dubakina, L.S. (1980): Baotite, a new find in the USSR. *Dokl. Akad. Nauk SSSR*, 252, pp. 1220-1223.

Smith, D.K. Jr. (1984): Uranium mineralogy. In: *Uranium Geochemistry, Mineralogy, Geology, Exploration and Resources.* (B. DeVivo, F. Ippolito, G. Capaldi, P.R. Simpson Eds.), Institute of Mining and Metallurgy, London, pp. 43-88.

Smolin, Yu.I. and Shepelev, Yu.F. (1970): The crystal structures of the rare earth pyrosilicates. *Acta Crystallogr.* B26, pp. 484-492.

Smyk, M.C., Taylor, R.P., Jones, P.C. and Kingston, D.M. (1993): Geology and geochemistry of the west Deadhorse Creek rare-metal occurrence, northwestern Ontario. *Explor. Mining Geol.* 2, pp. 245-251.

Stern, T.W., Stieff, L.R., Girhard, M.N. and Meyrowitz, R. (1956): The occurrence and properties of metatyuyamunite, *Kemi* 1, pp. 337-351.

Tollo, R.P. and Haggerty, S.E. (1987): Nb-Cr rutile in the Orapa kimberlite, Botswana. *Can. Mineral.* 25, pp. 251-264.

Ushakov, S.V., Gong, W., Yagovkina, M.M., Helean, K.B., Lutze, W. and Ewing, R.C. (1999): Solid solutions of Ce, U and Th in zircon. *Ceram. Trans.* 93, pp. 357-363.

Valeyev, O.K. (1996): Complex scandium–vanadium-iron ores of the Pervomayskoye deposit of the Krivoy Rog basin, *Doklady Akademii Nauk Ukrainy* 5, pp. 85-89.

Valter, A.A., Khomenko, V.M., Sharkin, O.P. and Yakolev, V.M. (1994): A vanadian aegirine in alkaline metasomatites from Zheltye Vody. *Doklady Akademii Nauk Ukrainy* 3, pp. 110-116. (in Russian)

Vasconcelos, P.M. (1999): K-Ar and $^{40}Ar/^{39}Ar$ geochronology of weathering processes. *Annual Review of Earth and Planetary Sciences*, 27, pp. 183-229.

Voloshin, A.V. and Pakhomovskii, YA, A. (1986): *Minerals and Evolution of Mineral Formation in the Amazonitic Pegmatites of the Kola Peninsula.* Nauka Press, Leningrad, Russia. (in Russian).

_____., _____., and Tyusheva, F.N. (1983): Keiviite, $Yb_2Si_2O_7$, a new ytterbium silicate from amazonite pegmatites of the Kola Peninsula. *Mineral. Zh.* 5,pp. 94-99 (in Russian).

_____., _____., and _____. (1985): Keiviite-(Y)- a new yttrium diorthosilicate, and thalénite from amazonite pegmatites of the Kola Peninsula. Diortho- and triorthosilicates of yttrium. *Mineral. Zh.* 7, pp. 79-94 (in Russian).

Walker, J.W.R. (1967): Geology of the Jackfish-Middleton area, District of Thunder Bay. Ontario Department of Mines, Report 50. 41 p.

Wanty, R.B. and Goldhaber, M.B. (1992): Thermodynamics and kinetics of reactions involving vanadium in natural systems: accumulation of vanadium in sedimentary rocks. *Geochim. Cosmochim. Acta* 56, pp. 1471-1483.

Waychunas, G.A. (1991): Crystal chemistry of oxides and oxyhydroxides. In: *Oxide Minerals: petrologic and magnetic significance.* (D.H. Lindsley Ed.), Reviews in Mineralogy, 25, Mineral. Soc. Amer., pp. 11-68.

Weiblen, P.W. (1982): Keweenawan intrusive igneous rocks. *In: Geology and tectonics of the Lake Superior basin.* R.J. Wold and W.J. Hinze Eds. Geological Society of America, Memoir 156, pp. 57-82.

Whitney, J.A., Dorais, M.J., Stormer, J.C.Jr., Kline, S.W. and Matty, D.J. (1988): Magmatic conditions and development of chemical zonation in the Carpenter Ridge tuff, Central San Juan volcanic field, Colorado. *Amer. J. Sci.* 288, pp. 16-44.

Zak, K., Dobes, P and Vrana, S. (1997): Formation conditions of various calcite types and unusual alteration products of wollastonite in calcite marble near Nezdice (varied group of moldanubicium), Czech Republic. *Czech Geol. Soc.*, 42, pp. 17-25

Zhang, J., Ko, J., Hazen, R.M. and Prewitt, C.T. (1993): High-pressure crystal chemistry of $KAlSi_3O_8$ hollandite. *Am. Mineral.* 79, pp. 493-499.

Zhang, M., Suddaby, P., Thompson, R.N. and Dungan, M.A. (1993): The origins of contrasting zoning patterns in hyalophane from olivine leucitites, Northeast China. *Mineral. Mag.* 57, pp. 565-573.

APPENDIX A: ICP-MS Results of Rare-Earth Elements Concentrations within the Complex.

SAMPLE #	La	Ce	Pr	Nd	Pm	Sm	Eu	Gd	Tb	Dy	Ho	Er	Tm	Yb	Lu
87 BUN-01	48	94	12	50	-	25	14	63	23	210	58	230	42	325	53
87 BUN-02	10	27	4	21	-	8	4	16	5.2	40	9	30	5	33	5
87 BUN-03	8	23	4	20	-	9	4	19	5.9	43	10	32	5	35	5
87 BUN-04	140	305	36	125	-	21	5	21	5	34	6	16	2	11	2
87 BUN-05	255	505	60	205	-	38	13	45	9	47	8	19	2	12	2
88 BDH-01	12	11	1	5	-	2	1	5	2	14	4	11	2	15	2
88 BDH-03	12	28	3	14	-	5	2	9	3	17	3	10	2	12	2
88 BDH-04	5.7	11	1	5	-	2	0.58	3	1	10	2	6	1	5	1
88 BDH-05	14	48	8	53	-	44	24	110	36	280	59	170	27	195	26
88 BDH-07	8.7	27	4	25	-	12	8	29	10	92	22	70	12	84	11
88 BDH-08	10	20	2	6	-	1	0	1	0	1	0	1	0	1	0
88 BDH-09	310	605	69	260	-	47	14	47	9	52	9	24	3	19	3
88 BDH-11	720	1375	130	445	-	54	15	52	11	76	14	42	6	40	6
88 BDH-12	110	220	26	96	-	18	5	15	3	19	4	9	1	7	1
88 BDH-01Dup	11	11	1	5	-	2	1	5	2	14	3	11	2	15	2
Chondrite	0.237	0.637	0.0928	0.457	-	0.148	0.0563	0.199	0.0361	0.246	0.0546	0.16	0.0247	0.161	0.0246

Note: all values given in parts per million (ppm). Values obtained from authors of Smyk *et al.* (1993). Analyses were made at the Ontario Geoscience Laboratories using the ICP-OES technique after stepwise acid digestion (HF-$HClO_4$-HCl). The chondrite values from McDonough and Sun (1995) were used in the normalization.

APPENDIX B: Chondrite-normalized Rare-Earth Concentrations used to Generate Figure 1.4.

Sample #	La	Ce	Pr	Nd	Pm	Sm	Eu	Gd	Tb	Dy	Ho	Er	Tm	Yb	Lu
87 BUN-01	203	148	129	109	-	169	249	317	637	854	1062	1438	1700	2019	2154
87 BUN-02	42	42	44	46	-	55	62	80	144	163	159	188	186	205	187
87 BUN-03	35	36	40	44	-	61	73	95	163	175	179	200	202	217	203
87 BUN-04	591	479	388	274	-	142	96	106	139	138	115	100	73	68	65
87 BUN-05*	1076	793	647	449	-	257	231	226	235	191	141	119	89	75	61
88 BDH-01	51	17	11	10	-	14	21	24	44	57	64	69	81	93	85
88 BDH-03	51	44	36	31	-	32	39	45	69	69	62	63	65	75	69
88 BDH-04	24	17	13	11	-	11	10	16	33	41	40	38	34	30	26
88 BDH-05	59	75	91	116	-	297	426	553	997	1138	1081	1063	1093	1211	1057
88 BDH-07	37	42	45	55	-	81	144	146	277	374	403	438	486	522	447
88 BDH-08	42	31	21	13	-	6	4	4	5	5	5	5	5	5	5
88 BDH-09*	1308	950	744	569	-	318	249	236	244	211	170	150	134	118	114
88 BDH-11*	3038	2159	1401	974	-	365	266	261	305	309	256	263	255	248	248
88 BDH-12	464	345	280	210	-	122	91	75	75	77	68	58	49	42	33
88 BDH-01Dup	46	17	11	11	-	14	20	24	44	57	60	69	72	93	85

Note: Values were normalized to McDonough and Sun (1995); Bold-faced text and asterisk (*) indicate which samples were used to produce the graph.

APPENDIX C: Minerals Identified Within The Deadhorse Creek Complex.

Abundance	Main Mineralized Zone	Diatreme Breccia	Carbonatite Dike
Major:	Albite $NaAlSi_3O_8$	Potassium Feldspar $KAlSi_3O_8$	Calcite $CaCO_3$
(>20 modal %)	Calcite $CaCO_3$	Aegirine-Augite:	Dolomite - Ankerite:
	Potassium feldspar $KAlSi_3O_8$	$NaFeSi_2O_6$ - $CaMgSi_2O_6$	$(Ca,Mg)CO_3$ - $Ca(Fe,Mg)(CO_3)_2$
	Quartz SiO_2		Potassium Feldspar $KAlSi_3O_8$
Minor:	Apatite $Ca_5(PO_4)_3$	Apatite $Ca_5(PO_4)_3$	Chlorite $(Mg,Fe,Al)_6(Si,Al)_4O_{10}(OH)_8$
(5-15 modal %)	Dolomite $(Ca,Mg)CO_3$	Chlorite $(Mg,Fe,Al)_6(Si,Al)_4O_{10}(OH)_8$	Hematite Fe_2O_3
	HCaZr	Hematite Fe_2O_3	Pyrite FeS_2
	Phenacite $BeSiO_4$	Quartz SiO_2	Quartz SiO_2
	Titanite $CaTiOSiO_4$	Titanite $CaTiOSiO_4$	
	Zircon $ZrSiO_4$		
Trace:	Aegirine-jervisite $Na(Fe,Sc)Si_2O_6$	Allanite-Ce $(Ce,Ca,Y)_2(Al.Fe)_3(SiO_4)_3*(OH)$	Apatite $Ca_5(PO_4)_3$
(<5 modal %)	Aegirine-natalyite $Na(Fe,V)Si_2O_6$	Baotite $Ba_4(Ti,Nb)_8Si_4O_{28}Cl$	Barite $BaSO_4$
	Allanite-Ce $(Ce,Ca,Y)_2(Al.Fe)_3(SiO_4)_3*(OH)$	Barite $BaSO_4$	Calciobetafite? $Ca_2(Ti,Nb)_2(O,OH)_7$
	Anhydrite $CaSO_4$	Brabanite-Thorite $[CaTh(PO_4)_2 + ThSiO_4]$	Galena PbS
	Ba-Mn Hollandite $Ba(Mn^{4+},Mn^{2+})_8O_{16}$	Chalcopyrite $CuFeS_2$	HCaZr
	Barite $BaSO_4$	Cr-Hematite $(Fe,Cr)_2O_3$	Magnetite Fe_3O_4
	Barylite $BaBe_2Si_2O_7$	Galena PbS	Matraite Zns
	Biotite $K(Fe,Mg)_3(AlSi_3O_{10})(OH)_2$	Gersdorffite NiAsS	Monazite-Ce $(Ce,La,Th)PO_4$
	Ca-Mn-Silicate	Hematite Fe_2O_3	Calciosamarskite? $(Ca,Fe,Y,Y)NbO_4$

APPENDIX C: Continued.

Abundance	Main Mineralized Zone	Diatreme Breccia	Carbonatite Dike
Trace:	Chalcopyrite $CuFeS_2$	Hyalophane $(Ba,K)Si_3O_8$	Thorite $ThSiO_4$
	Chlorite $(Mg,Fe,Al)_6(Si,Al)_4O_{10}(OH)_8$	Ilmenite $FeTiO_3$	Uranophane? $Ca(UO_2)_2SiO_3$*2.5H2O
	Cobaltite CoAsS	Ilmenorutile $(Ti,Nb,Fe)O_2$	Xenotime YPO_4
	Coffinite $U(SiO_4)_{1-x}(OH)_x$	Magnesiocummingtonite $Mg_7Si_8O_{22}(OH)_2$	Zircon $ZrSiO_4$
	Crichtonite $(Sr,Y)(Ti,Fe,V)_{21}O_{38}$	Matraite (ZnS)	Scheelite $CaWO_4$
	Cummingtonite $(Mg,Fe)_7Si_8O_{22}(OH)_2$	Mn-ilmenite $(Fe,Mn)TiO_3$	
	Cuprite Cu_2O	Molybdenite MoS_2	
	Diopside $CaMgSi_2O_6$	Monazite-Ce $(Ce,La,Th)PO_4$	
	Enstatite $Mg_2Si_2O_6$	Rutile TiO_2	
	Eskolaite Cr_2O_3	Scheelite $CaWO_4$	
	Ferrosilite $(Fe,Mg)_2Si_2O_6$	Thorite $ThSiO_4$	
	Fluorite CaF_2	Thorogummite $Th(SiO_4)_{1-x}(OH)_{4x}$	
	Galena PbS	Zircon $ZrSiO_4$	
	Gedrite $Mg_5Al_2Si_6Al_2O_{22}(OH)_2$		
	Gersdorffite NiAsS		
	Glaucodot (Co,Fe)AsS		
	Hematite Fe_2O_3		
	Ilmenorutile $(Ti,Nb,V)O_2$		
	Johannsenite $CaMnSi_2O_6$		
	Kamacite (Fe,Ni)		
	Magnetite Fe_3O_4		
	Matraite ZnS		
	Mn-Ilmenite $(Fe,Mn)TiO_3$		

APPENDIX C: Continued

Abundance	Main Mineralized Zone	Diatreme Breccia	Carbonatite Dike
Trace:	Monazite-Ce $(Ce,La,Th)PO_4$		
	Pyrhotite $Fe_{1-x}S$		
	Pyrite FeS_2		
	Th-HCaZr		
	Thorite $ThSiO_4$		
	Thorogummite $Th(SiO_4)_{1-x}(OH)_{4x}$		
	Thortveitite $Sc_2Si_2O_7$		
	Titanite $CaTiOSiO_4$		
	Tyuyamunite $Ca(UO_2)_2V_2O_8*5\text{-}8H_2O$		
	U-HCaZr		
	Uraninite UO_2		
	Vanadian Spinel $Fe_{3-x}V_xO_4$		
	Vanadomalayaite $CaVOSiO_4$		
	Xenotime YPO_4		